THE UNIVERSITY of EDINBURGH
Institute for Materials and Processes
School of Engineering

Consolidant Particle Transport in Limestone, Concrete and Bone

Alanna S. Campbell

A thesis submitted to the University of Edinburgh
for the Degree of Doctor of Philosophy

March 2013

Declaration

I declare that this thesis has been composed by myself and is all my own work except where otherwise stated and has not been submitted for any other degree or professional qualification.

Alanna S. Campbell

March 2013

Acknowledgements

I would like to thank my supervisors Dr Andrea Hamilton and Professor Christopher Hall, both at the University of Edinburgh, for their support and advice. I also wish to acknowledge the assistance of the following people at the University of Edinburgh: Mr Mike Hall (for cutting stone samples), Dr Tim Stratford (for operating the Instron), Dr Gary Nichol (for permitting use of the D2 XRD when the D8 XRD was out of order), Mr Enzo Mangano (for instructing me on and then allowing me to operate the MIP), Dr Nicola Cayzer (for allowing me to operate the Philips XL30CP SEM-EDX system), Dr Christopher Jeffree (for granting access to the Hitachi 4700 SEM) and Mr Stephen Mitchell (for coating SEM samples and allowing me to operate the Hitachi 4700 SEM). Ms Sevasti Modestou and her Masters supervisor Dr Ioannis Ioannou, both at the University of Cyprus, are acknowledged for operating the Epslog Engineering WOMBAT Scratch Tool and the DRMS. Mr Jan Petrik is thanked for advice on thin section analysis. Dr Fiona Sillars at the University of Dundee is acknowledged for MIP operation allowing for my confirmation of my original bone MIP data. I would also like to thank Mr Martin Kierans at the University of Dundee (for coating SEM samples when our Gatan Alto 2500 cryo-preparation chamber was out of order).

I would also like to acknowledge the EPSRC Loan Pool for the loan of the Renishaw Raman InVia Microscope Spectrometer with thanks going in particular to Dr Richard Brownsword. Mr Mark Ware of Nanosight Ltd. is thanked for the session with the LM10. It is with much gratitude that I thank Dr Kath McSweeney at the University of Edinburgh for the provision of archaeological disarticulated human remains.

I would also like to acknowledge the funding source for this PhD which was the Engineering and Physical Sciences Research Council.

I am thankful to my colleague Isobel Griffin for her friendship. I am very grateful to my family, particularly Ms Anne Greep, for their support. This PhD would not have been possible without the continued support of my parents, James and Margaret, who are especially thanked.

Abstract

The use of chemically compatible nano and fine particle colloidal consolidants is a new development within the field of cultural heritage conservation and applied most widely so far to the historic built environment. The ability to introduce a significantly higher quantity of chemically compatible consolidant to a substrate in fewer treatments with the possibility for greater penetration and fewer possible side-effects compared to more established consolidants is a significant advantage.

This fundamental scientific study examines the effects of a colloidal calcium hydroxide (nanolime) consolidant on medieval and quarried limestone and autoclaved aerated concrete and the efficacy of a colloidal hydroxyapatite treatment on archaeological human bone. Both calcium hydroxide and hydroxyapatite were synthesised. Characterisation of both compounds was performed by X-ray diffraction spectroscopy and particle morphology was confirmed by electron microscopy. Particle size was determined by laser diffraction and particle tracking analysis techniques, used together to study these particle systems for the first time, and electron microscopy. The location of particles within treated substrates was established by electron and optical microscopy whilst effects on water transport were determined by imbibition experiments and numerical modelling. For the first time a modified sharp front model was applied to [particle-material]-material composites to aid the understanding of water transport in such materials. Mechanical testing was used to identify differences in material strength depending on treatment layer thickness and mercury intrusion porosimetry suggested extent of pore blocking.

It was found that non-classical effects occur in the calcium hydroxide system synthesised in this study and that particle stability can be influenced by reagent concentration. For the first time material sorptivity properties, modality and pore size distribution of Lincoln stone and archaeological bone are reported. The application of a nanolime consolidant to autoclaved aerated concrete allowed the nature of the particle transport through a highly complex material to be determined, showing that the particle concentration decreases with increasing penetration depth. Shallow nanolime particle penetration into limestone appeared ineffective on compressive strength. In a novel study the prospects of a hydroxyapatite consolidant treatment for

bone were also evaluated, finding the results to be inconclusive in this small study. For all consolidants a small reduction in material water sorptivity after treatment demonstrated the permeable nature of the treatment layer and suggests the avoidance of damage mechanisms due to highly restricted water transport. Knowledge of the efficacy and location of treatment particles and their affect on water movement, particularly in weathered material, within limestones and archaeological bone is important and was determined for all materials used in this study. This work adds to the understanding of such treatments and their capabilities and the nature of the porous materials used herein.

List of Tables

List of Figures

Contents

Chapter 1:

Introduction

This thesis aims to add to the scientific understanding of the particle transport of nano and fine particle consolidant suspensions through the porous media of limestone, autoclaved aerated concrete (AAC) and archaeological bone. This work has potential for applications in archaeology and conservation however, as this work provides a starting point, the techniques will need further development before they can be used in the field. Nanoparticles are becoming an increasingly valuable tool available to conservation scientists and conservators for preserving our cultural heritage for future generations. Due to this it is necessary to understand how these particles affect the materials they are used to conserve and how the materials affect particle movement.

Particles are generally classified according to diameter size where a diameter range from 2500 – 10000 nm are labelled coarse particles, fine particles cover a range from 100 – 2500 nm and a range of 1 – 100 nm are known as nanoparticles (or ultrafine particles) (Schwartz et al. 1999; Donaldson et al. 2004; BSI 2011; Potocnik 2011). However there is no internationally recognised size definition of a nanoparticle leading to nanoparticles being defined as such either according to material, field, application or a country's national standards (Hosokawa et al. 2012). Nanoparticles are a significant area of inorganic nanotechnology which is becoming increasingly important with ongoing research aimed at a wide variety of applications over many fields, from biomedical to electronics, in addition to that of the nanoparticles themselves (Zahn 2001; Baglioni et al. 2009; Abdullah et al. 2010; Webster et al. 2011).

Many inorganic compounds; from calcium based compounds such as calcium carbonate, calcium hydroxide and calcium sulphate, to magnesium hydroxide to hydroxyapatite can now be synthesised obtaining particles in the nanometer range (Baglioni & Giorgi 2006; Baglioni et al. 2006; Dei et al. 2006; Dei & Salvadori 2006; Mehra et al. 2007). There are many nanoparticle synthesis methods currently in use and it is not uncommon for there to be several methods for synthesising the one compound. Calcium hydroxide ($Ca(OH)_2$) nanoparticles are a good example of this in that they can be synthesised from elemental calcium, microemulsions, diols, and by precipitation from salt solutions (Ambrosi et al. 2001; Dei & Salvadori 2001; Dei & Nanni 2003; Ziegenbalg 2011). The reactions subsequently undertaken by

synthesised nanoparticles are also being studied with the carbonation of calcium hydroxide nanoparticles being one such example of this (Gomez-Villalba et al. 2010).

Despite detailed research on nanoparticles and nanotechnology only really occurring over the last half century, after the ideas behind nanoscience and nanotechnology were expressed by Richard Feynman in 1959, the discipline has grown to become a vast multidisciplinary field (Feynman 1992). Although modern science tends to claim nanoparticles, in actuality the first proven synthesis and use of such particles dates back to the Early Middle Ages (5^{th} – 10^{th} century) in Mesopotamia. Lustreware, pottery or porcelain with a metallic glaze coating, is so known due to the iridescent effect (or lustre) generated by the metallic nanoparticles of the glaze (Caiger-Smith 1985). Many museums currently house historic lustreware artefacts and some remaining buildings from the period contain lusterware tiles (Caiger-Smith 1985; British Museum 2012; Smithsonian Institution Collections 2012). When conserving such artefacts it should be beneficial to have a basic understanding of nanoparticles.

The safety of nanoparticles does cause a degree of concern due to the possible medical and environmental dangers posed by their use (Donaldson et al. 2004; Simeonova et al. 2007; Dimitrijević 2011). Due to the high surface to volume ratio such particles can be highly reactive and are capable of penetrating the cell membrane barrier of living organisms due to their size. As yet the risks posed by particle interactions with biological systems are largely unknown. As more research is carried out in this field it is reasonable to expect greater understanding of the health and environmental risks of nanoparticles to be obtained in the future.

Another area where much research is needed is that of particle transport. Particle movement through porous materials is an interesting area of study relevant to a wide range of fields and applications and is particularly prevalent within the environmental area especially within the field of waste disposal, such as nuclear waste (McDowell-Boyer et al. 1986; Baek & Pitt Jr 1996; Lavoie et al. 2011). The transport of contaminant particles through soil and bed rock is highly relevant as this can lead to contamination of groundwater aquifers resulting in unsafe water supplies.

It is well known that particle size, particularly in relation to pore diameter of the material, is of great importance regarding the transport abilities of a particle within a porous material as this will determine the ability of the particle to travel within the material pore structure (Cumbie & McKay 1999; Santos & Bedrikovetsky 2004).

Nanotechnology in general is also emerging in less common fields of practical science. One of the current fields where nanoparticle science is being used for significant real world applications is that of cultural heritage conservation (Baglioni 2006; Howe 2007; Baglioni 2009). Within the conservation field, there exists a wide range of subfields where nanoparticles are being developed and used, with current applications in stone, paper and wood conservation (Baglioni & Giorgi 2006; Baglioni et al. 2006; Giorgi et al. 2010; Kolinkeova et al. 2011).

Advantages in using nanoparticles are varied but tend to revolve around their size. With particles in the nanometer range, absorption into solid substances is greater which is desirable when consolidation of a substance/object is desired. This can be demonstrated with stone where the pore size can act as a sieve only allowing particles with a diameter smaller than the pores to enter the structure (Hirst 2011). Also the very small size of the particles in conjunction with the chemical compatibility of the particles with the solid substance (e.g. calcium hydroxide nanoparticles applied to limestone) suggests a more beneficial consolidation treatment (Lopez-Arce et al. 2009; Ziegenbalg 2011).

Recently a commercial nanolime treatment has been developed for stone conservation and is discussed in Chapter 2. Initial development and testing of this treatment has shown it to have great potential, however there are unanswered questions posed by conservators in the field. How large is the difference in the treatment capabilities between intact and weathered stone? If treating an artefact or building where the treatment can penetrate from the weathered layer into the undamaged layer below the surface, how would the different treatment effects on the two layers affect the whole object? Is the penetration depth of the treatment dependant on range of pore size or material structure? This thesis endeavours to add to the knowledge in this field.

Whilst a commercial nanolime treatment will be used in this study on porous building materials (limestones and AAC) the ease of obtaining stable $Ca(OH)_2$ particles via a wet synthesis method will be discussed to highlight the potential problems. The method will be investigated to determine how the reaction conditions affect the particle size distribution of the precipitated $Ca(OH)_2$ product. The particle size distributions of the synthesised $Ca(OH)_2$ and commercial nanolime will also be compared.

Many of the treatments currently used to conserve archaeological human remains are based on organic polymers or emulsions as is discussed in Chapter 2. Such treatments can, over time, have a detrimental effect on the bone causing, as an example, cracking. It is not uncommon for archaeologists and conservators in the field to wish for an alternative treatment which is chemically compatible. If one was to momentarily think of limestone conservation and the chemically compatible nanolime treatment created for this, one might pose the question as to why such a like for like treatment cannot be applied to archaeological bone. In this thesis this novel idea has been tested. By using a nano and fine particle hydroxyapatite (HAP) treatment on archaeological bone, which is hydroxyapatite, the thesis also aims to determine the feasibility of such a novel conservation treatment which is chemically compatible with the bone and, by its nature, ethically acceptable.

In summary, overall this thesis aims to answer the following questions:

- What is the nanolime penetration depth in a variety of porous building materials treated via capillary suction?
- Is the pore size range of a porous material or the nature if its structure a determining factor for nanolime treatment penetration depth?
- What are the effects of nanolime treatment on water movement within a variety of porous building materials?

- How does nanolime particle location and effects on water transport differ between medieval weathered, medieval unweathered and fresh quarried limestone?
- Does a hydroxyapatite suspension have the possibility to be a new chemically compatible conservation treatment for archaeological bone?

Chapter 2:
Literature Review and Background

2.1 Brief Overview of Particle Synthesis

Wet and dry syntheses are the main methods of synthesising nanoparticles. Wet synthesis refers to when the synthesis is performed in the liquid phase. Here crystallisation of particles occurs upon the mixing of liquid reagents. There are several types of wet synthesis including acid-base, sol-gel, hydrothermal and precipitation from salt solutions. In acid-base synthesis an acid and a base react to cause precipitation of a compound. Synthesis from a colloidal suspension reagent to give a network of polymers or particles is known as sol-gel synthesis. Crystallising compounds from aqueous solutions under high temperatures and vapour pressures is known as hydrothermal synthesis. In electrochemical methods, the synthesis is enhanced due to charge. Dry synthesis from powders can also be undertaken. Also deposition methods exist where a solid or powder undergoes chemical reactions within a plasma.

Several of these methods can be used to produce $Ca(OH)_2$ and HAP nanoparticles. $Ca(OH)_2$ can be produced from mixing salt and base solutions and from microemulsions and diols (Ambrosi et al. 2001; Dei & Salvadori 2001; Dei & Nanni 2003). HAP can be synthesised from salt reactions with acid, from diammonium hydrogen phosphate and calcium nitrate solutions and from mixing calcium hydroxide, dihydrogenphosphate and polymers in aqueous solution (Correia et al. 1996; Rao et al. 1997; Tseng et al. 2009). HAP has also been produced by the dry mechanical grinding of a mixture of dicalcium phosphate dihydrate and calcium oxide powders and by pseudomorphic replacement of calcium carbonate single crystals (Mochales et al. 2004; Kasioptas et al. 2008).

2.2 Brief Overview of Colloidal Particle Interactions

A suspension containing dispersed particles of between 1 nm to 1 μm in size which experiences slow sedimentation (up to several months) is called a colloidal system (ed. Goodwin 1982). Such suspensions often have a long shelf life, meaning that the particles exist in a stable state for a period of time. Such systems exist in two distinct types: monodisperse (where all the dispersed particles are approximately the same size) and polydisperse (where a range of particle sizes are present). Each system can be easily determined by particle sizing methods, such as laser diffraction (LD), as a monodisperse system will exhibit only a single peak in the particle size distribution (PSD) whilst polydisperse systems show two or more distinct peaks.

Agglomeration of particles occurs primarily due to van der Waals forces which cause particles to be attracted to each other. As larger particle clumps form they fall out of suspension and sediment.

Van der Waals forces are charge fluctuation forces which are caused by the fluctuation of magnetic fields and electric charges that exist within a material and between the material and its surrounding medium (e.g. a colloidal suspension). Charge fluctuation forces can alternatively be termed electrodynamic forces which include three forms of dipole-dipole interactions, each of which have free energies which vary with the inverse sixth power of the separation distance (Parsegian 2006).

In electric charge terms a dipole is a charge field over a molecule where two charges, q (positive) and –q (negative), exist and are separated by a distance l. The electric dipole moment, μ, is the product of the charge and distance. Permanent electric dipole moments exist when the molecule is polar whilst nonpolar molecules do not have permanent electric dipole moments but may instead gain temporary induced dipole moments. Such temporary dipoles occur when the electron field is temporarily polarised by a nearby polar molecule (Debye interaction) or fluctuations within the nonpolar molecule's electric field occur due to the movement of electrons (dispersion interaction, also known as London force) (Atkins 2001; Parsegian 2006).

The dispersion and Debye interactions are two varieties of the three dipole-dipole interactions with the other being the Keesom interaction which only concerns permanent dipoles (Parsegian 2006).

The interaction energy law (Equation 2-3) for two spheres based on van der Waals forces can be derived from the integration of the pair potential (Equation 2-1) assuming that the interaction occurs in a vacuum and is not retarded. The resulting interaction law contains the Hamaker constant (Equation 2-2) which typically has a value of about 10^{-19} J in a vacuum (Israelachvili 1991).

2-1) $$w(r) = -\frac{C}{r^6}$$

where w is the work or free energy, C is a positive coefficient and r is the distance.

2-2) $$A = \pi^2 C p_1 p_2$$

where A is the Hamaker constant, C is the coefficient from equation 2-1 and p_1 and p_2 are the number of atoms per unit volume present in sphere 1 and sphere 2.

2-3) $$W = \frac{-A}{6D} \frac{R_1 R_2}{(R_1+R_2)}$$

where W = work, A = Hamaker constant, D = distance, R_1 and R_2 are the radii of sphere 1 and sphere 2.

In a colloidal system there is a counter charge region of ions around a particle, known as the Stern layer, from the solution that adheres to the particle surface. Around the Stern layer is a second region, known as the diffuse layer, containing mobile ions of both charges. The combination of the counter charge region and the surrounding mobile ions is known as the double layer (Atkins & de Paula 2002). The Debye length ($1/\kappa$) is the thickness of the double layer and is determined by the properties of the liquid (Israelachvili 1991). Van der Waals forces can be screened when the Debye length is large allowing electrostatic forces to dominate. Likewise when the Debye length is small electrostatic forces have less effect on the system.

DLVO (Derjaguin-Landau-Verwey-Overbeek) theory includes non-retarded van der Waals forces and electrostatic double layer forces with the total potential energy, V_T, of the system being the product of the two components. Hydrogen bonding interactions and steric forces can also occur with steric forces dominating all forces at interparticle distances below 3 nm (Israelachvili 1991; Parsegian 2006), however these interactions and forces are not discussed here. In DLVO theory the van der Waals forces and electrostatic forces are separable (although in reality this is not actually the case).

The standard potential energy curve of DLVO, seen in Figure 2-1, is the resulting combination of both electrostatic and electrodynamic (van der Waals forces) parts of DLVO theory. Particles that are loosely aggregated occupy the secondary minimum and, due to the energy of this state, can be separated by agitation (stirring, etc.). The barrier represents the energy required for particles to go from the secondary minimum to the primary minimum. Once the energy barrier has been crossed into the primary minimum significant energy is required to re-cross the barrier. Such energy can be extremely difficult for particles to attain with the result that particles can be trapped in the primary minimum, the lowest energy state, causing the particles to become aggregated and the system sediments.

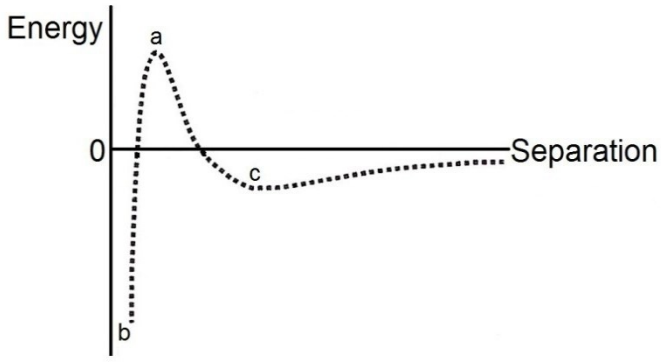

Figure 2-1: DLVO combined electrostatic electrodynamic energy versus separation curve. a = energy barrier, b = primary minimum and c = secondary minimum.

At high ionic strengths the double layer is compressed (small Debye length) and in the interaction energy curve of DLVO the potential energy barrier separating the primary and secondary minimums can decrease favouring van der Waals forces and the associated aggregation of the particles (Israelachvili 1991). Due to this electrostatic forces are screened at high ionic strength therefore they do not exist under these conditions due to the diffuse double layer. It is possible that molecules can occupy the secondary minimum however this is unlikely due to the agitation to the system under the reaction conditions used herein. Any secondary minimum particles that might be formed should be broken up by the system agitation. Electrodynamic forces (van der Waals) do exist under high ionic strength. Since these forces are responsible for particle agglomeration, particles should aggregate under high ionic strength conditions as there are no electrostatic forces present to maintain particle dispersion within the solution. It should be noted that over small distances van der Waals forces, largely unaffected by concentration and pH, will always be stronger than the repulsion of the double layer (Israelachvili 1991; Parsegian 2006).

2.3 Particle Sizing

Several methods for sizing particles exist, of which the most significant are discussed herein, many of which rely to a certain extent on light scattering. Light can interact with a particle in four ways: absorption, diffraction, reflection and refraction (Merkus 2009). The basis of light scattering is that light interactions with particles give rise to interference phenomena which in turn generate a distinctive scattering pattern (Merkus 2009). The intensity of light scattered, which affects the scattering pattern, at distinct angles depends on the particles' physical and optical properties (Merkus 2009). Light scattering of non-spherical particles depends on the particle orientation as different orientations generate different scattering patterns (Merkus 2009).

Several theories have been proposed to predict the scattering pattern of a particle although the main theories all work in the same way (Merkus 2009). If a particle's size and configuration is known, the way the particle scatters light can be accurately predicted generating a scattering pattern unique to that size of particle. The general expression for unpolarised light scattered by a spherical particle is given by Equation 2-4 (Merkus 2009),

2-4) $$I(\theta) = \frac{I_0}{2k^2a^2}\{[S_1(\theta)]^2 + [S_2(\theta)]^2\}$$

where $I(\theta)$ = total scattered intensity as a function of angle, θ = angle with respect to forward direction, I_o = intensity of incident light, k = wavenumber = $2\pi/\lambda$, a = distance from scatterer to detector, α = dimensionless size parameter = $\pi D/\lambda$, D = particle size, $S_1(\theta)$ = dimensionless, complex function describing the change of amplitude in the perpendicular polarised light as a function of angle and particle diameter, $S_2(\theta)$ = dimensionless, complex function describing the change of amplitude in the parallel polarised light as a function of angle and particle diameter (Merkus 2009).

Two of the specific main theories used in modern particle sizing are Fraunhofer and Mie theories.

Fraunhofer theory is one of the simplest available theories for predicting the scattering pattern of particles and requires no knowledge of the particle's optical properties. It can be described by Equation 2-5 (Merkus 2009),

2-5) $$I(\theta) = \frac{I_0}{k^2 a^2} \alpha^4 \left[\frac{J_1(\alpha \sin\theta)}{\alpha \sin\theta}\right]^2$$

where $I(\theta)$ = total scattered intensity as a function of angle, θ = angle with respect to forward direction, I_o = intensity of incident light, k = wavenumber = $2\pi/\lambda$, a = distance from scatterer to detector, α = dimensionless size parameter = $\pi D/\lambda$, D = particle size, J_1 = Bessel function of the first kind of order unity (Merkus 2009).

The limitations of this theory are that it assumes opaque disk shaped particles which light contacts at the outline only (Merkus 2009). However in reality most particles are not disk shaped and many are transparent or near so. Also only scattering in the near-forward direction at small θ is considered. Due to these assumptions it generally gives results which fluctuate for transparent small particles and hence this method is preferred for larger particles (Merkus 2009).

Mie theory is really a solution to Maxwell's equations that predicts the way light is scattered by spherical particles which is generally more accurate than the Fraunhofer supposition (Merkus 2009). However, in order to use Mie theory it is necessary to know the refractive index (RI) of the particles, the imaginary refractive index (iRI) of the particles (particle absorption) and the refractive index (RI) of the dispersant that the particles are in. All forms of light–particle interaction are included in the theory, hence the requirement of optical properties (Merkus 2009).

Optical properties are dependent upon not only the wavelength of light used, but also the particle shape, surface, crystal structure and any impurities present (Merkus 2009). The limitation here is that often the optical properties of the particles are not accurately known due to all the various components that affect the particles' optical properties (Merkus 2009). In order to achieve the best fit of the theory to generate an expected size distribution for analysis the optical properties of a particle

may be estimated or guessed. For particles larger than 100 μm a high degree of accuracy is required, due to this Fraunhofer theory may be more often used for large particles (Merkus 2009).

2.3.1 Laser Diffraction Technique

The technique of laser diffraction (LD) uses laser light scattered by a dispersion of particles producing a scattering pattern which is measured on a succession of detector elements positioned mostly in the forward direction over a series of angles (Merkus 2009). The scattering pattern is then transferred into a particle size distribution for the sample by deconvoluting the signals measured by the detector. The main theoretical models used are Fraunhofer and Mie theories although the anomalous diffraction model may also be used (Merkus 2009).

Particle concentration is important and is favoured to be low to medium (Merkus 2009). If the concentration is too low not enough scattering will occur so the scattered light signals will be too weak to reliably measure with good repeatability due to a low signal-to-noise ratio. If the concentration is too high then multiple scattering can occur, meaning that the light scattered by a particle has a high probability of being scattered again by other particles before reaching the detector. The percentage of incident light removed by the particles defines the concentration limits of the system and is termed the obscuration. The more particles in the beam line, the more incident light removed, the higher the obscuration (Merkus 2009).

In general laser diffraction techniques generate the particle size distribution based on volume for particles where the scattering behaviour can be matched with the theoretical scattering pattern based on known optical parameters as applied by light scattering theories.

2.3.2 Dynamic Light Scattering

The technique of dynamic light scattering (DLS) employs the concept of Brownian motion determining the rate of change of the scattered light intensity measured as a function of time at a specific angle (Merkus 2009). Intensity changes convert into diffusion coefficients which can be converted into particle size using the Stokes-Einstein equation given here as Equation 2-6 (Atkins 2002; Merkus 2009),

2-6) $$D = \frac{k_B T}{6\pi\eta R}$$

where D = diffusion constant, k_B = Boltzmann's constant, T = absolute temperature, η = viscosity, R = hydrodynamic particle diameter (Atkins 2002).

Assumptions utilised by this method are that the particles do not interact and have spherical morphology which can lead to particles being sized larger than they actually are due to interactions with the liquid dispersant that are not accounted for (Merkus 2009). The concentration of particles required in the system is between 10^{-2}-10^{-3}% out of necessity to avoid bias in the results (Merkus 2009).

2.3.3 Limitations of LD and DLS Techniques

It can be difficult to get meaningful data from polydisperse systems as the result is highly biased towards larger particles within a broad PSD, the analysis of which is naturally limited to resolving only greater than 3:1 diameter ratios. Thus for a polydisperse system the particles need to be a factor of 3:1 different in size to be distinctly defined separately (Carr 2006; Nanosight 2010). The techniques can be said to have a 'black-box' approach and so it is not always easy to know when things have gone wrong within the analysis. No direct concentration information is given in the results which show intensity percentage information where the PSD is of what percent signal was generated to what percentage. The heights of the peaks reflect intensity generated in the intensity of distribution profile for the section of the profile

which generated that part of the signal. Extrapolating back through the mass distribution to get the number distribution is liable to error (Carr 2006).

2.3.4 Nanoparticle Tracking Analysis

A recently developed technique which overcomes some of these limitations is nanoparticle tracking analysis (NTA) which was developed by NanoSight Ltd (NanoSight 2010). A class 1 laser is used to illuminate the sample particles, dispersed in a liquid medium, which are under Brownian motion with the paths being tracked using a CCD camera over a period of time, generally 10-20 seconds (Carr 2006; Carr 2010; NanoSight 2010). Nanoparticle Tracking Analysis (NTA) software then analyses the video and tracks each particle determining the diffusion coefficient and then solves the Stokes-Einstein equation to get the particles' size (Carr 2006; Filipe 2010; NanoSight 2010). Hence the size of each particle and the overall PSD in terms of the number of particles can be obtained. Due to this the results are not weighted towards larger particles as in LD and DLS, hence the true representation of the sample can be determined. The concentration of the sample is required to be low, within the range of 10^6-10^9/mL, so that the software can track individual particles (Carr 2010; NanoSight 2010). The maximum particle size is 1000 nm with the minimum particle size being 10-40 nm and is dependent on the camera resolution, material type and size, laser wavelength and power (Carr 2010; NanoSight 2010). The maximum particle size is set by the decreased Brownian motion of large particles (NanoSight 2010).

The technique holds significant advantages over other particle sizing techniques as particle concentration information is given as well as an idea of the true numbers of particles that are present in a PSD and resolving polydisperse systems well with an effective ratio of 1:1.25 (Carr 2006; Carr 2010; Filipe 2010; NanoSight 2010). The software can generate 3D graphical representations of the results in terms of number vs. intensity vs. size, showing clearly resolved peaks for each size class of particle present in the sample (Carr 2006; Carr 2010; NanoSight 2010). Another advantage is that the operator can actually see the particles which helps validate the results. No calibration is needed as the method is absolute and it is

only necessary to know the temperature and the solvent viscosity (Carr 2006; Carr 2010). Reproducibility is better than 2.5% with a general accuracy of 5%, although this can be up to 10% when operating within an optimum range (Carr 2010). Instead of the standard red laser, the system can be alternatively fitted with a green (532 nm) or blue (404 nm) laser making the system suitable for analysing fluorophores and quantum dots (Carr 2010).

A limitation of the technique is that Brownian motion is measured in 2 dimensions whilst the particles are free to move in 3 dimensions, however the mathematics behind the software accommodate for this and so it only need be considered as a possibility for analyses over short time scales (Carr 2006). Particles can also move in and out of the focal plane which can lead to the PSD being weighted towards the smaller particles in a polydisperse system as these move further and faster than larger particles (Carr 2010).

2.4 Particle Movement through Porous Materials

As a liquid flows through a porous material it can carry particles, providing the particles are small enough to enter the pore network of the material. The effectiveness of particle movement within a material is dependent on the particle size, the pore size range and properties of the material and the material's sorptivity for the liquid transporting the particles (Gronow 1986; Hall & Hoff 2012). The material properties that are most important are briefly introduced below.

2.4.1 Bulk Density

The bulk density (ρ_b) can give an indication of the total porosity of a material and can be calculated from mass and volume measurements (Equation 2-7) (Dadey et al. 1992; Hall & Hoff 2012).

2-7) $$\rho_b = \frac{M_s}{V}$$

where M_s is the sample dry mass and V is the sample volume.

2.4.2 Porosity

The porosity is an indication of the quantity of pores within a material which is important for determining the ease with which a liquid can be absorbed. There are two types of porosity: open porosity and effective porosity. The open porosity refers to the volume of the entire pore space of a material whilst the effective porosity is the pore space volume that can be filled at atmospheric pressure by way of liquid capillary rise. Due to this difference the open porosity will always be greater than the effective porosity.

There are several methods which can be used to measure the open porosity of a material. Some of the most common and simple of which are based on either gas pycnometry (penetration of gas into the pore structure of the material) or liquid saturation (a liquid penetrates the pore space and saturates the material) (Hall & Hoff 2012). In this study the liquid saturation technique has been used. This is a

gravimetric technique wherein the dry material is weighed (usually after drying in an oven and then cooling in a desiccator). The material is then saturated with water under a vacuum and then re-weighed. The porosity (*f*) of the material can then be given by Equation 2-8. The porosity can also be given as a percentage by multiplying the result of Equation 2-8 by 100.

2-8) $$f = \frac{w_s - w_d}{V \rho_w}$$

where w_s and w_d are the saturated and dry weights respectively, V is the bulk volume of the material and ρ_w is the water density (Hall & Hoff 2012).

2.4.3 Permeability

The ability of a porous material to allow liquid to pass through it is the permeability. According to the Kozeny – Carman equation permeability is related to porosity so that:

2-9) $$\kappa = \frac{f^3}{K\,(1-f)^2 S_v^2}$$

where f is porosity, K is the Kozeny constant and S_v is the specific surface. (Pettijohn et al. 1987; Holdich 2010).

2.4.4 Sorptivity

The sorptivity of a material is defined as 'the tendency of a material to absorp and transmit water and other liquids by capillarity' (Hall & Hoff 2012). As such sorptivity, which can be expressed as in Equation 2-10, is the rate at which the imbibing liquid moves through the pore structure and has the units mm/min$^{1/2}$.

2-10) $i = St^{1/2}$

where i is the cumulative absorption, S is the sorptivity and $t^{1/2}$ is the square root of time.

The sorptivity of a material can vary for every liquid as it is also dependent upon the properties of the liquid being imbibed (specifically the temperature, viscosity, surface tension and density) in addition to the properties of the material.

2.5 Porous Materials used in this Study

Two highly microporous limestones, autoclaved aerated concrete (AAC) and bone have been used in this study, each with a different pore size range.

Limestone, a sedimentary stone containing broken up and deposited fossil fragments, exists from many geological ages in numerous forms with many types native to the United Kingdom (Hudson 1971; Leary 1989; Taylor & Wilson 2003).

Portland stone, used here because of its popularity as a building material in the UK and its high microporosity, originates from the vast quarry on the isle of Portland in the south of England (Hudson 1971; Leary 1989). The term 'Portland Stone' covers three types of stone, all originating in the Isle of Portland quarries but having been quarried from three different depths, commercially called roach, whit bed and base bed (Hudson 1971; Leary 1989). Portland base bed has been used in this study.

Lincoln stone comes from a dedicated quarry in Lincolnshire, which is the source of all stone used by Lincoln Cathedral, located in the town of Lincoln, England, UK. This form of limestone is used in this study as it has a unimodal pore size distribution compared to the bimodal Portland stone (Figure 2-2) and it was possible to obtain quarried and medieval stone of different degrees of weathering. Both limestones are coarse bioclastic oolitic grainstones (Hudson 1971; this study).

Portland stone has been used most predominantly from the seventeenth century to the present day (Hudson 1971; Leary 1989) whilst Lincoln stone has been used since the High Middle Ages. Many historically important buildings are constructed from Portland stone including St Pauls Cathedral, Rufus Castle, the Banqueting Hall at Whitehall and Buckingham Palace (Hudson 1971; Leary 1989). Lincoln stone has been used almost exclusively for Lincoln Cathedral. The majority of the Cathedral we see today was built between 1185 and 1311 and was reputed to be the tallest building in the world upon completion until 1549. The Wren library, named after its architect Sir Christopher Wren, was added in the late 17th century (Lincoln Cathedral 2012). Today Lincoln Cathedral is renowned as one of the country's finest examples of Gothic architecture.

The Cathedral is undergoing a major restoration, during which damaged stone is being removed and replaced with fresh quarried stone. The Cathedral was kind enough to gift medieval stone, dating from the 1300's, removed from the south east transept triforum level of the Cathedral to our research group. Lincoln silver bed quarried stone, middle Jurassic, was obtained from Lincoln quarry (Atkin 2012).

Another naturally occurring material used in this study is archaeological bone. Bone is comprised of an organic fraction in conjunction with an inorganic matrix. Tropocollagen, a protein, is the principal constituent of the organic matrix of bone whilst hydroxyapatite, a mineral, provides the majority of the inorganic material (Ortner & Putschar 1981; Child 1995; Baker et al. 2005). However, in archaeological bone the inner marrow is no longer present.

Due to the arrangement of the collagen molecules and the atoms within hydroxyapatite both the protein and mineral matrices possess crystalline properties (Ortner & Putschar 1981). It can be noted that some elements can be substituted into the mineral component and can also be adsorbed onto the crystal surface (Ortner & Putschar 1981). Such elements can be detected by isotope analysis and Laser Induced Breakdown Spectroscopy (LIBS) resulting in the determination of environmental exposure, which can prove useful in determining provenance (Tykot et al. 1996; Price et al. 2000; Samek et al. 2001).

Archaeological bone is highly microporous and is non-distinctly bimodal in that it has two clear pore size ranges which are not completely separated from each other, unlike Portland stone (Figure 2-2).

Both archaeological bone and the two limestones are naturally occurring materials. By contrast, autoclaved aerated concrete (AAC) is a synthetic building material comprised of tobermorite, which is a calcium silicate hydrate mineral. This exists in a combined micro/macro structure of thin tobermorite 11 Å platelets packing in a matrix arrangement yielding a micro structure wherein exists coarse aeration pores formed in the course of foaming during material synthesis (Narayanan 2000). Due to this structure the AAC is broadly bimodal (Figure 2-2).

AAC is widely used today in construction. Due to this it has been subject to several investigations particularly as part of the European Commission funded Heat,

Air and Moisture Standards Development [HAMSTAD] Project (Roels et al. 2002; Roels et al. 2003; Adan et al. 2004; Roels et al. 2004; Ioannou et al. 2008).

This material is used in this study to test how far nanoparticles can be transported through a wide range of pore sizes. It is clear from Figure 2-2 that AAC has notable micro-porosity and large aeration pores.

During the course of this study mercury intrusion porosimetry (MIP) has been used to obtain the pore size distributions of the materials used herein. The results of the MIP investigations are shown in Figure 2-2.

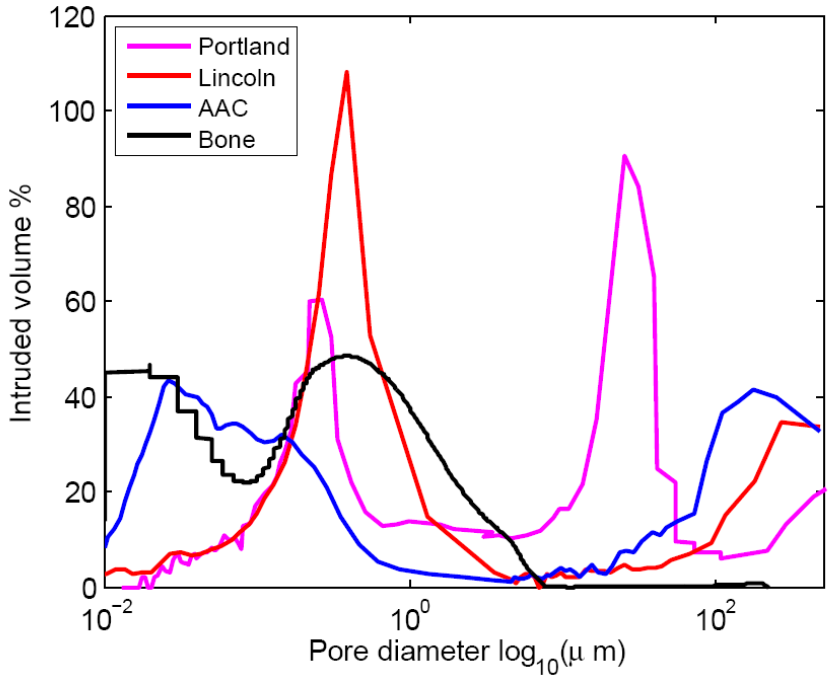

Figure 2-2: Pore size distribution comparison of materials used in this study obtained by MIP.

2.6 Materials Conservation

Throughout the ages limestone has been used as a material for artefacts and the built environment. One of the most ancient, notable and widely known set of limestone structures are those of the pyramids of the Egyptian Old Kingdom (ca. 2686 – 2181 BC, 3rd to 6th Dynasties) (Dunham 1956; Isler 2001). One of the oldest is The Pyramid of Djoser at Saqqara, built in 2630 – 2611 BC by Imhotep under the 3rd Dynasty Pharaoh Djoser, and is the first of the step pyramids constructed (Bard 2007). Limestone can also claim one of the largest and oldest statues in the world, the Sphinx, created by Paraoh Khafre ca. 2600 BC in the 4rth Dynasty (Hawass 1998; Hadingham 2010), a piece of which lies in the British Museum (British Museum 2011).

It is clear that conservation of limestone is relevant to both the built environment and museum artefacts (Hawass 1998; Ambrosi et al. 2001; Bradley 2005; Dei & Salvadori 2006; Doehne & Price 2010). Processes of deterioration, such as salt crystallisation in pores and freeze-thaw damage, can cause cracking and are linked with water absorption (Hudson 1971; Hall & Hoff 2012).

The conservation of human remains and bone artefacts is also highly relevant but has additional complications. Human remains conservation is a highly sensitive topic and one with many moral, cultural and ethical responsibilities (McGowan & LaRoche 1996). The integrity of human remains is of scientific importance in terms of future research and study (DCMS 2005).

In addition to the scientific importance of human remains their integrity is also significant culturally with many belief systems throughout the world placing great importance on the care of the dead wherein non-desecration, even for scientific gains, is paramount (McGowan & LaRoche 1996; DCMS 2005). For all human remains the principle of minimum intervention should be upheld and, where conservation is required, the principle of reversibility should ideally be employed whilst avoiding treatments that compromise, damage or contaminate the bone (Appelbaum 1987; Johnson 1994; DCMS 2005; CCI 2007). It should be noted that current conservation treatments can affect the ability to chemically analyse bone, rendering standard chemical tests such as DNA, radiocarbon dating and isotope

analysis useless (Sullivan & Krueger 1981; Johnson 1994; Grant 2007). Care must be taken when cleaning, drying and even storing and displaying archaeological remains to guard against delamination, softening, shrinkage, cracking and light damage (Grant 2007; Stone 2010). Prior to conserving any bone the effect of the treatment on the ability to perform future analysis must be considered (Johnson 1994; Grant 2007). In some situations it will be preferable to allow deterioration rather than to constrain future analysis.

It is beyond the scope of this study to discuss conservation ethics and policy. However, it can be noted that for all historical objects and buildings conservation policy and ethics play a large role in possible treatment options or even whether the object should be treated at all (Doehne & Price 2010).

2.6.1 Methods of Materials Conservation

There are currently many available materials for conserving stone; lime, acrylates, epoxides, polymers, silicic acid esters, carbonic acid esters, mortars, cements and plasters (Baglioni et al. 1997; Baglioni & Giorgi 2006; Baglioni et al. 2006; Dei & Salvadori 2006; Doehne & Price 2010; Ziegenbalg 2011). Each of these can give problems in the long term with compatibility and stability which can lead to the stone being degraded by the treatment over long periods of time (Baglioni & Giorgi 2006; Baglioni et al. 2006; Ziegenbalg 2011). $Ba(OH)_2$, water glass and colloidal silica solutions are also used (Baglioni & Giorgi 2006; Baglioni et al. 2006; Ziegenbalg 2011).

One of the oldest and most compatible treatments for limestone is lime water. However, treating with limewater can be problematic due to its low solubility (Hall & Hoff 2012; Hirst 2011).

Similarly issues surround current bone conservation methods. The main methods for bone conservation are based on organic polymers. These are predominantly resins (cellulose-nitrates, methyl arcylate/ethyl methacrylate copolymers, polyvinyl acetates and polyvinyl butyrals) and emulsions (polyvinyl acetates, polyvinyl acetate/polyvinyl alcohols and acrylics) (Johnson 1994; Lovell et al. 2004; Lopez-Polin et al. 2008). Some resin examples are Acryloid B-72 (also

known as Paraloid B-72, methyl arcylate/ethyl methacrylate copolymer), Butvar B-98 (polyvinyl butyral), Duco Cement (cellulose-nitrate) and Vinylite (polyvinyl acetate). Some examples of emulsions are Elmer's Glue-all (polyvinyl acetate/polyvinyl alcohol), Vinamul (polyvinyl acetate) and Rhoplex (acrylic) (Johnson 1994; Lovell et al. 2004). Some natural resins, such as agar jelly and gum dammar, are also utilised as well as glues such as isinglass (Johnson 1994).

However, the polymer and glue treatments can have a detrimental effect on the material over the long term. These treatments are subject to slow discolouration, embrittlement and sometimes shrinkage which can cause the surface of the bone to crack. In addition the use of such treatments can remove the possibility to perform future chemical analysis such as isotope or DNA testing due to the resulting contamination of the conserved material (Johnson 1994; Grant 2007).

2.6.2 Nanoparticles for Limestone Conservation

A recently developed conservation method aims to consolidate limestone by application of calcium hydroxide nanoparticles (Giorgi et al. 2000; Taglieri et al. 2008; Lopez-Arce et al. 2009; Giorgi et al. 2010). These particles penetrate into the material and carbonate to form calcite which has both a consolidating and strengthening effect on the material (Drdácký et al. 2009). Other nanoparticles are also being developed for use in conservation such as $Mg(OH)_2$, $BaCO_3$ and $CaSO_4$ because of their small size and the possibility for deeper penetration (Baglioni & Giorgi 2006; Baglioni et al. 2006; Ziegenbalg 2011). There are two main commercial nanolimes in existence today: CaLoSiL (produced by IBZ-Salzchemie GmbH & Co.KG based in Germany) and Nanorestore (produced by CSGI Consortium at the University of Florence, Italy). CaLoSiL has been used where a commercial product has been studied as part of this thesis.

CaLoSiL is lime nanoparticles suspended in alcohol and has been specifically developed for consolidating calcareous historic materials (Ziegenbalg 2008; Drdácký et al. 2009; Ziegenbalg et al. 2010). It is supplied in a range of concentrations and solvents denoted by the identifier after the brand name, e.g. CaLoSiL E5 consists of 5g nanolime per litre of ethanol. CaLoSiL is synthesised from elemental calcium and

water with the reaction producing no by-products (Ziegenbalg 2011). It was developed as part of the STONECORE project (Stone Conservation for the Refurbishment of Buildings), a multinational European research project including academic institutions and private companies which ran from 2008 – 2011 and was funded by the 7th Framework Programme of the European Commission (Ziegenbalg 2011). The aim of the project was to develop and apply compatible nano-materials specifically for natural and artificial stone conservation in conjunction with the development of non-destructive stone assessment methods (Ziegenbalg 2011).

CaLoSiL is not only compatible with stone but the high concentration of lime makes it better for treating stone than lime water as the mid-range concentration, CaLoSiL E25, carries 25 g of nanolime per litre of EtOH into the stone compared to 1.6 g of lime per liter of water. Once inside the stone the nanolime works by carbonating to form calcite according to Equation 2-11:

2-11) $$Ca(OH)_2 + CO_2 \rightarrow CaCO_3 + H_2O$$

This reaction requires time and depends on the humidity of the air and the temperature as well as the quantity of carbon dioxide (Ziegenbalg 2011). For complete carbonation of 1 g of $Ca(OH)_2$, which requires 0.59 g of CO_2, around 8 L of air is needed. It should be noted that carbonation will take longer when particles are trapped inside the pore structure. To speed up this reaction it is possible to use a carbonizing agent such as DiLoCarb (produced by IBZ-Salzchemie GmbH & Co.KG).

Findings from the project, presented at a series of public meetings, showed porosity reductions of up to 5% post CaLoSiL treatment with little effect on water transport properties (Slížková 2011) based on intact Maastricht stone. A large portion of the project looked at consolidation effects on mortar and stone power (Maryniak-Piaszczynski 2011). The efficacy of CaLoSiL in consolidating sandstone was examined by Maryniak-Piaszczynski et al. (2008) who found that CaLoSiL with a concentration less than 36 g/L in combination with Funcosil silicic ester successfully consolidated surface flakes, however no quantitative analysis was carried out. Where

other tests were carried out on stone it was discovered that treatment could lead to the formation of a white haze on the stone surface as a consequence of the treatment (Kolinkeova 2011; Slížková 2011). The use of CaLoSiL in conjunction with ethyl silicates suggested that this treatment could, under certain circumstances be more beneficial than CaLoSiL treatment alone (Maryniak-Piaszczynski 2011). Studies have also suggested that CaLoSiL can be used for the removal of microbial growth from stone without damaging the stone itself (Askew 2011; Ziegenbalg 2011).

Nanolimes appear to be a good consolidant for calcareous stone, however the knowledge to date must be increased, particularly in terms of the long term efficacy of the treatment. Also at present few clear treatment guidelines exist. In addition the effect of nanolimes, including penetration depth, on a wide variety of stones is as yet unknown. The STONECORE Project, which ended in 2011, sought to shed some light on the topic, in addition to producing CaLoSiL. An English Heritage Project which began in 2011 seeks to determine application guidelines for CaLoSiL on a selection of weathered limestones (Bath, Chilmark, Reigate and Beer) and understand the effect of this treatment, including penetration depth, on these stones and how performance is affected (Henry 2011).

The study undertaken for this thesis has looked at nanoparticle location and effect on water transport in weathered and unweathered medieval stone and in two intact limestones with different pore size ranges treated by imbibition. The impact weathering has on the ability of a porous material to transport particles can be seen by comparing the results of tests on weathered and unweathered stone. AAC, as a model material, is an extreme example of a material composed of very small pores connected to very big pores. By comparison of the limestone results with the outcome of applying nanoparticles to AAC it was possible to determine if a material's pore network structure is more important for penetration depth than its pore size range.

2.6.3 Synthetic Hydroxyapatite Applications to Bone

Regarding the conservation of archaeological bone, particularly human remains, new treatments are needed which are fully compatible with the bone matrix and do not interfere with chemical testing. In medicine hydroxyapatite is being investigated as a bone replacement material. Synthetic hydroxyapatite is beginning to be used in surgery wherein it is grafted onto healthy bone which in the initial testing proves fruitful as there are no material compatibility issues (Beck-Coon et al. 1991; Heilmann et al. 2007). From the successes of implanting synthetic hydroxyapatite into healthy bone it seems reasonable to expect that a hydroxyapatite colloidal conservation treatment should be both compatible with the bone matrix and have a minimal effect on chemical testing.

Chapter 3:
Calcium Hydroxide Nano and Fine Particles

Nanoparticles are of increasing interest in the heritage conservation field due to the possibilities of new treatments for consolidating damaged artefacts and structures (Baglioni & Giorgi 2006; Baglioni et al. 2006). One such innovation has, over the past decade, seen the emergence of calcium hydroxide nanoparticles ("nanolimes") begin to be employed as a treatment for the consolidation of friable limestone and lime mortars; from precious Italian frescos to historic castles (Ambrosi et al. 2001; Dobrzyńska-Musiela 2011).

This chapter looks at the effect that reaction conditions have on $Ca(OH)_2$ product particle size. The ease of producing stable, unaggregated $Ca(OH)_2$ nanoparticles by this wet synthesis is also discussed. A commercially available nanolime is also investigated allowing a comparison to be drawn between the particle size of the synthesised and commercial nanolimes.

Two particle sizing techniques were used to measure the PSD of the synthesised and commercial particles: the Mastersizer instrument LD system and the Nanosight NTA technique. As previously discussed these two laser-based particle size measurement techniques have different strengths and limitations and measure particles in different ways. When using these techniques together was hoped that a clearer understanding of both the overall PSD and the submicron PSD can be obtained than would be possible by using only one system.

3.1 Synthesis and Analysis of Calcium Hydroxide Particles

This section deals with the synthesis and analysis of calcium hydroxide colloids. Laboratory synthesis methods were investigated to understand the impact of experimental parameters on particle size and stability.

The synthesis methods used were based on the procedure reported by Ambrosi et al. (2001), producing colloidal particles of calcium hydroxide. A series of experiments were designed to enable the determination of how experimental factors affect the particle size of the product. By fixing several factors and altering one variable it was possible to determine the combination of reagent concentrations and temperatures that yield the smallest PSD and the impact on particle stability. The balanced equation (3-1) for the reaction is given below:

3-1) $$CaCl_2 + 2NaOH \rightarrow Ca(OH)_2 + 2NaCl$$

This shows that for every mole of $CaCl_2$ two moles of NaOH are required to ensure full reaction thus forming one mole of $Ca(OH)_2$ and two moles of NaCl.

3.1.1 Particle Synthesis: Experimental Procedure

Four sets of experiments were devised. In each set all but one of the experimental conditions were fixed. For each experimental set the basic procedure remained the same. The required solution of calcium chloride was obtained by dissolving the correct weight of calcium chloride dihydrate in the required volume of de-ionised water. The solution of sodium hydroxide was obtained in the same way. Solutions were stirred, rapidly mixed then continuously stirred at 300 rpm for 5 minutes. Where temperature was varied the mixture was removed from the heat and allowed to settle and cool for 15 minutes before use.

The first set of experiments served to vary the reactant concentrations (Table 3-1) in accordance with the balanced equation for the reaction. This set of experiments was performed at room temperature.

In the second experimental set, performed at room temperature, the $CaCl_2$ concentration was varied whilst the NaOH concentration was constant (Table 3-1) so that $CaCl_2$ was in excess. The balanced equations (3-2 to 3-4) for the reactions of experiments 2 – 4 are given below:

3-2) $$3CaCl_2 + 2NaOH \rightarrow Ca(OH)_2 + 2NaCl + 2CaCl_2$$

3-3) $$5CaCl_2 + 2NaOH \rightarrow Ca(OH)_2 + 2NaCl + 4CaCl_2$$

3-4) $$7CaCl_2 + 2NaOH \rightarrow Ca(OH)_2 + 2NaCl + 6CaCl_2$$

The NaOH concentration was varied in the third experimental set whilst keeping the $CaCl_2$ concentration constant (Table 3-1). Here the NaOH was in excess. This set of experiments was performed at room temperature. The balanced equations (3-5 to 3-9) for the reactions of experiments 2 – 6 are given below:

3-5) $$CaCl_2 + 4NaOH \rightarrow Ca(OH)_2 + 2NaCl + 2NaOH$$

3-6) $$CaCl_2 + 6NaOH \rightarrow Ca(OH)_2 + 2NaCl + 4NaOH$$

3-7) $$CaCl_2 + 8NaOH \rightarrow Ca(OH)_2 + 2NaCl + 6NaOH$$

3-8) $$CaCl_2 + 10NaOH \rightarrow Ca(OH)_2 + 2NaCl + 8NaOH$$

3-9) $$CaCl_2 + 20NaOH \rightarrow Ca(OH)_2 + 2NaCl + 18NaOH$$

The fourth experimental set varied the reaction temperature whilst both reactant concentrations were kept constant (Table 3-1).

	Reagents		Supernatant Solution							Solid Product	
Set	$CaCl_2$ mol/kgw	NaOH mol/kgw	Ca^{2+} mol/kgw	Cl^- mol/kgw	Na^+ mol/kgw	OH^- mol/kgw	IS mol/kgw	pH	SI $Ca(OH)_2$	$Ca(OH)_2$ mol	T (ºC)
1.1	0.1	0.2	0.0237	0.1000	0.1000	0.0474	0.1711	12.4940	0.78	0.0263	RT
1.2	0.2	0.4	0.0256	0.2000	0.2000	0.0511	0.2767	12.5060	1.39	0.0744	RT
1.3	0.3	0.6	0.0268	0.3000	0.3000	0.0536	0.3804	12.5110	1.72	0.1232	RT
1.4	0.4	0.8	0.0277	0.4000	0.4000	0.0554	0.4830	12.5130	1.94	0.1723	RT
2.1	0.1	0.2	0.0237	0.1000	0.1000	0.0474	0.1711	12.4940	0.78	0.0263	RT
2.2	0.3	0.2	0.1163	0.3000	0.1000	0.0148	0.4489	12.1720	0.94	0.0337	RT
2.3	0.5	0.2	0.2160	0.5000	0.1000	0.0321	0.7481	12.0500	0.94	0.0340	RT
2.4	0.7	0.2	0.3165	0.7000	0.1000	0.0330	1.0500	11.9700	0.91	0.0335	RT
3.1	0.1	0.2	0.0237	0.1000	0.1000	0.0474	0.1711	12.4940	0.78	0.0263	RT
3.2	0.1	0.4	0.0054	0.1000	0.2000	0.1108	0.2162	12.8890	1.22	0.0446	RT
3.3	0.1	0.6	0.0024	0.1000	0.3000	0.2047	0.3071	13.1510	1.44	0.0476	RT
3.4	0.1	0.8	0.0015	0.1000	0.4000	0.3030	0.4046	13.3160	1.57	0.0485	RT
3.5	0.1	1.0	0.0011	0.1000	0.5000	0.4023	0.5034	13.4350	1.67	0.0488	RT
3.6	0.1	2.0	0.0006	0.1000	1.0000	0.9012	1.0020	13.7900	1.90	0.0494	RT
4.1	0.3	0.6	0.0268	0.3000	0.3000	0.0536	0.3804	12.5110	1.72	0.1232	RT
4.2	0.3	0.6	0.0279	0.3000	0.3000	0.0558	0.3837	11.7660	1.65	0.1221	50
4.3	0.3	0.6	0.0292	0.3000	0.3000	0.0583	0.3875	11.2350	1.58	0.1208	70
4.4	0.3	0.6	0.0308	0.3000	0.3000	0.0615	0.3923	10.8010	1.50	0.1192	90

Table 3-1: Reaction temperatures, concentrations of reagents and products and ionic strengths (IS) and portlandite saturation index (SI) of electrolyte solutions used in each experiment of each experimental set (calculated using Pitzer method in computer program PhreeqC).

3.1.2 X-Ray Diffraction Analysis

A sample of synthesised particles was prepared for XRD analysis using the synthesis experimental procedure outlined above for the third experiment of set 1. A sample of volume 5 mL was withdrawn from the resulting suspension. This sample suspension was washed with 100 mL EtOH and allowed to settle for an hour prior to the wash being decanted. The sample suspension was then used for XRD.

A small quantity of sample was arranged into a thin layer on the sample disk of the sample holder by pipetting onto the glass sample disk and drying under a light source. This was repeated until enough particles were present on the sample disk for analysis. The sample was then scanned in a Bruker D8 XRD spectrometer using a step size of 0.069^{o}, at a time per step of 1.5s, over a 2-θ range of $5 – 90^{o}$. The obtained diffraction pattern could then be compared to the inbuilt chemical database in the EVA program on the instrument computer to identify the compound synthesised.

The resulting XRD pattern for the synthesised sample was matched to the library pattern for $Ca(OH)_2$ (Figure 3-1) showing that $Ca(OH)_2$ had been synthesised with no undesirable precipitation of NaCl.

The experimental-library match indicates that, due to the hexagonal crystal system, the synthesised $Ca(OH)_2$ particles should possess hexagonal morphology which was confirmed by SEM analysis.

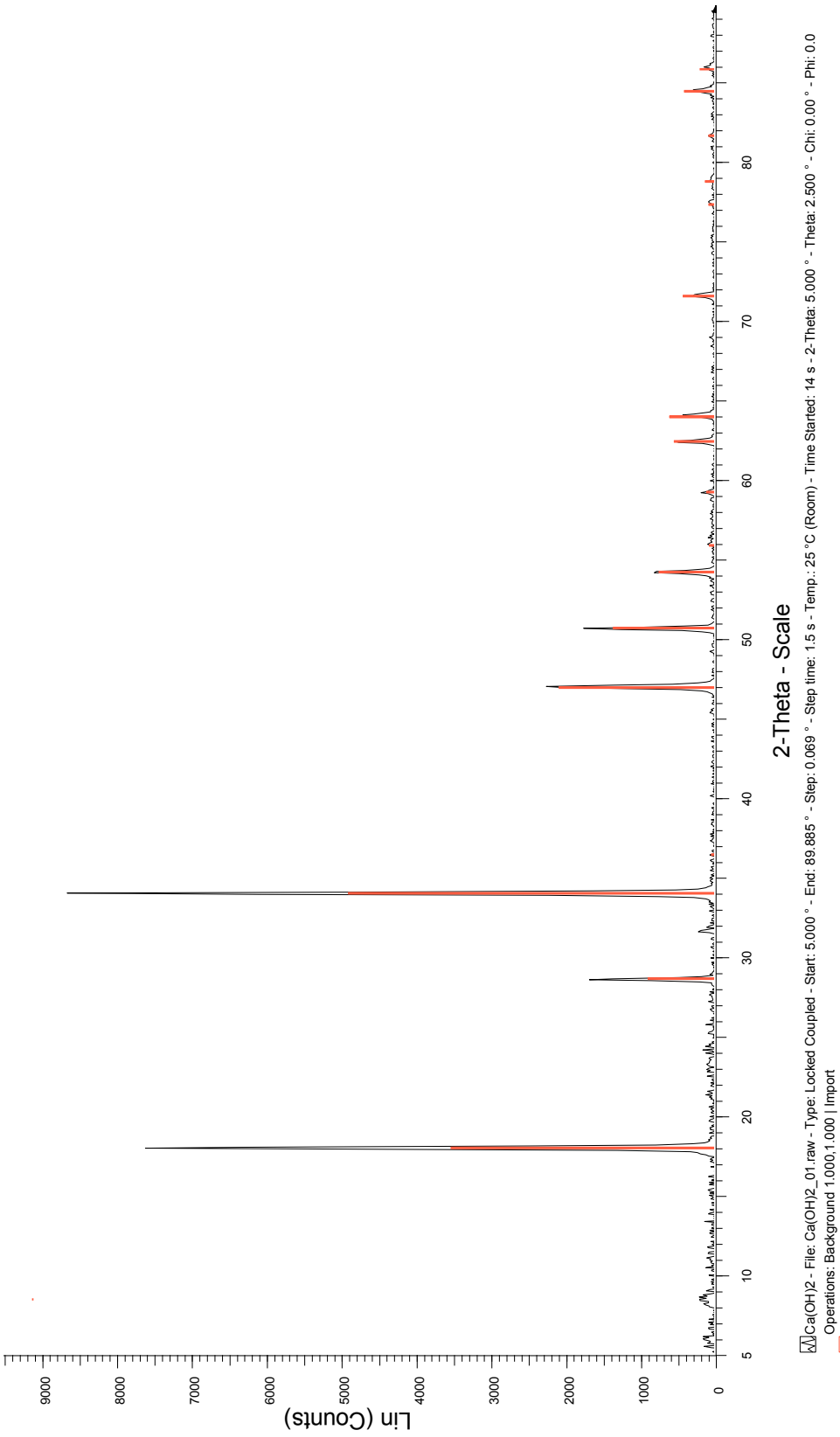

Figure 3-1: XRD spectrum obtained from synthesised $Ca(OH)_2$ compared to library pattern.

3.1.3 Particle Sizing by LD Experimental Procedure

After allowing a synthesis mixture to cool for 15 minutes a sample of the particles was withdrawn for PSD analysis.

The long bench Mastersizer S fitted with the MSX1 sample cell and 300 RF lens was used to measure product particle size. The background was set using 100 ml of ethanol at a rotor speed of 1000 rpm. Once the background measurement was set the sample was added to the cell until the obscuration registered within the optimal zone. Ten measurements were taken for the sample, one per minute over ten minutes, which were saved for analysis.

For each experiment in each set three batches of product were synthesised and analysed, thus giving a total of thirty PSDs for each experiment of each set. This data was used to obtain an average data set over the thirty PSD measurements for each experiment of each set.

3.1.4 Analysing PSD Data

The PSD data was analysed using a normal distribution which is a continuous probability distribution based on a Gaussian function (Equation 3-10) (Kirkup & Frenkel 2006). The equation (3-10) is:

3-10) $$p(x) = \frac{1}{\sqrt{2\pi\sigma^2}} e^{-\frac{(x-\mu)^2}{2\sigma^2}}$$

where μ is the mean (the peak position) and σ^2 is the variance, which is related to the width and can be equivalently given as σ, the standard deviation of the population.

The equation can be alternatively noted as:

3-11) $$y = a \exp\left[-\frac{1}{2}\left(\frac{x-\mu}{\sigma}\right)^2\right]$$

where:

3-12) $$a = \frac{1}{\sqrt{2\pi\sigma^2}}$$

A Gaussian function was used to fit an overall distribution to the experimental PSD data, producing several peaks in the distribution envelope. Depending on the number of peaks within an experimental PSD a corresponding number component fit was used for analysis and fitting. For example: a four-component fit would be fitted to an experimental PSD which, by its shape, appeared to contain four distinct peaks. Analysis returned a set of three numbers (the mean, standard deviation and area) for each peak within a given distribution. This allowed the identification of the individual peaks in addition to enabling a good overall distribution fit.

The mean, standard deviation and area could then be compared for each mean PSD data for each experiment of each experimental set. This allowed the identification of PSD changes due to altering experiment conditions.

3.1.5 Particle Sizing by LD Results

It was generally found necessary to fit the PSD data with either a four- or five-component fit, an example of which can be seen in Figure 3-2. For full data see Appendix B. In order to view the results clearly the data was displayed on a $\log_{10}$ scale against the arbitrary intensity.

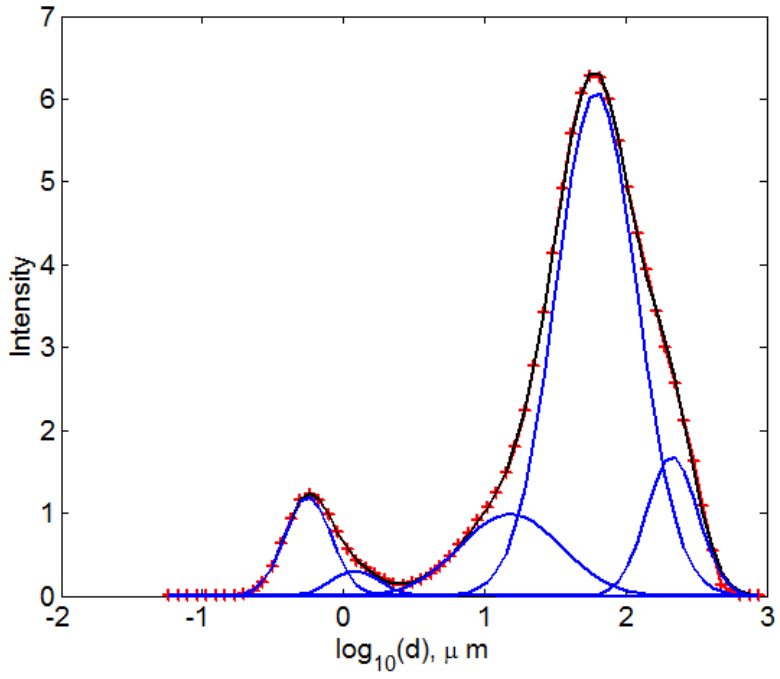

Figure 3-2: Peak fitting of mean Set 1 Experiment 1 experimental data (red stars) with a five-component fit. The figure shows how five peaks (blue lines) combine to produce the overall PSD, the fit line of which is shown in black.

In general for each individual sample in a set of experiments it was found that over time the PSD width increased such that the last measurement of a sample exhibited a wider PSD with particles increasing in size compared to the first measurement. This suggests that some of the particles in the sample could be agglomerating over the course of the experiment (minutes). Generally as progression was made through the experiments of each set the initial five-component fit became a four-component fit of less width than that originally observed.

Taking experiment set 3 as an example it can be seen that a five-component fit is necessary to explain the overall mean PSD distribution for both the first and second experimental results of this set. For all other experiments of this set the overall mean PSD fit can be satisfied by a four-component fit. This occurs in conjunction with a decrease in overall PSD width meaning that overall the particles become smaller in size with each experiment in the set. The data for each peak contained within the overall PSD distribution for the mean results of each experiment

of each set are contained in Tables 3-2 to 3-5. Comparisons showing how the PSD changes according to progression through the experiments of each set can be found in Figure 3-3. The changes in the submicron region with reactant vessel ionic strength are shown in Figure 3-4.

Experiment	Peak	μ ($\log_{10}$(d), μm)	σ ($\log_{10}$(d), μm)	Area ($\log_{10}$(d), μm^2)	Percentage of particles
1	1	-0.25	0.16	0.49	7.39
1	2	0.08	0.17	0.13	1.97
1	3	1.17	0.35	0.84	12.65
1	4	1.79	0.29	4.44	66.72
1	5	2.33	0.18	0.75	11.27
2	1	-0.22	0.14	1.79	26.73
2	2	0.09	0.27	0.38	5.73
2	3	1.10	0.29	1.29	19.30
2	4	1.44	0.18	3.23	48.24
3	1	-0.22	0.14	1.95	29.09
3	2	0.11	0.25	0.61	9.16
3	3	0.91	0.26	1.30	19.47
3	4	1.22	0.19	2.83	42.27
4	1	-0.22	0.14	1.75	25.82
4	2	0.15	0.27	0.61	8.96
4	3	0.89	0.23	1.27	18.78
4	4	1.18	0.19	3.15	46.45

Table 3-2: Numerical data resulting from the peak fitting shown graphically in Figures B-1 to B-4, Set 1 experiments (Appendix B).

Experiment	Peak	μ ($\log_{10}$(d), μm)	σ ($\log_{10}$(d), μm)	Area ($\log_{10}$(d), μm^2)	Percentage of particles
1	1	-0.25	0.16	0.49	7.39
1	2	0.08	0.17	0.13	1.97
1	3	1.17	0.35	0.84	12.65
1	4	1.79	0.29	4.44	66.72
1	5	2.33	0.18	0.75	11.27
2	1	-0.27	0.16	0.57	8.58
2	2	-0.03	0.23	0.42	6.35
2	3	1.49	0.36	1.63	24.62
2	4	1.76	0.21	3.90	58.95
2	5	2.42	0.12	0.10	1.51
3	1	-0.24	0.14	0.72	10.87
3	2	-0.003	0.21	0.46	6.98
3	3	1.34	0.30	1.57	23.61
3	4	1.67	0.19	3.89	58.54
4	1	-0.23	0.15	0.91	13.64
4	2	0.05	0.25	0.61	9.23
4	3	1.25	0.32	1.66	24.99
4	4	1.61	0.23	3.47	52.14

Table 3-3: Numerical data resulting from the peak fitting shown graphically in Figures B-1 and B-5 to B-7, Set 2 experiments (Appendix B).

Experiment	Peak	μ (log_{10}(d), μm)	σ (log_{10}(d), μm)	Area (log_{10}(d), μm^2)	Percentage of particles
1	1	-0.25	0.16	0.49	7.39
1	2	0.08	0.17	0.13	1.97
1	3	1.17	0.35	0.84	12.65
1	4	1.79	0.29	4.44	66.72
1	5	2.33	0.18	0.75	11.27
2	1	-0.23	0.16	0.58	8.74
2	2	0.01	0.19	0.23	3.41
2	3	1.51	0.37	1.36	20.56
2	4	1.77	0.22	3.43	51.78
2	5	2.41	0.20	1.03	15.51
3	1	-0.21	0.15	1.73	25.87
3	2	0.08	0.24	0.85	12.77
3	3	0.96	0.25	1.35	20.18
3	4	1.26	0.19	2.75	41.18
4	1	-0.19	0.15	2.14	31.96
4	2	0.07	0.21	0.72	10.72
4	3	0.82	0.25	1.25	18.65
4	4	1.13	0.20	2.58	38.66
5	1	-0.23	0.14	2.30	34.66
5	2	0.03	0.20	0.70	10.54
5	3	0.47	0.14	0.26	3.86
5	4	1.01	0.26	3.39	50.95
6	1	-0.26	0.12	2.31	34.76
6	2	-0.09	0.11	0.57	8.57
6	3	0.31	0.28	1.16	17.41
6	4	0.81	0.21	2.61	39.26

Table 3-4: Numerical data resulting from the peak fitting shown graphically in Figures B-1 and B-8 to B-12, Set 3 experiments (Appendix B).

Experiment	Peak	μ (log_{10}(d), μm)	σ (log_{10}(d), μm)	Area (log_{10}(d), μm^2)	Percentage of particles
1	1	-0.22	0.14	1.95	29.09
1	2	0.11	0.25	0.61	9.16
1	3	0.91	0.26	1.30	19.47
1	4	1.22	0.19	2.83	42.27
2	1	-0.22	0.15	1.88	28.31
2	2	0.08	0.23	0.74	11.18
2	3	0.81	0.29	1.25	18.73
2	4	1.18	0.22	2.78	41.78
3	1	-0.22	0.14	1.90	28.44
3	2	0.15	0.27	0.67	10.10
3	3	0.88	0.25	1.39	20.89
3	4	1.20	0.19	2.70	40.57
4	1	-0.21	0.15	1.90	28.47
4	2	0.17	0.27	0.79	11.87
4	3	0.84	0.23	1.59	23.85
4	4	1.19	0.21	2.39	35.81

Table 3-5: Numerical data resulting from the peak fitting shown graphically in Figures B-13 to B-16, Set 4 experiments (Appendix B).

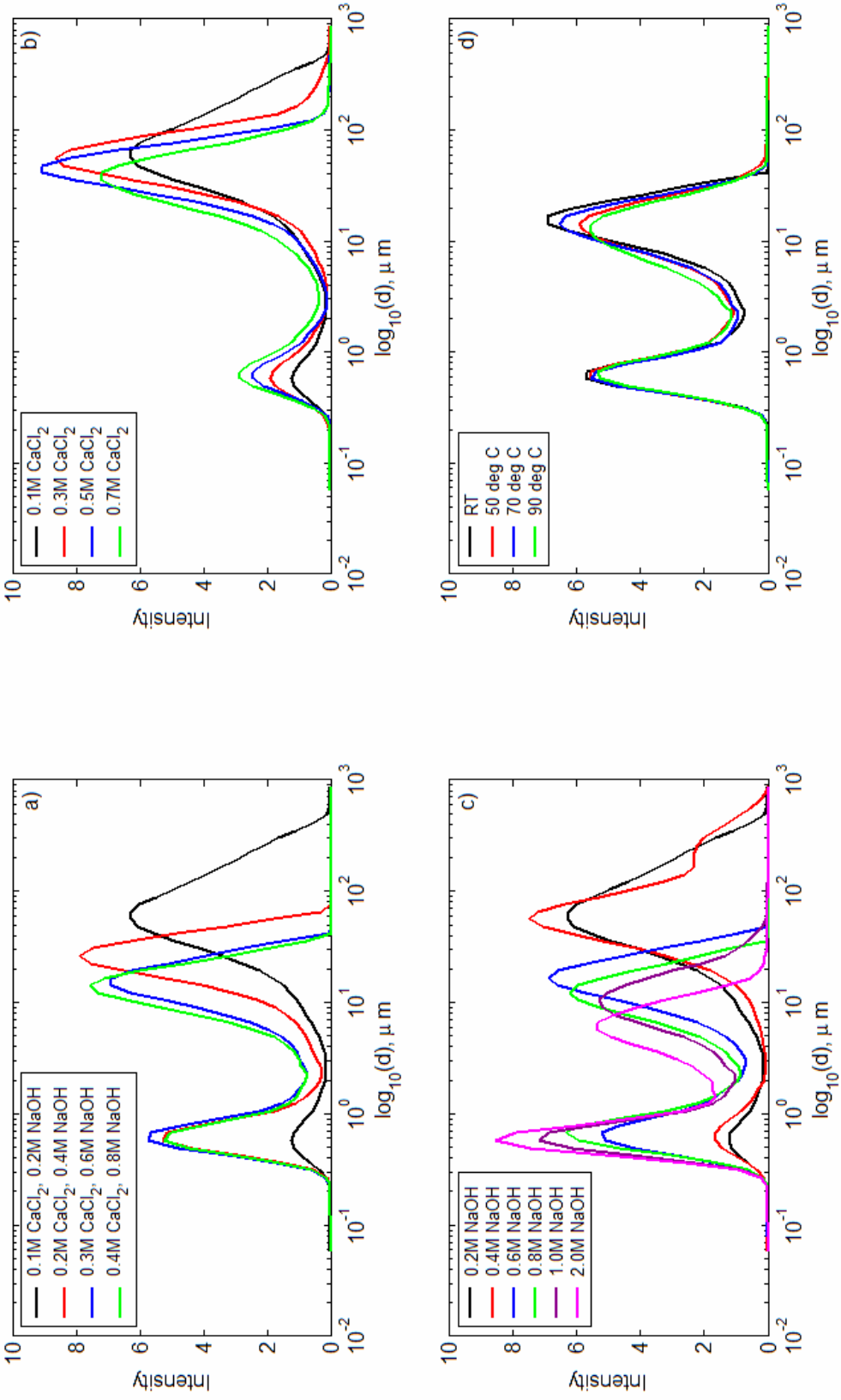

Figure 3-3: Graphical mean PSD data for $Ca(OH)_2$ precipitated from synthesis experiments of a) set 1, b) set 2, c) set 3 and d) set 4.

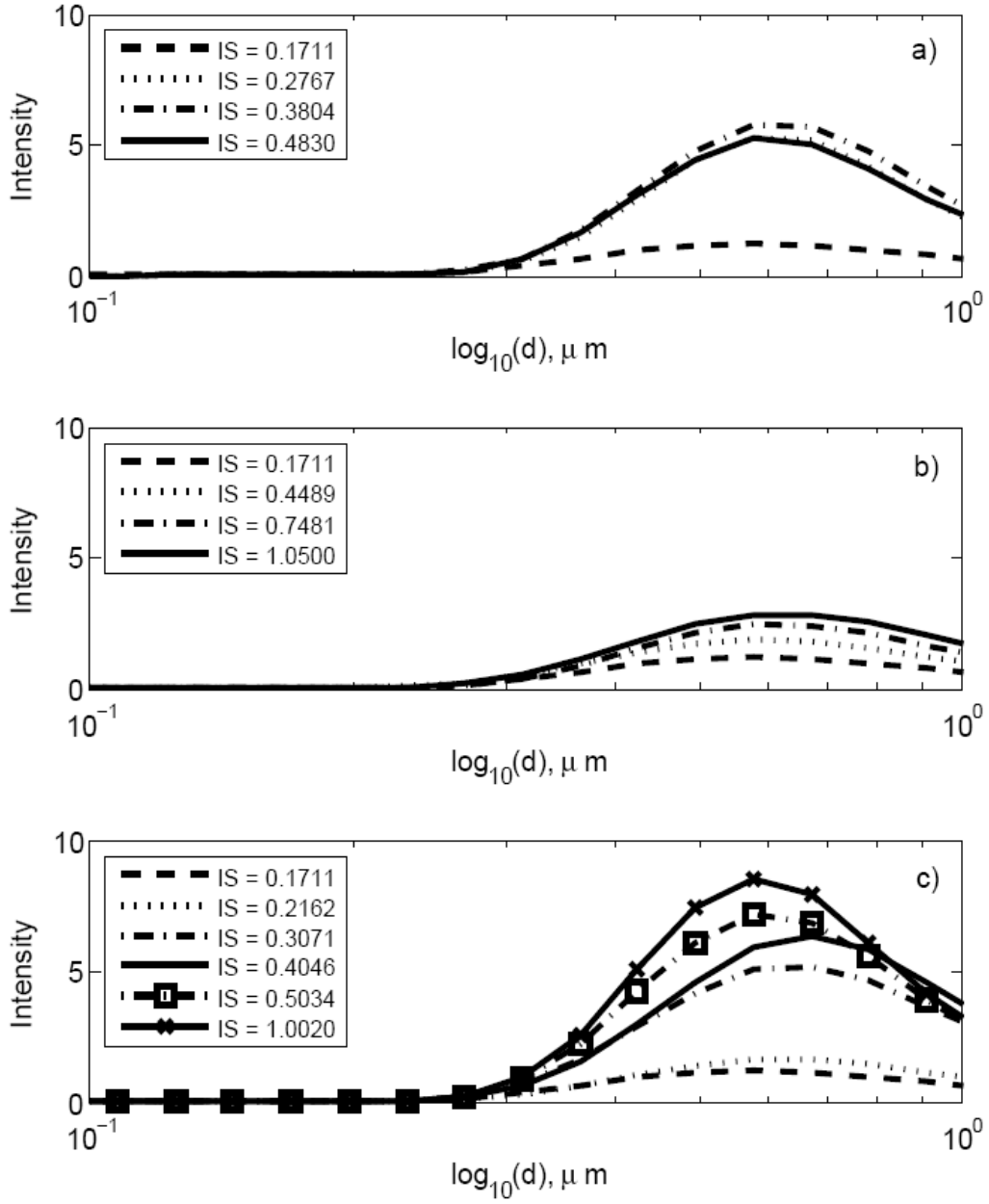

Figure 3-4: Differences in submicron particle size distribution according to ionic strength for a) set 1, b) set 2 and c) set 3 particle synthesis experiments.

The reagents are increased according to the balanced reaction equation for set 1 with the result that particle size is decreased through increasing particle stability. The results suggest that $CaCl_2$ 0.3 M and NaOH 0.6 M concentrations promote the largest quantity of particle formation.

Set 2 increases the Ca^{2+} and Cl^- ion concentrations which results in a decreasing pH with the overall result throughout the set of poor particle stability with a very small primary peak containing individual and small groups of particles and a very large secondary peak of larger aggregates. This result is in agreement with Plassard et al. (2005) who witness that in a C-S-H system an increase in the divalent ion concentration, causing a decrease in Debye length and therefore a decrease in electrostatic repulsion, leads to greater particle attraction. The result of this set shows an overall similar result to Plassard et al. (2005) but here the decreasing pH is important. Since the particle surface charge is positive (Giorgi et al. 2002; Elakneswaran et al. 2009) the Ca^{2+} concentration is not as relevant. The surface charge will change with pH (Nazzal & Wiesner 1994; Yousuf et al. 1995; Israelachvili 2006) going from positive, through zero (point of zero charge (PZC)), to negative. For $Ca(OH)_2$ the expected PZC is between a pH of 12.7 – 12.9 (El Shafei 1996). As the pH is decreased and the ionic strength is increased the Debye length should decrease (Israelachvili 2006; Lee et al. 2009) meaning that particles move closer together and are within the range of van der Waals forces. As Cl^- ions exist in a much higher concentration than OH^- ions the double layer should contain more Cl^-. Since the effective radius of Cl^- ions is larger than that of OH^- ions (Masterton et al. 1971; Shannon 1976) the overall width of the double layer should be increased leading to the slight increase in stability seen from experiment 1 to experiment 4 of the set. In this set the highest concentration of particles of size < 1 μm are obtained when using reagent concentrations of $CaCl_2$ 0.7 M and NaOH 0.2 M. Despite this being the best result of the set it is not much better than the first experiment of set 1 and is observed to be the poorest set in yielding particles < 1 μm in size suggesting that NaOH is more important for particle formation and stability.

Na^+ ion concentration and pH are increased in set 3 resulting in a systematic decrease in particle size and extent of aggregation. Theoretically as pH increases, the surface charge of $Ca(OH)_2$ particles will decrease. With very high pH (> 13) the

surface should be negatively charged meaning that monovalent anions should now be replaced by divalent cations. However due to the very low concentration of Ca^{2+}, substitution of some divalent counter ions with Na^{+} counter ions can occur in the Stern layer. This effect on the nature of the double layer would result in an increase in particle repulsion due to the induction of entropic effects which is expected according to DLVO theory. A $CaCl_2$ concentration of 0.1 M and NaOH concentration of 2.0 M give the best result of this set with a sizeable quantity of particles of size < 1 μm with increased system stability.

The fourth set results suggest that temperature does not have a significant effect on particles < 1 μm diameter, using reagent concentrations of 0.3 M and 0.6 M for $CaCl_2$ and NaOH respectively. However the results do suggest that particle stability is marginally increased due to the slight decrease in the area of the fourth peak in the distribution, within the distinct secondary peak, above 10 μm which corresponds to area increases in the second and third peaks, also within the distinct secondary peak, below this size (see Appendix B).

In summary overall increasing the NaOH concentration in set 3 shows a marked increase in particle formation and stability, increasing $CaCl_2$ concentration in set 2 shows a slight increase in particle formation and stability and increasing both reagent concentrations together shows an increase in particle formation and stability. Raising temperature in set 4 shows a very slight decrease in the extent of large particle aggregation.

It can be seen that increasing the NaOH concentration has a far more significant effect on the PSD than an increase in the $CaCl_2$ concentration suggesting that a basic solution aids the formation and stability of small $Ca(OH)_2$ particles when using this wet synthesis method. As suggested by Plassard et al. (2005) this could be due to the presence of excess Na cations in conjunction with a low Ca concentration in the solution at high pH which results in a degree of counter ion substitution and a corresponding increase in repulsion. From the pH values of set 3 it can be seen that for the first and second experiments of the set the particles should have a positive surface charge, meaning that the Stern layer is composed of anions. For all other experiments in this set the Stern layer should be formed by cations due to the

particles now having a negative surface charge due to the pH being > 13. According to DLVO theory increasing pH will increase repulsion. Due to this all systems that become more stable with increasing pH, sets 1 and 3, are in line with classical DLVO.

It can be seen that higher ionic strength solutions in all sets lead to slower aggregation and therefore a more stable suspension, which is contrary to classical DLVO. It is also apparent that this systematic increase in ionic strength throughout all the sets occurs in conjunction with an increase in pH only in sets 1 and 3. The pH decreases throughout sets 2 and 4. This suggests that the decrease in pH, and the corresponding decrease in repulsive forces, of set 2 should, by DLVO, favor aggregation. Possibly this is not truly seen due to the effective ionic radii affecting the double layer. In set 4 the decrease in Debye length due to decreasing pH and increasing ionic strength (both due to a decreased saturation index with temperature for $Ca(OH)_2$) should suggest that aggregation increases systematically throughout the set. However the results actually show that the PSD width and primary peak remains stable.

Plassard et al. (2005) find that for a C-S-H (negative) surface increasing pH results in overall decreased repulsion which is contrary to classical DLVO and the results of this study. However, Plassard et al. (2005) also find that ionic strength is a negligible factor in their system compared to pH, a finding that is in agreement with the results of this study. This suggests that for these systems increasing pH is the stronger effect regardless of particle surface charge. Plassard et al. (2005) also find that at high pH a large excess of Na^+ results in dominant repulsion through entropic effects which is in agreement with the results of this study.

The width of the PSD was not found to vary significantly in set 4. This suggests that at these concentrations increasing temperature does not affect PSD width but increasing pH does. Again this is likely due to entropic effects occurring for a pH above 13.

Overall the largest quantity of particles <1 μm and the smallest particle size range are both obtained from reagent concentrations of 0.1 M and 2.0 M for $CaCl_2$ and NaOH respectively at room temperature. However the quantity of particles

formed is lower than for the balanced equation reaction of $CaCl_2$ 0.3 M and NaOH 0.6 M which produces the largest quantity of particles.

Due to the observed increase in PSD of all samples over time and the unexpected large particles evident in all PSDs it is reasonable to assume aggregation occurs. SEM was used to investigate the possibility of the presence of agglomerates in addition to well defined individual particles.

3.1.6 Particle Sizing by NTA Experimental Procedure

A Nanosight Ltd. LM 10 instrument with Nanoparticle Tracking Analysis software version 2.0 was used to obtain a PSD of synthesised $Ca(OH)_2$ (precipitated from 0.3 M $CaCl_2$ and 0.6 M NaOH at room temperature) by way of particle visualisation and motion tracking. Samples were taken from the top layer and from the bottom of the sample bottle. A 1 in 10000 dilution of a sample was obtained and injected into the instrument optical cell. The laser illuminated the particles whilst the sample was recorded by a video camera. The video was then analysed by the NTA software to obtain a PSD of the sample.

3.1.7 Particle Sizing by NTA Results

Using NTA it was discovered that the fine particles existed in groups within the distribution which was found to be much more complex than for the wide ranging PSD obtained by LD. A log normal distribution was fitted to the NTA PSD for both the top and bottom levels of the sample which were found to require an eleven-component and thirteen-component fit respectively (Figure 3-5).

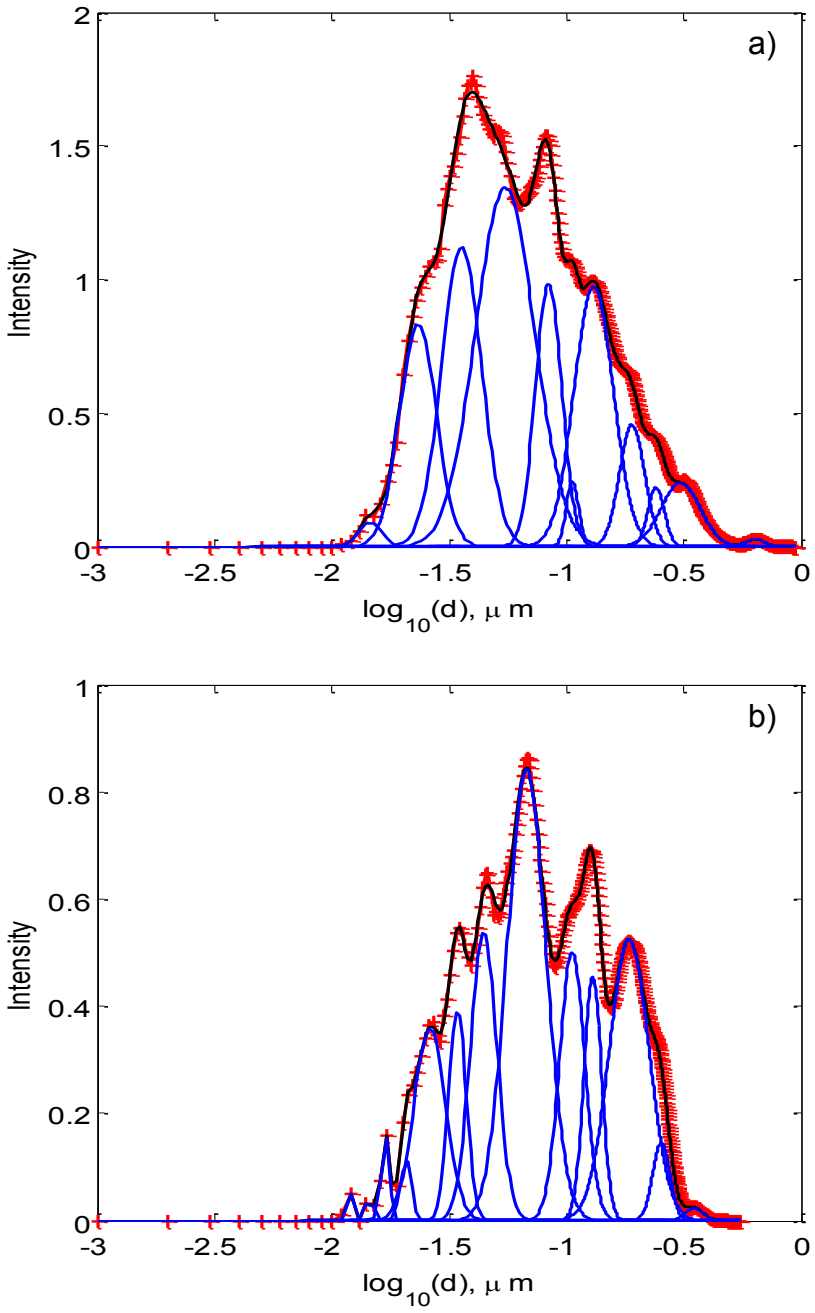

Figure 3-5: Peak fitting of PSD data (red stars) for $Ca(OH)_2$ a) top and b) bottom samples with an eleven-component fit and thirteen-component fit respectively. The figures show how the peaks (blue lines) combine to produce the overall PSD, the fit line of which is shown in black.

The 3D graphical map (Figure 3-6) of particle concentration generated by the Nanosight was found to be in good agreement with the calculated percentage of particles present within each peak of the fit (Tables 3-6).

Overall there is a greater intensity reported in the top layer (Figure 3-6) of the sample coinciding with a marginally wider PSD and greater calculated peak area (Table 3-6) suggesting the majority of the nano and fine particles are located near the surface of the suspension after the stirring has ceased.

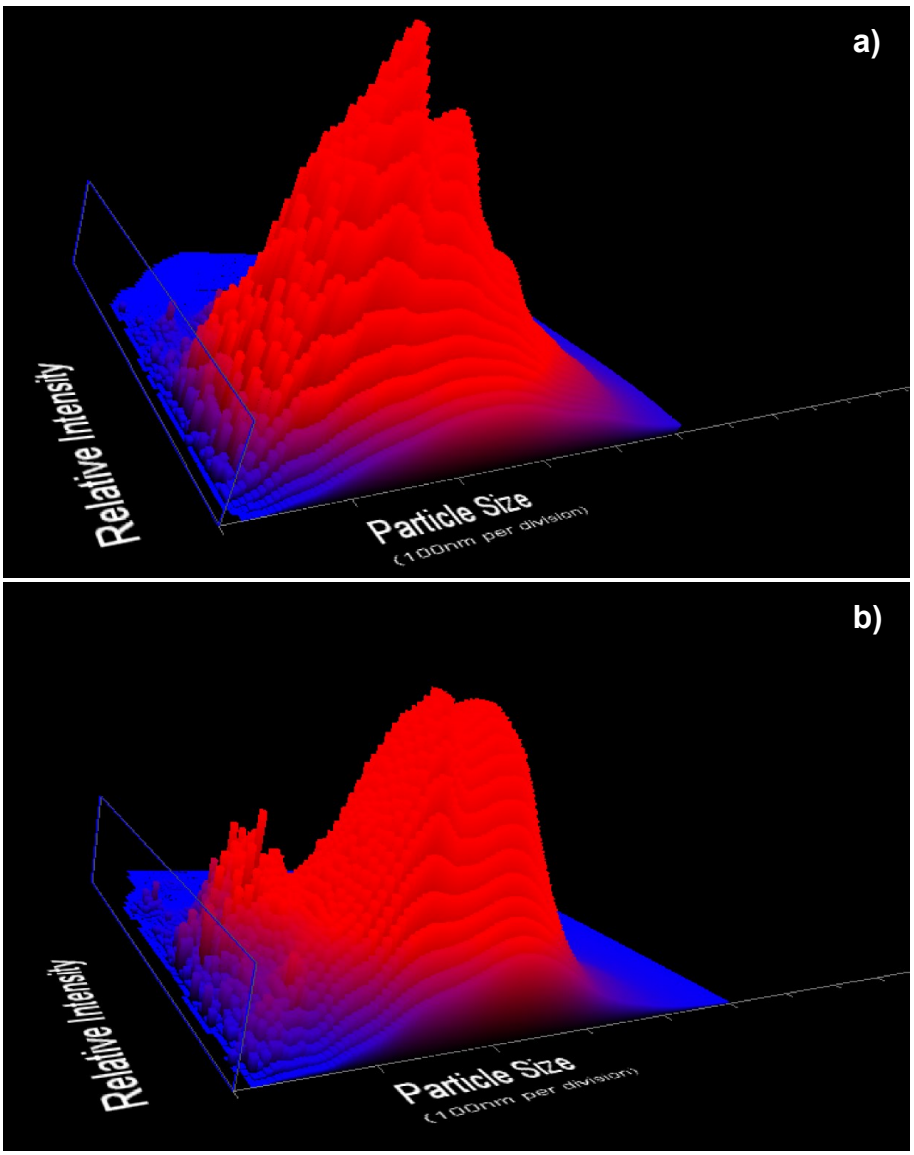

Figure 3-6: 3D Graphical PSD for $Ca(OH)_2$ a) top and b) bottom samples giving indication of the number and intensity of particles of each size within the distribution. Blue shows areas of lowest particle concentration. Red shows areas of highest particle concentration.

Sample	Peak	μ (log_{10}(d), μm)	σ (log_{10}(d), μm)	Area (log_{10}(d), μm^2)	Percentage of particles
Top	1	-1.83	0.05	0.01	0.94
	2	-1.64	0.07	0.14	10.45
	3	-1.45	0.10	0.31	23.30
	4	-1.24	0.12	0.39	29.22
	5	-1.08	0.05	0.12	9.34
	6	-0.98	0.03	0.02	1.18
	7	-0.88	0.09	0.21	15.72
	8	-0.72	0.05	0.06	4.35
	9	-0.62	0.04	0.02	1.54
	10	-0.51	0.08	0.05	3.75
	11	-0.19	0.04	0.003	0.22
Bottom	1	-1.91	0.005	0.02	2.55
	2	-1.84	0.01	0.002	0.29
	3	-1.77	0.02	0.007	1.15
	4	-1.68	0.02	0.007	1.06
	5	-1.58	0.07	0.06	9.86
	6	-1.46	0.04	0.04	5.97
	7	-1.35	0.06	0.08	12.26
	8	-1.17	0.08	0.17	28.30
	9	-0.98	0.05	0.07	10.96
	10	-0.89	0.04	0.04	6.95
	11	-0.73	0.08	0.11	18.14
	12	-0.60	0.04	0.01	2.16
	13	-0.45	0.04	0.002	0.36

Table 3-6: Numerical data resulting from the peak fitting shown graphically in Figure 3-5.

NTA can allow the determination of the < 1 μm region to a much greater degree than LD and can make clear features within the range obscured by the heavy agglomeration of particles and the limitations of LD itself.

3.1.8 SEM Imaging of Particles

A small quantity of sample was dropped by pipette onto a SEM sample stub and allowed to dry. All samples were coated with a thin Au layer, which minimised charging effects when viewing the samples at high magnification, in preparation for analysis. A Hitachi S-4700 SEM was employed to image the samples at a variety of magnifications.

SEM allowed the hexagonal morphology of the $Ca(OH)_2$ particles to be clearly seen, which complements the crystallographic XRD identification.

SEM images of particles generated in the first experiment of set 1 (Figure 3-7) suggest that they are reasonably weak particles and that the centre of the particles

implode under vacuum leaving the hexagonal shell reasonably intact. It can also be seen that the particle size is larger than that visible in later SEM images. This is in accordance with PSD's of this experiment.

Figure 3-7: SEM image of $Ca(OH)_2$ particles from set 1, experiment 1, synthesis. It can be seen that the center of the particles appear to have imploded leaving the frame intact. Scale bar is 20 μm.

Particles generated in the other experiments of set 1 (Figure 3-8) appear solid in their hexagonal morphology in that they have not imploded under vacuum. There is also the suggestion of some particles sticking together forming aggregated clumps of particles. Such aggregates could be misrepresented by PSD techniques as large particles instead of a group of smaller particles clumped together. Despite the presence of NaCl as indicated by testing with $AgNO_3$ no NaCl precipitation is evident in many of the SEM images. The $AgNO_3$ test is highly sensitive and so with only a very small quantity of NaCl present in the whole sample the test would still yield a positive result.

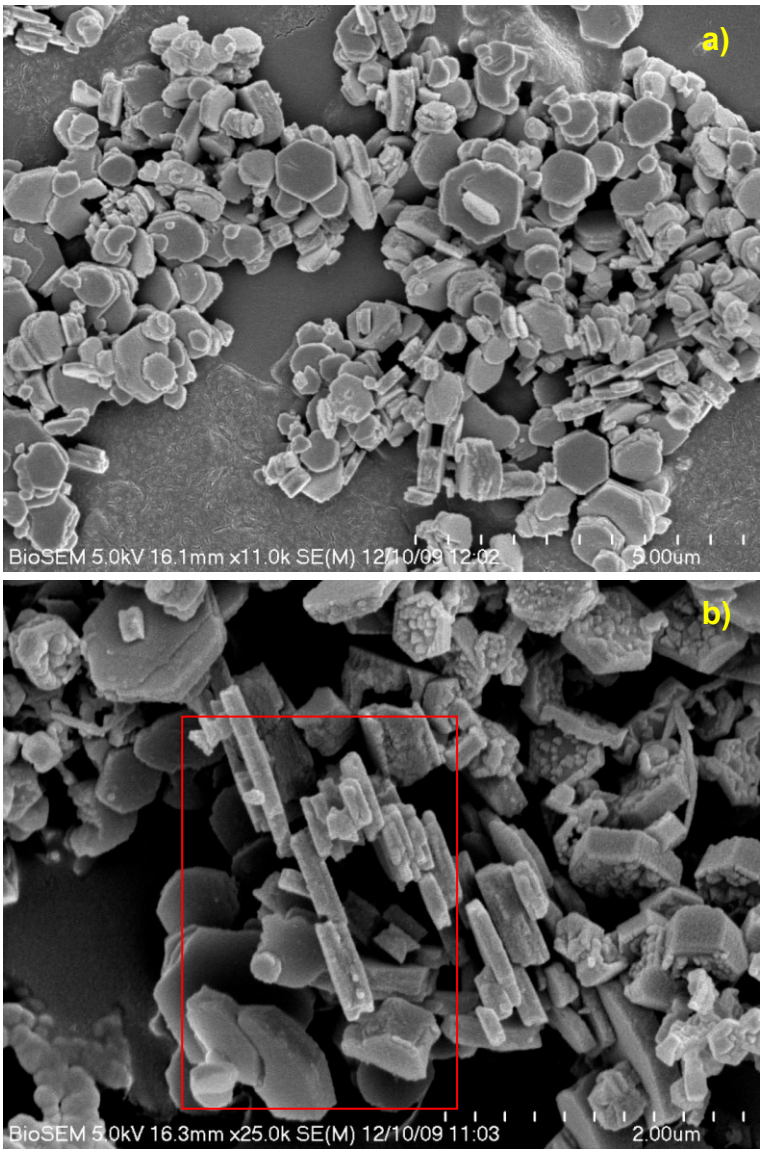

Figure 3-8: SEM images of $Ca(OH)_2$ particles from a) set 1, experiment 2, synthesis (scale bar is 5 μm) and b) set 1, experiment 3, synthesis (scale bar is 2 μm). Clear examples of aggregated particles are present within the red box.

After exposure to air gradually the particles carbonate due to reaction with atmospheric carbon dioxide. The particles undergo morphological changes in the reaction and become triangular dagger-like structures (Figure 3-9) in addition to having an apparent increase in size.

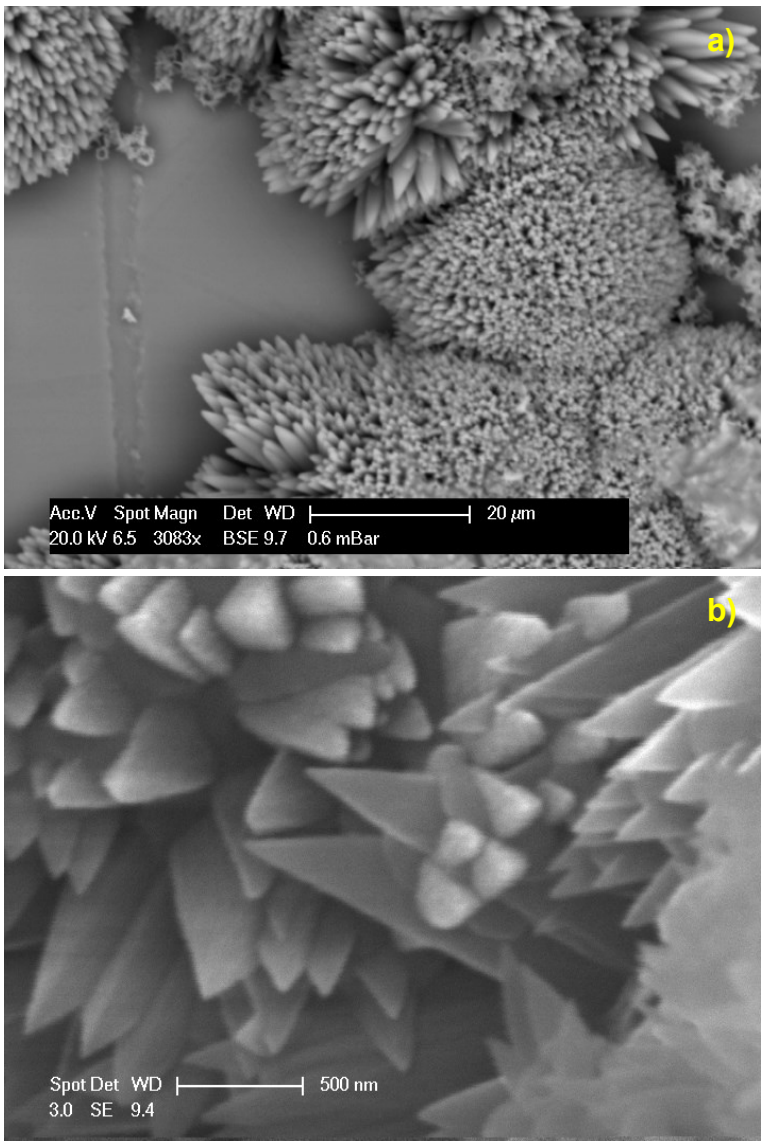

Figure 3-9: SEM images of $Ca(OH)_2$ particles carbonated by exposure to air over 1 week, a) scale bar is 20 µm, b) scale bar is 500 nm. The images show the dagger-like morphology obtained from slow carbonation in air.

3.1.9 Discussion

It is clear from the XRD results that the product of the synthesis is indeed $Ca(OH)_2$ particles. The SEM imaging shows that the particles have a hexagonal morphology.

Reaction conditions can strongly alter the PSD of the resulting product particles. It was found that altering base concentration resulted in the largest influence on PSD followed by altering both reagent concentrations in line with the

reaction balanced equation. Altering the $CaCl_2$ concentration by contrast was found to have a far less significant effect on the PSD and nano and fine particles in particular. Varying temperature was found not to significantly affect the PSD width and had only a slight effect on the nano and fine particle region compared to increasing reagent concentration. It was also found that the higher the pH and Na^+ concentration the lower the degree of aggregation and therefore the higher the suspension stability.

These results suggest that pH and ion concentration are of more importance as determining factors than ionic strength which is in agreement with the results of Plassard et al. (2005). This therefore suggests that under the conditions of high pH and ion concentrations aggregation is not as favoured as standard colloid stability theory may suggest considering solutions of high ionic strength. The reason for standard colloid stability theory stating that at high ionic strengths particles should aggregate is due to the effect of the high ionic strength compressing the diffuse double layer therefore allowing the attractive forces to have a stronger effect than repulsive forces (Israelachvili 2006). It has been shown that DLVO cannot always adequately describe colloid stability in concentrated salt solutions. Hamilton et al. (2010) observed an extra repulsion at short range which screened the attractive forces in a potassium sulphate system.

Mastersizer PSD data suggests that agglomeration of some particles can occur over time and that temperature does not significantly alter the PSD width of synthesised $Ca(OH)_2$ particles. The largest decrease in particle size (decrease in PSD width) systematically throughout an experimental set was found to occur in set 3 with experiment 6 giving the smallest distribution. As particle size (overall taken as PSD width) is linked to stability this shows that aggregation is less prevalent under the conditions of set 3 and therefore the stability of the suspension over the time length of the experiment is greater. Here the surface charge of the particles has passed through the PZC, due to the pH now being over 13, meaning that the surface charge is now negative (El Shafei 1996). Consequently the Stern layer is now composed of positively charged ions such that substitution of divalent cations with monovalent cations results in entropic effects. Due to the noticeably marked increase in particle formation and stability below 1 μm it may be reasonable to suggest that a

negative surface charge in combination with high pH and Na^+ concentration supports particle repulsion. In terms of particle yield the best result was obtained with the balanced reaction equation conditions with concentrations of 0.3 M and 0.6 M for $CaCl_2$ and NaOH respectively at room temperature.

It is apparent that the Nanosight PSD results are more in keeping with the visualization of the particles by SEM than the Mastersizer PSD results. The Nanosight technique is not highly biased towards larger particles unlike with the LD technique and so can give a more accurate representation of the sample distribution in the size range below 1 μm.

It should be noted that the Mastersizer gives results in terms of equivalent spherical volume whereas the Nanosight can give the results in terms of concentration, number and volume. When the NTA volume results are plotted on the same graph as the LD volume results it can be seen that there is a high level of agreement between the two techniques (Figure 3-10).

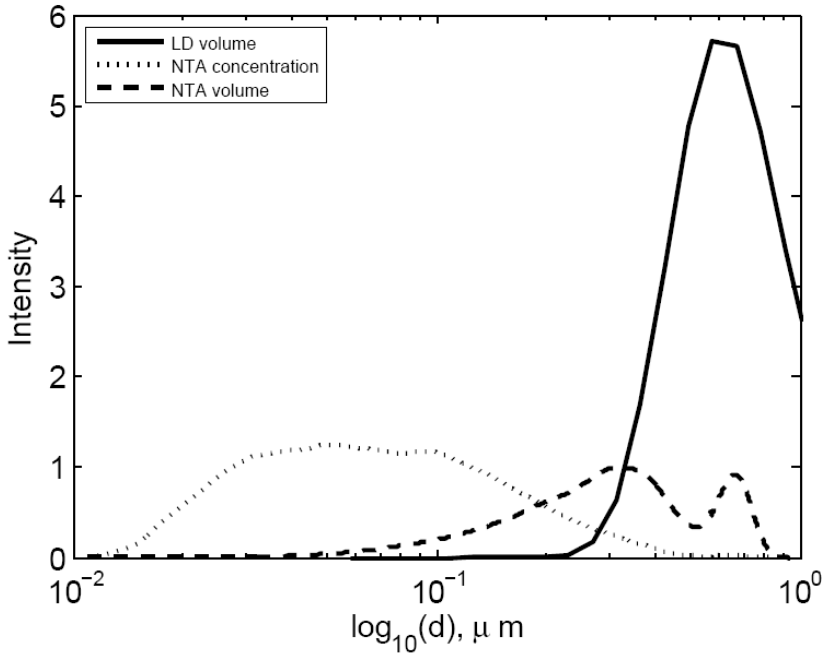

Figure 3-10: Submicron region comparison for LD and NTA PSD graphs of particles formed from set 1 experiment 3 synthesis reaction.

Using both the LD Mastersizer technique in conjunction with the Nanosight NTA system allows better definition of the submicron PSD region as well as providing clear information on the overall PSD.

From SEM images it is clear that the $Ca(OH)_2$ particles possess hexagonal morphology and that synthesis at room temperature with very low concentration reagents results in weak particles. It is apparent in SEM images that the majority of particles have a diameter below 1 μm which is in agreement with the Nanosight results. Also noticeable is that groups of particles clump together forming aggregates which could reasonably account for the larger particles observed in the PSDs obtained by the LD technique.

Natural carbonation in air of the hexagonal $Ca(OH)_2$ particles resulted in triangular dagger-like $CaCO_3$ particles which appear to have a larger size than the original particles. Although it was unlikely that significant carbonisation had occurred within the time of PDS analysis a small amount of carbonisation cannot be completely ruled out and could also be a contributing factor to the gradual increase in PSD over time.

Ambrosi et al. (2001) measure the size of their particles by SEM and TEM. They do not use a particle distribution sizing technique. The quantity of particles able to be clearly mounted on SEM and TEM stubs is very small in order to view the particles as seen in Ambrosi et al.'s images (Figure 3-11). Therefore, to represent the entire precipitate formed a great many, well over 100, SEM and TEM stubs would need to be prepared, imaged and analysed. In their paper Ambrosi et al. (2001) speak of the particles as having the length of the hexagonal particle sides between 100 – 300 nm. They do not discuss the size ranges of aggregated particles or degree of aggregation. It is possible that the particles they see in their SEM and TEM images are, as they suggest single particles, and that the larger aggregated clumps of particles have just not been transferred to the sample stubs simply due to the sheer number of samples required. Alternatively it is possible that aggregates are present in their images and they have just sized the individual particles composing the aggregate. Also the size estimates of Ambrosi et al. (2001) are the lengths and thicknesses of the sides of the hexagonal particles not the particle diameter.

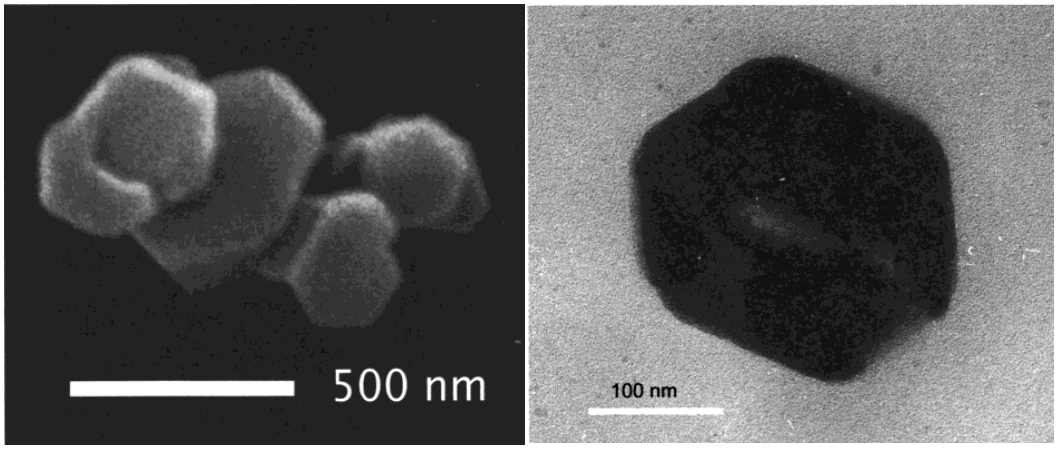

Figure 3-11: Images of Ambrosi et al.'s particles taken from Ambrosi et al. (2001). Left: SEM image of $Ca(OH)_2$ particles, scale bar 500 nm. Right: TEM micrograph of a single $Ca(OH)_2$ particle, scale bar 100 nm.

The SEM images of this study are comparable to those of Ambrosi et al. (2001) as are the individual single particle dimensions obtained in this study by NTA and SEM. By using proper particle sizing techniques to size the $Ca(OH)_2$ produced in this study, the aggregation and how this is affected by reaction conditions, can be clearly seen. The SEM images of this study also show that aggregation occurs edge to edge.

3.2 Commercially Available Calcium Hydroxide Nanoparticles

A commercially available nanolime, known as CaLoSiL, was created as part of the STONECORE Project (Ziegenbalg 2008) and has been extensively used in field test sites in this European Multinational Project (Maryniak-Piaszczynski et al. 2008; Askew 2011; Ziegenbalg 2011). Despite this, not much knowledge about this product and its abilities in the heritage conservation field is known. In this section this commercial nanolime has been analysed so that it can be compared with laboratory synthesised nanolimes discussed previously.

3.2.1 X-Ray Diffraction Analysis

XRD analysis, to confirm that the commercial product was indeed $Ca(OH)_2$, was performed according to the procedure described in section 3.1.2.

The resulting XRD pattern for the commercial CaLoSiL sample can be matched to the library pattern for $Ca(OH)_2$ (Figure 3-12) meaning that the commercial product is indeed $Ca(OH)_2$ in the absence of additives. It could also be noted that there are no significant differences between the commercial product and the synthesised $Ca(OH)_2$ from their XRD spectra.

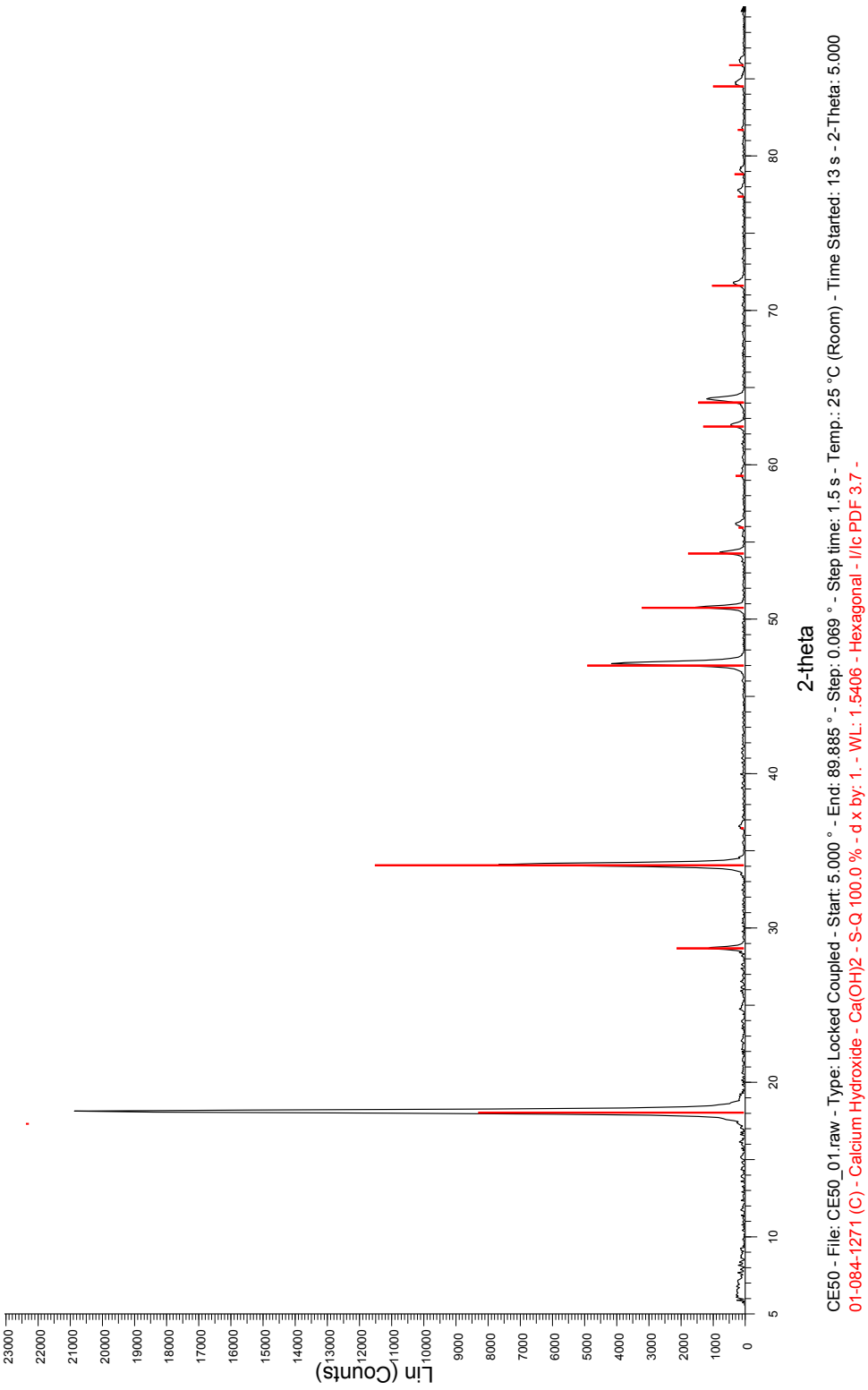

Figure 3-12: XRD spectrum obtained from CaLoSiL compared to library pattern.

3.2.2 Particle Sizing by LD

Particle sizing was carried out, in a Mastersizer S as previously described in section 3.1.3, on CaLoSiL and carbonated CaLoSiL samples. CaLoSiL was carbonated with a DiLoCarb/H_2O mixture where DiLoCarb was a diethyl carbonate specifically meant for carbonating CaLoSiL. This was carried out to determine the effect of carbonation on the PSD of CaLoSiL.

It was found that a one-component fit was sufficient to fit the experimental data for CaLoSiL as can be seen in Figure 3-13a. Data was plotted on a log scale for ease of viewing. The PSD is of high concentration (Table 3-7) and shows that the particles are all significantly < 1 μm in size. This shows that the CaLoSiL suspension completely consists of highly stable particles meaning that the repulsive forces dominate the system preventing aggregation.

Carbonation results in an increased variance of the original peak and the formation of a second peak representing particles above 1 μm diameter which accounts for approximately 35 % of the particles (Figure 3-13b and Table 3-7). This suggests that carbonation results in an increase in particle size and an increase in particle agglomeration suggesting the repulsive forces are now less effective. It is also possible that not all CaLoSiL particles have been carbonated, in which case there would be a mixture of $Ca(OH)_2$ and $CaCO_3$ particles within the suspension. Depending on pH this could lead to a complex system as the pH at PZC (pH_{PZC}) of both species is different ($Ca(OH)_2$ pH_{PZC} = 12.7 – 12.9 (El Shafei 1996), $CaCO_3$ pH_{PZC} = 8 – 9.5 (Somasundaran & Agar 1967)).

Sample	Peak	μ (log_{10}(d), μm)	σ (log_{10}(d), μm)	Area (log_{10}(d), μm^2)	Percentage of particles
CaLoSiL	1	-0.32	0.07	6.54	100.00
Carbonated CaLoSiL	1	-0.19	0.14	4.32	64.29
	2	0.65	0.29	2.40	35.71

Table 3-7: Numerical data resulting from the peak fitting shown graphically in Figure 3-13.

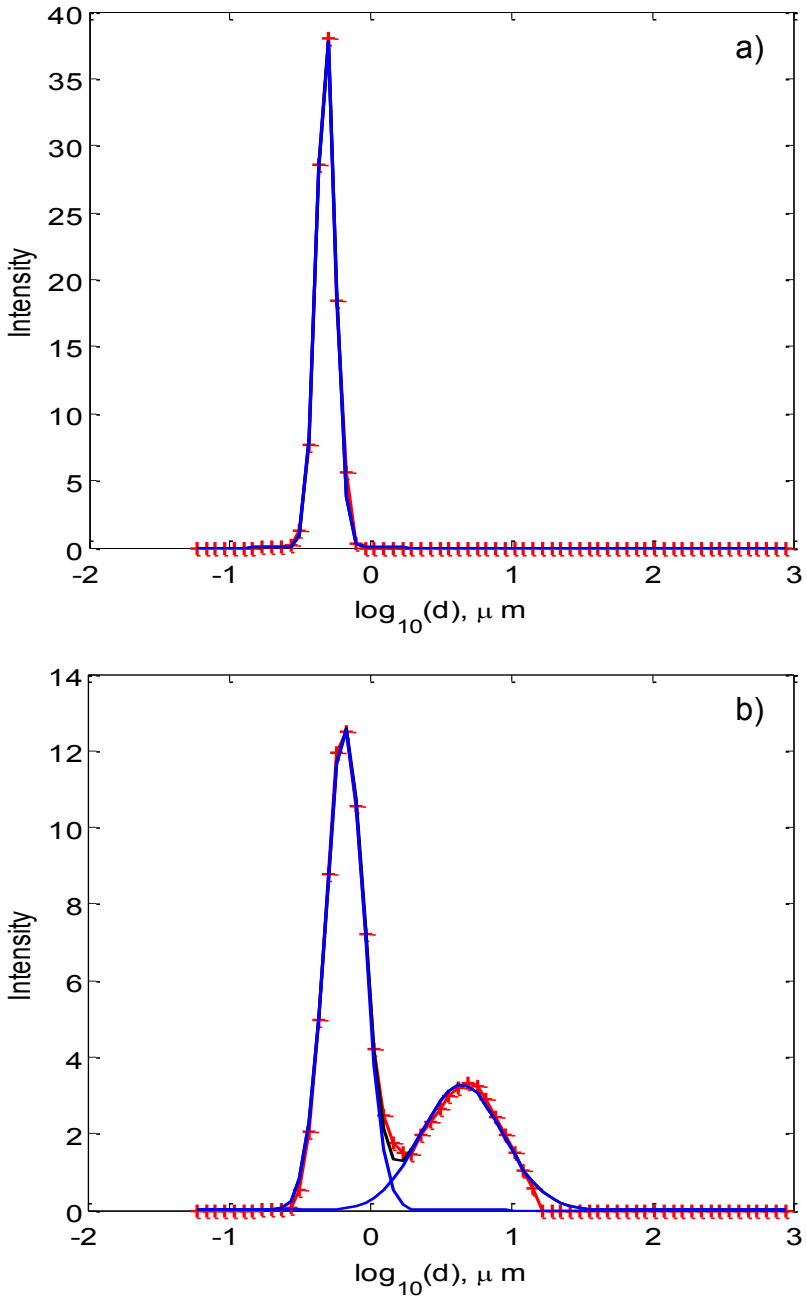

Figure 3-13: Peak fitting of mean experimental data (red stars) for a) CaLoSiL with one-component fit (in blue) and b) carbonated CaLoSiL (calcite) with two-component fit (in blue). The figure shows the fit line of each PSD in black.

3.2.3 Particle Sizing by NTA

Analysis of Calosil and carbonated CaLoSiL by NTA was carried out as described in section 3.1.6.

It was found that the particles are all < 400 nm in size and occur in three clear groups (Figure 3-14). It can be seen in Figure 3-16 that the greatest concentration of particles exists in the size range 100 – 250 nm meaning that these are in fact fine particles not nanoparticles due to the recognised definition of the two (as discussed in Chapter 1). In fact only approximately 30 % of particles present in CaLoSiL are by proper definition nanoparticles.

It can be seen that the fine and nano particles existed in groups within the distribution which was found to be much more complex than for the PSD obtained from LD. A log normal distribution was fitted to the NTA PSD for both the uncarbonated and carbonated samples which were found to require a five- and thirteen-component fit respectively (Figure 3-14).

The 3D graphical map (Figure 3-15) of particle concentration generated by the Nanosight was found to be in good agreement with the calculated percentage of particles present within each peak of the fit (Table 3-8).

Sample	Peak	μ ($\log_{10}$(d), μm)	σ ($\log_{10}$(d), μm)	Area ($\log_{10}$(d), μm^2)	Percentage of particles
CaLoSiL	1	-1.24	0.09	0.09	6.37
	2	-1.11	0.07	0.35	24.10
	3	-0.99	0.07	0.36	24.88
	4	-0.89	0.03	0.11	7.76
	5	-0.81	0.10	0.54	36.91
Carbonated CaLoSiL	1	-1.91	0.01	0.001	0.36
	2	-1.86	0.01	0.0004	0.29
	3	-1.78	0.01	0.001	0.64
	4	-1.68	0.03	0.01	5.20
	5	-1.54	0.06	0.02	11.12
	6	-1.41	0.09	0.02	13.54
	7	-1.27	0.07	0.02	16.11
	8	-1.18	0.03	0.01	6.41
	9	-1.09	0.05	0.02	11.33
	10	-0.89	0.04	0.02	12.97
	11	-0.77	0.04	0.01	4.85
	12	-0.59	0.03	0.01	4.35
	13	-0.55	0.12	0.02	12.83

Table 3-8: Numerical data resulting from the peak fitting shown graphically in Figure 3-14.

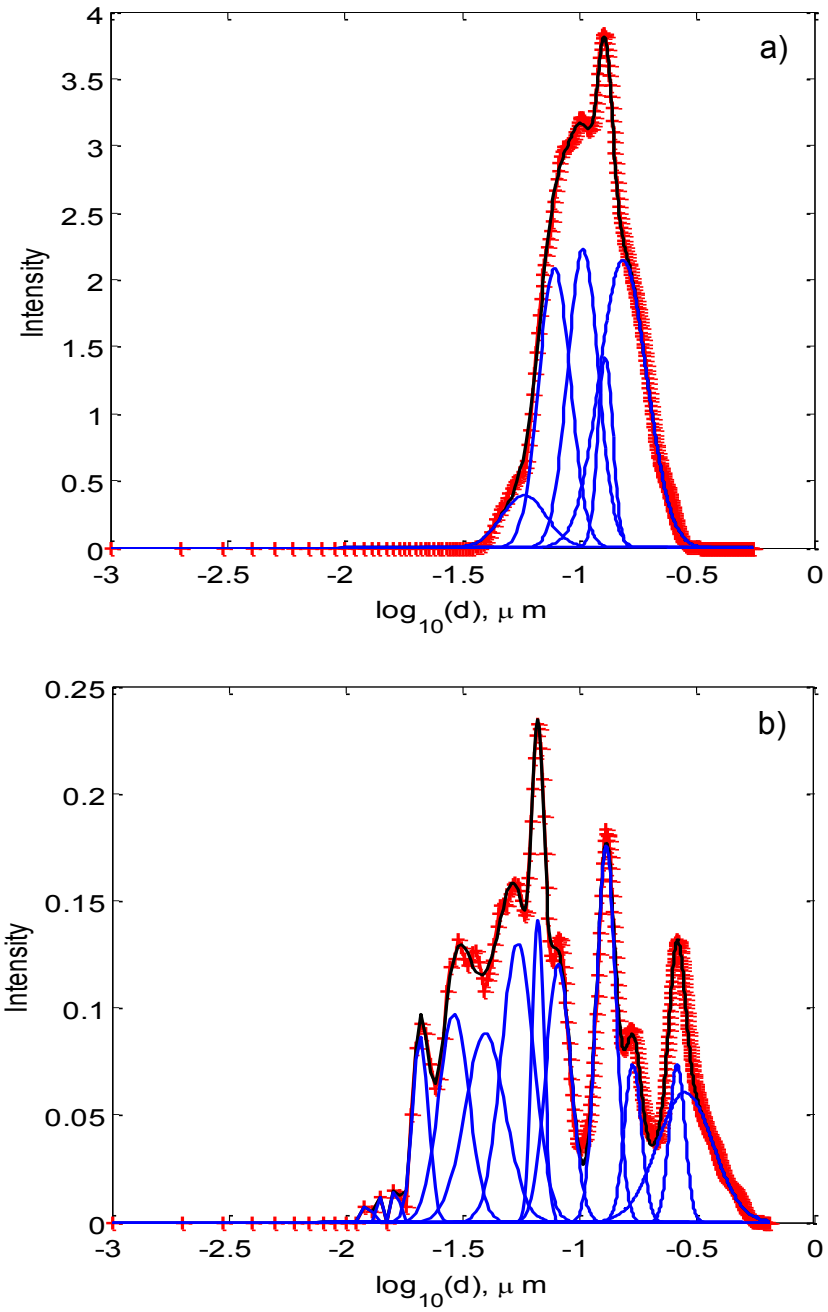

Figure 3-14: Peak fitting of PSD data (red stars) for a) CaLoSiL E25 sample with five-component fit and b) carbonated CaLoSiL E25 sample with thirteen-component fit. The figures show how the peaks (blue lines) combine to produce the overall PSD, the fit line of which is shown in black.

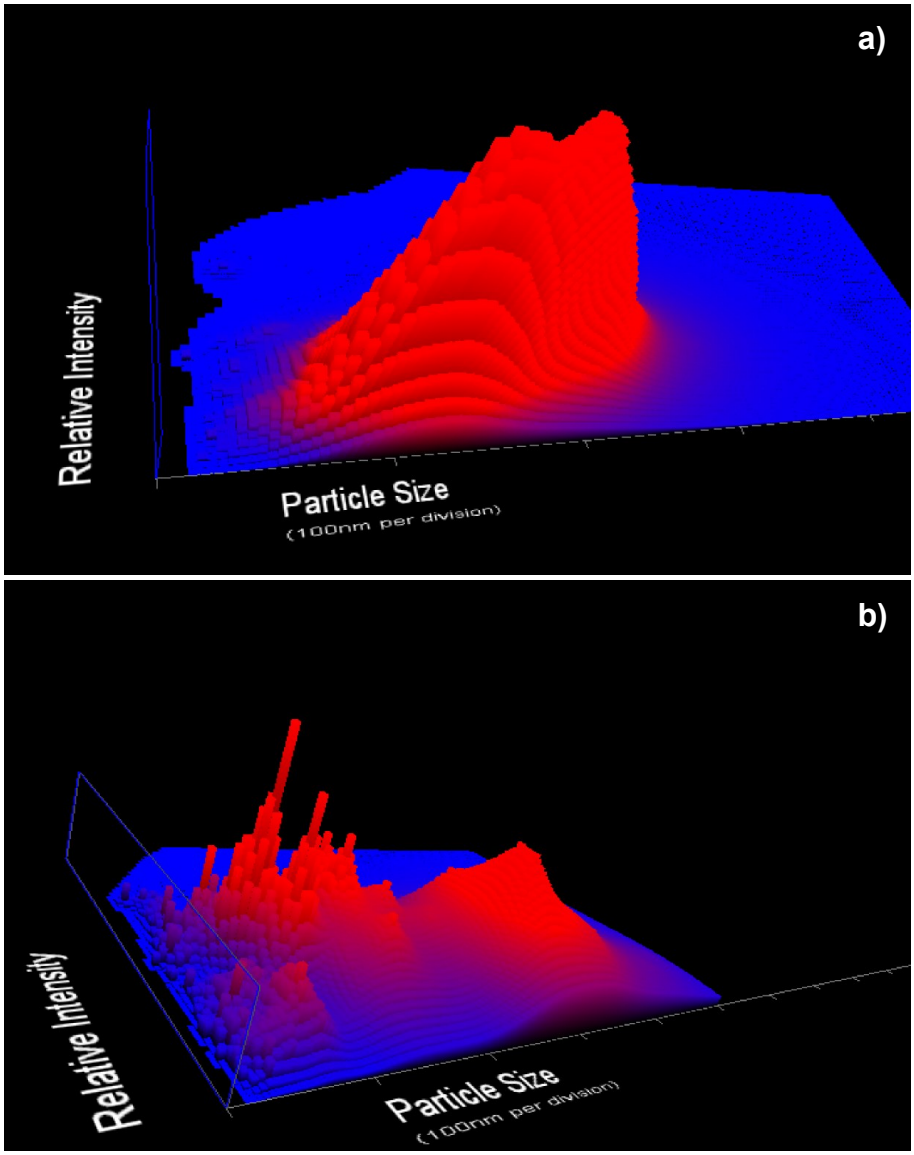

Figure 3-15: 3D Graphical particle size data for a) CaLoSiL and b) carbonated CaLoSiL samples giving indication of the number and intensity of particles of each size within the distribution. Blue shows areas of lowest particle concentration. Red shows areas of highest particle concentration.

After carbonation there is a noticeable change in the PSD which becomes slightly wider, now reaching up to about 550 nm, and is in three clear sections, each of which contains several size groups of particles (Figure 3-15b). It could be possible that the low nm particles have avoided carbonation whilst the larger particles are now

calcite; however this is by no means certain. It can be seen in Figure 3-16b that the greatest concentration of particles exists throughout the PSD in several apparent particle groups.

All the detail exhibited in the NTA data is not visible in the LD data due to the limitations of LD under 1 μm. Overall there is a greater intensity reported in the uncarbonated CaLoSiL sample (Figure 3-15a) whilst the carbonated sample exhibits a lower arbitrary intensity in conjunction with a wider PSD and lower calculated peak area (Table 3-8). This suggests that carbonation of the particles could either increase particle size or frequency of agglomeration as seen within the NTA range.

3.2.4 SEM Imaging of Particles

Samples of CaLoSiL and carbonated CaLoSiL, coated with a thin Au-Ta layer, were analysed by SEM as previously described in section 3.1.8.

SEM allowed the hexagonal platelet morphology of CaLoSiL to be clearly seen. It can be seen in Figure 3-16a that all particles have dimensions below 300 nm, which is in accordance with the Nanosight results and in close agreement with the Mastersizer PSD. After carbonation the particles are anhedral (Figure 3-16b) and again the observed size range was found to be in good agreement with that of the particle sizing techniques.

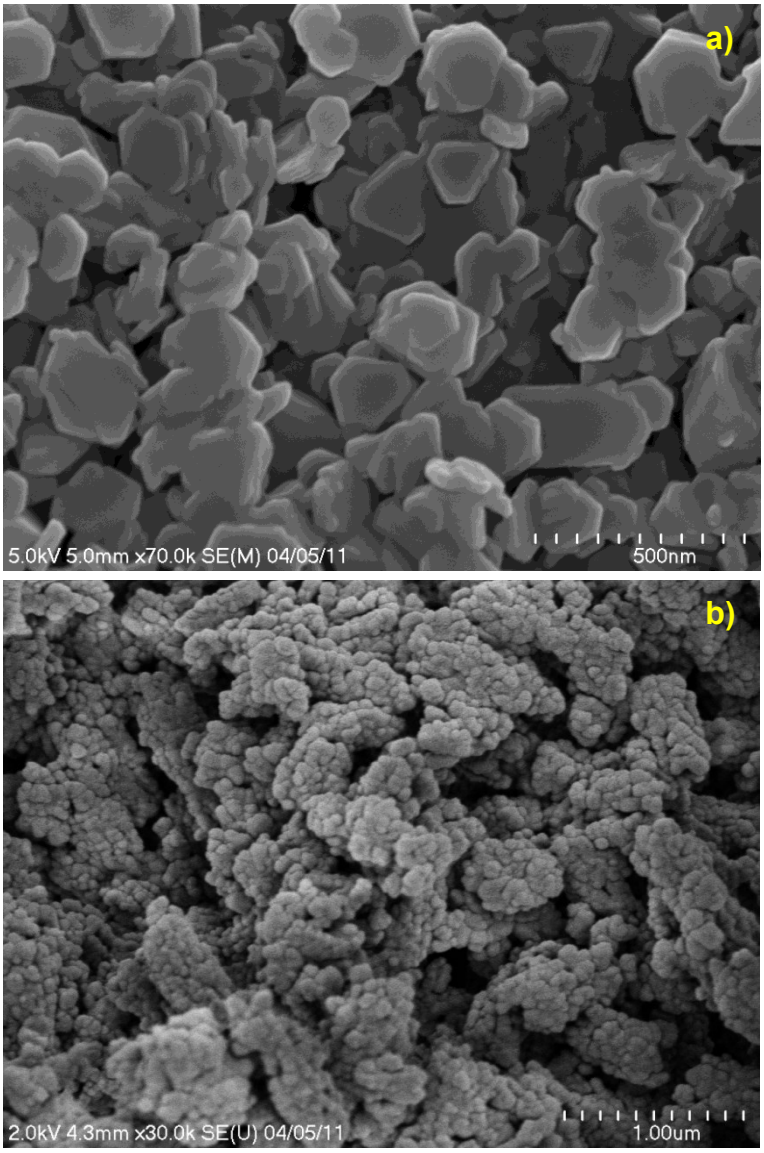

Figure 3-16: SEM image of a) CaLoSiL, showing hexagonal particle morphology (scale bar is 500 nm) and b) carbonated CaLoSiL, showing anhedral morphology (scale bar is 1 μm).

3.2.5 Discussion

It is clear from the XRD results that CaLoSiL does indeed consist of $Ca(OH)_2$ particles without any significant sign of additives. From SEM images it is clear that the CaLoSiL particles possess hexagonal morphology, becoming anhedral after carbonation, and have a diameter below 500 nm which is in agreement with the Nanosight results and in close agreement with the Mastersizer results. An anhedral structure is formed after carbonation due to the fast rate of reaction compared with natural reaction in air.

The Mastersizer PSD results show that the particles exist in one clear group and that all are significantly below 1 μm in size. After carbonation there is an increase in the PSD width in conjunction with the formation of a clear second group of particles. This suggests that repulsive forces dominate the system in the case of pure CaLoSiL and that the effect of these forces are reduced overall, compared with the effect of the systems attractive forces, after carbonation.

It is apparent that the CaLoSiL Nanosight volume PSD results are in reasonable agreement with the Mastersizer volume PSD results and the visualization of the particles by SEM. The results for carbonated CaLoSiL are in reasonable agreement with the Mastersizer data, however the Nanosight does not suggest such a large size increase. The Nanosight data is also much clearer resolved and exhibits more detail such that it can be seen that the particles do not exist in one clear group but in fact occupy five and thirteen size groups for uncarbonated and carbonated CaLoSiL respectively.

An attempt was made to study carbonation of CaLoSiL in the Nanosight but was discarded due to finding that the DiLoCarb/water mixture registered on the instrument as containing particles which would not be able to be distinguished from the $Ca(OH)_2$ particles.

It is clear that despite being marketed as a ‘nanolime’ only 30% of CaLoSiL particles are true nanoparticles (Schwartz et al. 1999; Donaldson et al. 2004; BSI 2011, Potocnik 2011) with the majority being more accurately defined as fine particles.

3.3 Conclusions

Both the wet synthesised $Ca(OH)_2$ and commercial CaLoSiL have hexagonal morphology and are present in both nano and fine particles. It was also seen that aggregation tends to occur in an edge to edge orientation.

It can be concluded that sustaining submicron particles or submicron agglomerates formed by this wet synthesis method is very difficult due to the instability of this state over time under these conditions. Due to particle aggregation it is difficult to obtain stable nano and fine particles, although the stability in this region is improved slightly by increasing pH. Obtaining true nanoparticles alone appears improbable as even the commercial product consists of a majority (approximately 70 %) of particles that should truly be defined as fine particles (Schwartz et al. 1999; Donaldson et al. 2004; BSI 2011, Potocnik 2011).

The rate of carbonation is instrumental in determining the structure of carbonated particles. Dagger-like morphology is obtained through slow natural carbonation in air whilst fast carbonation with a carbonising agent leads to an amorphous particle structure. Carbonation destabilises the CaLoSiL suspension allowing the well dispersed particles to agglomerate as they are altered from $Ca(OH)_2$ to $CaCO_3$.

This could be seen as a desirable effect when applying the treatment with the aim of conserving the surface of an object or structure. First the CaLoSiL suspension is applied to the surface where it would penetrate a certain distance. This treatment could be repeated if desired. Then the application of the carbonising agent would carbonate the particles, causing them to change morphology and allow them to agglomerate slightly. This would theoretically decrease the ability of particles to travel within the structure and increase the likelihood of particles adhering to the matrix of the material thereby consolidating the surface and immediate subsurface region of the material. In such situations the amorphous nature of the carbonated particles would be preferential to the dagger morphology observed from slow natural air carbonation as it would enable greater surface contact between particles and between the particles and the pore structure of the material.

Chapter 4:
Calcium Hydroxide Nanoparticles Applied to Limestone

Limestone conservation is relevant to both the built environment and museum artefacts (Ambrosi et al. 2001; Bradley 2005; Dei & Salvadori 2006). Processes of deterioration, such as salt crystallisation in pores and freeze-thaw damage, can cause cracking and are mediated by water transport (Hudson 1971; Hall & Hoff 2002). A recently developed conservation method aims to consolidate limestone by application of calcium hydroxide nanoparticles (Giorgi et al. 2000, Giorgi et al. 2010) which penetrate into the material and through carbonation form calcite resulting in consolidation and material strengthening (Drdácký et al. 2009).

Use of colloidal $Ca(OH)_2$ suspended in alcohol to consolidate stone is on the rise, particularly in Europe where several institutions and private companies have been engaging in both laboratory based research and field applications of this relatively new treatment (Ambrosi et al. 2001; Dei et al. 2006; Dei & Salvadori 2006; Daniele & Taglieri 2010; Ziegenbalg 2011; D'Armada & Hirst 2012). Part of the appeal lies in the ability to introduce a far greater concentration of lime to the substrate and to deeper penetration depths compared with traditional limewater treatments (D'Armada & Hirst 2012). Despite much research being undertaken over the last decade conservators require further information particularly regarding weathered stone (D'Armada & Hirst 2012). By focusing on a specific example (such as CaLoSiL, a commercial product developed for consolidating calcareous historic materials) a clearer explanation can be made. More research, particularly on weathered stone, is needed, due to much of the scientific testing and laboratory study of the effects of CaLoSiL having been undertaken on crushed stone, plaster or mortar as opposed to whole significantly sized pieces of weathered stone (Stonecore 2012). There is surprisingly little documentation regarding the use of CaLoSiL on weathered stone, even in field studies, and due to the nature of working on-site significant information, such as penetration depth and effect on water transport, has not been clearly determined (D'Armada & Hirst 2012; Stonecore 2012).

In this chapter the penetration depth and effects of CaLoSiL on water uptake in Portland and Lincoln stones are determined. These British limestones were used due to availability and relevance for British stone conservators who would find it beneficial to know the penetration depth of CaLoSiL they could reasonably expect in these stones and the resulting effect on water transport. Quarried Portland stone was

used to determine how fresh bimodal stone would react to different concentrations and number of CaLoSiL treatments. Weathered and unweathered medieval Lincoln stone was used to determine if the degree of weathering would give rise to differences in treatment effectiveness. Quarried Lincoln stone was also used to determine how the effect of CaLoSiL treatment differs between quarried and historical stone of various degrees of weathering. This study investigated ethanol based solutions of the minimum (5 g per litre (E5)), mid-range (25 g per litre (E25)) and maximum concentrations (50g per litre (E50)) on Portland stone and E25 on Lincoln stone. The adhesive strength of a nanolime based mortar known commercially as Repair Mortar, which was designed to repair detached surface pieces and is composed of calcium hydroxide and calcium carbonate nanoparticles in ethanol, (Maryniak-Piaszczynski & Ziegenbalg 2010) was also determined.

4.1 Treatment Effects on Quarried Portland Limestone

This section describes the effects on Portland limestone of colloidal calcium hydroxide nanoparticles dispersed in ethanol, available commercially under the trade name CaLoSiL. The effects of this conservation treatment on water uptake by the stone are discussed for the first time along with pore clogging by the treatment. Deterioration processes are driven by water flux; therefore understanding the impact on water movement and pore filling is essential. For the first time a numerical two-layer Sharp Front model of water absorption was applied to describe the imbibition behaviour exhibited by the samples. Depth penetration of the nanoparticles was investigated through scratching and drilling techniques which are novel methods for quantifying consolidation.

4.1.1 Portland Limestone

Portland limestone was chosen because of its popularity as a building material in the UK and its large fraction of small pores. Portland Base Bed (Figure 4-1) is a coarse bioclastic oolitic grainstone (Hudson 1971) with a bimodal pore size distribution (Dubelaar et al. 2003). Mercury intrusion porosimetry (MIP) data showed two pore throat size peaks characteristic of a bimodal structure with the maximum peak in the range 0.1 – 1.0 μm and a second peak at 2 – 20 μm giving a micro-porosity of around 60% (pores < 1 μm) as calculated from data published by Dubelaar et al. (2003, figure 5) presented here in Figure 4-2. The CaLoSiL particles have a diameter range of 0.05 – 0.25 μm which means that according to Figure 4-2, showing cumulative intruded pore volume against pore diameter, 35% of the pore space is accessible to the largest particle while 90% is accessible to the smallest particle. This highlights the high microporosity of Portland Base Bed and the need to achieve very small particles if deep absorption is desirable.

Figure 4-1: Photograph of Portland stone used in this study. The oolitic nature of the stone can be seen. The ruler provides a scale.

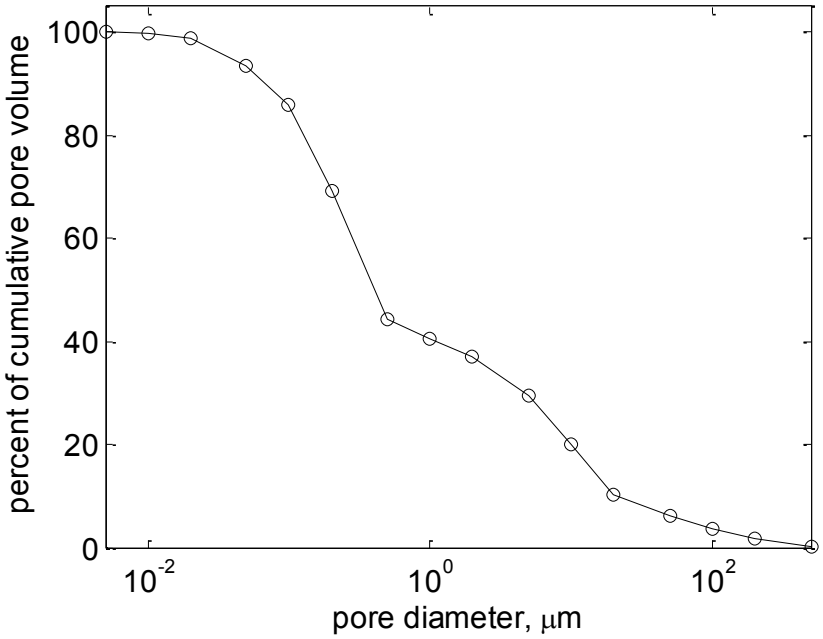

Figure 4-2: Percentage of cumulative pore volume against pore diameter from MIP data taken from Dubelaar et al. 2003.

4.1.2 Imbibition Experimental Procedure

Water and ethanol capillary absorption rate data was obtained using the standard procedure (Gummerson et al. 1980; Hall & Hoff 2012) on nine Portland stone blocks of approximately 7 cm × 7 cm × 9 cm. Initially dry material was placed in contact with the test liquid in a shallow tray at room temperature (Figure 4-3). The weight gain of each sample was measured at 5 minute intervals over a 30 minute time period. Samples were exposed to de-ionised water and ethanol imbibitions before treatment and again after the final treatment and carbonation. This was performed to determine the sorptivity of each of the 9 samples before and after treatment.

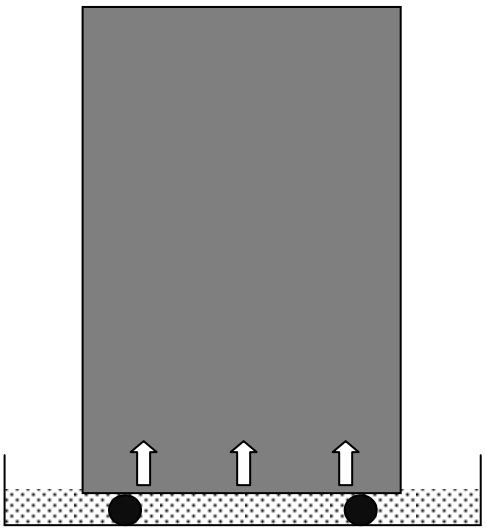

Figure 4-3: Diagram of imbibition experiment showing a sample block sitting on supports in a dish containing the imbibition liquid. The arrows show the direction of liquid uptake.

Treatment of the quarried Portland stone blocks with CaLoSiL was undertaken using the standard procedure for capillary absorption of a liquid (Gummerson et al. 1980; Hall & Hoff 2012) at room temperature (Figure 4-3). The weight gain of each sample was measured every 5 minutes and at the end of the treatment uptake after 30 minutes. E5, E25 and E50 CaLoSiL suspensions were used here. Samples were subjected to 1, 5 or 10 treatment cycles to identify any differences due to number of treatments. A total of 9 samples were used, 3 for each CaLoSiL concentration, with a sample exposed to 1, 5 or 10 treatments. Samples

were oven dried overnight at 80°C after each treatment, then allowed to cool before the next treatment. After the final treatment, the treatment in the samples was carbonated using a commercial ethanol based diethyl carbonate known as DiLoCarb-E. This reacted with the calcium hydroxide particles to produce calcite faster than reaction with atmospheric CO_2 alone. A solution was made using a 1:1 ratio by mass of DiLoCarb-E to de-ionised water and allowed to absorb into the blocks for 4.5 hours to ensure full exposure to the solution.

4.1.3 Imbibition Results

Sorptivity was measured with water and ethanol prior to treatment, CaLoSiL sorptivity was measured during treatment and water sorptivity was measured after treatment and carbonation with DiLoCarb-E. From this data, the mass of CaLoSiL actually in the stone, the expected mass of CaLoSiL in the stone, expected volume percent of pores filled and how far up the stone the CaLoSiL solution or water should travel (height of rise) could be determined. In calculating the expected volume percent of pores filled, an estimate was made of the amount of trapped air in the pores by comparing the capillary moisture content (obtained by imbibition) and total moisture content (obtained by vacuum saturation). Air trapping in Portland Base Bed was 16 – 25% of the total pore space.

The change in composite sorptivity ranged from 3 – 15% varying with treatment type (E5, E25 and E50) and number of treatments as shown in Table 4-1. From mass measurements before and after treatment (and carbonation) it became clear that fewer CaLoSiL particles were entering the stone than expected (see Table 4-1) with roughly 5 – 37% of the expected mass of CaLoSiL particles actually remaining in the stone. This suggested two possible models for the distribution of particles within the stone: a thin dense layer or a wide sparse layer. Scratching and DRMS could detect no difference in resistance as discussed below, therefore further tests were carried out to determine the treatment penetration depth.

	E5			E25			E50		
Property	1×E5	5×E5	10×E5	1×E25	5×E25	10×E25	1×E50	5×E50	10×E50
Sw(u) (mm / $min^{½}$)	0.47	0.28	0.42	0.35	0.25	0.34	0.46	0.34	0.26
Sw(tc) (mm / $min^{½}$)	0.43	0.25	0.35	0.32	0.22	0.30	0.45	0.33	0.23
Se(u) (mm / $min^{½}$)	0.32	0.21	0.28	0.25	0.18	0.24	0.34	0.24	0.19
Se(tc) (mm / $min^{½}$)	0.32	0.20	0.28	0.24	0.17	0.24	0.33	0.25	0.19
HORw (mm)	13.2	7.5	10.7	9.6	6.6	8.7	13.4	9.6	6.2
HORe (mm)	9.6	5.9	8.1	7.4	5.1	6.8	9.8	7.4	5.6
vol %	0.22	1.1	2.2	1.1	5.5	11.1	2.2	11.1	22.1
$mass_e$ (g)	0.05	0.15	0.35	0.2	0.63	1.65	0.41	1.74	2.45
$mass_a$ (g)	>0.01	0.04	0.07	>0.01	0.05	0.21	0.10	0.12	0.14

Table 4-1: Measured and calculated property values for CaLoSiL and DiLoCarb-E treated Portland stone. Sw(u) is the water sorptivity of the block prior to any treatment. Sw(tc) is the water sorptivity of the block after a set number of treatments (1, 5 or 10) with CaLoSiL and then carbonated with DiLoCarb-E. Se(u) is the ethanol sorptivity of the block prior to any treatment. Se(tc) is the ethanol sorptivity of the block after a set number of treatments (1, 5 or 10) with CaLoSiL and then carbonated with DiLoCarb-E. HORw and HORe (height of rise) is how far up the block the imbibing liquid (water and ethanol respectively) travels and was calculated from the final imbibition test with water on the carbonated block. Actual mass, $mass_a$, of particles in the block was measured gravimetrically after oven drying and between CaLoSiL treatment cycles. The $mass_e$, expected mass, was calculated from known mass of CaLoSiL solution entering the stone with each cycle and the vol %, expected volume percent, of pore space filled was calculated from the expected mass.

It can be seen (Table 4-2) that the CaLoSiL suspension sorptivity is less than that of pure ethanol. This is due to the presence of the CaLoSiL particles which reduce the ethanol sorptivity by an average of 21% as the particles are carried into the stone. Overall, when the experiment runs to 10 treatments, the CaLoSiL sorptivity decreases as number of treatments increase although the sorptivity does increase in the middle of the treatment cycle. This increase occurs after 3 – 4 treatments in all samples where the experiment finished after 5 treatments. By the end of the 3rd or 4th treatment the build up of white mist on the surface was so extreme that wiping the surface between treatments was necessary to remove build-up which then allows the stone surface to be accessed by the imbibing solution. The high degree of surface build-up was not anticipated thus wiping was not performed from the first treatment. After initial wiping, the sorptivity seemed to increase again and the stones were wiped after every treatment. The second decrease in nanolime sorptivity is not due to significant surface coating but to pore blocking in the stone interior.

	Sn (mm / $min^{½}$)								
No. of treatments	E5			E25			E50		
	1×E5	5×E5	10×E5	1×E25	5×E25	10×E25	1×E50	5×E50	10×E50
1	0.264	0.173	0.223	0.214	0.144	0.195	0.223	0.191	0.146
2	-	0.156	0.228	-	0.137	0.189	-	0.193	0.146
3	-	0.175	0.231	-	0.130	0.206	-	0.193	0.144
4	-	0.172	0.217	-	0.149	0.197	-	0.194	0.146
5	-	0.169	0.212	-	0.149	0.195	-	0.187	0.146
6	-	-	0.203	-	-	0.195	-	-	0.145
7	-	-	0.198	-	-	0.191	-	-	0.145
8	-	-	0.195	-	-	0.178	-	-	0.143
9	-	-	0.189	-	-	0.179	-	-	0.141
10	-	-	0.186	-	-	0.178	-	-	0.139

Table 4-2: Variation of CaLoSiL sorptivity, Sn, with treatment type and number.

Overall, the water sorptivity (S) of the composite sample (CaLoSiL layer and bare stone) was reduced by at least half of the final reduction observed (after 10 treatments) after the first treatment for E5 and E25. E50 however appeared to reduce the sorptivity by very little until 10 treatments.

High water sorptivity reduction, resulting in an impermeable thin layer is not desirable as it may encourage surface flaking from salt crystallisation or freeze-thaw. This smaller reduction in sorptivity, produced by CaLoSiL absorption, is more likely to avoid these damage mechanisms. The efficacy of CaLoSiL in consolidating stone was examined by Maryniak-Piaszczynski et al. (2008) who found that CaLoSiL with a concentration less than 36 g/L in combination with Funcosil silicic ester successfully consolidated surface flakes, however no quantitative analysis was carried out. Maryniak-Piaszczynski et al. (2008) also found that CaLoSiL concentrations over 36g/L produced a white mist on the stone surface which is in agreement with my observations (Figure 4-4). It was noticeable that the white mist extended above the area of the stones that had been in direct contact with the treatment. The nature of this white mist can be clearly seen using scanning electron microscopy (SEM) (section 4.1.4).

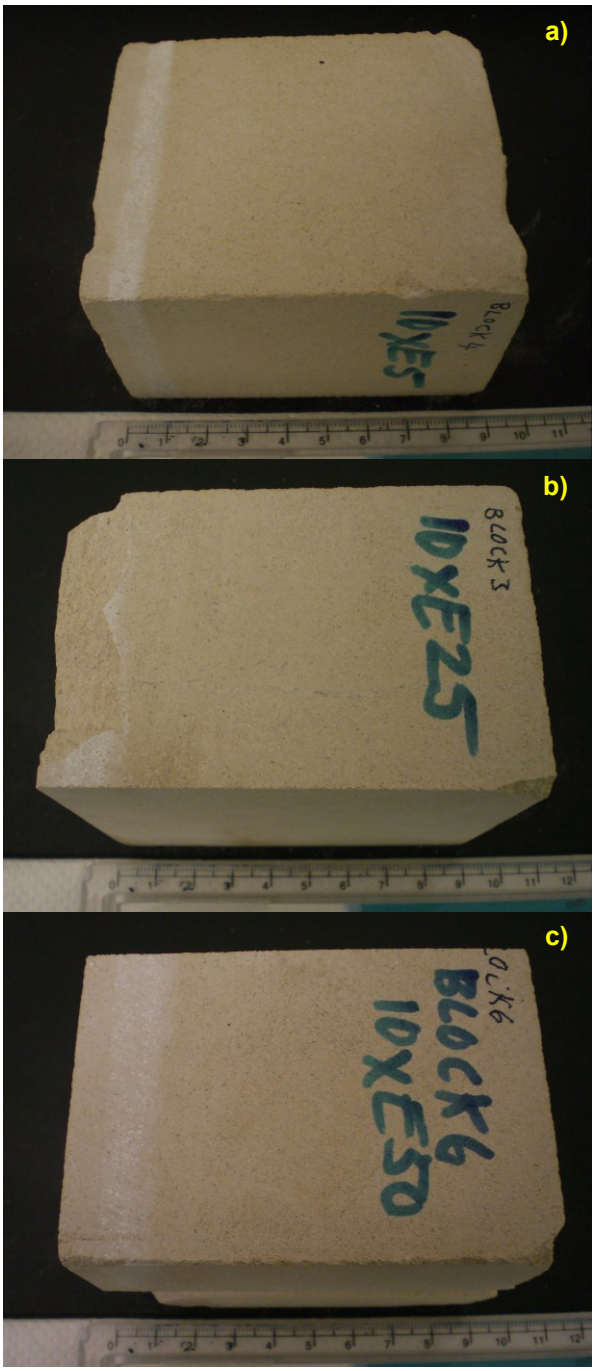

Figure 4-4: Photographs of treated Portland stone blocks treated with a) 10×E5, b) 10×E25 (missing sections of treated area were removed for SEM and optical microscopy investigations) and c) 10×E50. The images show the white treatment build-up on the surface of the stones (left side of all stones) which can be clearly seen in contrast with the rest of the stones which have not encountered the treatment. The ruler in each image gives scale.

4.1.4 SEM Imaging

Stone chips were removed from an untreated reference stone and a stone treated with five treatment cycles of E50 before and after carbonation. These stone fragments were coated with a thin Ta-Au layer and imaged by SEM as described in section 3.1.8.

Figure 4-5 shows SEM images of stone treated with five cycles of E50 before and after carbonation compared to the surface of untreated stone. After treatment with E50, there was a surface layer of hexagonal platelet CaLoSiL particles, which became anhedral after reaction with DiLoCarb-E.

These results show that the white mist is comprised of a build-up of CaLoSiL particles on the surface of the treated stone. Having such a strong surface build-up of CaLoSiL particles implies that the particles have difficulty breaching the stone surface to a certain degree. If the particles were easily able to penetrate into the pore network they would travel away from the surface into the stone. It is reasonable to postulate that the visible strength of the white mist build-up on the surface may increase with successive treatments. This will be influenced by the pore diameters, concentration of treatment applied and the number of applications.

The greater the quantity of particles applied to the surface, through either higher concentrated suspensions or higher number of treatments, increases the likelihood of the smallest accessible pores being blocked. Larger pores can be lined by particles thereby reducing the available pore diameter through which other particles can pass. Both pore blocking and pore lining can have the effect of restricting paths available for future particle movement.

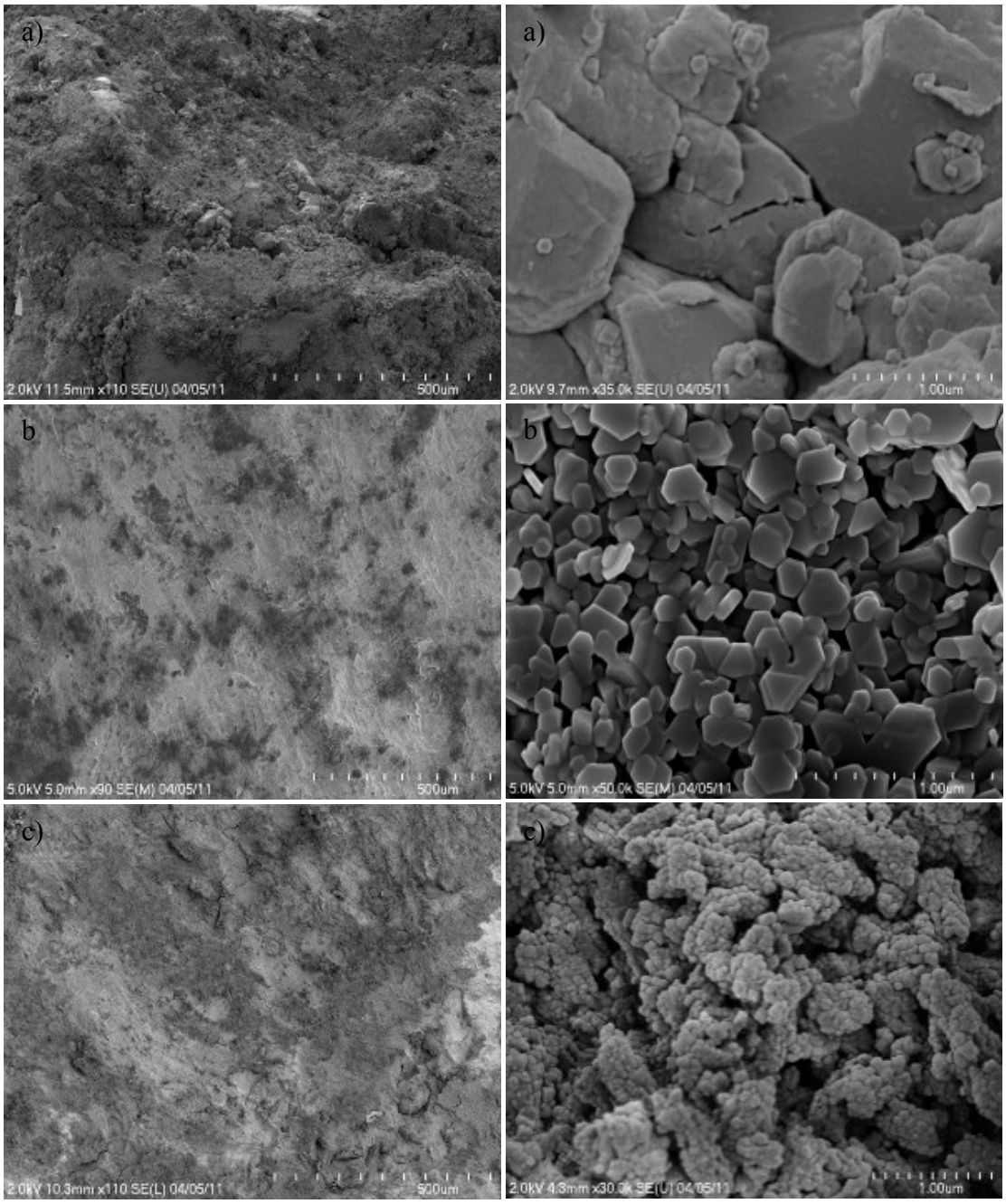

Figure 4-5: SEM images showing, at different magnifications a) (top, left and right) untreated Portland stone, b) (middle, left and right) treated Portland stone, and c) (bottom, left and right) treated and carbonated Portland Stone. For all left images the scale bar is 500 μm. For all right images the scale bar is 1 μm.

4.1.5 Penetration Depth Experimental Procedure

A micro-destructive method known as the 'scratch' test was used with the aim of determining treatment depth. By tracing several shallow grooves on the surface of the stone the depth penetration of the treatment into the stone could be determined. The normal (F^c_n) and tangential (F^c_s) forces acting on the cutter as the sample surface was scratched were recorded. Gradually the depth of cut could be increased. The instrument employed for these tests was an Epslog Engineering WOMBAT Scratch Tool equipped with a 10 mm wide sharp diamond cutter. Data analysis was performed using Epslog Engineering software. The scratches were carved into the stone samples at a depth of 0.10 cm along the entire length of the samples. This test was carried out at the University of Cyprus by Ms Modestou.

Drilling tests were also performed at the University of Cyprus by Ms Modestou using a Drilling Resistance Measurement System (DRMS) to obtain precise readings. The device, supplied by SINT Technology, was set to operate at 600 rpm using a 5 mm diameter diamond drill bit while the holes were drilled to a depth of 30 mm. This system enables precise drilling resistance measurements on stone, providing a prediction of toughness and uniaxial compressive or flexural strength.

I also identified the location of the CaLoSiL particles within the stone by means of optical microscopy at the University of Edinburgh. Dry stones were cut after CaLoSiL imbibition and tested with phenolphthalein indicator which turned the $Ca(OH)_2$ pink. The stones were then examined under a stereo microscope fitted with a camera. Imaging software was then used to determine the depth of CaLoSiL penetration.

4.1.6 Penetration Depth Results

WOMBAT and DRMS tests (Figure 4-6) do not detect any real difference in resistance between blank reference and treated samples. This showed that CaLoSiL was not adding resistance to the material through its action which suggested that it might be possible that the treatment was only lining the pores and not acting to block them. If the treatment was increasing the surface strength of the material the initial

force applied would be expected to be significantly higher than, and very quickly drop to, the force required for the rest of the sample. Results in Table 4-1 showing the expected volume percentage of pore space filled is an expression of the maximum possible mass of particles entering the stone only and does not differentiate between particles blocking pores and lining them.

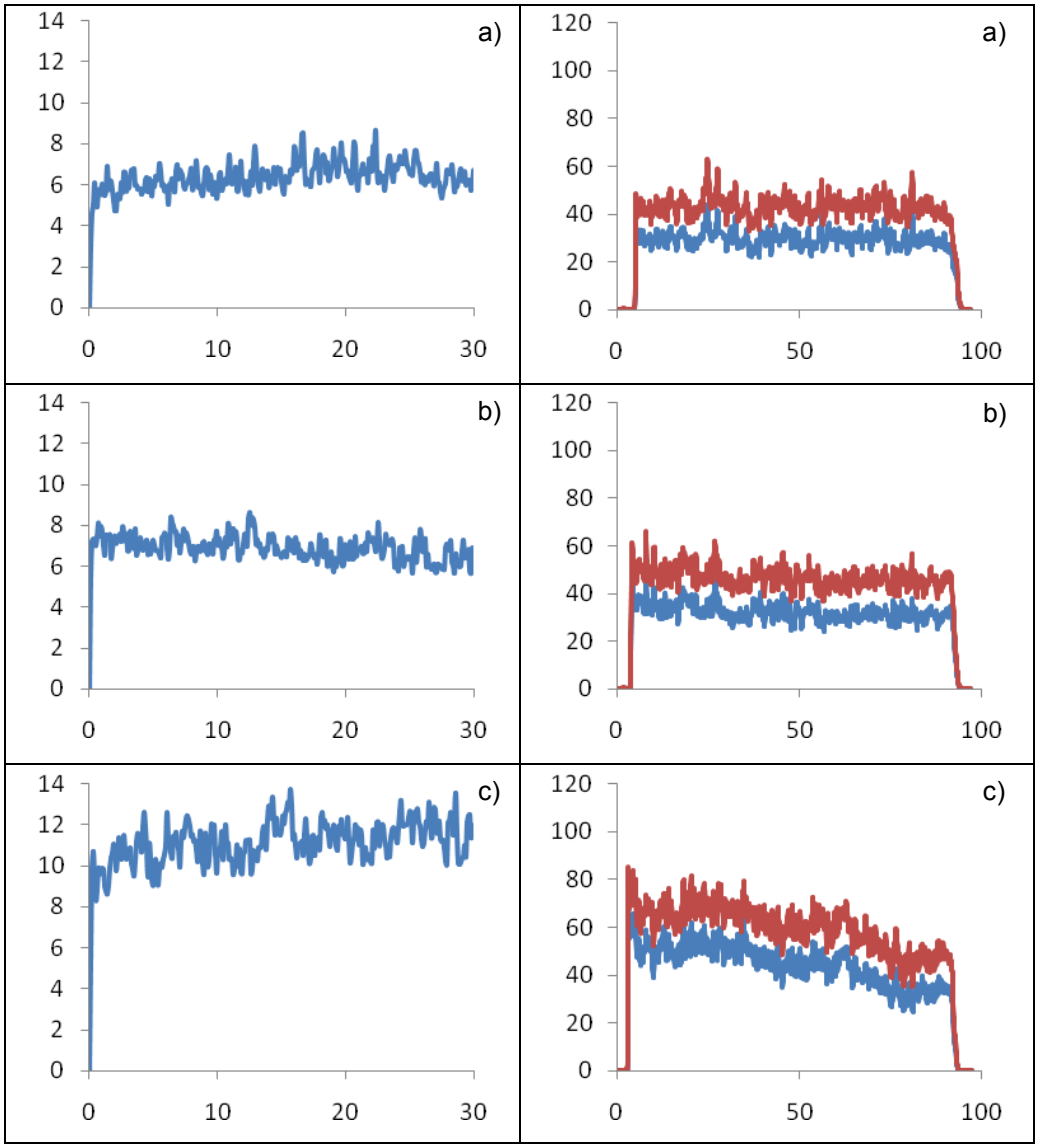

Figure 4-6: DRMS (left) and WOMBAT (right) data for E50 stone samples with a) one treatment cycle, b) five treatment cycles and c) ten treatment cycles. All y-axes are force in N and x-axes are distance travelled in mm. For WOMBAT data red line is tangential force and blue line is normal force.

Through optical microscopy it was found that the depth of penetration was no more than 400 μm (Figure 4-7). This is in agreement with the imbibition results and suggests that CaLoSiL forms a thin and dense layer, opposed to a wide sparse layer, in the stone. The properties of this CaLoSiL layer were determined by modelling as discussed below. It was clear that CaLoSiL did not penetrate far into this stone and as such could only be used to treat surface features. The bimodal pore structure of Portland Base Bed with its high percentage of fine pores is perhaps unusual but should accommodate 35 – 90% of the CaLoSiL particles.

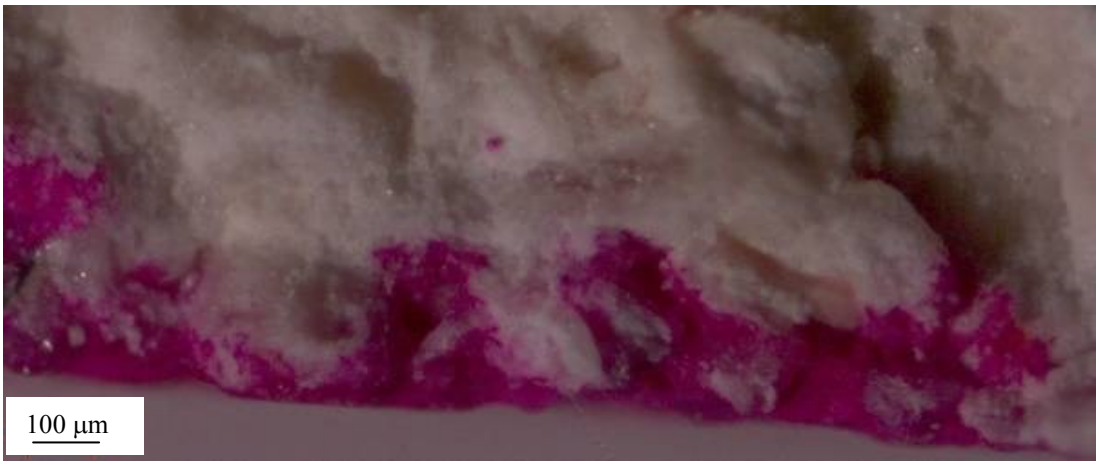

Figure 4-7: Stereomicroscope image of Portland stone treated with one CaLoSiL E25 imbibition exposed to phenolphthalein (pink region shows positive reaction indicating presence of CaLoSiL). Scale bar is 100 μm.

4.1.7 Modelling Procedure

All samples are treated as two-layer composite materials into which the capillary absorption of water was analysed using Sharp Front theory (Wilson et al. 1995; Hall & Hoff 2012). The CaLoSiL treated layer and untreated stone were considered two layers, A (of fixed length L) and B (indefinite length). Water was applied to the face of A and the wet front progressed through the composite. Known variables were the measured sorptivity of the composite, sorptivity of the untreated stone and the layer thickness (without carbonation) as determined by optical microscopy. Unknowns were the sorptivity, porosity and permeability of the CaLoSil treated layer, which could be estimated from gravimetric data of particle uptake. Knowing this allowed

the determination of the water transport properties of the CaLoSiL layer itself and then pore filling. Water rise into the sample ($i_1 + i_2$ in mm) is given by Equations 4-1 and 4-2. Equation 4-1 shows the contribution of the treated layer:

4-1) $$i_1 = S_A(t_1)^{1/2}$$

4-2) $$i_2 = S_B(t_2 + L^2X)^{1/2} - LY$$

where:

4-3) $$X = \left(\frac{f_B}{S_B}\right)^2 \left(\frac{K_B}{K_A}\right)^2 - \left(\frac{f_A}{S_A}\right)^2$$

4-4) $$Y = f_B \frac{K_B}{K_A} - f_A$$

Here *S, f, K* and *t* are the sorptivity, porosity, permeability and time respectively (subscript indicates material) and *L* is the length of the CaLoSiL layer.

4.1.8 Modelling Results

Water transport properties of the CaLoSiL layer and pore filling were investigated using depth information from optical microscopy and by comparing experimental imbibition data (after treatment and carbonation) with predicted imbibition from the sharp front model. Shown in Figure 4-8 is water uptake in a block treated ten times with E25 and carbonated with DiLoCarb-E. Fitting the experimental data with the model confirmed that CaLoSiL existed as a very thin layer which was known to be approximately 0.4 mm thick (from optical microscopy) reducing the porosity from 19% to 14% in the treated layer, based on the known quantity of CaLoSiL particles in the stone after 10 treatments. The corresponding estimated permeability reduction was around 60%, based on the relationship between permeability and porosity. Sorptivity of the layer was difficult to determine experimentally as the layer was very thin but it was also estimated from the porosity reduction (for detail on sorptivity, permeability and porosity, and how they are related, see Chapter 2).

As shown in Figure 4-8, the upwards curve modelled at early time (blue line) before one minute corresponds to water flow through the thin CaLoSiL layer. The

downwards curve in the experimental data (black circles) at later time probably resulted from a band of stone with lower sorptivity. Portland Base Bed is known to have features such as vugs, small to medium sized cavities usually lined with crystals, (Roels 2000) which affect water movement. As the thickness of the CaLoSiL layer is increased the curve becomes increasingly like the red curve (shown here with a layer thickness of 5 mm). As the experimental data did not agree with the fit of the red curve this confirmed that the CaLoSiL layer was thin and remained permeable.

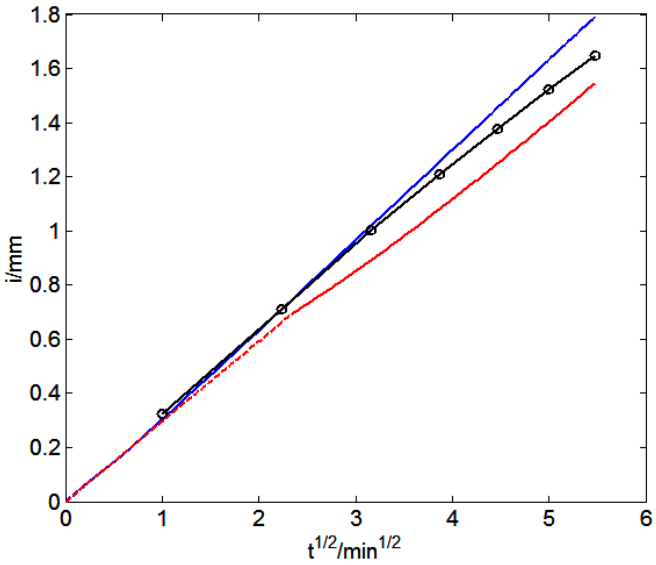

Figure 4-8: Model (blue and red) versus experimental (black) water uptake data for Portland stone after ten treatments of CaLoSiL E25 and carbonated. Blue dashed curve (s = 0.30, K = 0.0004, f = 0.14, L = 0.4 mm) is uptake through A, blue solid curve (s = 0.33, K = 0.0005, f = 0.19) is uptake through B. Red dashed curve (s = 0.30, K = 0.0004, f = 0.14, L = 5 mm) is uptake through A, red solid curve (s = 0.33, K = 0.0005, f = 0.19) is uptake through B.

4.1.9 Discussion

Treatment of intact Portland Base Bed with CaloSiL resulted in a measured 2 – 15% reduction in stone sorptivity varying with number of treatments and CaLoSiL concentration. The first application resulted in the most sizable reduction in measured sorptivity overall. CaLoSiL was found to exist as a very thin permeable layer (~0.4 mm thickness) and ten treatments of E25 resulted in a porosity reduction from 19% to 14% in the CaLoSiL layer and estimated permeability reduction by 60%, in this case, in the layer. The compressive strength of CaLoSiL treated stone appeared unaffected as determined by DRMS and scratch tests. Imbibition with CaLoSiL resulted in a very thin layer which did not significantly block pores. Despite the small CaLoSiL particle size, it did not travel far into the pore network in this case.

4.2 Treatment Effects on Quarried and Medieval Lincoln Limestone

This section describes the effects of commercially available CaLoSiL on Lincoln limestone. Water uptake tests on Medieval and quarried untreated samples and samples exposed to CaLoSiL treatment were used to investigate the effect of the particles on imbibition behaviour. The water transport properties were modelled in a Sharp Front analysis and compared to the experimental data. The effect of particles on open pore space is also discussed as is depth of penetration. How water uptake differs between the unweathered and weathered surfaces of medieval Lincoln stone will also be discussed. Portland stone, as previously noted, was fresh and unweathered. As previously mentioned this medieval Lincoln stone has both weathered and unweathered regions and is being used here to understand how the treatment is absorbed into friable weathered stone.

Although Lincoln stone has been almost exclusively used for Lincoln Cathedral, and so this study is relevant to the future care of this historic landmark; how the treatment affects similar weathered, unweathered and quarried stone is of wider interest to the conservation community.

4.2.1 Lincoln Limestone

Lincoln is a rarely used limestone, almost exclusively used for Lincoln Cathedral (UK), a gothic Cathedral dating from the late 12^{th} century. The quarried Lincoln stone (Lincoln silver bed, middle Jurassic, bed depth 333 mm) was from Lincoln Quarry whilst the weathered medieval stone dating from the 1300's was removed from Lincoln Cathedral (south east transept triforum level) during a recent restoration project.

Lincoln limestone was used as it was possible to obtain new quarried, weathered and unweathered stone exposed since the Middle Ages. In this study it was found that Lincoln is a highly microporous bioclastic oolitic grainstone with a unimodal pore size distribution with a pore throat size range of 0.01 – 10 μm.

The pore size distribution of each stone type (quarried, medieval weathered and medieval unweathered) was measured by mercury porosimetry (Figure 4-9). A known mass of sample, held within the sample cell, was subjected to LP then HP intrusion and extrusion MIP using a Quantachrome Porosimeter. The resulting merged data was analysed to determine the pore size distribution of each of the samples.

The resulting MIP graphs can be seen in Figures 4-9 & 4-10. The quarried stone was taken from a different area of the quarry from where the medieval stone originated several hundred years ago. Stone originating from different locations within a quarry will show some variety in pore size and pore size distribution. As such relating the newly quarried stone to the medieval in terms of porosity is not useful. MIP indicates that weathered medieval stone has the lowest porosity whilst the unweathered end of the stone block has the highest porosity.

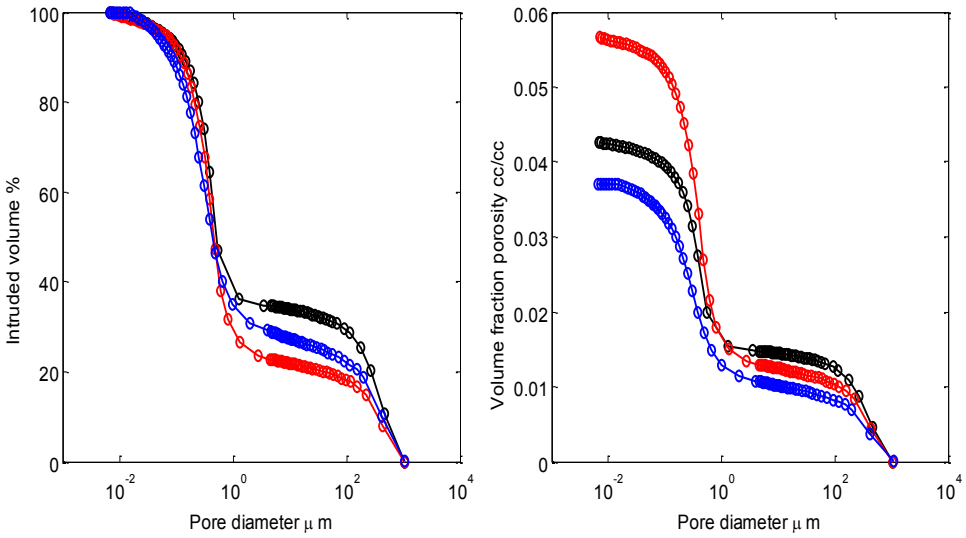

Figure 4-9. MIP data for Lincoln Stone showing intruded volume % (left) and volume fraction porosity (right) for quarried stone (black), medieval unweathered stone (red) and medieval weathered stone (blue).

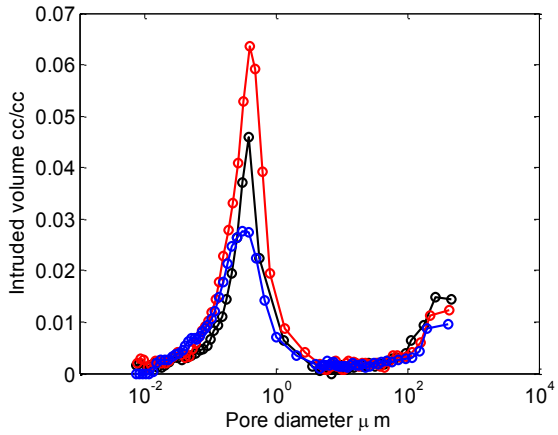

Figure 4-10. Lincoln Stone pore size distributions for quarried stone (black), medieval unweathered stone (red) and medieval weathered stone (blue).

XRD analysis was carried out on a slice of medieval stone to determine the mineralogy of the stone and any minerals causing pore blocking, such as gypsum. The weathered surface layer was removed and labelled as level 1. The slice was then sectioned horizontally at 1 cm intervals from the top to the bottom of the block giving five height levels which were labelled from 2 (top level) to 6 (bottom level). This gave a total of six levels including the surface weathered layer (Figure 4-11).

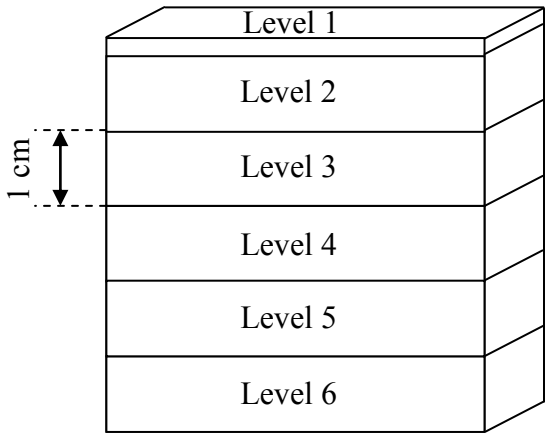

Figure 4-11: Diagram showing sections of medieval Lincoln stone slice taken for XRD analysis.

A small amount of sample was arranged into a thin layer on the sample disk of the sample holder for X-ray analysis. Each sample was analysed as described in section 3.1.2.

XRD (Figure 4-12 showing data for level 1 (all layers exhibited the same spectra)) shows that the only mineral phase present is calcite, gypsum did not form. It must be noted that the detection limit of this technique is 5% of the sample (University of Exeter 2013). This means that other components may be present in the sample but are unable to be detected with this technique due to having a concentration below the detection limit.

Photographs of quarried and medieval stones were taken and can be seen in Figure 4-13. It appears that the decay of the weathered stone is due to natural weathering.

SEM imaging was carried out on samples (Au-Pd coated to minimise charging effects) taken from the surface of the weathered side of the medieval stone and the opposite, unweathered surface. A sample of quarried stone was also imaged for comparison with medieval samples (Figure 4-14). The medieval weathered sample appeared more solid and compacted than the medieval intact unweathered sample. As such capillary rise should be greater in the unweathered medieval sample than the weathered medieval sample.

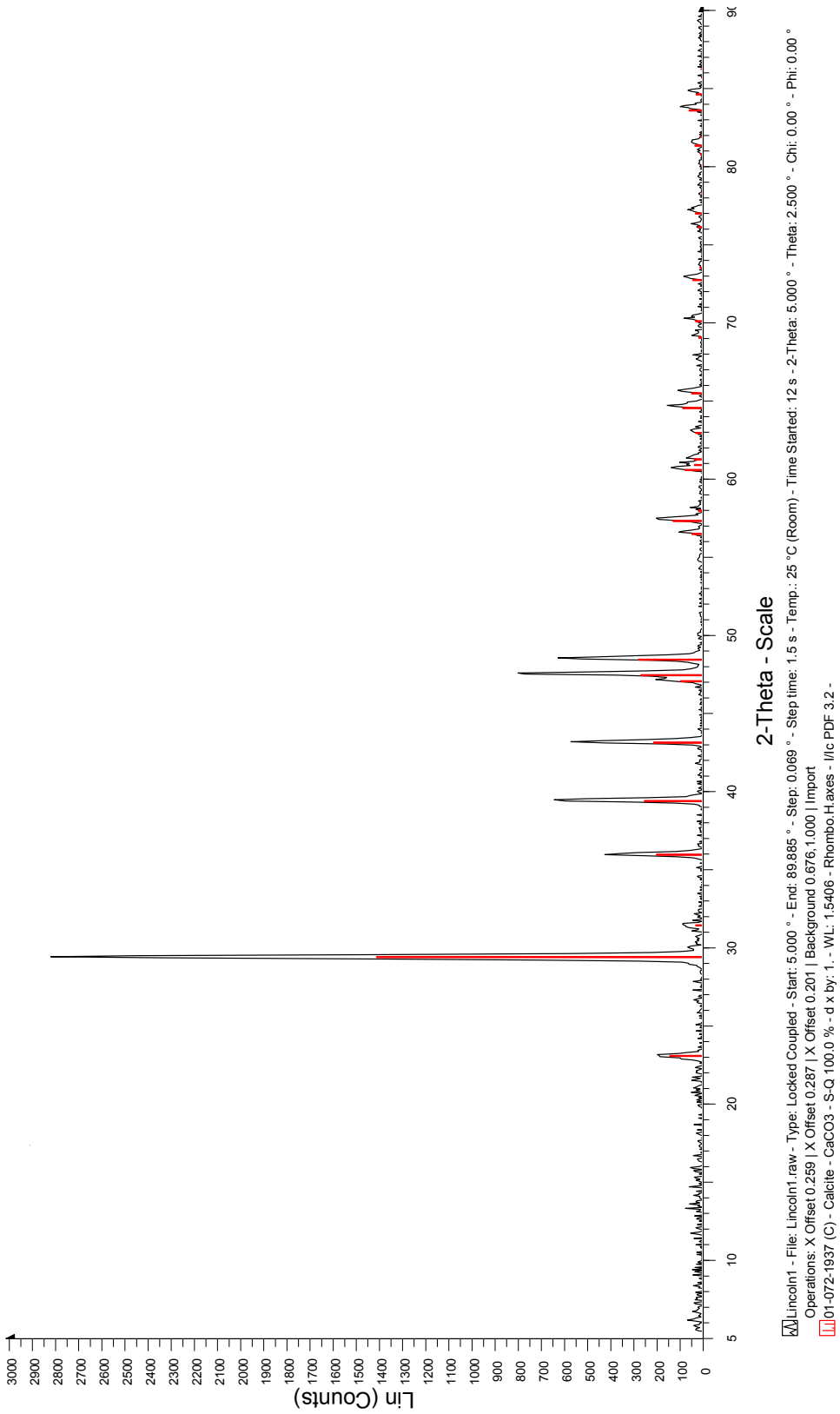

Figure 4-12: XRD spectrum of Medieval Lincoln stone showing only Calcite is present.

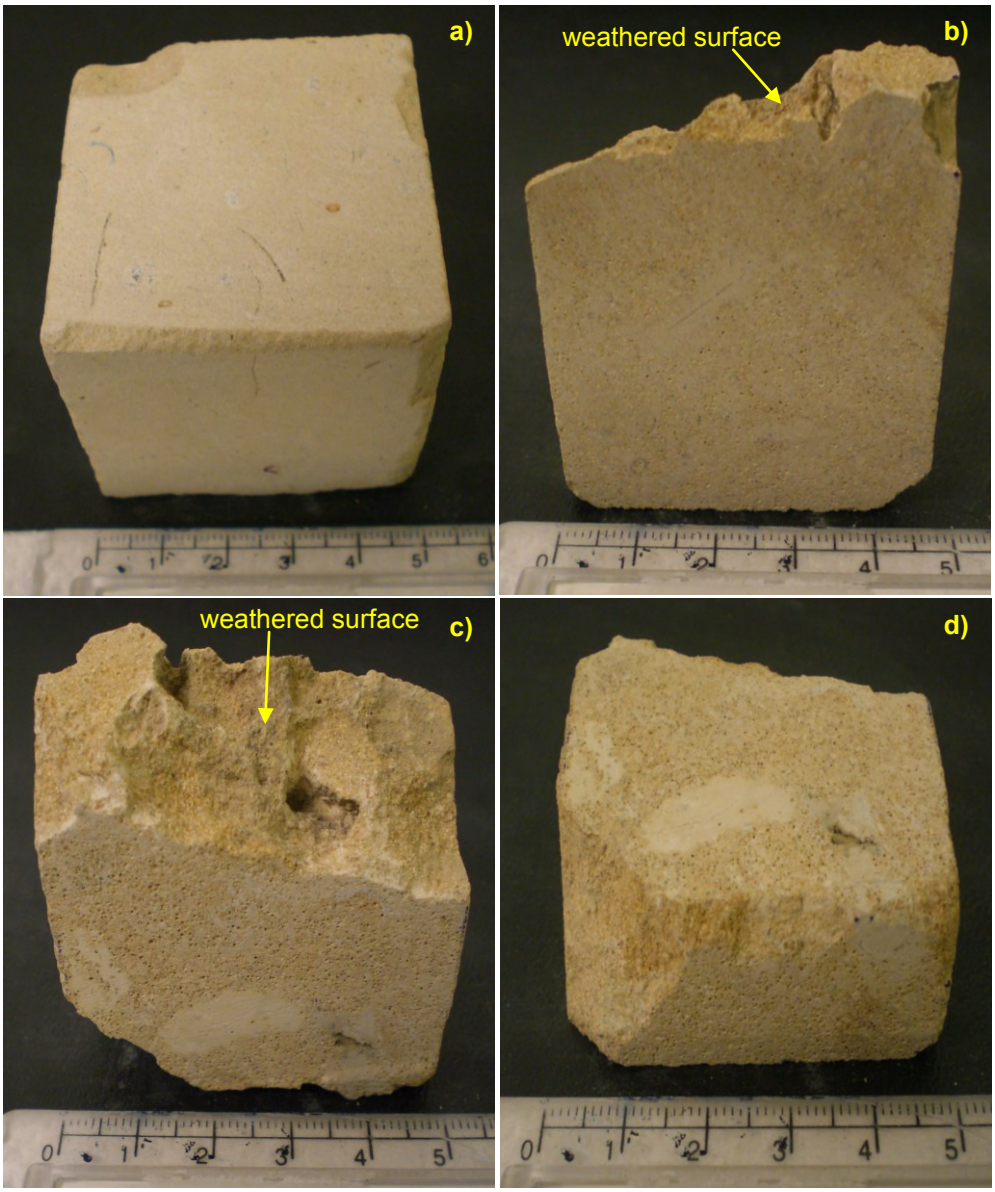

Figure 4-13: Photographs showing a) quarried Lincoln stone, b) the cross section of a medieval Lincoln stone showing the inside of the stone c) the outside of the same medieval Lincoln stone seen in b) here showing the top weathered surface and d) the outside of the same medieval Lincoln stone here showing the unweathered base of the stone (the left corner of the base was taken for SEM). The ruler in all images provides a scale.

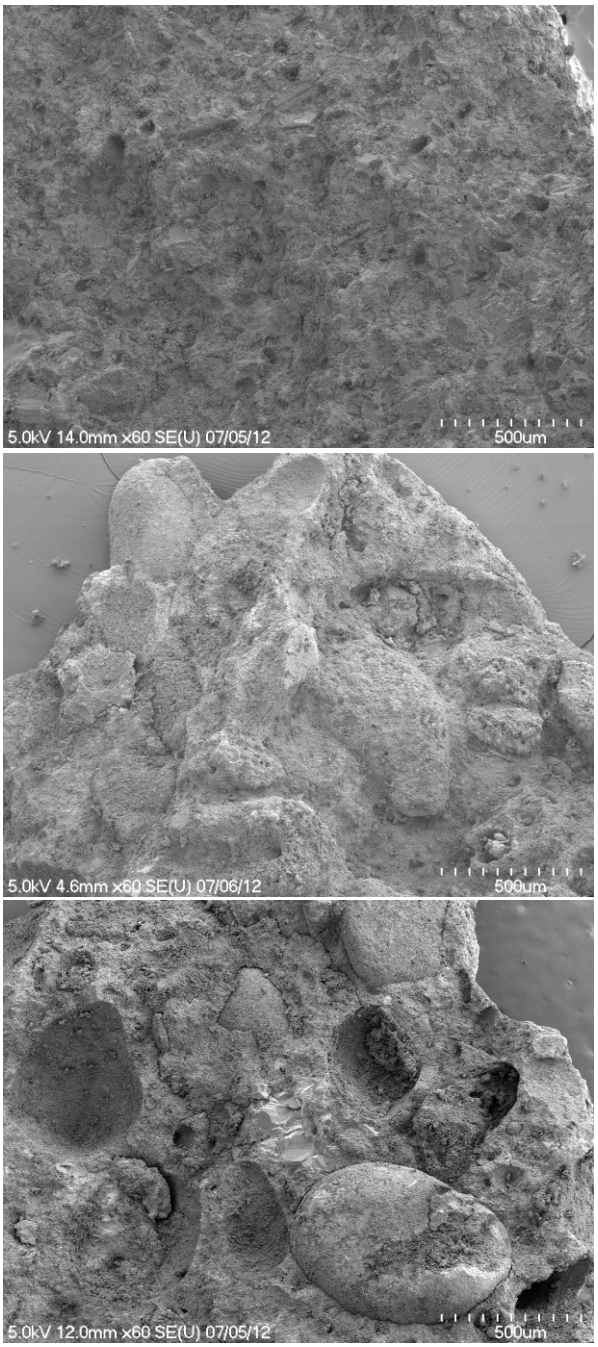

Figure 4-14: SEM images showing untreated a) (top) Quarried Lincoln stone, b) (middle) Weathered Medieval Lincoln stone and c) (bottom) Unweathered Medieval Lincoln stone. For all images the scale bar is 500 μm.

Light microscopy of thin sections of material can be used to gain an understanding of the material's composition and effects of ageing (Adams & Mackenzie 1984; Hughes & Cuthbert 2000). A thin section the length of the medieval stone was taken to determine the nature of the fossil composition of the stone. From imaging a medieval stone thin section using optical microscopy it was determined that Lincoln is a microporous bioclastic oolitic grainstone. The two main forms of calcite present in the stone (Figure 4-15) are microcrystalline calcite, micrite (the fine grained matrix of the stone) and sparite (carbonate cement or re-crystallisation) (Flugel 2004).

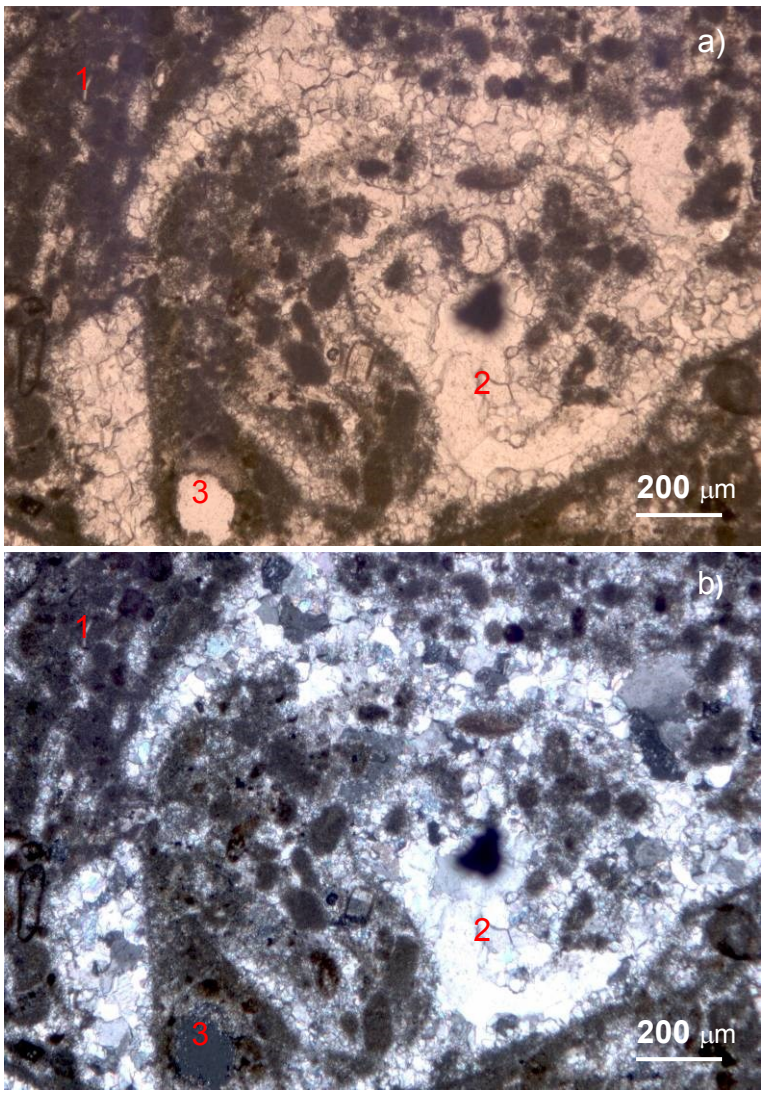

Figure 4-15: Optical microscope images of a medieval Lincoln stone thin section under a) PL and b) XPL showing: 1) micrite, 2) sparite and 3) pore. The scale bar for all images is 200 μm.

The weathered surface of the stone appears to consist primarily of micrite. Some secondary infill appears in the sample where calcite has formed on the inside of a pore. In addition to original pores in the material, pores now exist where compaction damage and general deterioration of fossils has occurred resulting in the creation of a pore within some fossils (Figure 4-17a, mid right edge). Compromise boundaries exist in the stone due to the presence of drusy mosaics, a pore-filling cement mosaic, where calcite crystals have grown in interparticle voids. The stone also contains poorly preserved ooids, shells, peloids and bioclasts, which are skeletal particles. The subtypes of bioclasts present are molluscs, echinoderms and foraminifera in the form of endothyracids, echinoid spines and textularia (Adams & Mackenzie 1984; Karim & Ameen 2011). The thin section was examined under both polarised light (PL) and cross polarised light (XPL). Examples of components present in the stone are shown in Figures 4-16 & 4-17.

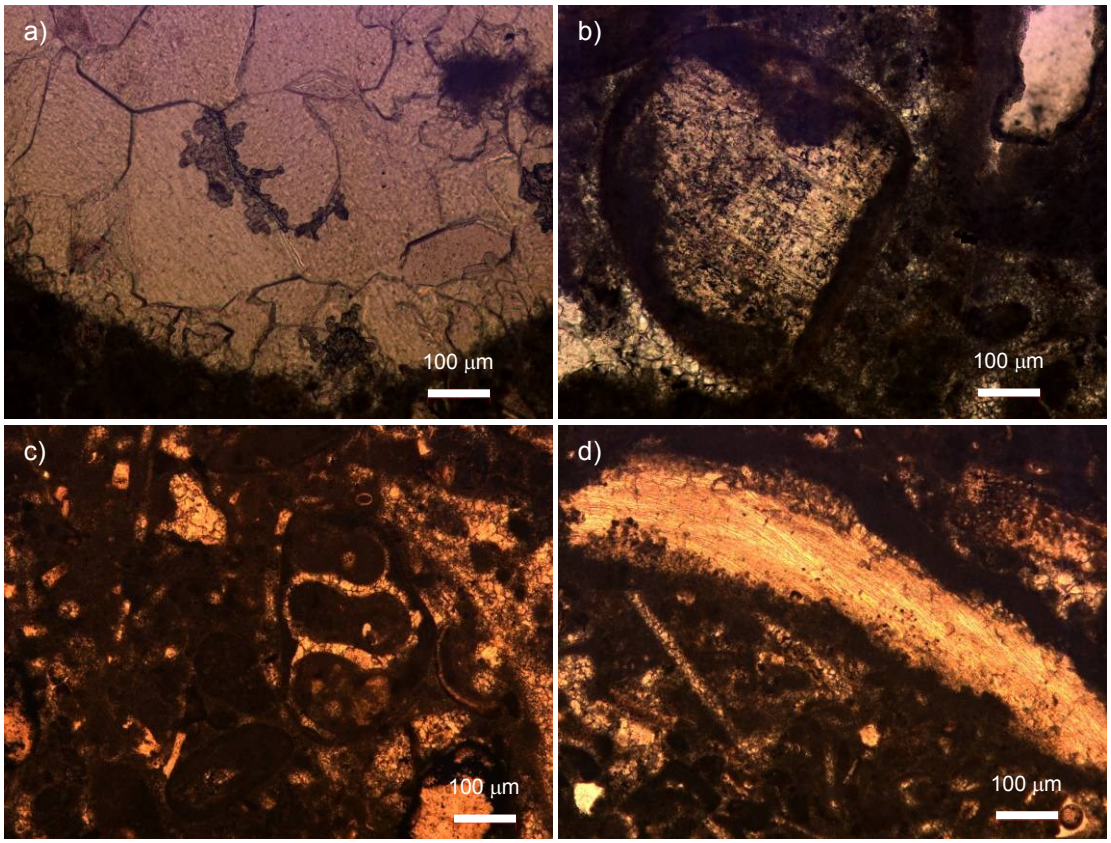

Figure 4-16: PL optical microscope images of a) drusy mosaic, b) echinoderm, c) endothyracid and d) mollusk in Medieval Lincoln stone. The scale bar for all images is 100 μm.

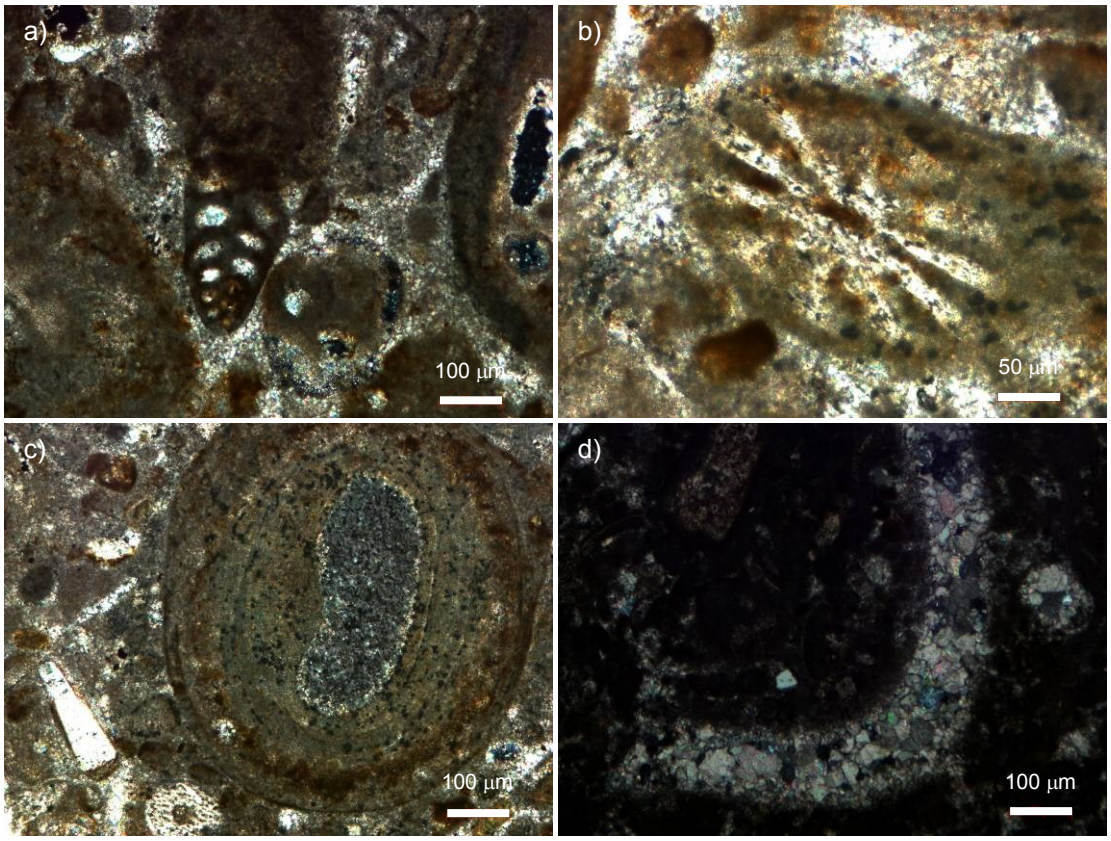

Figure 4-17: XPL optical microscope images of a) bioclast, b) echinoid spine, c) poorly preserved ooid and d) shell in Medieval Lincoln stone. The scale bar for all images is 100 μm.

Overall, the weathered surface shows greater pore blocking, compaction and micrite concentration than the unweathered surface.

Vacuum saturation was used to determine the porosity in both quarried and medieval stone. It was found that quarried and medieval Lincoln have a bulk density of 2283.9 kg/m^3 and 2151.5 kg/m^3 and porosities of 14.36% and 16.15% respectively.

4.2.2 Imbibition

Water capillary absorption rate data was obtained using the standard procedure (Gummerson et al. 1980; Hall & Hoff 2012) as previously described in section 4.1.2 on samples 50 mm × 50 mm × 50 mm (quarried) and 50 mm × 50 mm × 10 mm (medieval) (see Figure 4-18) within an environmental chamber at 25°C. The experiments were conducted for 196 min. It was important that the test was of longer duration than the CaLoSiL treatment so as to allow the wet front to advance significantly into the material beyond the treated layer. Samples were exposed to water imbibitions before treatment, and after each treatment and carbonation then samples were oven dried between tests and treatments. When performing the uptake into the weathered stone care was taken to ensure that only the weathered layer was in contact with the imbibing liquid.

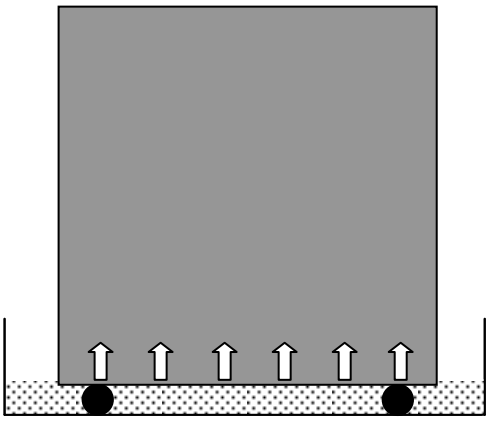

Figure 4-18: Diagram of imbibition experiment showing a sample block (50 mm wide × 50 mm high for all types of Lincoln stone) sitting on supports in a dish containing the imbibition liquid. The arrows show the direction of liquid uptake.

Treatment of quarried and Medieval Lincoln stone blocks with CaLoSiL E25 was undertaken as described in section 4.1.2 in an environmental chamber at 25°C. The weight gain of the sample was measured at whole $t^{1/2}$ values and at the end of the treatment uptake after 64 minutes. Samples were subject to 2 treatment cycles, treated with CaLoSiL then carbonated with DiLoCarb after each treatment, to identify any differences due to number of treatments.

Figure 4-19 shows the experimental water imbibition data (expressed as cumulative absorbed volume/unit inflow area, i vs. time$^{1/2}$). The calculated relevant properties of water uptake and particle absorption are given in Table 4-3.

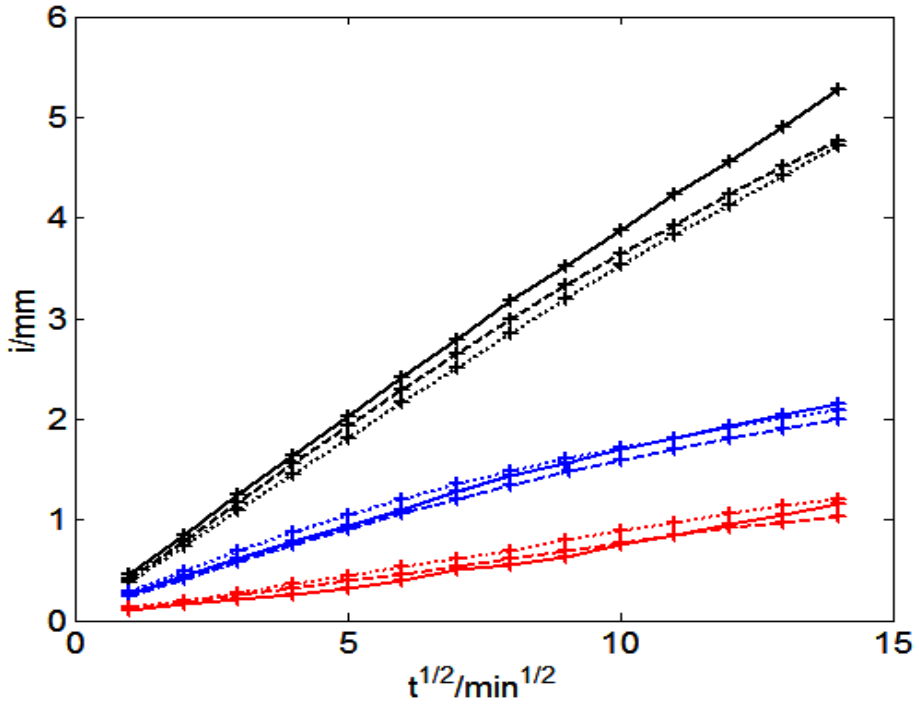

Figure 4-19: Water sorptivity curves for Lincoln stone. Graph shows untreated quarried stone (black line), treated quarried stone (black dashed line), re-treated quarried stone (black dotted line), untreated medieval unweathered stone (blue line), treated medieval unweathered stone (blue dashed line), re-treated medieval unweathered stone (blue dotted line), untreated medieval weathered stone (red line), treated medieval weathered stone (red dashed line) and re-treated medieval weathered stone (red dotted line). i is cumulative absorption in mm.

There is a marked difference in the untreated sorptivity for weathered and unweathered medieval stone. The change in composite sorptivity varied with stone type and number of treatments from 6 – 11% as shown in Table 4-3. From mass measurements before and after treatment (and carbonation) it became clear that fewer particles were entering the stone than expected (see Table 4-3) with roughly 44 – 98% of the overall expected mass of CaLoSiL particles actually remaining in the stone. This suggested two possible models for the distribution of particles within the stone: a thin dense layer or a wide sparse layer.

Property	$Quarried_1$	$Quarried_2$	$Medieval_{w1}$	$Medieval_{w2}$	$Medieval_{u1}$	$Medieval_{u2}$
Sw(u) (mm / $min^{½}$)	0.370	0.370	0.082	0.082	0.146	0.146
Sw(t) (mm / $min^{½}$)	0.338	0.336	0.073	0.085	0.136	0.137
Se(u) (mm / $min^{½}$)	0.220	0.220	0.079	0.079	0.121	0.121
Se(t) (mm / $min^{½}$)	0.199	0.208	0.089	0.098	0.092	0.097
Sn (mm / $min^{½}$)	0.191	0.190	0.058	0.066	0.107	0.122
HORw(u) (mm)	27.76	27.76	6.08	6.08	11.34	11.34
HORw(t) (mm)	25.11	24.81	5.46	6.36	10.50	11.03
HORe(u) (mm)	16.70	16.70	6.22	6.22	9.81	9.81
HORe(t) (mm)	15.01	15.23	6.43	6.94	7.28	7.98
HORn (mm)	8.31	8.29	2.68	3.04	4.92	5.71
vol %	1.1	2.2	1.0	1.9	1.0	1.9
$mass_e$ (g)	0.057	0.115	0.005	0.010	0.009	0.020
$mass_a$ (g)	0.04	0.05	0.03	0.01	<0.01	0.01

Table 4-3: Measured and calculated property values for treated Lincoln stone. $Quarried_1$, $Medieval_{w1}$ and $Medieval_{u1}$ are after first treatment. $Quarried_2$, $Medieval_{w2}$ and $Medieval_{u2}$ are after second treatment. Sw(u) is the water sorptivity of the stone prior to any treatment. Sw(t) is the water sorptivity of the stone after treatment. Se(u) is the ethanol sorptivity of the stone prior to any treatment. Se(t) is the ethanol sorptivity of the stone after treatment. Sn is the CaLoSiL treatment sorptivity. HORw(u), HORw(t) and HORe(u), HORe(t) (height of rise) are how far up the untreated and treated stone the imbibing water and ethanol respectively travels and was calculated from the imbibition test. HORn is how far up the stone the imbibing CaLoSiL nanolime treatment travels and was calculated from the imbibition test. Vol % is the expected volume % of pore space filled. $Mass_e$ is the expected mass of particles entering and was calculated from known mass of nanolime entering the stone with each cycle and the expected volume percent of particles was calculated from the expected mass. $Mass_a$ is the actual mass of particles entering and was measured gravimetrically after oven drying and between treatment cycles.

There is a difference, due to the presence of CaLoSiL particles, in the sorptivity of pure EtOH and the CaLoSiL E25 suspension. It can be said that the presence of particles causes a reduction (average reduction in sorptivity of 17% over all samples) in EtOH sorptivity by making it harder for a material to take in the suspension via capillary suction.

It can be seen that the particles do not cause large reductions in water sorptivity. The two opposite ends of the medieval stone (weathered surface and opposite unweathered surface) vary significantly in their sorptivity values. There is a sorptivity difference between the weathered and unweathered faces of 43.9% (water sorptivity), 34.2% (ethanol sorptivity) and 45.7% (CaLoSiL sorptivity). Capillary uptake is far less effective in the weathered surface than the intact unweathered surface considering HOR. There are visual differences between the weathered and unweathered surfaces of medieval stone which have been discussed earlier. The higher sorptivity of the unweathered surface suggests pore blocking in the weathered surface.

Whilst it is expected that the order of sorptivity, especially water sorptivity, from highest to lowest would be quarried, medieval unweathered intact and medieval weathered stone (which is the order seen from the uptake experiments conducted in this study) it must be noted that no direct comparison between the quarried and medieval stone can reasonably be drawn. This is due to the new stone being quarried from a different location and depth within the quarry from the medieval stone quarried approximately 800 years earlier. Therefore the quarried stone used in this study, whilst being Lincoln stone, is not exactly the same subtype of stone as the medieval stone samples taken from the Cathedral and was not formed in exactly the same conditions. However the results above give an indication of how currently quarried stone can be expected to age.

There is also relevance for the conservation of the Cathedral itself as sections of medieval stone work have and are being removed and replaced by freshly quarried stone. The difference in water transport properties of the quarried and medieval stone mean that these two ages of stone can be expected to behave differently when exposed to rain, with rainwater penetrating to a greater depth in the restored sections

of the building composed of quarried stone than areas of original stonework. As the quarried stone hardens and ages with atmospheric exposure the degree of difference in water transport will decrease.

4.2.3 Penetration Depth

Treatment of the Lincoln stones with CaLoSiL resulted in a lightly visible white mist (particle build-up) on the surface of the stones that had been exposed to the treatment. This build-up was visibly the same as can be seen on Portland stone (Figure 4-4). After treating another quarried and medieval weathered stone and cutting, before carbonation, then treating with phenolphthalein indicator the height of the treatment within the stones could be determined.

After treatment with phenolphthalein indicator it could be seen that the pink colour signifying a positive reaction with the indicator was visible to a height of 0.45 mm and up to 0.56 mm for the quarried and medieval stones respectively (Figure 4-20) under optical microscopy. The quarried stone obtained this penetration depth consistently throughout the sample but the medieval stones only rarely obtained this depth at various points with a depth of 0.2 mm consistently achieved (Figure 4-20). The properties of this CaLoSiL layer were determined by modelling as discussed below. It was seen that the CaLoSiL did not penetrate far into this stone and as such could only be used to treat surface features.

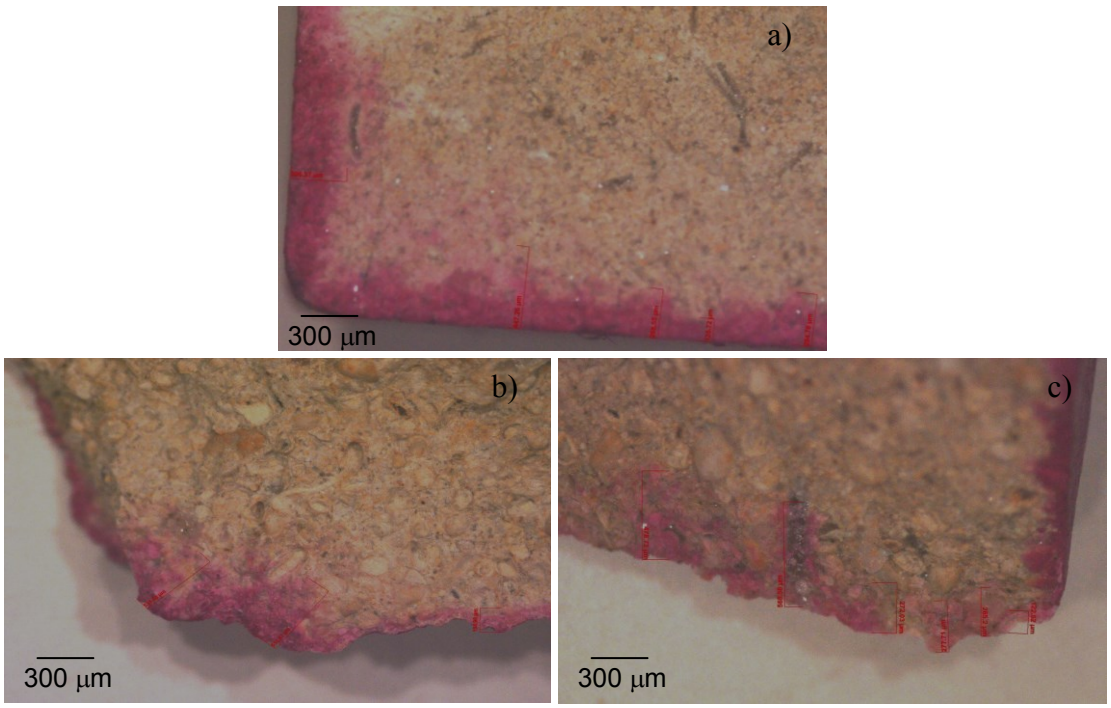

Figure 4-20: Optical microscope images of nanolime treated Lincoln stone tested with phenolphthalein (pink region signifies positive reaction): a) quarried, b) medieval unweathered and c) medieval weathered. The scale bar for all images is 300 μm.

4.2.4 Modelling

Modelling was carried out as described in section 4.1.7 using a two-layer Sharp Front model. The point at which layers A and B intersect is known as the junction, which the water reaches at time t_j. Known variables were the sorptivity of the composite, sorptivity of the untreated stone and the layer thickness as determined by microscopy. Unknowns were the sorptivity, porosity and permeability of the particle layer, which could be estimated from gravimetric data of particle uptake. Water rise into the sample ($i1 + i2$ in mm) is given by Equations 4-1 and 4-2 (in this case time is from zero to tj (t_1) and tj to 196 min (t_2)).

Water transport properties of the CaLoSiL layer and pore filling were investigated using depth information from optical microscopy and by comparing experimental imbibition data (after treatment and carbonation) with predicted imbibition from the sharp front model.

Figure 4-21 shows water uptake in a quarried, a medieval weathered and a medieval unweathered stone treated with CaLoSiL and carbonated with a diethyl carbonate. Fitting the experimental data with the model confirmed that treatment particles existed as a very thin layer which was known to be 0.4 mm thick (from optical microscopy), reducing the porosity from 14% to 11.8% for quarried and from 16% to 15.5% for weathered medieval and unweathered medieval stone based on the known quantity of particles in the stone after treatment (determined gravimetrically). The corresponding estimated permeability reduction was around 40%, <1% and <1% respectively for quarried, weathered medieval and unweathered medieval stones based on the relationship between permeability and porosity. This is understandable due to the nature of the medieval samples compared to the quarried sample and the relationship between permeability and porosity. Sorptivity of the layer was difficult to determine experimentally as the layer was very thin but it was also estimated from the porosity reduction.

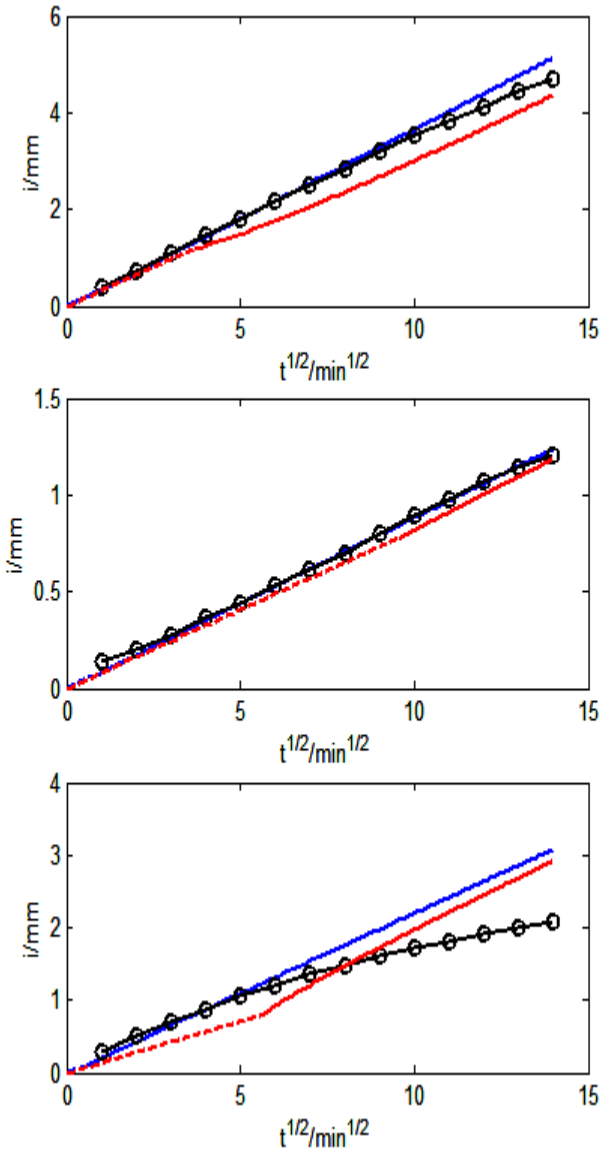

Figure 4-21: a (top), b (middle) and c (bottom). Model (blue and red) versus experimental (black) water uptake data for Lincoln stone after treatments with nanolime and carbonated. a) Quarried: blue dashed curve (*s* = 0.32, *K* = 0.0003, f = 0.12, L = 0.4 mm) is uptake through A, blue solid curve (*s* = 0.37, *K* = 0.0005, f = 0.14) is uptake through B. Red dashed curve (*s* = 0.32, *K* = 0.0003, f = 0.12, L = 10 mm) is uptake through A, red solid curve (*s* = 0.37, *K* = 0.0005, f = 0.14) is uptake through B. b) Weathered Medieval: blue dashed curve (*s* = 0.08, *K* = 0.0005, f = 0.155, L = 0.4 mm) is uptake through A, blue solid curve (*s* = 0.09, *K* = 0.0005, f = 0.16) is uptake through B. Red dashed curve (*s* = 0.08, *K* = 0.0005, f = 0.155, L = 5 mm) is uptake through A, red solid curve (*s* = 0.09, *K* = 0.0005, f = 0.16) is uptake through B. c) Unweathered Medieval: blue dashed curve (*s* = 0.14, *K* = 0.0005, f = 0.155, L = 0.4 mm) is uptake through A, blue solid curve (*s* = 0.22, *K* = 0.0005, f = 0.16) is uptake through B. Red dashed curve (*s* = 0.14, *K* = 0.0005, f = 0.155, L = 5 mm) is uptake through A, red solid curve (*s* = 0.22, *K* = 0.0005, f = 0.16) is uptake through B.

As shown in Figure 4-21, the upwards curve modelled at early time (blue line) before one minute corresponds to water flow through the thin CaLoSiL layer. The downwards curve in the experimental data (black circles) at later time probably resulted from a band of stone with lower sorptivity. If the particle layer was thicker than say 5 mm, there would be an upwards curve in the sorptivity plot as shown by the red line which was not observed. This confirmed that the particle layer was thin and remained permeable.

4.2.5 SEM Imaging

Stone chips were removed from both the weathered surface and the opposite inside unweathered face of the medieval stone slice used for imbibition experiments in addition to an untreated stone slice that neighboured the slice taken for MIP analysis. Stone chips were also removed from a quarried stone. All fragments were coated with a thin Au-Pd layer and imaged by SEM as described in section 3.1.8.

SEM imaging showed differences in the quarried and medieval stones before and after treatment and particle carbonation (Figure 4-22). The presence of particles can be seen and are of anhedral form upon completion of carbonation.

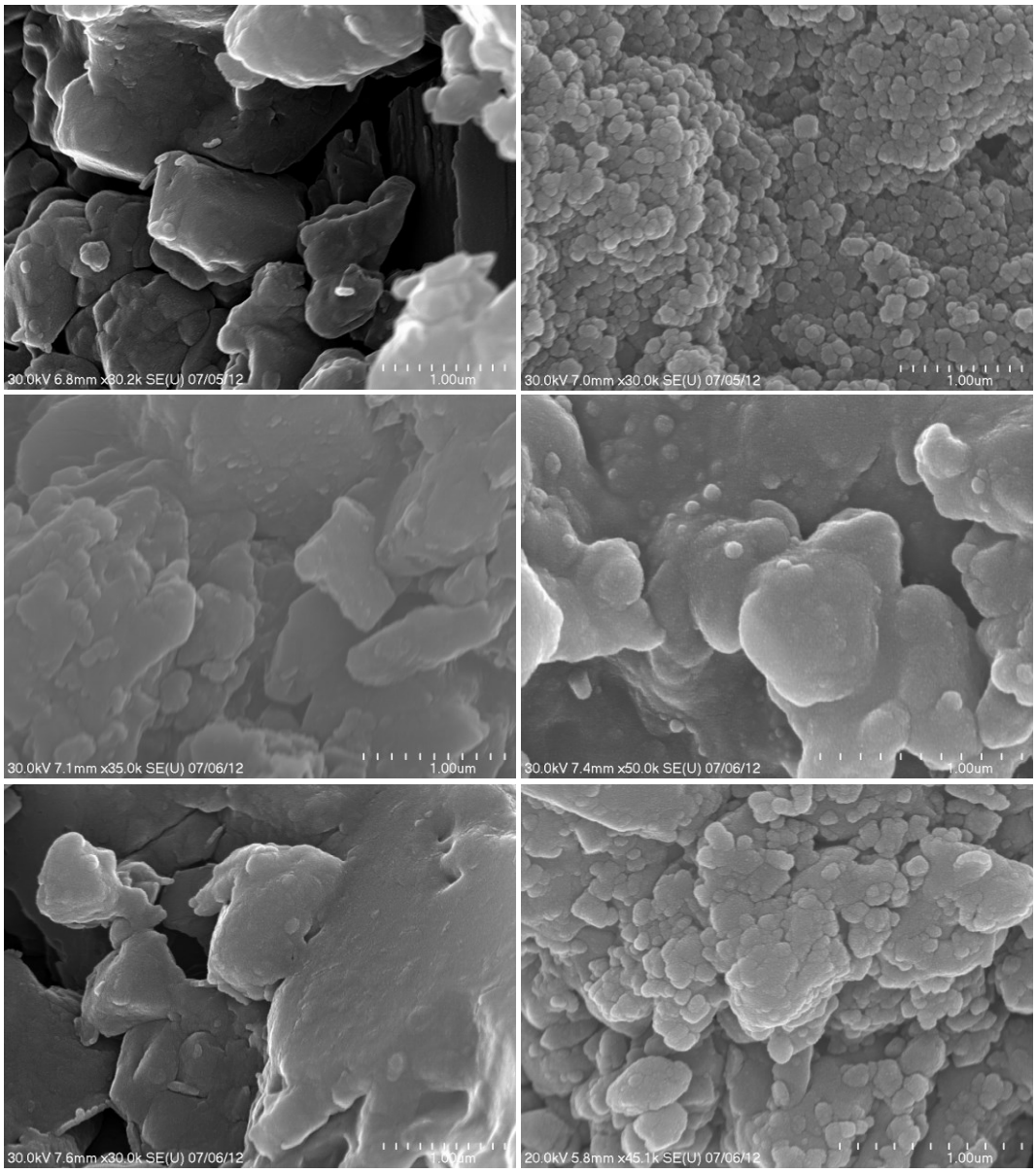

Figure 4-22: SEM images showing untreated (left) and treated (right) a) (top) Quarried Lincoln stone, b) (middle) Weathered Medieval Lincoln stone and c) (bottom) Unweathered Medieval Lincoln stone. The untreated images show the plain stone and the treated images show the stone covered by particles. The scale bar for all images is 1 μm.

4.2.6 Discussion

Lincoln is a highly microporous bioclastic oolitic grainstone with a unimodal pore size distribution with a pore throat size range of 0.01 – 10 μm observed from MIP data. The stone contains drusy mosaics, poorly preserved ooids, shells, peloids and bioclasts. There are several subtypes of bioclasts present in the stone; molluscs, echinoderms and foraminifera in the form of endothyracids, echinoid spines and textularia. Calcite is present in the forms of sparite and micrite. Calcite movement has occurred within the medieval stone with calcite moving towards both weathered and unweathered surfaces.

Treatment of Lincoln Stone with CaLoSiL resulted in a sorptivity reduction of between 6 – 11% varying with number of treatments and stone type. Particles were found to exist as a very thin permeable layer (approximately 0.4 mm thickness) and resulted in a porosity reduction of 2.2 % (quarried) and 0.5 % (weathered and unweathered medieval). The permeability reduction in the treated layer was estimated to be 40% (quarried) and <1% (weathered and unweathered medieval). Imbibition with CaLoSiL resulted in a very thin layer which did not significantly block pores. Despite the small CaLoSiL particle size, it did not travel far into the pore network in this case under these treatment parameters.

MIP suggests that weathered medieval stone has the smallest degree of porosity most likely from pore blocking, whilst the unweathered medieval stone has by comparison a higher degree of porosity. This suggests that the pore size distribution may be altered by weathering. It may be possible that case hardening has occurred as about 1 cm below the surface there was a noticeable increase in porosity visible in the thin section. Despite this both weathered and unweathered medieval stone absorb only a very small mass of particles (quarried stone absorbs five times more particles, although this is still a small amount in comparison with the expected mass of particles absorbed).

The water repellency index (R) (Appendix C) is proportional to the reduction in water sorptivity caused by the material repelling water. Although the main application of this is to soils, it could provide an indication here of how the sorptivity exhibited by the various types of Lincoln stone is below what would be expected. As

shown in Table 4-4 the pattern exhibited by the Sw (Table 4-3) follows the pattern of R except for cases where the Se is increased.

The contact angle of water with the stone has an effect on the capillary uptake of the liquid (Appendix C). As can be seen in Table 4-4 quarried stone has the lowest theoretical contact angle, based on the equation in Appendix C, suggesting that this stone should exhibit the highest water sorptivity of the three Lincoln stone types, which is observed experimentally (Table 4-3). Medieval unweathered stone has a theoretical contact angle higher than that of quarried stone and just within the range for the stone to be hydrophilic, suggesting that the sorptivity for this stone should be lower than that of quarried stone as is seen. The theoretical contact angle for weathered medieval stone is within the intermediate range suggesting that whilst the stone is not completely hydrophilic it is not completely hydrophobic either. It can be seen that treatment with nanolime increases the theoretical contact angle for the weathered medieval stone which decreases the water sorptivity whilst increasing the ethanol sorptivity. For quarried and unweathered medieval stones the theoretical contact angle and sorptivities experience a decrease after one treatment and then increase slightly after the second treatment.

Property	Quarried	$Medieval_w$	$Medieval_u$
R(u)	1.16	1.88	1.62
R(1t)	1.15	2.38	1.32
R(2t)	1.21	2.25	1.38
θ_w(u)	45	74	69
θ_w(1t)	44	80	57
θ_w(2t)	49	79	60

Table 4-4: Calculated water repellency index (R) and water contact angle (θ) for Lincoln stone ($Medieval_w$ = weathered medieval, $Medieval_u$ = unweathered medieval). u is untreated, 1t is after one treatment and 2t is after second treatment.

In the absence of incomplete wetting, the sorptivity of a material measured with a series of liquids should vary as (σ/η) where σ is the surface tension and η is the viscosity (Taylor et al. 2000; Hall & Hoff 2012). Figure 4-23 shows this comparison for Lincoln stone. It can be seen that all types of Lincoln stone exhibit a degree of water repellencey with that of the weathered medieval stone being the most marked. This therefore confirms the findings of the calculated R and θ_w values. As has been previously reported, some limestones do show quite a high degree of water repellency (Taylor et al. 2000; Ioannou et a. 2004). The results here on Lincoln stone confirm another limestone as being known to exhibit this phenomenon.

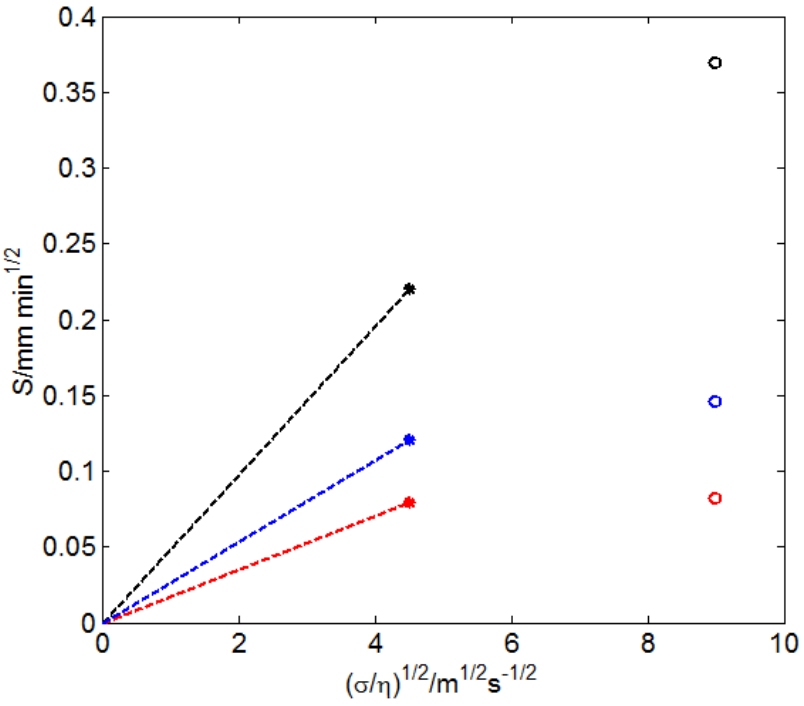

Figure 4-23: Sorptivity (S) versus $(\sigma/\eta)^{1/2}$ graphs for water (o) and ethanol (*) absorption into quarried (black), unweathered medieval (blue) and weathered medieval (red) Lincoln stones.

The results give an indication of how currently quarried stone can be expected to age and the extent of differences between sections of replaced and original stonework comprising Lincoln Cathedral.

4.3 Calcium Hydroxide Nanoparticles as an Adhesive

In this section the efficacy of a CaLoSiL-based Repair Mortar (a product of IBZ-Salzchemie Gmbh & Co.KG marketed under the name Repair Mortar) as an adhesive for repairing detached surface features was assessed through lap shear strength of repaired stone.

4.3.1 Shear Test Experimental Procedure

Repair Mortar was used to join two cut Portland stone blocks, each 800 cm^3 (10 cm × 10 cm × 8 cm). The blocks were painted with a high-contrast speckle pattern to allow the slip displacement across the joint to be assessed using digital image correlation (DIC) (Bisby & Take 2009). The samples were shear tested using an Instron 4505 universal test machine. A gradual force was applied to the dividing plane to generate 0.15 mm per minute crosshead speed whilst the load and crosshead displacement were recorded. The Instron instrument was operated by Dr Tim Stratford whilst in my presence. A novel sample mounting method excluding the use of metal plates and clamps (Figure 4-24) was employed due to the ease with which the joint failed when mounting in the traditional way was attempted. The samples were mounted on two metal rods with a cardboard plate positioned on top of the joint (Figure 4-24). The crosshead was lowered so that it contacted the cardboard plate and distributed the force evenly across the joint. Force was applied to the joint until failure occurred.

Images of the samples under load were taken every two seconds then DIC was performed using GeoPIV software to identify the displacement corresponding to the maximum load at which failure occurred. The crosshead displacement for this test was equal to the movement of the top of the specimen relative to the bottom of the specimen.

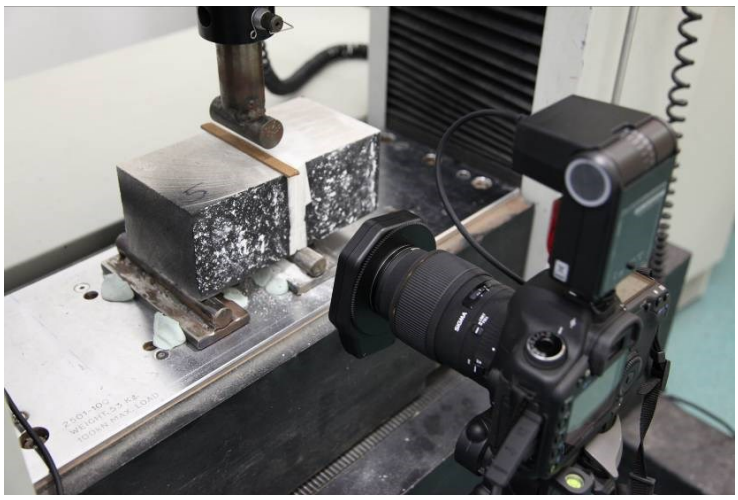

Figure 4-24: Photograph showing a sample mounted in the Instron prior to slip testing. The camera positioned in front of the sample was fitted with a macro lens and was used to take images of the speckle pattern visible on the sample for DIC analysis.

4.3.2 Shear Test Results

The mortar shear strength increased over time (Figure 4-25). The mortar was five times as strong after 25 hours as it was after 15 minutes. The rate of strength increase was found to reduce over time. The average adhesive strength from a series of measurements was 0.020 N/mm^2, 0.034 N/mm^2 and 0.099 N/mm^2 when tested 15 minutes, 25 minutes and 25 hours respectively after attachment with repair mortar.

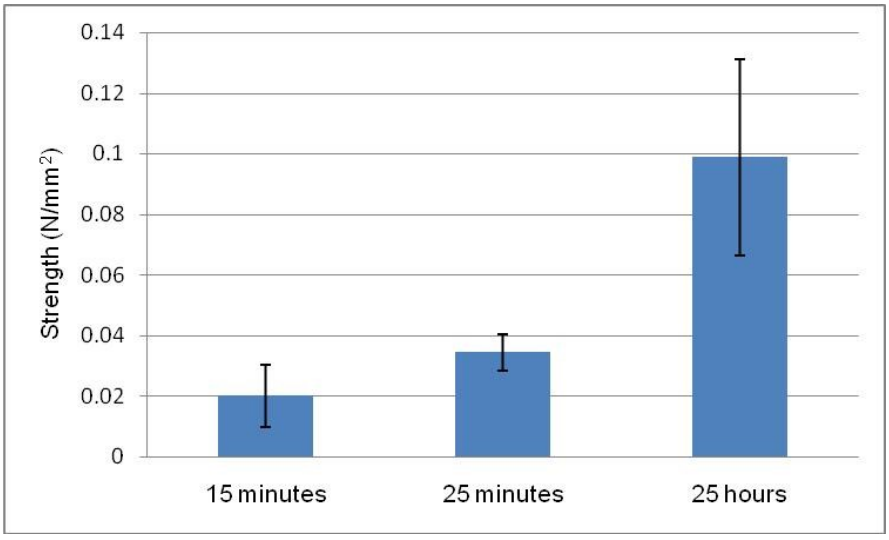

Figure 4-25: Comparison of adhesive strength with time.

Figure 4-26 gives an indication of the local joint behaviour under load for samples tested at 25 minutes and 25 hours after forming the adhesive joint. The figure shows the crosshead displacement of the machine (which was the combination of shear displacement across the adhesive joint and "bedding in" of the loading supports into the masonry blocks); however, the difference in stiffness in the two groups of specimens was clear and indicated by the dashed lines on the plot. It was noted that the samples tested after 25 hours required a larger force to cause adhesive failure than for those tested after 25 minutes, thus the adhesive bond was stronger with time. The slip displacement was the distance one of the blocks comprising the sample was able to move before the adhesive bond failed and starts from zero on the x-axis. Negative x-axis values represent sample and loading support "bedding in". It was observed that the displacement allowed before failure was very small for both sets of samples and reduced with time, therefore reducing the likelihood of being able to reposition stuck items.

It was hoped that DIC could be used to measure the local displacement behaviour across the dividing plane, but this method was not reliable due to the very small displacements involved (as can be seen from the x-axis values in Figure 4-26).

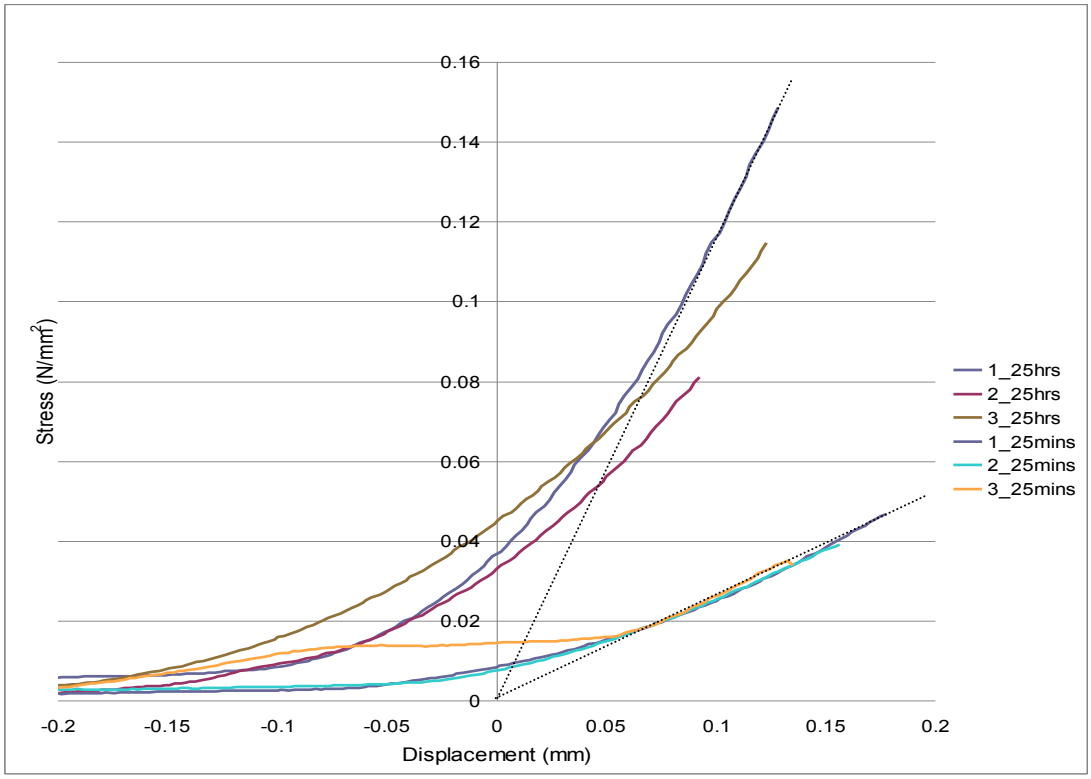

Figure 4-26: Stress versus crosshead displacement at different times.

It can be seen that post-failure the mortar was powdery and that the surface of the mortared face differed also with time, appearing less friable after 25 hours compared with the surface after 25 minutes (Figure 4-27). This suggested natural carbonation was responsible for the strength increase (DiLoCarb-E was not used with repair mortar). Failed samples were tested with phenolphthalein causing uncarbonated material to become pink (Figure 4-28). It was found that after 25 hours the mortar near the edges of the sample had carbonated whereas after 25 minutes no carbonation had occurred.

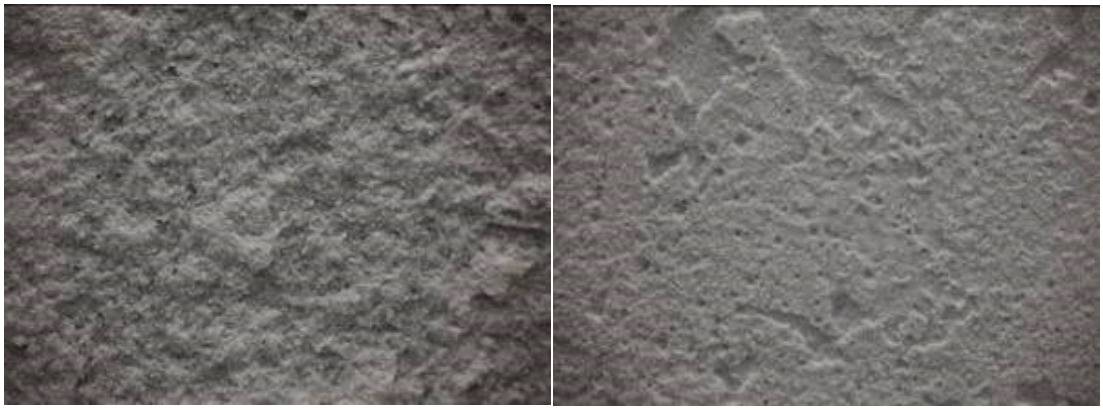

Figure 4-27: Failed surface at 25 minutes (left) and 25 hours (right).

Figure 4-28: Phenolphthalein treated failure surfaces exposed by strength testing 25 minutes (left) and 25 hours (right) after adhesion. Pink areas, with higher pH, are uncarbonated.

4.3.3 Discussion

For Repair Mortar it was found that a displacement shift of < 0.2 mm was sufficient to give adhesive failure. This signified approximately by how much an object stuck with Repair Mortar could be repositioned. Shear strength of the repair mortar was found to increase with time, probably due to carbonation with maximum strength during the time period studied obtained after 25 hours which probably resulted from carbonation as the tests using phenolphthalein indicator suggested. During the time periods explored the adhesive bond strength was notably less than the tensile strength of the stone itself. While the force per unit area generated by the weight of the re-attached fragment is less than the initial strength of the mortar-stone adhesive bond, the use of this adhesive is favourable.

4.4 Conclusions

Treatment of monomodal and bimodal microporous limestone with CaLoSiL results in a small reduction in stone sorptivity. The CaLoSiL particles exist and occupy a thin layer (approximately 0.4 mm) at and just below the surface of the stone. This thin layer is permeable and results in only a small reduction in stone porosity in this region with a corresponding reduction in permeability within the layer of up to approximately 60%. CaLoSiL particles do not appear to significantly block the stone pores.

Due to the above, damage that comes from strong inhibition of water movement within stone should not be a consequence of this treatment. Whilst CaLoSiL may consolidate surfaces to reduce friability, as suggested by the STONECORE Project, the compressive strength of the stone under study here was unaffected.

Comparable results are obtained on both Portland (bimodal) and Lincoln (unimodal) quarried stone suggesting that, at least for highly microporous stone, modality does not noticeably affect the behavior and effect of CaLoSiL treatment.

For a Portland stone, with water and ethanol sorptivities of 0.47 mm $min^{-1/2}$ and 0.32 mm $min^{-1/2}$ respectively, there is an R value of 1.33 and a contact angle of 57.25^{o}. After one treatment on this stone the R value increased to 1.45 coinciding with a contact angle increase to 63.08^{o} meaning that the degree of hydrophilicity in the stone is marginally decreased in accordance with a lower water sorptivity. It has been found that all the Lincoln limestones show a degree of water repellency.

It was determined that Lincoln is a highly microporous bioclastic oolitic grainstone with a unimodal pore size distribution with a pore throat size range of 0.01 – 10 μm. Weathered medieval Lincoln stone gained 97.9% of the expected mass of particles absorbed over the entire treatment course, whilst unweathered medieval and quarried Lincoln stone gained only 51.2 and 47.4% respectively. This shows that weathered stone will absorb a mass of particles nearly equal to the calculated expected absorbed mass whereas unweathered aged stone and quarried stone will absorb approximately half of the mass expected. Such information could be useful to conservators if they want to obtain a specific mass gain of particles within a material.

A displacement shift of < 0.2 mm was sufficient to give adhesive failure for Repair Mortar. A gradual increase in shear strength was most likely due to carbonation. While the force per unit area generated by the weight of the re-attached fragment is less than the initial strength of the mortar-stone adhesive bond, the use of this adhesive is favourable.

CaLoSiL can be used to consolidate friable stone surfaces by particle uptake. It could be seen from comparing the internal height (depth) of treatment (from cut stones after treatment) and the surface treatment height (height of white mist on the surface) that the internal height of treatment is less than that on the surface. This suggests that the movement of particles is slowed within the pore structure compared to along the edge of the pore structure (surface of the material). It is possible that alternative methods of application (drip feed, injection, etc.) could produce greater penetration depths within the material by the application of a force to drive the particles further into the pore structure. CaLoSiL suspensions of isopropanol, a longer chained alcohol, are currently being recommended by the manufacturer for deeper penetration away from the surface (IBZ-Salzchemie Gmbh & Co.KG 2013). A nanoparticle based Repair Mortar can be used re-attach light fragments. If a more substantial repair is required then more traditional mortars may perform better.

Chapter 5:
Calcium Hydroxide Nanoparticle Effects on AAC

Autoclaved aerated concrete (AAC) is mainly tobermorite and exists in a combined micro/macro structure of thin tobermorite 11 Å platelets packing in a matrix arrangement yielding a micro structure which houses coarse aeration pores (Narayanan & Ramamurthy 2000). These circular aeration pores are spherical cavities formed as calcium hydroxide, aluminium powder and water react forming hydrogen gas which foams creating gas bubbles within the mixture before being replaced by air (Narayanan & Ramamurthy 2000). The aeration pores are connected via the microstructure of the matrix which possesses a high suction capability due to the thin tobermorite platelets.

Due to the wide use of AAC as a building material it has been subject to several investigations particularly as part of the European Commission funded Heat, Air and Moisture Standards Development [HAMSTAD] Project (Roels et al. 2002; Roels et al. 2003; Adan et al. 2004; Roels et al. 2004; Ioannou et al. 2008). The well defined pore structure of AAC, with aeration pores and connected microscale porosity, provides a model material with which to determine the transport path and final destination of nanoparticles. AAC is a model material here as, due to the combination of large and micro pores, it allows the interaction of particles with dramatically different pore sizes to be seen.

Particle movement through porous materials is an area of study relevant to a wide range of environmental science applications including nuclear waste disposal and water filtration (McDowell-Boyer et al. 1986; Baek & Pitt Jr. 1996; Waite et al. 1998; Lavoie et al. 2011). Whilst it is known that particle size (Cumbie & McKay 1999; Santos & Bedrikovetsky 2004) particularly in relation to pore diameter of the material, is of great importance regarding the transport abilities of a particle within a porous material, it is unclear the effect gravity will have on nanoparticle transport within a multi-modal pore network. Whilst the transport of nanoparticles is of great interest, the interaction of the nanoparticles with the pore wall of the material has an impact on whether particles adhere or are moved further along the pore network.

5.1 Treatment Effects on AAC

Autoclaved aerated concrete (Figure 5-1) of density 450 kg m^{-3} and porosity 0.82 features a thin microstructured matrix of tobermorite 11 Å platelets in conjunction with macro porosity due to aeration pores. Reported here are the results of water uptake tests on untreated samples and samples exposed to a colloidal nanolime treatment to investigate the effect of the particles on imbibition behaviour. The water transport properties are modelled using Sharp Front analysis and compared to the experimental data. The transport of the particles within the material and the effect on open pore space is also looked at.

Figure 5-1: Photograph of an AAC sample prior to treatment. The macro pores of the material can be clearly seen. The ruler provides the scale.

The $Ca(OH)_2$ nanoparticles used in this study form a current commercial calcareous stone conservation treatment known as CaLoSiL, for which the effect of a very thin layer on water transport within a highly microporous material has been previously identified (Campbell et al. 2011). The resulting behavior due to a variety of layer thicknesses and the determination of associated particle movement is of

great interest, particularly within materials of both coarse and fine porosity, especially in the environmental field including water purification and nuclear waste storage.

CaLoSiL E25 was used here. These particles have a diameter range of 0.05 – 0.25 μm (Ziegenbalg 2008) which is in the same range as that of the AAC micropores (Roels et al. 2002; Roels et al. 2003; Ioannou et al. 2008), the matrix porosity which accounts for a volume fraction porosity of 0.275±0.013 sd. The AAC used here was supplied for the HAMSTAD project by Ytong, Denmark. It is known (Roels et al. 2003; Ioannou et al. 2008) that this material has a volume fraction porosity of 0.822±0.007 s.d., a bulk density of 449.5±14.9 s.d. kg m^{-3} and a matrix sorptivity of 0.23±0.03 s.d. mm $min^{-1/2}$.

5.1.1 Imbibition

Water capillary absorption rate data was obtained using the standard procedure (Gummerson et al. 1980; Hall & Hoff 2012), as described in section 4.1.2, although here four AAC squares of 125 cm^3 (5 cm × 5 cm × 5 cm) were tested (Figure 5-2) over an extended period of time to a final time of ~60 h when the entire block was completely saturated. It was important that the test was of long duration so as to allow the wet front to advance significantly into the material.

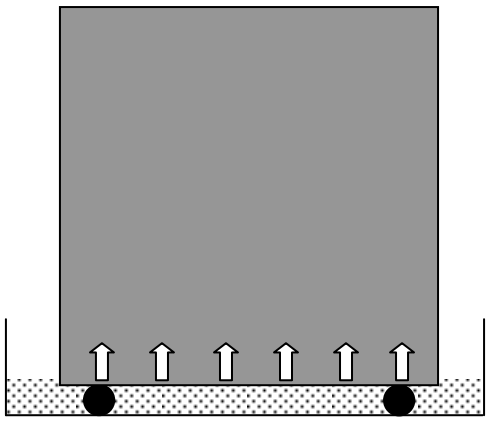

Figure 5-2: Diagram of imbibition of liquids into AAC. Arrows show direction of liquid uptake.

Each AAC block was successively exposed to three different treatment levels where particles were allowed to penetrate to heights of 1 cm (30 minutes), 2.5 cm (7 days) and 5 cm (21 days) (the top of the AAC block). These three successive treatments are called “thin”, “medium” and “thick”.

All blocks were carbonated after each treatment with DiLoCarb using a solution of a 1:1 ratio of DiLoCarb-E to water. The blocks were soaked in this solution for 15 minutes to ensure full surface exposure to the solution and left in foil overnight. They were then oven dried and cooled after each carbonation then subjected to water uptake as previously described. This enabled the water sorptivities of each block to be obtained in the untreated, thin layer, medium layer and thick layer treatment states.

From Ioannou et al. (2008) it is known that capillary absorption is primarily due to the matrix porosity of the material because of the low capillary suction present in aeration pores and gravitational effects. It is also known (Ioannou et al. 2008) that there are four numerically identifiable stages defined within an AAC sorptivity curve: early time sorptivity showing edge effects (1); a transitional stage (2); capillary rise into the matrix pores (3) and a terminal stage where absorption is much slower as the wet front reaches the top of the block (4).

Figure 5-3 shows the experimental water imbibition data for one block which is representative of all four samples (expressed as cumulative absorbed volume/unit inflow area, i vs. the root time, $t^{1/2}$). Here it can be seen how the four stages of water absorption within an AAC material are affected by a nanoparticle treatment of varying layer thickness. It is seen that the sorptivity values for the medium and thick layers of the same block lie significantly below that of its blank value whilst the value for the thin layer is higher (Table 5-1). In calculating the expected volume percent of pores filled, an estimate was made of the amount of trapped air in the pores by comparing the capillary moisture content (obtained by imbibition) and total moisture content (obtained by vacuum saturation). Air trapping in AAC was 25% of the total pore space. It should also be noted that the calculated HOR is greater than the height of the block because water is still moving through the system, by evaporative transport, after water has reached the top of the block.

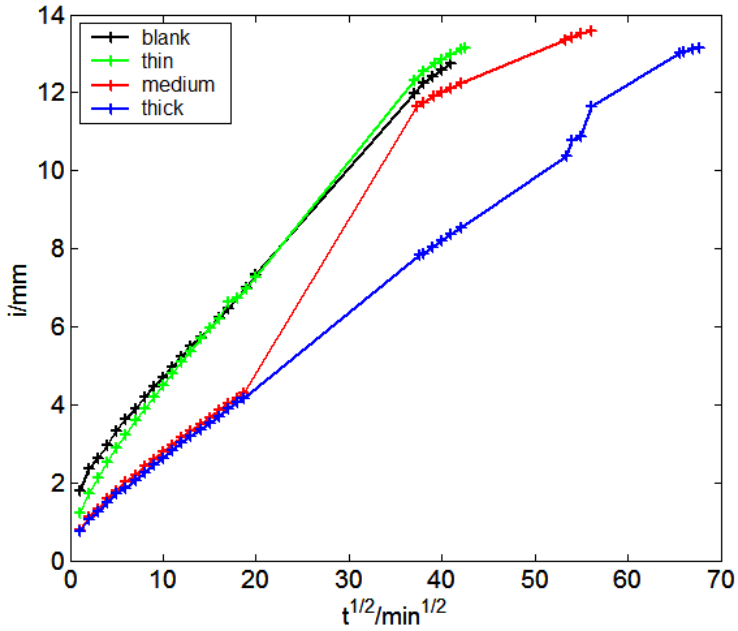

Figure 5-3: Water sorptivity curves for a typical AAC sample. Graph shows untreated blank, thin layer, medium layer and thick layer water uptake data.

Figure 5-4 shows successive nanoparticle imbibition data for the same AAC block. The absorption of the nanoparticle treatment within the block decreases with increasing duration and height of treatment (Table 5-1). It can be seen (Figure 5-4) that there is little difference between the initial sorptivity graph of the medium treatment and the entire thin layer treatment sorptivity graph. This is due to the thin layer treatment having deposited a comparatively small mass of particles in the material prior to retreatment to achieve the medium level. Therefore, the addition of the medium layer treatment to the material is relatively unhindered by particles deposited previously. The marked difference between the thin/medium curves and the thick layer treatment curve suggests the second (medium) treatment deposits significantly more particles than the first. After the initial wetting stage of the sorptivity curve the decrease in slope (Sn) is due to the incoming particles being hindered by the existing particles within the material, particularly within the first 1 cm of HOR where the distribution of particles is most concentrated, as is clear from SEM images.

Property	Untreated	Thin	Medium	Thick
Sw_m (mm / min^{½})	0.269	0.290	0.239	0.186
Sw_c (mm / min^{½})	0.269	0.299	0.193	0.187
Sn (mm / min^{½})	NA	0.467	0.112	0.065
HORw (mm)	52.5	62.7	59.3	59.4
HORn (mm)	NA	12.3	35.9	53.7
vol %	NA	20.4	20.4	20.4
$mass_e$ (g)	NA	8.76	25.58	38.22
$mass_a$ (g)	NA	0.01	1.03	2.04

Table 5-1: Measured and calculated property values for CaLoSiL and DiLoCarb-E treated AAC. Sw_m, Sw_c and Sn are the matrix water sorptivity, composite water sorptivity and nanolime sorptivity of the block respectively. HOR (height of rise) is how far up the block the imbibing liquid (w = water, n = nanolime) travels and was calculated from the imbibition test/treatment with the liquid (for water on treated block the block was carbonated). Actual mass, $mass_a$, of particles in the block was measured gravimetrically after oven drying and between CaLoSiL treatment cycles. The $mass_e$, expected mass, was calculated from known mass of CaLoSiL solution entering the AAC with each cycle. vol %, expected volume percent, of pore space filled was calculated from the expected mass.

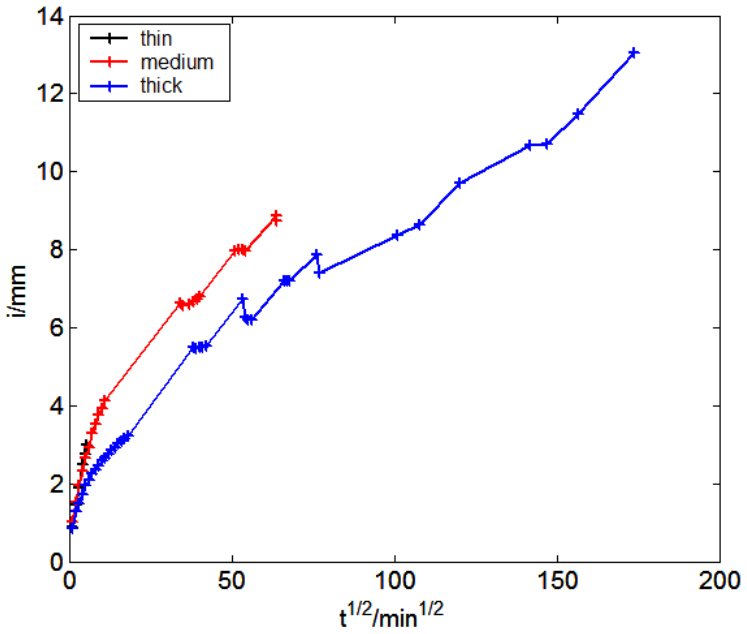

Figure 5-4: CaLoSiL sorptivity curves for a typical AAC sample. Graph shows thin layer, medium layer and thick layer nanolime uptake data.

The mass of particles actually in the material can be seen in Table 5-1. These masses themselves suggest what is confirmed by SEM, that the distribution of particles is uneven within the samples and the lowest level is the most heavily concentrated area of the structure. Water uptake in the aeration pores only occurs for the first 2 – 3 mm of the block (Ioannou et al. 2008) and matrix pores transport most of the imbibing liquid or suspension. The decrease in matrix water sorptivity ranged from 7 – 30% varying with increasing layer thickness of treatment. For all experiments the material can be described as a layered composite with AB signifying the presence of nanoparticles (A) within the AAC material (B).

The water wet front passes through the thin particle layer of the "thin" blocks, confirmed by a lower stage 1 sorptivity compared with the untreated sample, so that the wet front is only going through untreated material during stage 3. Because the uptake was slowed through stage 1 due to the particle layer and then as the wet front moves into stage 3 the front is no longer inhibited and the rate of flow increases to match that of the untreated sample the slope here appears slightly greater compared to the untreated sample.

For the medium treated layer, in which a higher concentration and height penetration by particles exists compared to the thin layer, stage 1 of the sorptivity curve occurs through a more densely packed particle layer than that present within the thin sample accounting for a lower stage 1 sorptivity. As the wet front moves into stage 3 it is still passing through the particle layer, which is now becoming increasingly less dense, until no particles exist and the material is now untreated. The wet front is then able to move more rapidly in the material accounting for the notable rise in capillary uptake in the second part of stage 3.

The particle layer is thicker again in the thick sample with the wet front passing through a densely populated area in stage 1, similar to the medium layer experiment. The particle concentration progressively decreases with sample height again similar in nature to the medium experiment. Therefore the stage 3 composite sorptivity is less than that of the other experiments due to a more concentrated region of particles present in stage 3 than in any other sample. The particles are present as the wet front moves into stage 4 because the entire block is treated.

A blank untreated AAC block with a water sorptivity of 0.1501 $mm/min^{1/2}$ has an ethanol sorptivity of 0.1163 $mm/min^{1/2}$ with a corresponding HOR of 50.0 mm and 52.4 mm respectively. It should be stressed that the high variability of AAC means that these values are not representative of all blocks used. This block has a calculated R of 1.51 and a calculated θ_w of 65.31^o therefore AAC can be defined as wetting.

A white treatment build-up can be seen (Figure 5-5) on the surface of the AAC which reaches above the area of the sample that was in contact with the treatment suspension (this is the same for limestone).

Figure 5-5: Photograph of a slice of an AAC sample treated to the thick layer (section of block missing was removed for investigation by optical microscopy). The treatment build-up on the surface of the sample can be clearly seen. The ruler provides the scale.

5.1.2 Penetration Depth

Treatment of each AAC block with CaLoSiL resulted in a visible white mist on the surface of the blocks that had been exposed to the treatment. This haze was increasingly visible the longer the blocks had been treated. Three blocks were tested here: one treated for 30 minutes resulting in a thin layer, one treated to half way up

the block and the final block treated to the top. All blocks were not carbonated and were cut and tested with phenolphthalein to determine the internal height of treatment.

After cutting each block and treating with phenolphthalein indicator it could be seen that the pink colour, signifying a positive reaction with the indicator, was visible to a height of approximately 1 cm, approximately 2.5 cm and the full height of the block (5 cm) for the thin, medium and thick layer samples respectively (Figure 5-6). It was noted that for both the medium and thick samples the strength of the pink colour decreased with increasing height, showing that the majority of the particles were present in the lower part of the sample blocks.

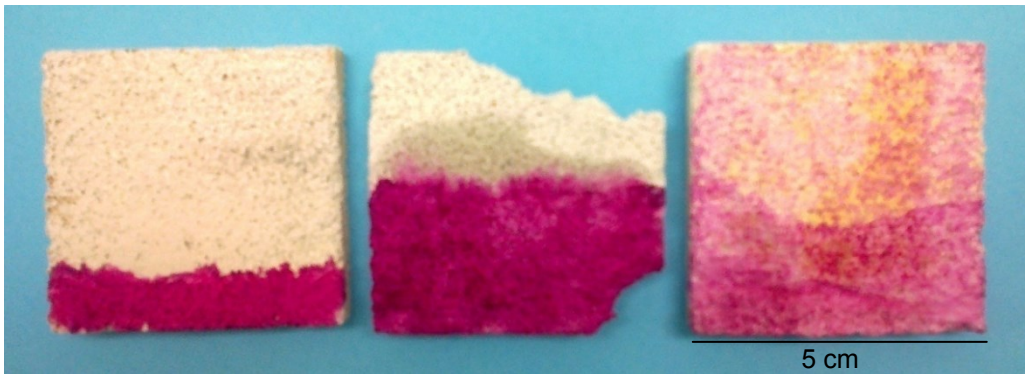

Figure 5-6: Photograph showing the internal height of treatment and extent of positive reaction with phenolphthalein indicator for (left to right) a thin layer sample, a medium layer sample and a thick layer sample. Scale bar is 5 cm.

5.1.3 SEM Imaging

The location of the nanolime particles within the AAC was determined by SEM. A treated AAC sample of thick treatment layer was cut according to Figure 5-7 allowing the interior of the material to be characterised by SEM as previously described in section 3.1.8.

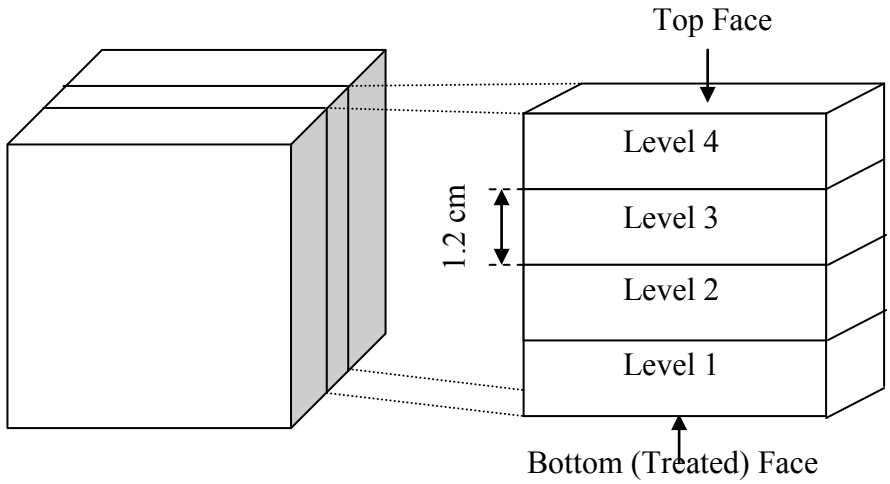

Figure 5-7: Diagram showing how sample sections were obtained from a treated AAC block.

The SEM images in Figure 5-8 and Figure 5-9 clearly show both the unusual AAC bimodal structure and the $Ca(OH)_2$ particles within the material. Carbonation is seen to have occurred as calcium hydroxide carbonates naturally in air.

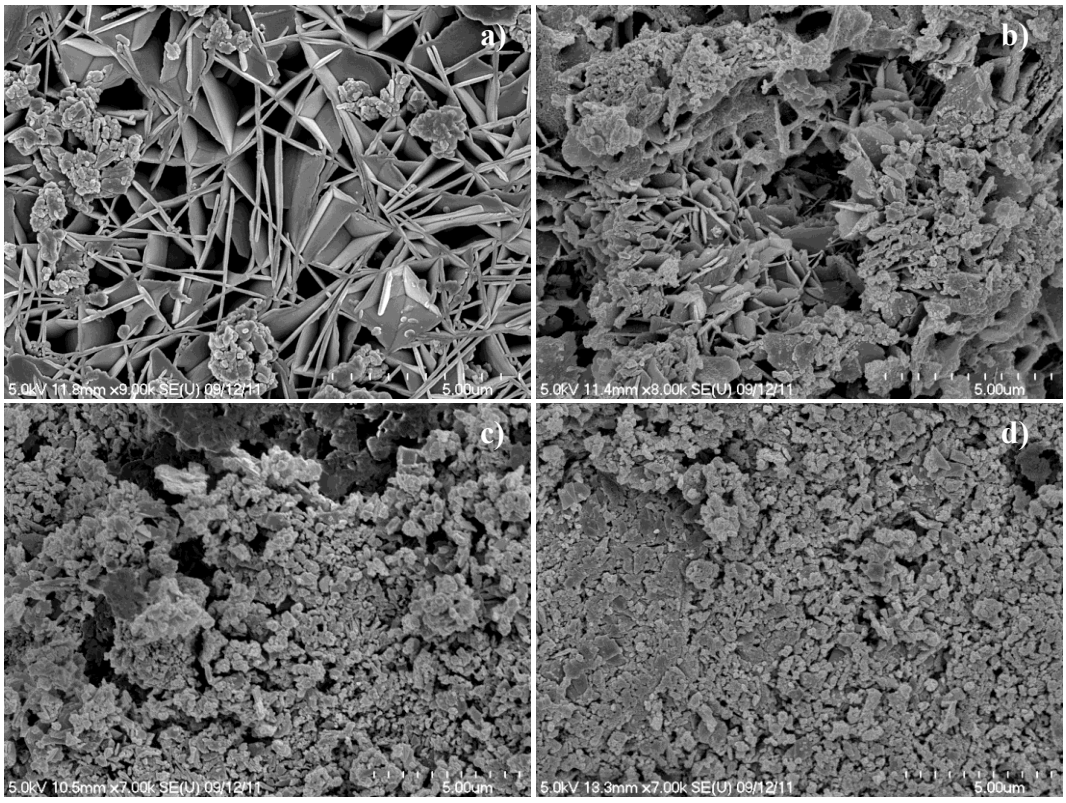

Figure 5-8: High magnification SEM images of treated AAC showing the inside of the material and in a) showing tobermorite platelets comprising the matrix structure of the material and treatment particles (particles seen in images are carbonated), the concentration of which can be seen to visibly increase and obscure the tobermorite network going from images a – d corresponding to four different hight levels within the sample: a) level 4; b) level 3; c) level 2; and d) level 1. Scale bar for all images is 5 µm.

As can be seen in Figure 5-8 the treatment particles have travelled by capillary absorption through the matrix pores. In both Figure 5-8 and Figure 5-9 it can be seen that particle concentration decreases with height and distribution of the particles within the sample is uneven. It is reasonable to expect pore blocking to increase with exposure to increasing particle concentration. In Figure 5-9 it can also be seen that the aeration pores are no longer interconnected, thus isolating these pores and thereby reducing the open porosity of the material.

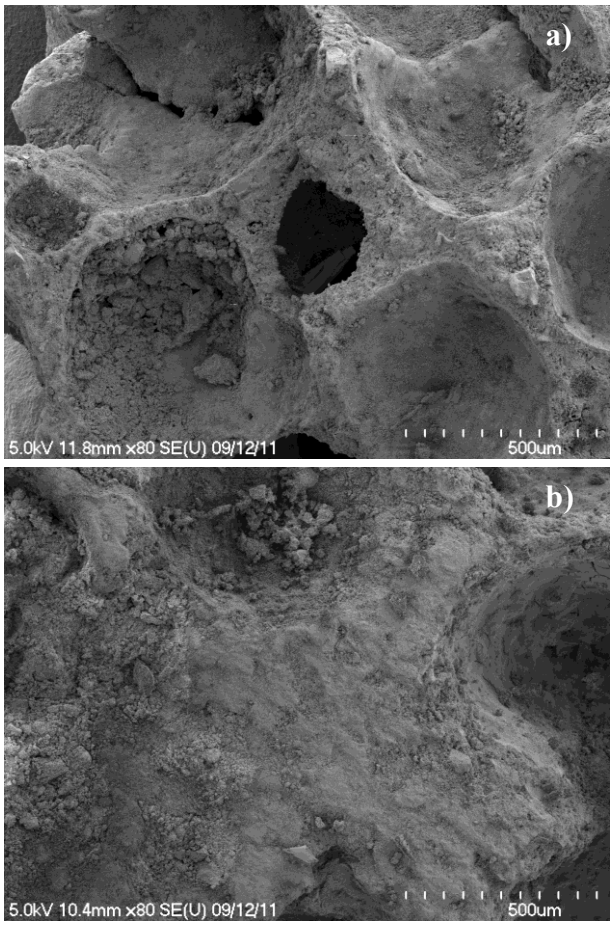

Figure 5-9: Low magnification SEM images of treated AAC showing the internal macrostructure of the material: a) level 4; and b) level 1 of the sample. Scale bar for all images is 500 µm.

5.1.4 MIP

An uncarbonated block of each set (thin, medium and thick particle layer) was used for MIP analysis. Each block was cut so as to isolate a middle slice in the vertical direction. This slice was sectioned horizontally at 1.2 cm intervals from the top to the bottom of the block giving at total of four height levels which were labelled from 1 (bottom level) to 4 (top level) (see Figure 5-7). Each height level of a sample block was prepared and analysed as previously described in Chapter 4.

The pore size distribution of each sample was measured (Figure 5-10). It was determined that the thickness of the treatment layer affected the open porosity of the

material. This suggested less open pore space in the sample due to particles lining and blocking the meso channels connecting the aeration pores and micropores of the matrix forming the aeration pore walls. The natural presence of the ink-bottle effect (Koronthalyova 2011) where large pores can be accessed via the matrix pores or throats leading to an overestimation of the quantity of small pores could, by the addition of particles into the pore structure, also be induced due to the lining and blocking of meso-channels and matrix pores forming the aeration pore walls.

It is possible that pore blocking and pore lining are occurring simultaneously within the sample. In pore lining, a layering of particles within the pores could occur, particularly in the matrix walls, surrounding the macro pores and their interconnecting channels, leading to a decrease in the available pore diameter and aeration pore isolation. The treatment will also give rise to pore blocking. Pore blocking of the matrix can be seen particularly well in the differentiated pore size distribution data (Figure 5-11) for the fourth level of the thick layered sample where high pressure porosity, the matrix porosity, is reduced by 15 % peak area compared to the blank sample. A summary of the measured and calculated property values obtained from the MIP experiments for the matrix portion of the untreated and treated AAC blocks is provided in Table 5-2 where it can be seen that the volume fraction matrix porosity of the blank sample was found to be in good agreement with the values of Ioannou et al. (2008).

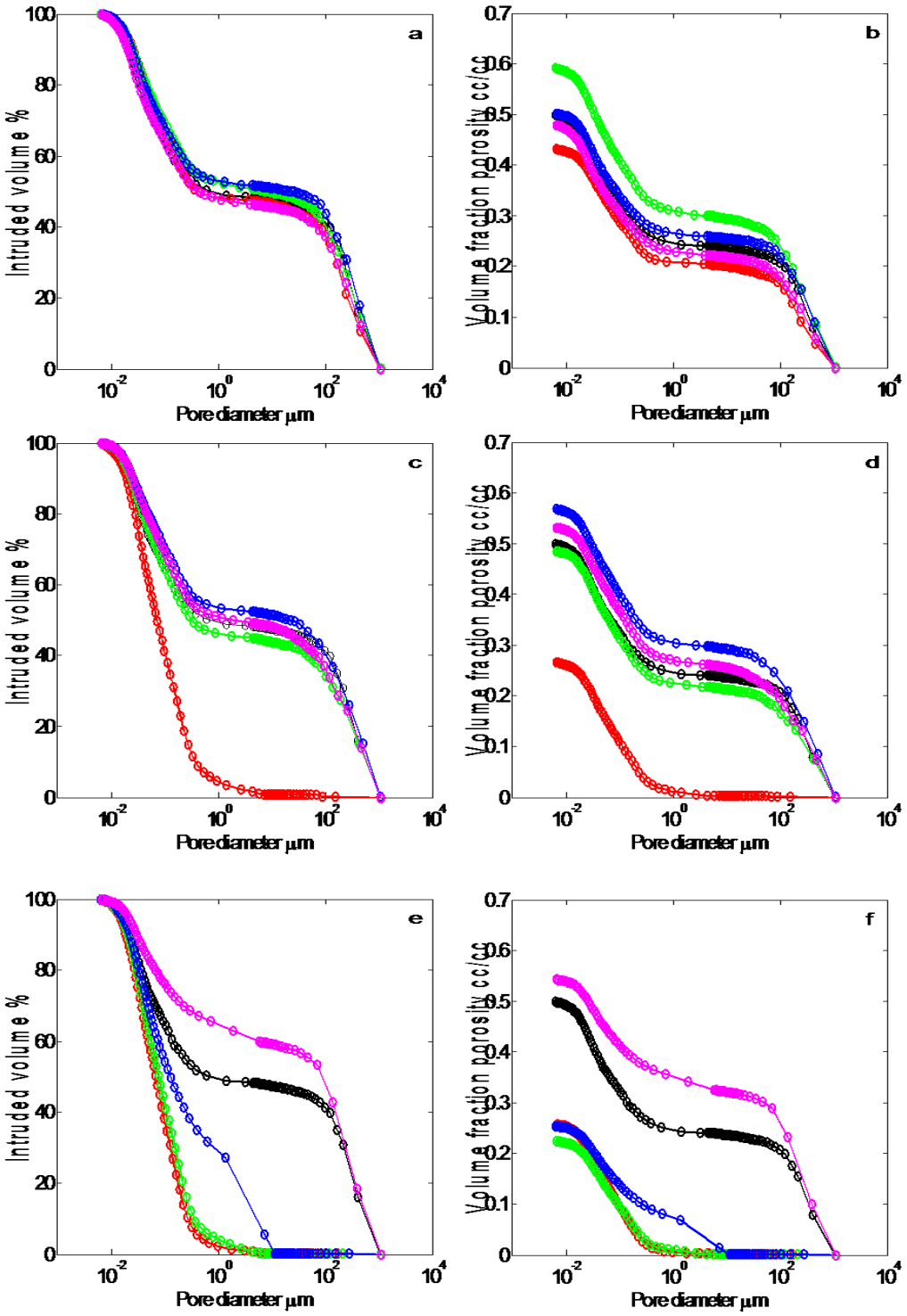

Figure 5-10. MIP data for AAC blocks of different treatment layer thicknesses. a) and b) show intruded volume % and volume fraction porosity for a thin layer. c) and d) show intruded volume % and volume fraction porosity for a medium thickness layer. e) and f) show intruded volume % and volume fraction porosity for a thick layer. In all graphs blank reference AAC sample (black), AAC block level 1 (red), AAC block level 2 (green), AAC block level 3 (blue) and AAC block level 4 (magenta).

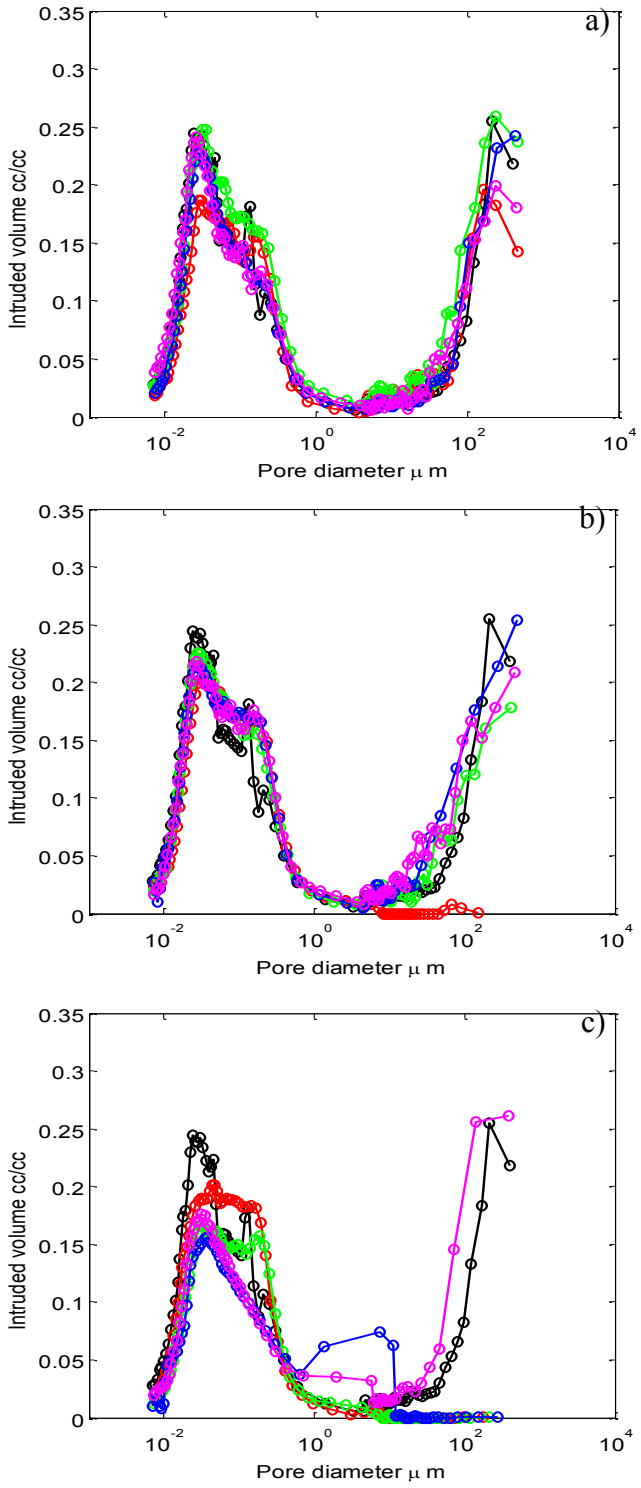

Figure 5-11: Differentiated MIP data for AAC blocks of different treatment layer thicknesses. a) shows the pore size distribution for an AAC block containing a thin layer. b) shows the pore size distribution for an AAC block containing a medium thickness layer. c) shows the pore size distribution for an AAC block containing a thick layer. In all graphs blank reference AAC sample (black), AAC block level 1 (red), AAC block level 2 (green), AAC block level 3 (blue) and AAC block level 4 (magenta).

Sample	M_s g	V_i cc	V_i cc/g	f_m cc/cc	V_T cc	V_T cc/g	f cc/cc
Blank	0.5196	0.2983	0.5741	0.26	0.5775	1.1114	0.50
$L1_{thin}$	0.5786	0.2924	0.5054	0.23	0.5563	0.9615	0.43
$L2_{thin}$	0.4557	0.2950	0.6474	0.29	0.5997	1.3160	0.59
$L3_{thin}$	0.6067	0.3272	0.5393	0.24	0.6776	1.1169	0.50
$L4_{thin}$	0.4560	0.2611	0.5726	0.26	0.4868	1.0675	048
$L1_{medium}$	0.5171	0.3021	0.5935	0.27	0.3069	0.5935	0.27
$L2_{medium}$	0.4926	0.2931	0.5950	0.27	0.5324	1.0808	0.49
$L3_{medium}$	0.5183	0.3125	0.6029	0.27	0.6558	1.2653	0.57
$L4_{medium}$	0.5026	0.3020	0.6009	0.27	0.5946	1.1830	0.53
$L1_{thick}$	0.5799	0.3290	0.5673	0.25	0.3322	0.5729	0.26
$L2_{thick}$	0.6120	0.3029	0.4949	0.22	0.3052	0.4987	0.22
$L3_{thick}$	0.6496	0.2938	0.4523	0.20	0.3665	0.5642	0.25
$L4_{thick}$	0.4947	0.2343	0.4736	0.21	0.5985	1.2098	0.54

Table 5-2: Measured and calculated property values obtained from the MIP experiments for untreated and CaLoSiL treated AAC blocks. M_s is the sample mass in grams. V_i is the intruded Hg volume intraparticle given in cc (experimental data) and in cc/g (calculated from sample mass and V_i cc). V_T is the total intruded Hg volume given in cc (experimental data) and in cc/g (calculated from sample mass and V_T cc). f_m is the volume fraction matrix porosity and is calculated from V_i cc/g and the bulk density. f is the total volume fraction porosity and is calculated from V_T cc/g and the bulk density. The level of the sample is noted as L1 – 4 with L1 being the bottom level and L4 the top level. M_s is of the value plus or minus 1 standard balance error (0.0008 g). V_i and V_T are of the value plus or minus 1 standard balance error (0.0008 g). f and f_m are of the value plus or minus 1 standard deviation including balance error (0.016 g).

From Figure 5-11 and Table 5-2 it can be seen that there is very little difference between the thin sample and blank reference with the exception that level 1 of the thin sample contains slightly less micro and macro porosity. This suggests a stronger pore blocking effect occurs, rather than pore lining in this level. In the medium sample level 1 shows macro pore obstruction with little difference between the micro region of all levels. The macro pores of the thick sample have been obstructed in all levels except level 4 with an opening up of macro porosity beginning in level 3. This suggests that fewer particles are reaching level 3 compared to the previous levels. Level 4 exhibits aeration pore accessibility and micro pore blocking. Upon reaching level 4, the quantity of particles in this layer has significantly decreased compared to previous levels with the differentiation suggesting that the majority of particles in this layer pore block. By comparing level 1 and level 4 it can be seen that level 1 has a greater degree of microporosity. This would seem to prove that pore lining affecting aeration pores, which causes these pores to be visible at smaller pore sizes, exists along-side matrix pore blocking.

5.1.5 Modelling

All treated AAC blocks could be considered as two-layer (three-layer for the medium block) composite materials into which the capillary absorption of water could be analysed using Sharp Front theory (Wilson 1995; Hall and Hoff 2012). Modelling was carried out as described in section 4.1.7. The point at which layers A and B intersect is known as the junction, which the water reaches at time t_j. Known variables were the sorptivity of the composite, sorptivity of the untreated stone and the layer thickness as determined by microscopy. Unknowns were the sorptivity, porosity and permeability of the particle layer, which could be estimated from MIP data. Knowing this allowed determination of the water transport properties of the particle layer itself and then pore filling. Water rise into the sample ($i_1 + i_2$ in mm) is given by Equations 4-1 and 4-2 where Equation 4-1 shows the contribution of the treated layer. Here time from zero to *tj* is t_1 and *tj* to 196 min is t_2.

The above model was expanded to a three layer model for the block of medium treatment height. Here A and B were treatment layers, of length *L1* and *L2*, with different properties and C represented the untreated AAC material. Representation of i_1 is Equation 4-1 with i_2 and i_3 represented by Equations 5-1 and 5-2:

5-1) $$i_2 = S_B\left(t_2 + (L1)^2(X1)\right)^{1/2} - (L1)(Y1)$$

5-2) $$i_3 = S_C\left(t_3 + (L2)^2(X2)\right)^{1/2} - (L2)(Y2)$$

where:

5-3) $$X1 = \left(\frac{f_B}{S_B}\right)^2 \left(\frac{K_B}{K_A}\right)^2 - \left(\frac{f_A}{S_A}\right)^2$$

5-4) $$Y\,1 = f_B \frac{K_B}{K_A} - f_A$$

5-5) $$X2 = \left(\frac{f_C}{S_C}\right)^2 \left(\frac{K_C}{K_B}\right)^2 - \left(\frac{f_B}{S_B}\right)^2$$

5-6) $$Y2 = f_C \frac{K_C}{K_B} - f_B$$

Here *S, f, K,* t_1 and t_2 are the sorptivity, porosity, permeability and time from zero to *tj* (t_1) and *tj* to 196 min (t_2) respectively (subscript indicates material), *L1* is the length of the dense CaLoSiL layer and *L2* is the length of the sparse CaLoSiL layer.

The uptake due to aeration pores was also modelled using a SF model in the form of a capillary rise with gravity (CRG) (Hall and Hoff 2002) which is based on Equation 5-7. By defining dimensionless variables *I* and *T* (Equations 5-8 and 5-9) it is then possible to integrate Equation 5-7 to obtain Equation 5-10. By allowing the junction, *j*, to equal 1 T_j can be written as in Equation 5-11. It is then possible to calculate *i* and *t* from *I* and *T* (Equations 5-12 and 5-13) which can then be plotted to show the uptake by aeration pores only.

5-7) $$\frac{di}{dt} = \frac{S^2}{2i_\infty}\left(\frac{i_\infty}{i} - 1\right)$$

5-8) $$I = \frac{i}{i_\infty}$$

5-9) $$T = \left(\frac{S^2}{2i_\infty^2}\right)t$$

5-10) $$T = -\ln(1 - I) - I$$

5-11) $$T_j = \log\left(\frac{1}{1-I_j}\right) - I_j$$

5-12) $$i = I \times i_\infty$$

5-13) $$t = \frac{T}{\left(\frac{Sa^2}{2i_\infty^2}\right)}$$

Here *Sa* is sorptivity (sorptivity at early time minus matrix sorptivity). *S, I, T, i*, and *t* are sorptivity, dimensionless absorption, dimensionless time, absorption and time respectively.

Water transport properties of the $Ca(OH)_2$ layer and pore filling were investigated using depth information from optical and electron microscopy and by comparing experimental imbibition data (after treatment and carbonation) with predicted imbibition from the sharp front model.

Figure 5-12 shows water uptake in an AAC block treated to heights of a) thin, b) medium and c) thick nanolime layer and carbonated with DiLoCarb. Fitting the experimental data with the models confirmed that treatment particles existed as a thin, medium and thick layer respectively which was known to be 10.0 mm, 25.0 mm and 50.0 mm thick. The permeability and porosity values used in the model are from MIP data files and were calculated by the instrument. All porosity and permeability numbers include the variability of the test block. As is discussed in the MIP section different blocks were used for MIP testing for each height of treatment.

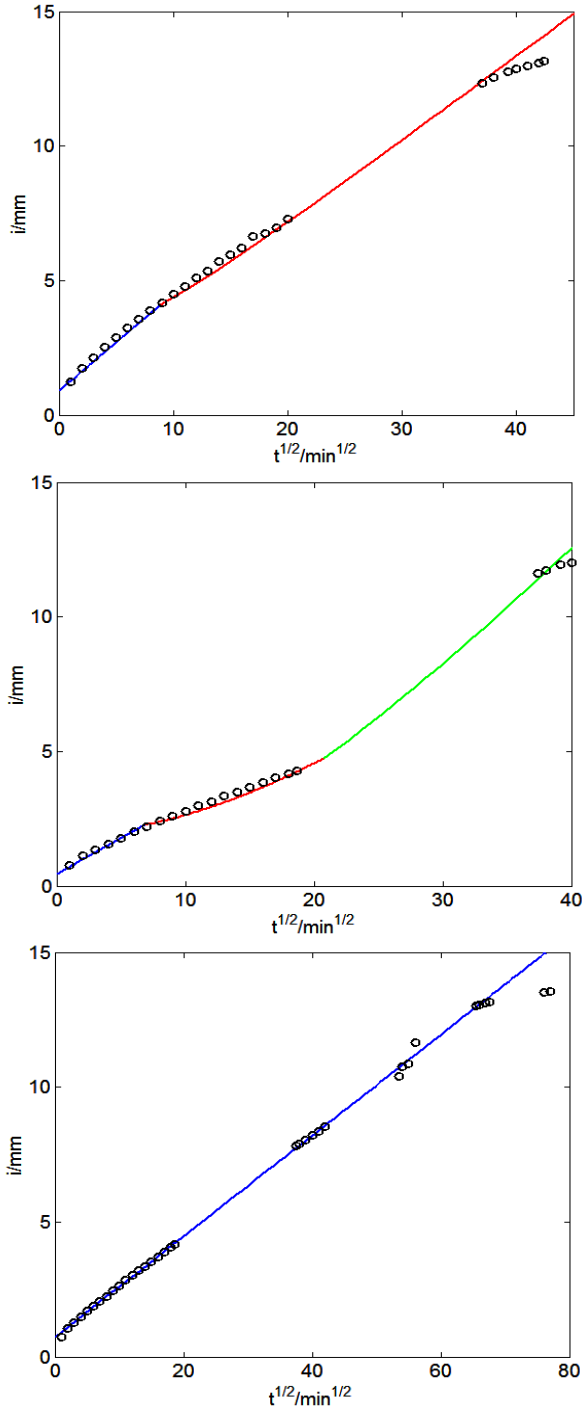

Figure 5-12: a (top), b (middle) and c (bottom). Model versus experimental (black) water uptake data for an AAC block after treatment with nanolime and carbonated. a) blue curve (s = 0.36, K = 0.009, f = 0.32 (A), L = 10 mm) is uptake through A, red curve (s = 0.32, K = 0.01, f = 0.35) is uptake through B for thin block, b) blue curve (s = 0.26, K = 0.002, f = 0.30 (A), L = 6 mm) is uptake through A, red curve (s = 0.43, K = 0.09, f = 0.47 (A), L = 19 mm) is uptake through B and green curve (s = 0.52, K = 0.01, f = 0.59) is uptake through C for medium block and c) blue curve (s = 0.19, K = 0.002, f = 0.29 (A), L = 50 mm) is uptake through A for thick block .

As shown in Figure 5-12, the upwards curve modelled at early time (blue line) corresponds to water flow through the A particle layer. The downwards curve in the experimental data (black circles) at later time resulted from the wet front reaching the top of the AAC block where sorptivity slows. If the particle layer was thicker or thinner than the observed depth the model would not match the experimental data. Due to this the models confirmed the height and nature of the particle layer and that pore blocking or lining occurred.

It is known that (Ioannou et al. 2008) absorption by aeration pores only occurs for the first 2 – 3 mm due to the large pore size. Modelling of the aeration pore water uptake showed that for an AAC block tested by imbibition at each level of treatment as the height of treatment increased the activity of the aeration pores decreased. This is due to the region of active aeration pores being exposed to treatment suspension for an increasing length of time, thereby resulting in the particles being most concentrated in this region. Due to this the active aeration pores and pore throats are being increasingly lined and obstructed by particles. This is confirmed by modelling in Figures 5-13 to 5-16 where the aeration pore activity is seen to progressively decrease from blank untreated through to thick layer treatment sample states due to increasing particle concentration. This modelling confirms the observations of the sorptivity modelling and the experimental uptake data.

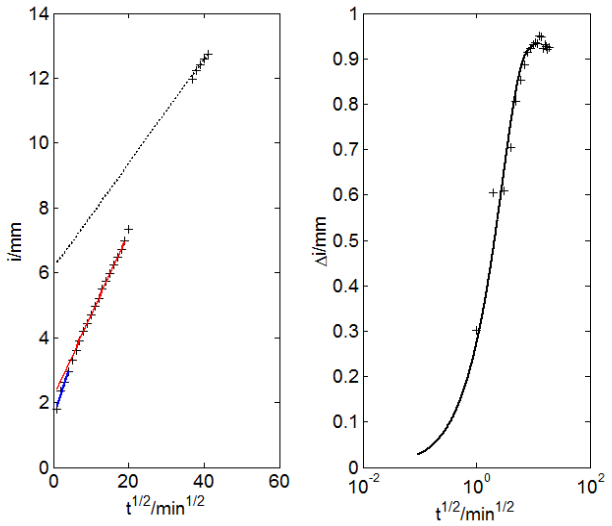

Figure 5-13: Graph showing capillary water absorption in an AAC block (untreated). Left: I vs t1/2 where: Sm (red), initial stage 1 uptake (blue), stage 4 (dotted line) shown by back extrapolation of late time data, experimental data points are marked by crosses. Right: estimated absorption by aeration pores: line is CRG model fitted to experimental data points (crosses).

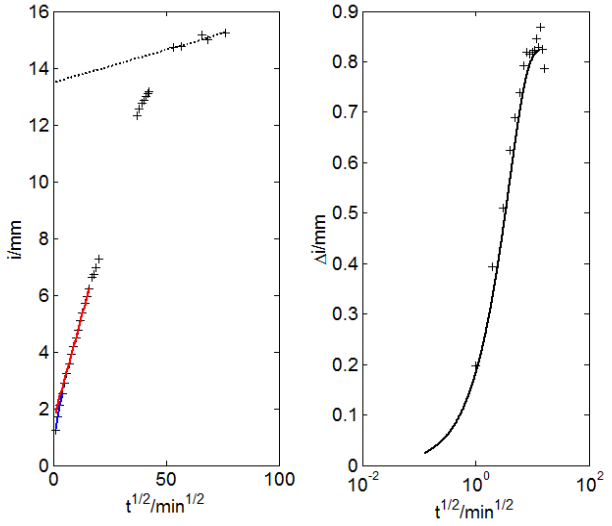

Figure 5-14: Graph showing capillary water absorption in an AAC block (thin layer). Left: I vs $t^{1/2}$ where: Sm (red), initial stage 1 uptake (blue), stage 4 (dotted line) shown by back extrapolation of late time data, experimental data points are marked by crosses. Right: estimated absorption by aeration pores: line is CRG model fitted to experimental data points (crosses).

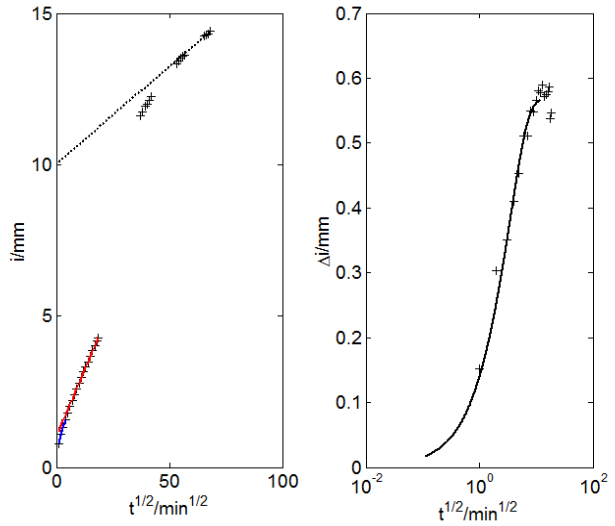

Figure 5-15: Graph showing capillary water absorption in an AAC block (medium layer). Left: I vs $t^{1/2}$ where: Sm (red), initial stage 1 uptake (blue), stage 4 (dotted line) shown by back extrapolation of late time data, experimental data points are marked by crosses. Right: estimated absorption by aeration pores: line is CRG model fitted to experimental data points (crosses).

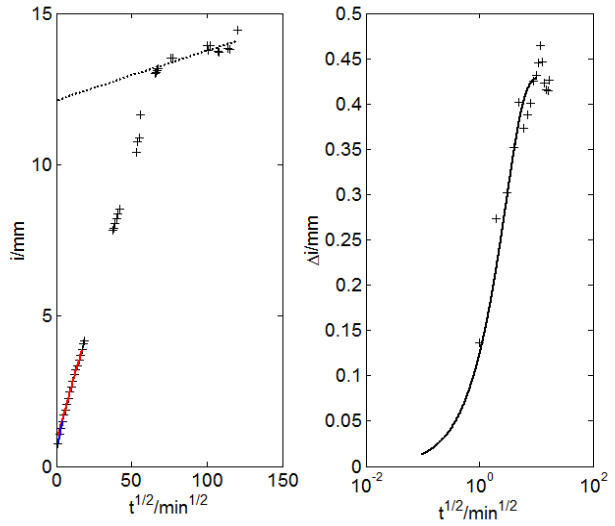

Figure 5-16: Graph showing capillary water absorption in an AAC block (thick layer). Left: I vs $t^{1/2}$ where: Sm (red), initial stage 1 uptake (blue), stage 4 (dotted line) shown by back extrapolation of late time data, experimental data points are marked by crosses. Right: estimated absorption by aeration pores: line is CRG model fitted to experimental data points (crosses).

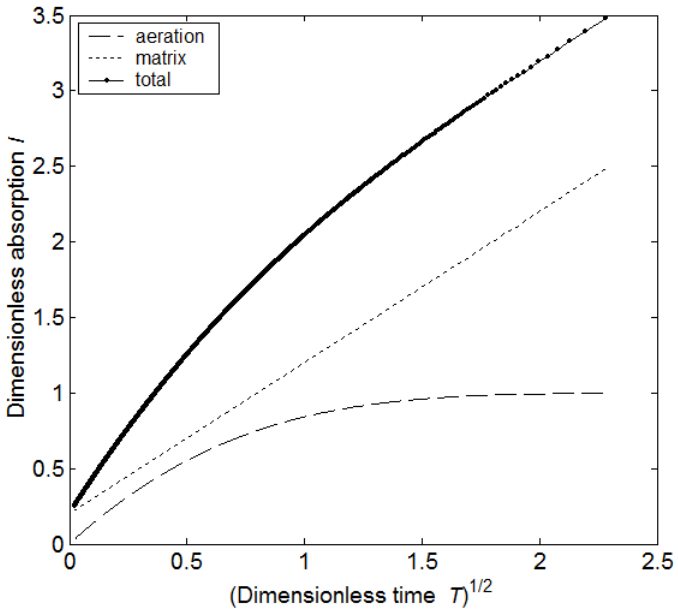

Figure 5-17: Breakdown of pore type contributions to the overall sorptivity for an AAC block.

Figure 5-17 shows the breakdown of pore type contributions for the uptake of water within an AAC block. It can be seen that the aeration pore contribution flat lines corresponding to the maximum uptake possible in these pores. In contrast the matrix component increases on a straight line showing that the matrix pores are solely responsible for water uptake to the top of the AAC block.

5.1.6 Discussion

The results suggest that a particle suspension, with particles less than 0.25 μm, can travel up to 5 cm into the AAC structure by capillary absorption. The distribution of these particles within the micro/macro structure is uneven with the densest population of particles near the bottom wicking face of the material and becoming increasingly less concentrated with increasing height (Figure 5-18).

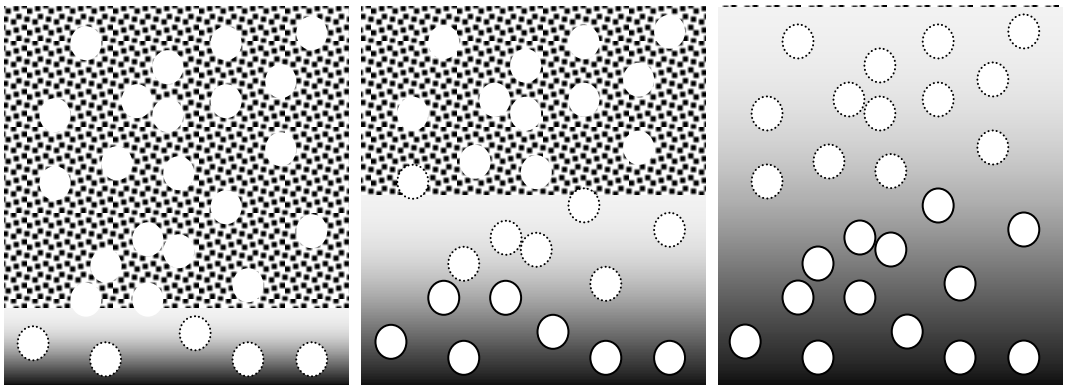

Figure 5-18: Diagram showing particle location within (from left to right) a thin layer AAC sample, a medium layer AAC sample and a thick layer AAC sample.

SEM confirms the presence and distribution of particles within all layers of the thick sample and suggests pore lining and blocking occur which have a strongly isolating effect on the large aeration pores thereby affecting the open porosity of the material.

Treatment of AAC with $Ca(OH)_2$ resulted in a reduction in matrix sorptivity of up to 30%, a porosity reduction of up to 1% in the treated layer and an estimated permeability reduction by up to 3% in the layer varying with treatment layer thickness. The particle treated layer within the material remains and a high matrix sorptivity reduction is avoided. This is because, above 1 cm, the particle concentration gradually thins as it nears the top of the block (Figure 5-18).

Despite having a greater quantity of micropores compared to the two limestones studied in Chapter 4 of this study it can be seen that the particle penetration depth into AAC is much greater. Both the limestones in this study are compact dense blocks of stone whereas AAC is naturally constructed of open channels formed by spacing between the tobermorite platelets. This difference can be clearly seen in the SEM images of Figure 5-19. These findings suggest that the pore structure of a material is a more important factor for determining particle transport than a material's pore size distribution.

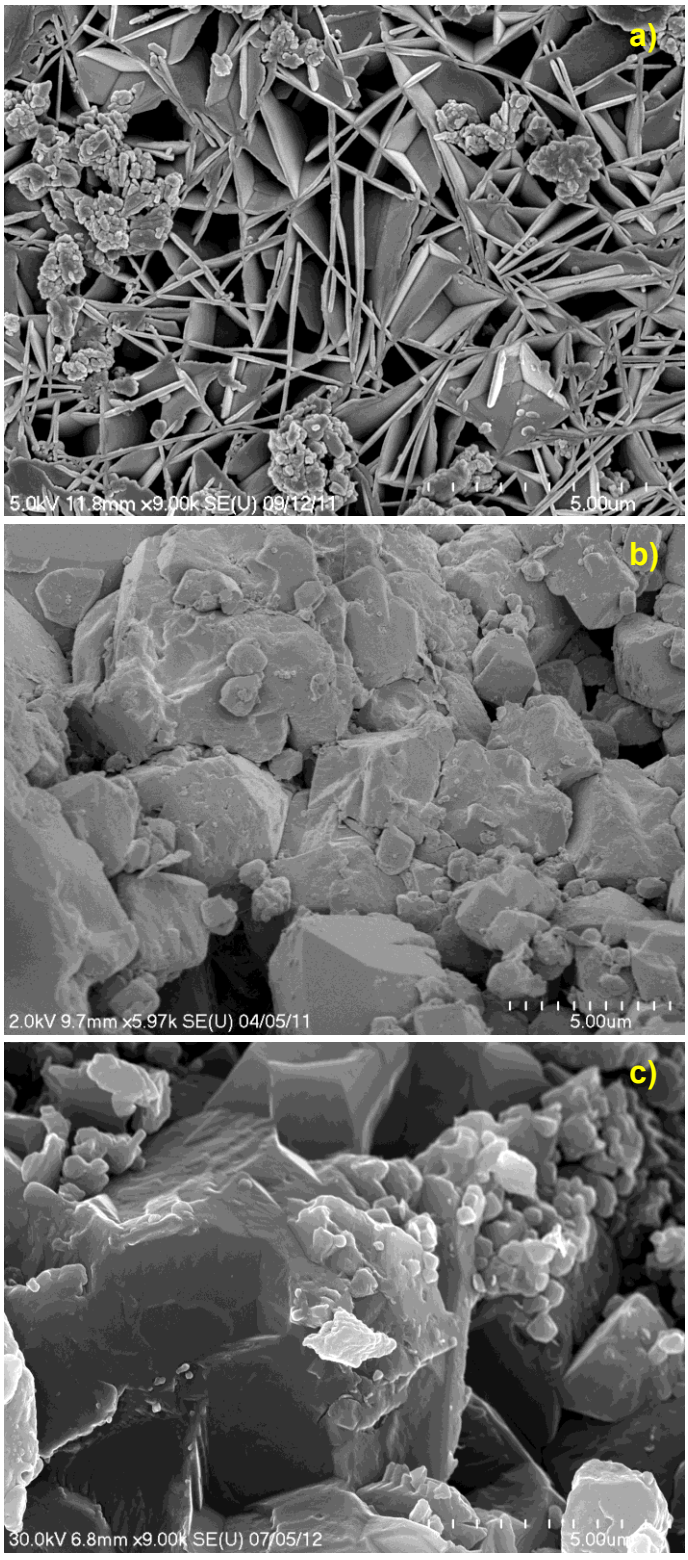

Figure 5-19: SEM images showing material structure differences between a) AAC (particle clumps here are nanolime treatment, b) Portland (untreated) and c) Lincoln (untreated).

Modelling by two and three layer SF model confirms treatment layer thickness and nature of the layer. Aeration pore activity modelling confirms that as the base of the block is exposed to nanolime suspension for increasing lengths of time the concentration of the particles causes pore and pore throat lining causing a decrease in the activity of the aeration pores.

It was found that the volume fraction matrix porosity of the blank sample obtained from MIP analysis was in good agreement with the values of Ioannou et al. (2008) and thus further validates the reported data and explanations due to the second method agreement herein.

For samples highly concentrated with particles aeration pores become isolated and removed from open porosity due to blocking and lining of surrounding matrix and interconnecting channels. The lining induces the ink bottle effect causing the aeration pores to appear in the high pressure region of the MIP curves. Pore blocking always occurs and is dominant and can mask the extent of lining.

5.2 Conclusions

The properties of untreated AAC have been shown to be in good agreement with Ioannou et al. (2008). As different test methods have been used in this study this confirms the findings of Ioannou et al. (2008) by way of second method agreement.

Experiments and theoretical modelling have shown that a nanoparticle suspension can deliver particles up to a height of 5 cm (the top of the block) by capillary absorption by AAC matrix pores. The particle layer is most concentrated within the bottom 1 cm of the block with the layer becoming increasingly less dense with increasing height (Figure 5-18). The presence of nanoparticles within the material induces the ink bottle effect which occurs along-side pore blocking. From MIP data it can be seen that pore blocking is the dominating effect.

These results show that the distance travelled within a material by nanoparticles in suspension is determined by the particles' ability to move through the pore network. Blocking and lining of pores can hinder movement and affect the micro/macro pore nature of the material. When considering these results in comparison with the results on limestone (Chapter 4) it can be seen that the pore network structure of a material is more important in determining the distance particles can travel than its' pore size distribution (providing the particle size is compatible with the pore size).

These experiments on AAC have demonstrated that it is possible to get large HOR of CaLoSiL in a material.

Chapter 6:
Hydroxyapatite Particles Applied to Archaeological Bone

As previously discussed, colloidal suspensions are being increasingly applied within the heritage conservation field but have not yet been used on archaeological bone. The compatibility in size between synthesised hydroxyapatite particles and the pore size of weathered bone suggested treatment with colloids could work. In addition, chemically compatible particles of hydroxyapatite can be straightforwardly synthesised from solution which allowed enough particles to be made to test this potential new treatment.

In this chapter hydroxyapatite (HAP) particles are synthesised, analysed and applied to archaeological bone and the treatment's efficacy is determined.

6.1 Hydroxyapatite Particle Synthesis and Analysis

The synthesis method used was the procedure given by Tseng et al (2009) with a longer mixing time. As per Tseng et al. (2009) $Ca(OH)_2$ (0.85 g), $Ca(H_2PO_4)_2$ (1.25 g) and polyethylene glycol, PEG, (4.0 g) were added to 30 mL de-ionised H_2O. The resulting mixture was placed onto a hotplate at 65 ^oC with continuous stirring for approximately 1 hour resulting in a thick white milky suspension. The suspension was placed into a furnace and heated to 900 ^oC at a rate of 5 ^oC per minute then held at temperature for 30 minutes producing a white powder.

6.1.1 X-Ray Diffraction Analysis

XRD was carried out as described in section 3.1.2 with the exception that a Bruker D2 Phaser XRD spectrometer was used.

The XRD results (Figure 6-1) show that the product is synthetic hydroxyapatite, $Ca_{10}(PO_4)_6(OH)_2$, with a hexagonal unit cell structure and an additional beta tri-calcium phosphate component which is a common impurity (Tseng et al. 2009). This impurity is identified by the EVA program as synthetic whitlockite. Several non-mineral compounds have been characterized under the name of whitlockite, which is a solid solution series, and phases of beta tri-calcium phosphate are known under this moniker (Calvaro & Gopal 1975; Mathew & Takagi 2001; ed. Konigsberger & Konigsberger 2006).

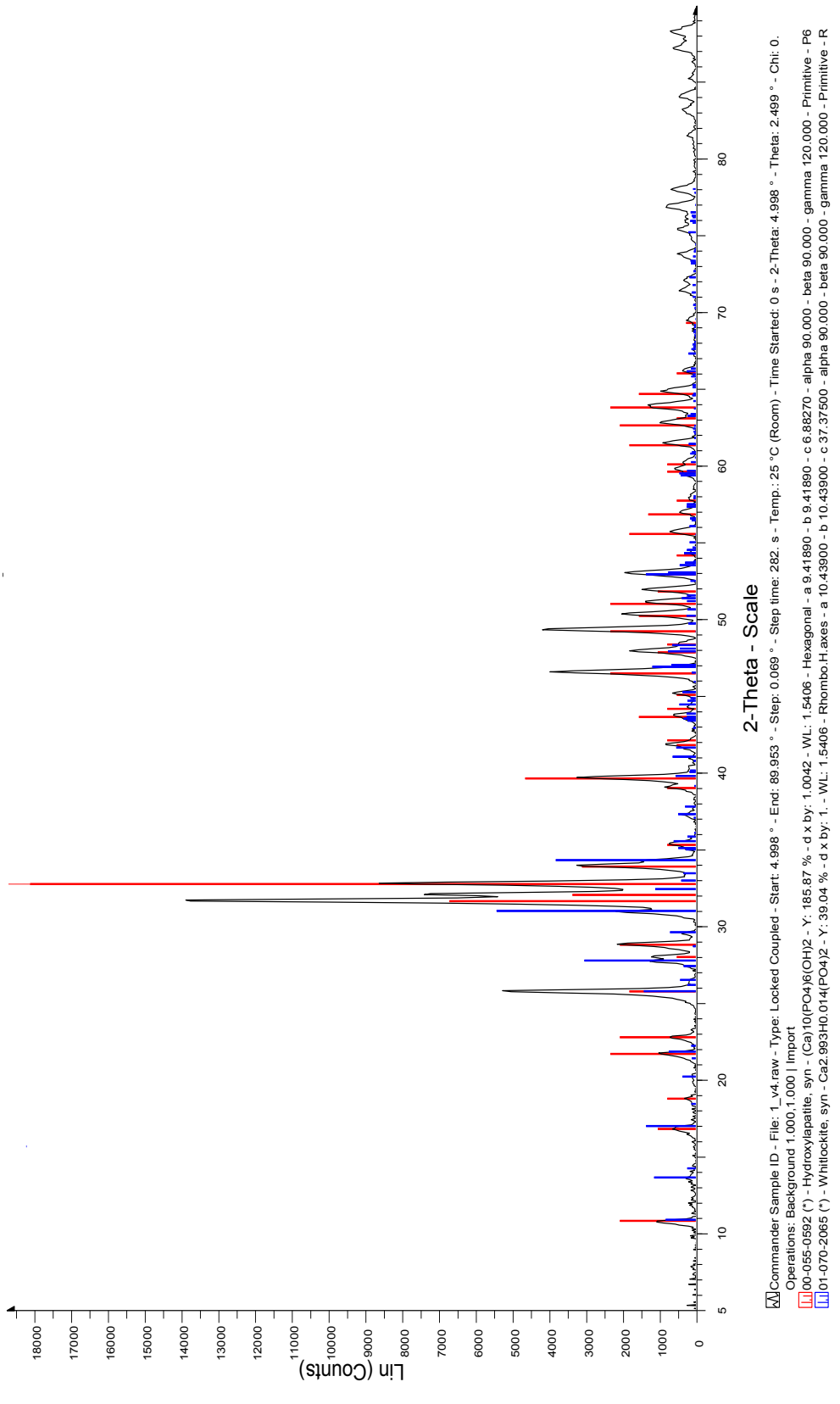

Figure 6-1: XRD spectrum obtained from synthesised HAP compared to library patterns.

6.1.2 Particle Sizing by LD

The long bench Mastersizer S was used as described in section 3.1.3 to measure product particle size.

It was necessary to fit the PSD data with a three-component fit (Figure 6-2). In order to view the results clearly the data was displayed on a $\log_{10}$ scale against the arbitrary intensity. Data for each peak contained within the overall PSD distribution for the mean results are given in Table 6-1.

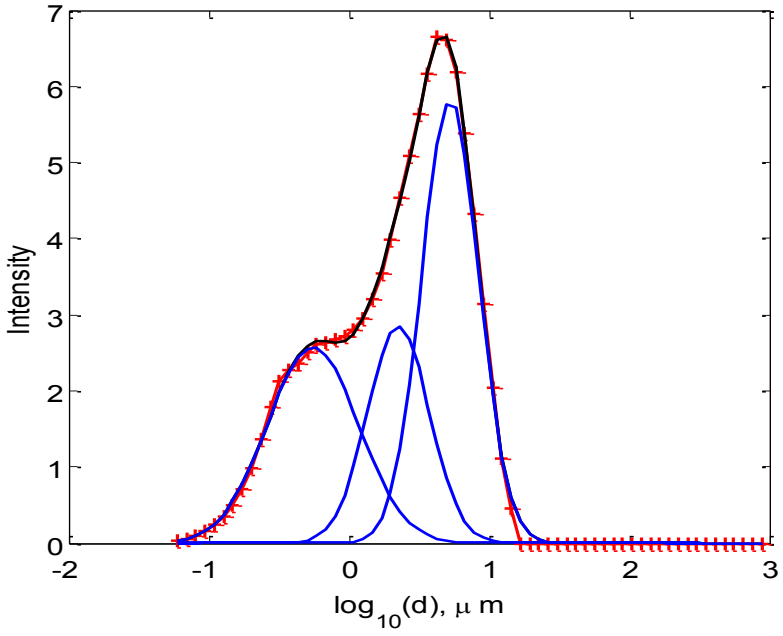

Figure 6-2: Peak fitting of mean HAP experimental data (red stars) with three-component fit. The figure shows how three peaks (blue lines) combine to produce the overall PSD, the fit line of which is shown in black.

Peak	μ ($\log_{10}$(d), μm)	σ ($\log_{10}$(d), μm)	Area ($\log_{10}$(d), μm^2)	Percentage of particles
1	-0.27	0.33	2.10	31.52
2	0.35	0.22	1.58	23.74
3	0.72	0.20	2.98	44.73

Table 6-1: Numerical data resulting from the peak fitting shown graphically in Figure 6-2.

It can be seen that the HAP particles have a size range including agglomerates of between 0.02 – 15 μm. The data suggests that few truly small or single particles are formed and sustained for a sizable length of time prior to developing at least a small degree of agglomeration. Factors affecting surface charge include the solution, any additives, system equilibration, ion effects and pH and can be reasonably complex (Somasundaran 1968; Matsumoto et al. 1989; Gbureck et al. 2002; Cooper & Hunt 2005; Harding et al. 2005). However the results here suggest that the attractive forces within the system dominate causing particle attraction.

6.1.3 Particle Sizing by NTA

Sample particle sizing by NTA was carried out as described in section 3.1.6. A solution of 5g of particles per 100 ml of EtOH was synthesised then diluted 1:10000 for analysis.

It was discovered that the fine particles existed in discrete groups within the distribution which was found to be much more complex than for the wide ranging PSD obtained from LD. The NTA PSD for the sample was found to require a nine-component fit (Figure 6-3) and was displayed on a $\log_{10}$ scale against the arbitrary intensity.

The 3D graphical map (Figure 6-4) of particle concentration generated by the Nanosight was found to be in good agreement with the calculated percentage of particles present within each peak of the fit (Table 6-2).

Peak	μ ($\log_{10}$(d), μm)	σ ($\log_{10}$(d), μm)	Area ($\log_{10}$(d), μm^2)	Percentage of particles
1	-1.75	0.01	0.003	0.13
2	-1.49	0.13	0.06	3.36
3	-1.36	0.08	0.14	7.05
4	-1.08	0.11	0.66	34.53
5	-0.93	0.06	0.48	24.89
6	-0.82	0.04	0.15	7.97
7	-0.73	0.06	0.36	18.61
8	-0.63	0.12	0.06	3.27
9	-0.37	0.03	0.004	0.19

Table 6-2: Numerical data resulting from the peak fitting shown graphically in Figure 6-3.

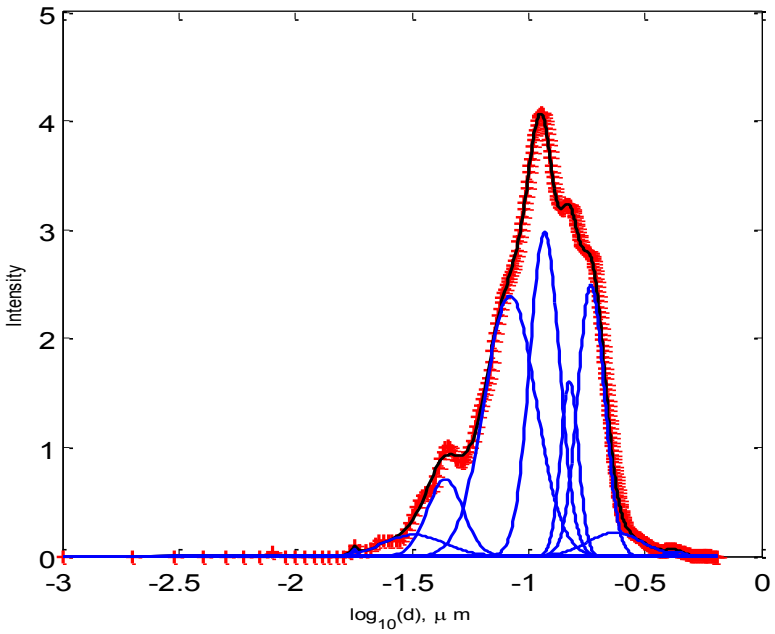

Figure 6-3: Peak fitting of mean HAP experimental data (red stars) with nine-component fit. The figure shows how nine peaks (blue lines) combine to produce the overall PSD, the fit line of which is shown in black.

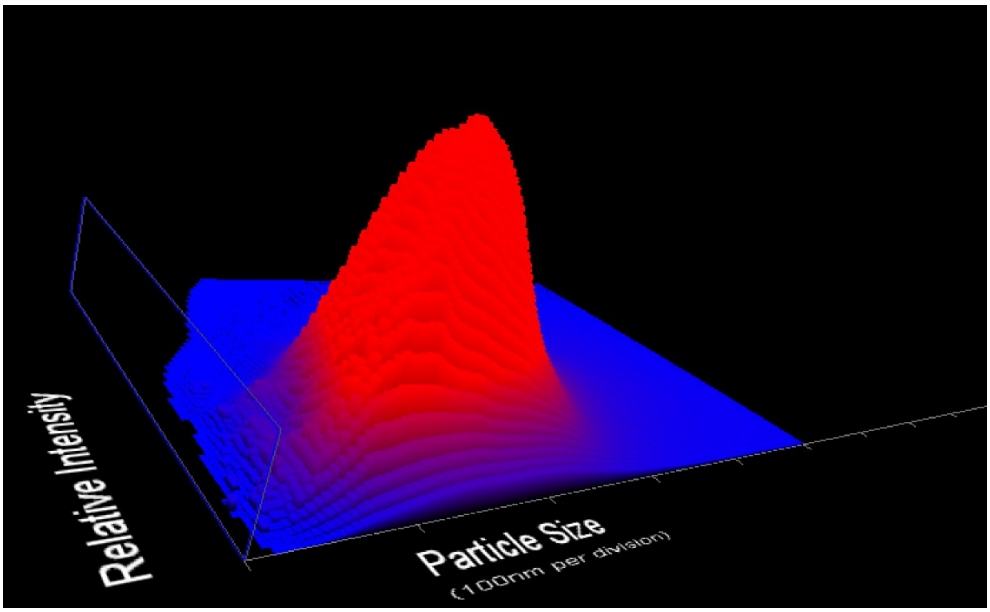

Figure 6-4: 3D Graphical PSD for HAP sample giving indication of the number and intensity of particles of each size within the distribution. Blue shows areas of lowest particle concentration. Red shows areas of highest particle concentration.

It is clear from Tables 6-1 and 6-2 that NTA can determine the size of particles less than 1 μm to a much greater degree than LD and can clarify features within the range obscured by the heavy agglomeration of particles and the limitations of LD itself.

As found from this technique HAP particles have a size range, excluding large agglomerates only visible by LD, of 0.02 – 0.6 μm. The visualization of the sample by NTA allows the distinction between large particles and agglomerates. All particles have a single light scattering center whereas large agglomerates have multi (two or more) light scattering centers (Filipe et al. 2010). This shows that these aggregates are comprised of either several particles (forming one aggregate) or two or more aggregates forming a larger agglomerate. Due to this it can be said that particles are small and have a narrow size range with the remainder of the PSD range caused by aggregation.

6.1.4 SEM Imaging of Particles

SEM imaging of a sample was carried out as described in section 3.1.8 using a thin Ta-Au coating.

SEM imaging (Figure 6-5) showed the amorphous structure of the particles and how the particles were easily agglomerated.

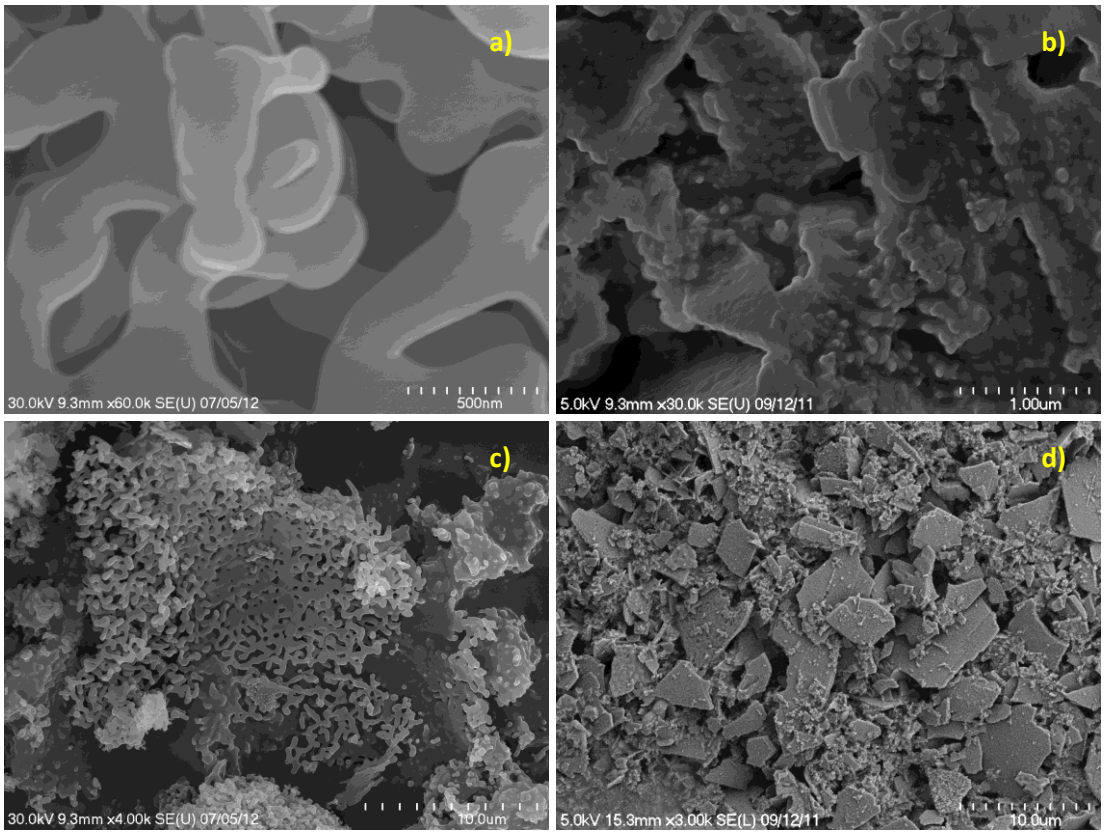

Figure 6-5: SEM images of HAP powder on carbon tape at a variety of magnifications and 30 kV (a and c) and 5 kV acceleration voltages (b and d). A greater working distance of 15.3 mm was used in d) compared to 9.3 mm in all other images. The images show the particle network structure and large agglomerate clumps at a variety of magnifications. The scale bar for image a) is 500 nm, for image b) it is 1 µm and for images c) and d) the scale bar is 10 µm. All images are secondary electron images with only d) being collected on the lower detector and all other images being collected on the upper detector.

The size range determined by LD and NTA is confirmed visually by SEM which shows that individual particles tend to coalesce (Figures 6-5a, 6-5c). These particles together form the clumps visible in Figures 6-5b and 6-5d. This shows that a degree of agglomeration is continually present as all structures seen within the sample are formed by the particle network structure seen in Figure 6-5a. These images are very similar to those of Tseng et al. (2009).

6.1.5 Discussion

This synthesis procedure results in the formation of HAP particles which exhibit some degree of agglomeration. The particles are mostly synthetic hydroxyapatite with minor beta tri-calcium phosphate (BTCP).

According to Tseng et al. (2009) this BTCP should not be present when HAP is synthesised using PEG, however this was found not to be the case for all samples. It is known (Wang et al. 2005) that pure HAP can transform to produce some BTCP at 900^{o}C. This is the temperature reached and sustained for 30 minutes during this synthesis process also used by Tseng et al. (2009) who say PEG inhibits formation by delaying phase transformation at 900^{o}C and that in syntheses using PEG, BTCP is not formed in the reaction at 900^{o}C within 30 minutes. However, BTCP is formed in the reaction presented here. Porcelain can induce the decomposition of HAP allowing formation of BTCP (El Briak-Benabdeslam et al. 2008).

The HAP particles have a size range, including all agglomerates, of between 0.02 – 15 μm. This is smaller than the sizes reported by Tseng et al. (2009) (30 – 36 μm) for particles synthesized without PEG but larger than sizes reported (50 – 600 nm) for synthesis with PEG. Excluding large agglomerates the particles synthesised in this study have a size range of 0.02 – 0.6 μm (20 – 600 nm) which is very similar to the results of Tseng et al. (2009).

Fusing between particles is visible in SEM images where at high magnification these links can be seen (Figure 6-5). In the SEM images of the HAP samples synthesised in this study it was not possible to obtain an image of a single particle, all particles had fused. It could be seen that the platelet-like larger agglomerates were formed from the same particle network. The HAP agglomerate structure seen in the SEM images of this study are similar to those of Tseng et al. (2009).

6.2 Treatment of Archaeological Bone with Hydroxyapatite Particle Suspension

This section describes the effects of a synthesised HAP suspension on archaeological bone. Water uptake tests on medieval untreated samples and samples exposed to the HAP treatment were used to investigate the effect of the particles on imbibition behaviour. The water transport properties were fitted to a Sharp Front model and compared to the experimental data. The effect of particles on open pore space is also discussed as is depth of penetration.

The possibility of a completely chemically compatible conservation treatment for archaeological bone is highly relevant within the conservation field. Thus the practicality of such a treatment is considered here.

6.2.1 Archaeological Bone

Medieval archaeological fragmentary disarticulated human remains were supplied by the Archaeology Department of the University of Edinburgh.

The bones were analysed by Raman spectroscopy to check composition, which was dominated by hydroxyapatite. Optical images of an ulna fragment showing the different textures of the surface were also obtained by the instrument (Figure 6-6). The colours in Figure 6-7 could indicate that an Fe compound (possibly lepidocrocite), a Ca compound and possibly pyrolusite are most likely responsible for the red, white and black areas respectively (Edwards and Chalmers 2005). Positive identification was not possible due to fluorescence and weak peaks.

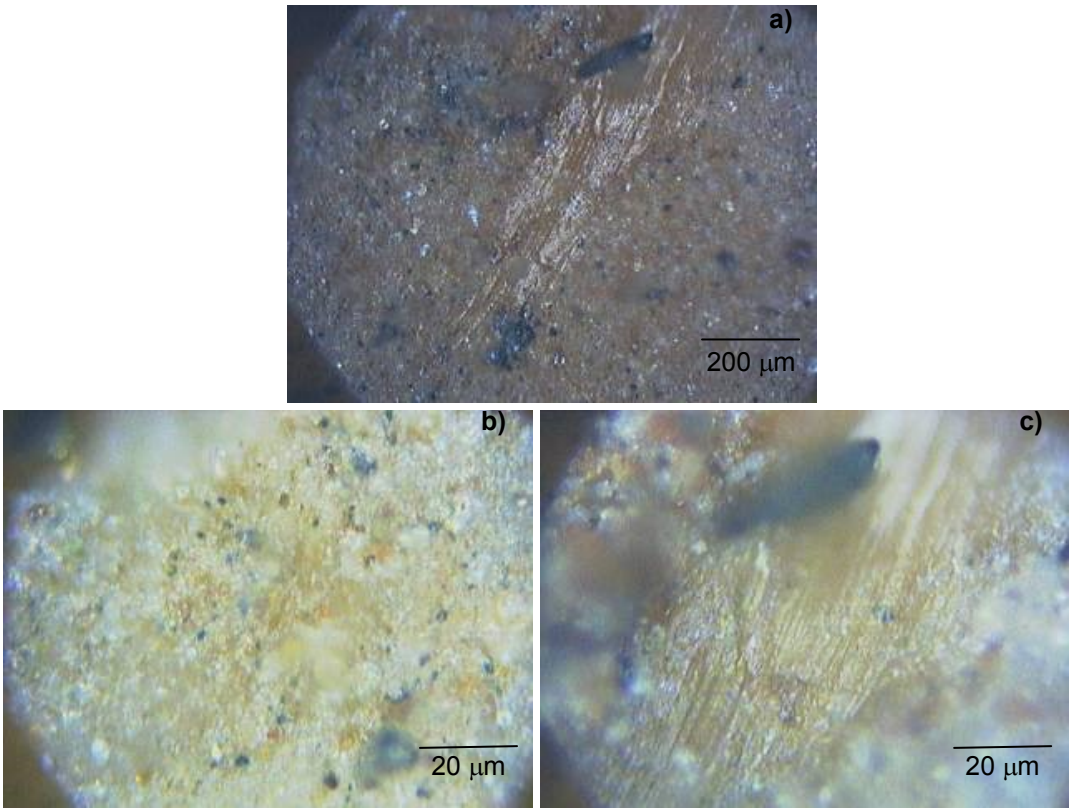

Figure 6-6: Optical images obtained from the Raman instrument of an area of an ulna fragment. For image a) the scale bar is 200 μm. For images b) and c) the scale bar is 20 μm.

A portion of bone was removed and prepared for MIP analysis. The resulting data showed that the bone was bimodal with two distinct pore size ranges of 0.004 – 0.15 μm and 0.15 – 5 μm (4 – 150 nm and 150 – 5000 nm). The modality of the bone can be seen clearly in Figure 6-7 where the MIP data has been differentiated. Due to these results it can be said that the bone is highly microporous. My MIP findings were confirmed by way of a second MIP test conducted by Dr Fiona Sillars at the University of Dundee.

As previously discussed the HAP particles have a size range including large agglomerates of between 0.02 – 15 μm and excluding large agglomerates of 0.02 – 0.6 μm. Therefore the size range of the free particles lies within the pore size range of the bone and so only larger agglomerates should be excluded from the pore structure.

The bulk density, porosity and quantity of air trapping of a selection of bones were determined (Chapter 2 & Appendix C) to be 1279.9 ± 195.1 kg m^{-3}, 51.6 ± 4.4 % and 1.4 % respectively.

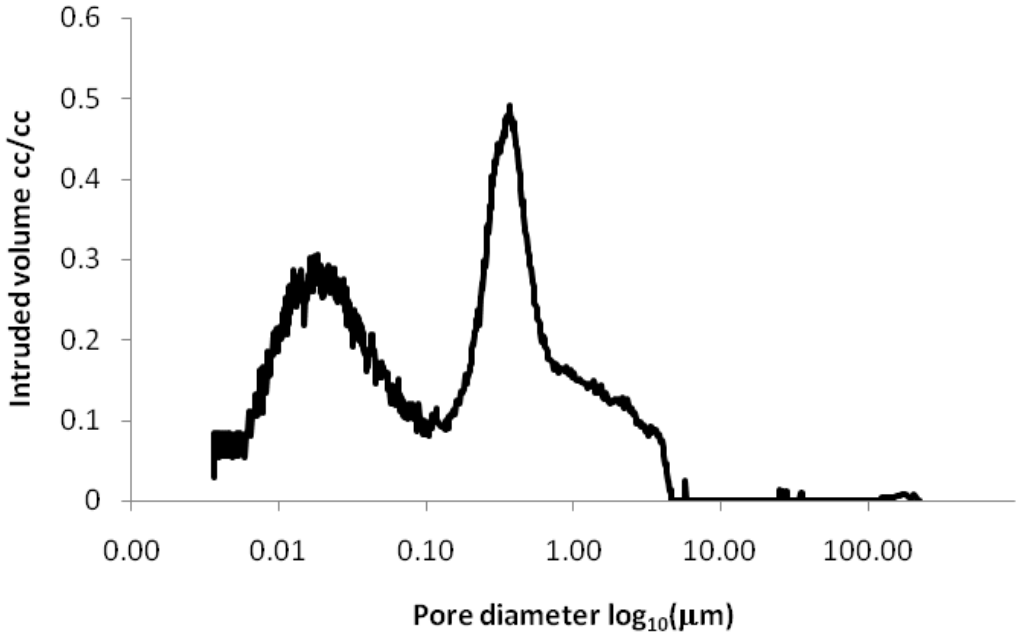

Figure 6-7: Differentiation of the volume fraction porosity archaeological bone MIP curve.

SEM images can show the difference between the compact (cortical) outer bone and the trabecular (cancellous) inner bone (Figure 6-8). Mineralised fibres can also be seen within the bone (Figures 6-8c, 6-8e). The findings of SEM images obtained in this study are comparable to those of Wang et al. (2010) and show the expected structure for both bone types.

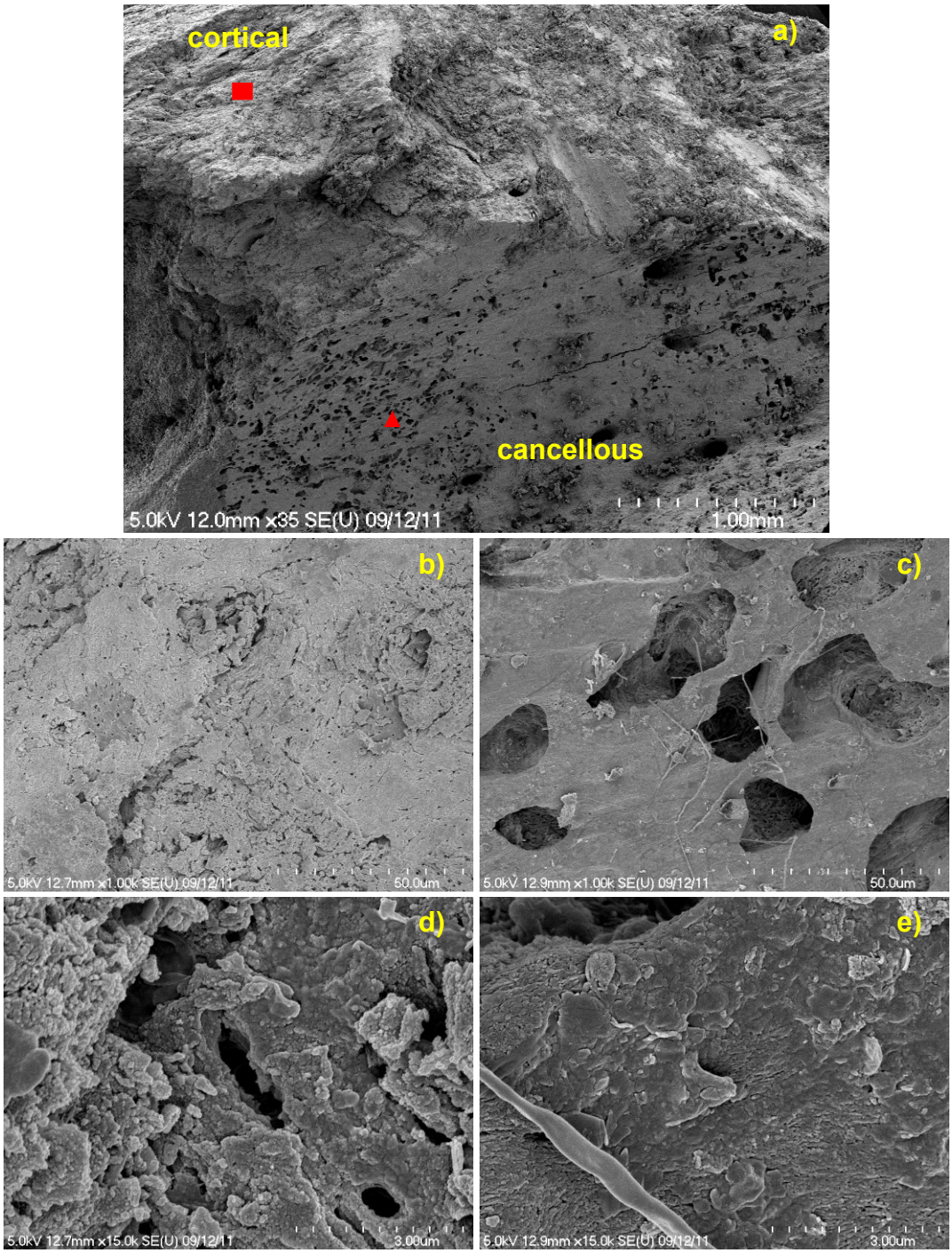

Figure 6-8: SEM images showing cortical bone (b and d) and cancellous bone (c and e). a) shows a bone cross section at low magnification with a scale bar of 1 mm. b) shows cortical bone with a scale bar of 50 mm. c) shows cancellous bone with noticeable mineralised fibres with a scale bar of 50 mm. d) shows cortical bone with a scale bar of 3 mm. e) shows cancellous bone with a mineral fibre with a scale bar of 3 mm. ■ shows area on bone where images b) and d) were taken. ▲ shows area on bone where images c) and e) were taken.

6.2.2 Imbibition

Water and ethanol capillary absorption rate data was obtained using the standard procedure (Gummerson et al. 1980; Hall & Hoff 2012) as described in section 4.1.2 on a Medieval era disarticulated ulna bone fragment (Figures 6-9 & 6-10) approximately 85.12 mm^3 (excluding hollow) in an environmental chamber at 25^oC. The sample was subjected to water and ethanol imbibitions before and after each treatment and was oven dried between tests and treatments.

Figure 6-9: Photograph of ulna bone fragment, dating from the medieval era, used for uptake experiments. Ruler provides a scale.

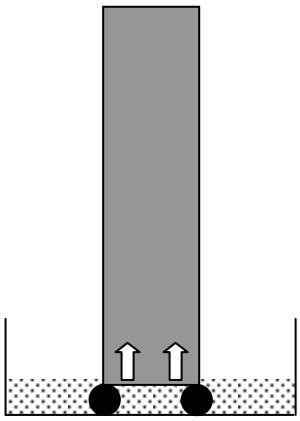

Figure 6-10: Diagram of imbibition of liquids into archaeological bone. Arrows show direction of liquid uptake.

Treatment of the bone with a HAP suspension (25g hydroxyapatite per 100 ml EtOH) was undertaken in an environmental chamber at 25°C as described in section 4.1.2. The weight gain of the sample was measured at whole $t^{1/2}$ values and at the end of the treatment uptake after 60 minutes. Samples were subject to 2 treatment cycles to identify any differences due to number of treatments.

Figure 6-11 shows the experimental water imbibition data (expressed as cumulative absorbed volume/unit inflow area, i vs. the root time, $t^{1/2}$). The calculated relevant properties of water uptake and particle absorption are given in Table 6-3. The sorptivity plot to the top of the bone is shown in Figure 6-12.

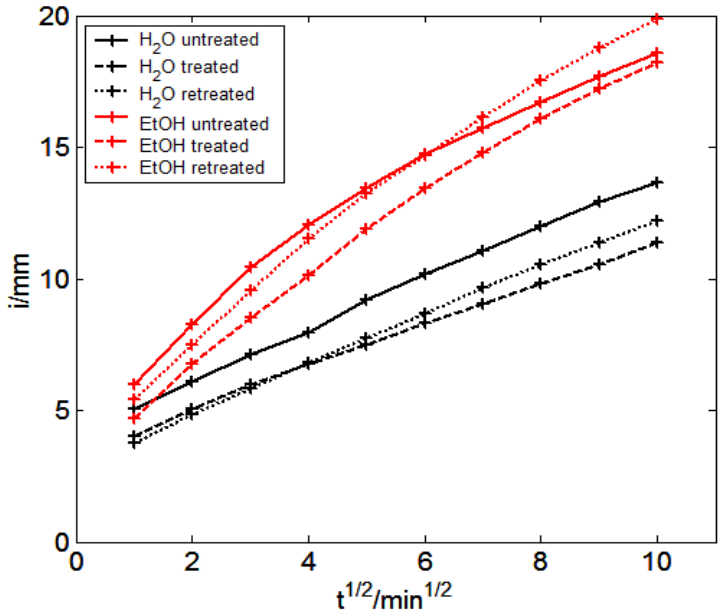

Figure 6-11: Water and ethanol sorptivity curves for archaeological bone. Graph shows untreated bone, treated bone and retreated bone. i is cumulative absorption in mm.

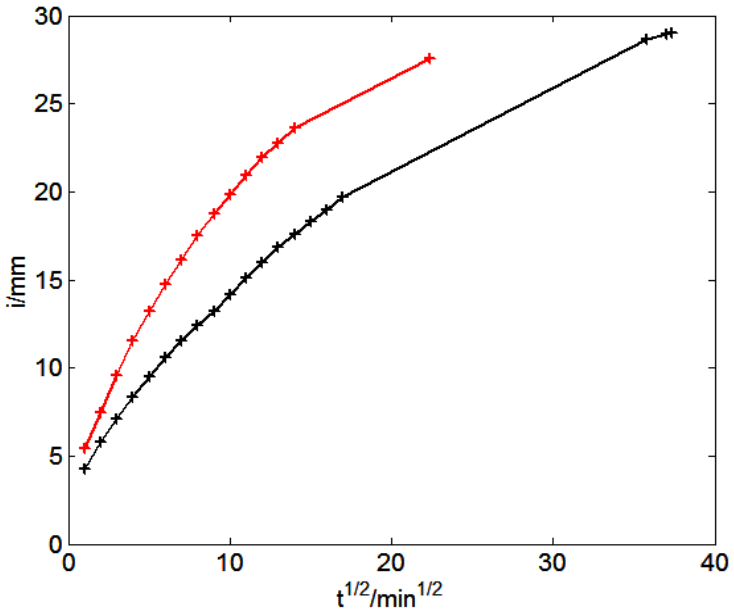

Figure 6-12: Water (black) and ethanol (red) sorptivity curves (long time) for archaeological bone. Graph shows uptake into and to the top of the retreated bone sample. i is cumulative absorption in mm.

It can be seen that there is a marked difference in the sorptivity of the untreated bone for water and ethanol with ethanol being of a higher sorptivity than water. This is unusual in solid materials, particularly in building structural materials (it could be argued that bone can be included here as it is a main building material of a vertebrate life form), however is a relatively common phenomenon in soils. Ethanol can exhibit a higher sorptivity than water in hydrophobic and intermediate materials where water uptake is repelled to a degree. In the absence of water repellence, the sorptivity of a material measured with a series of liquids should vary as (σ/η) where σ is the surface tension and η is the viscosity (Taylor et al. 2000; Hall & Hoff 2012). Figure 6-13 shows this comparison for bone. It can be seen that the water data point has a significantly lower slope to zero than that for ethanol indicating partial wetting. This is confirmed by the calculated R and θ_w values for bone which were calculated according to Appendix C and are given in Table 6-3.

Property	1st Treatment	2nd Treatment
Sw(u) (mm / min^{½})	0.9710	0.9710
Sw(t) (mm / min^{½})	0.7974	0.9389
Se(u) (mm / min^{½})	1.3526	1.3526
Se(t) (mm / min^{½})	1.5026	1.6017
Sh (mm / min^{½})	0.2235	0.2379
HORw(u) (mm)	26.49	26.49
HORw(t) (mm)	22.05	23.67
HORe(u) (mm)	35.99	35.99
HORe(t) (mm)	35.26	38.49
HORh (mm)	19.55	18.82
R(u)	2.72	2.72
R(t)	3.67	3.33
θ_w(u)	82.57	82.57
θ_w(t)	85.95	85.06
vol %	40.50	40.50
mass$_e$ (g)	1.955	1.681
mass$_a$ (g)	0.02	0.02

Table 6-3: Measured and calculated property values for treated bone after first treatment and after second treatment. u is untreated and t is treated. Sw is the water sorptivity of the bone. Se is the ethanol sorptivity of the bone. Sh is the HAP treatment sorptivity of the bone. R is the index of water repellence for the bone. θ_w is the water contact angle. HORw, and HORe (height of rise) are how far up the bone the imbibing water and ethanol respectively travels and was calculated from the imbibition test. HORh is how far up the bone the imbibing HAP treatment travels and was calculated from the imbibition test. Vol % is the expected volume % of pore space filled. Mass$_e$ is the expected mass of particles entering and was calculated from known mass of HAP entering the bone with each cycle and the expected volume percent of particles was calculated from the expected mass. Mass$_a$ is the actual mass of particles entering and was measured gravimetrically after oven drying and between treatment cycles.

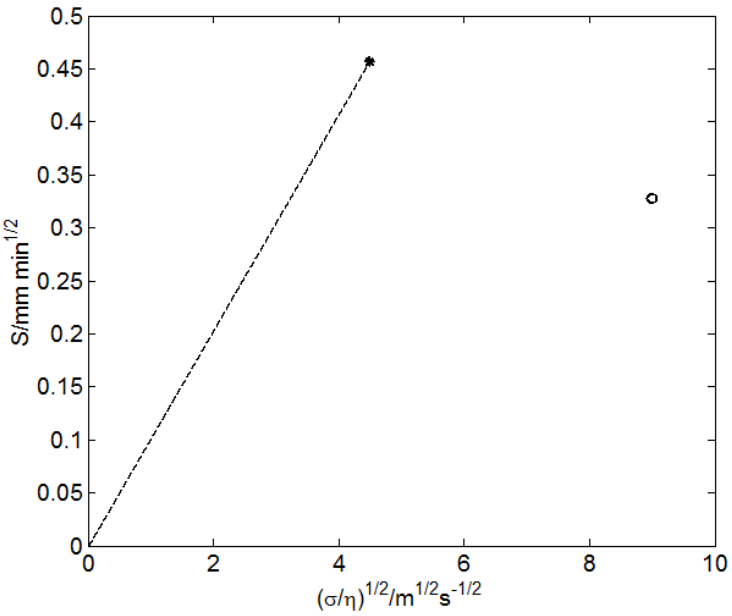

Figure 6-13: Sorptivity (S) versus $(\sigma/\eta)^{1/2}$ graphs for water (o) and ethanol (*) absorption into bone.

The change in composite water and ethanol sorptivities ranged from 2 – 13% and 8 – 14% respectively varying number of treatments as shown in Table 6-3. From mass measurements before and after treatment it became clear that fewer particles were entering the bone than expected (see Table 6-3) with roughly 4% of the overall expected mass of HAP particles actually remaining in the bone.

Imbibing to the top of the bone gives a water sorptivity of 0.6386 mm/min$^{1/2}$ and an ethanol sorptivity of 1.0949 mm/min$^{1/2}$ with a corresponding HOR of 18.9 mm and 18.1 mm respectively (Figure 6-12).

There is a difference, due to the presence of HAP particles, in the sorptivity of pure EtOH and the HAP ethanol suspension. It can be said that the presence of particles causes a reduction of approximately 83% in EtOH sorptivity by making it harder for a material to absorb the suspension via capillary suction. It can be seen that the particles avoid causing large reductions in water sorptivity.

6.2.3 Penetration Depth

SEM was used to determine the degree of penetration of HAP particles into a sample bone. Bone chips were removed from an archaeological vertebral fragment treated by dropping the treatment solution onto the piece's outer surface. Additional bone portions were obtained from an untreated clavicle section. These bone fragments were coated with a thin Ta-Au layer and imaged as described in section 3.1.8. The aim was to see if particles had managed to travel to the inner surface of the bone, which was approximately 2 mm thick. Also the bone used for uptake experiments was split to see if particles were within the bone.

Treatment of bone with HAP suspension resulted in a lightly visible white mist (particle build-up) on the surface of the bone in and slightly above the region that had been exposed to the treatment.

After treatment the presence of particles can be seen and are agglomerate clumps on both the outside (Figure 6-14a) and inside (Figure 6-14b) of the bone. The agglomerate clumps range up to a diameter of 3 μm on the outside of the bone and up to a diameter of 0.8 μm on the inside of the bone.

The bone used for uptake studies was hollow (Figure 6-9) and was split to give two semicircular lengths of bone approximately 3 mm thick. The particles penetrated through the thickness (3 mm) of the bone and were visible from the base up to approximately 6 mm height. This suggests that the particles were able to travel up through the bone matrix to a height of approximately 6 mm.

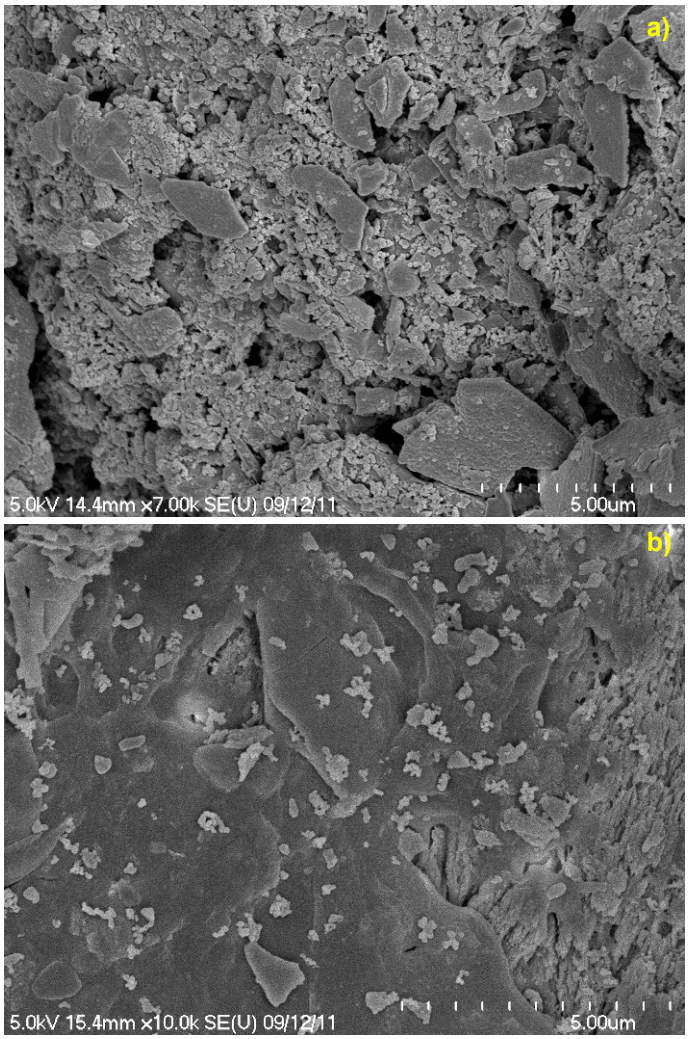

Figure 6-14: SEM images of treated bone showing: a) outside surface covered by HAP agglomerates and b) inside surface with the presence of a low concentration of HAP agglomerates. Both images have a scale bar of 5 μm.

6.2.4 Modelling

After treatment the bone could be considered a two-layer composite material into which the capillary absorption of water was analysed using Sharp Front theory (Wilson et al. 1995; Hall & Hoff 2012). Modelling was carried out as described in section 4.1.7. Known variables were the sorptivity of the composite, sorptivity of the untreated bone and the layer thickness as determined by optical microscopy. Unknowns were the sorptivity, porosity and permeability of the hydroxyapatite layer, which could be estimated from gravimetric data of particle uptake and MIP data.

Water transport properties of the HAP layer and pore filling were investigated by comparing experimental imbibition data with predicted imbibition from the Sharp Front model. Fitting the experimental data with the model confirmed that treatment particles existed as a thin layer which was known to be approximately 6.0 mm thick, reducing the porosity in the treated layer from 51.6% to 51.4%, based on the known quantity of particles in the bone after treatment (determined gravimetrically). The corresponding estimated permeability reduction was around 1%.

As shown in Figure 6-15, the upwards curve modelled at early time (blue line) before nine minutes corresponds to water flow through the particle layer. The experimental data (black circles) is shown to fit the model for a permeable particle layer of 6 mm (blue line). If the particle layer was as thick as 17 mm, the curve in the sorptivity plot would be higher as shown in the upper curve of the red line which was not observed. Alternatively if the particle layer was thinner, say 0.4 mm, the curve would be below the experimental data (green line). This confirmed that the particle layer was approximately 6 mm thick and remained permeable.

This model shows that the presence of the HAP particles in the bone cause the water sorptivity to alter such that the material becomes more wetting in this region. The decrease in sorptivity after the treated layer is due to the partial wetting nature of the bone matrix.

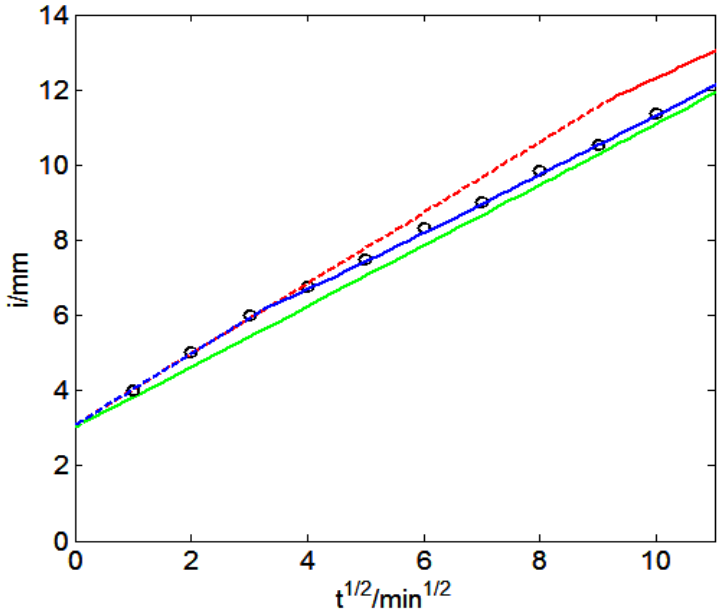

Figure 6-15: Model (red, green and blue lines) versus experimental (black circles) water uptake data for bone after treatment showing the effect of three different treatment layer thicknesses. Green dashed curve (*s* = 0.94, *K* = 0.0012, f = 0.511, L = 0.4 mm) is uptake through A, green solid curve (*s* = 0.81, *K* = 0.0012, f = 0.516) is uptake through B. Blue dashed curve (*s* = 0.94, *K* = 0.0012, f = 0.511, L = 6 mm) is uptake through A, blue solid curve (*s* = 0.81, *K* = 0.0012, f = 0.516) is uptake through B. Red dashed curve (*s* = 0.94, *K* = 0.0012, f = 0.511, L = 17 mm) is uptake through A, red solid curve (*s* = 0.81, *K* = 0.0012, f = 0.516) is uptake through B.

6.2.5 Strength Testing

Bone samples were compression tested using an Instron 4505 universal test machine. A force was applied to each sample to generate 0.2 mm per minute crosshead speed whilst the load and crosshead displacement were recorded. The Instron instrument was operated in my presence by Dr Tim Stratford. Untreated blank reference samples and treated samples (five of each sample type) for tests both parallel and perpendicular to the long axis of the bone (Figure 6-16) were studied to gain mean and standard deviations in the results for each sample set. The long axis of the bone runs in the direction along the bone fibres (Figure 6-17).

Two bones were used here. Both (disarticulated tibia and ulna fragments) were cut into small squares approximately 10 mm x 10 mm by bone thickness (approximately 5 mm). Some of these samples were then were exposed to ten

treatment cycles of HAP suspension (25 g hydroxyapatite per 1 litre of ethanol). This was applied by dripping the solution from a pipette onto the bone and allowing drying before the next application.

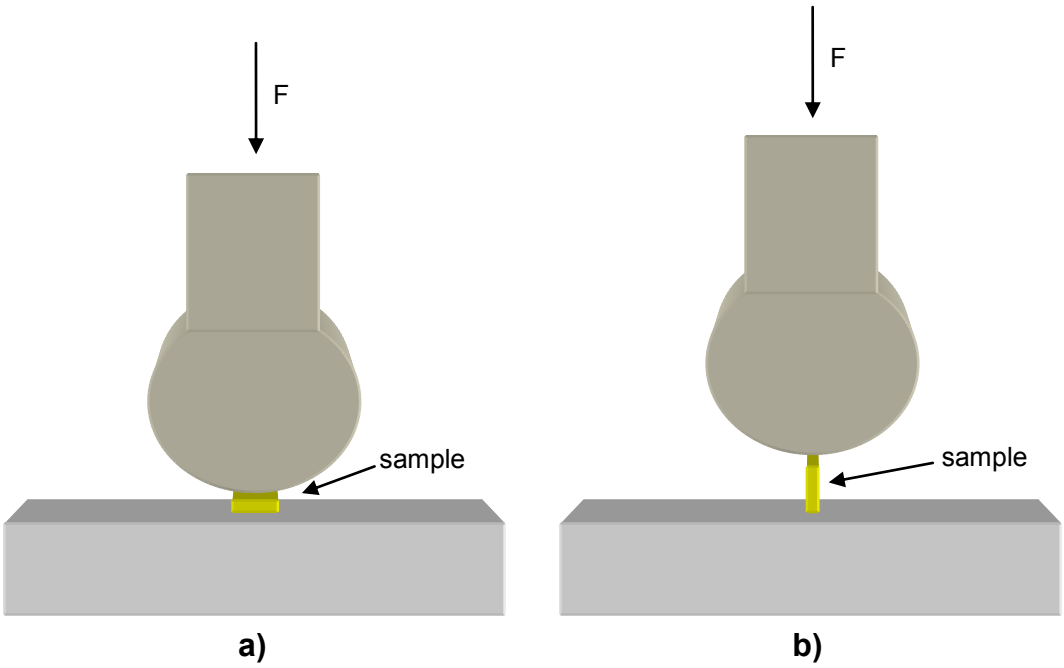

Figure 6-16: Diagram showing orientation of bone for compression strength tests. a) perpendicular to the long axis of the bone and b) parallel to the long axis of the bone. F is force applied and arrow shows directionality of force.

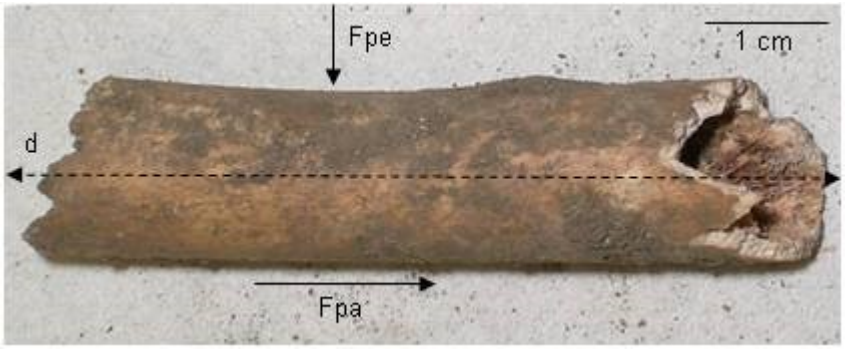

Figure 6-17: Diagram showing directionality of bone. d is direction of bone (long axis). Fpa is direction of force applied parallel to d. Fpe is direction of force applied perpendicular to d.

A set of typical graphs resulting from testing are shown in Figure 6-18. There does not appear to be a very significant difference between the three treated and untreated samples when including the standard deviation. As can be seen in Figures 6-19 and 6-20 the error bars of both the untreated and treated samples overlap for both orientations of testing.

As would be expected the required force applied to instigate failure parallel to the direction of the bone is greater than that required to induce failure perpendicular to the bone direction. It can be seen from the results of the tibia bone in Figures 6-19 and 6-20 that this bone appears to be ten times stronger along its direction than perpendicular to its primary growth axis.

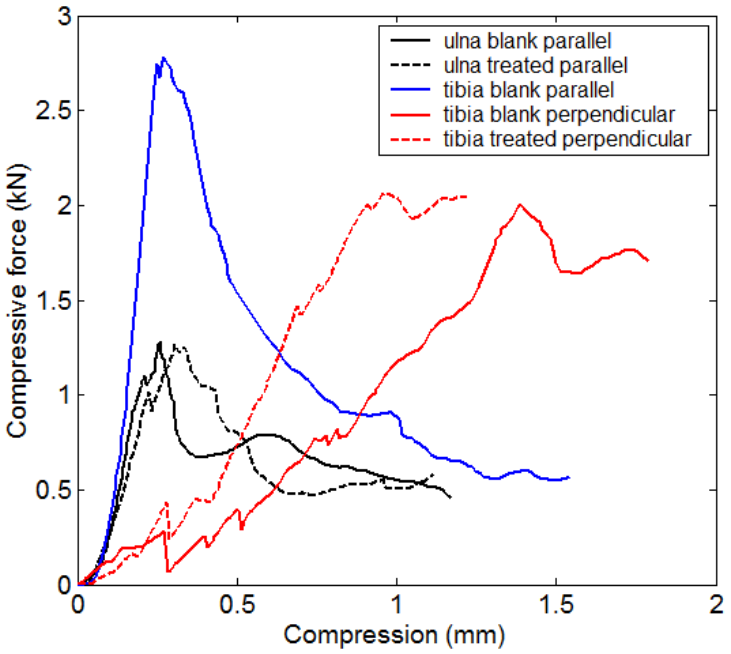

Figure 6-18: Plot of compressive force versus displacement for bone samples.

The failure point of bone tested perpendicular to the long axis can be seen in Figure 6-18 and is the point where the curve reaches a maximum then experiences an almost completely vertical drop. After this the curve again begins to increase however this is due to the bone having nowhere to go as the load continues to be

applied. A similar behavior is exhibited in tests parallel to the long axis. This occurs as once the failure point has been reached the bone did not simply split in half and collapse but instead compacted as cracks formed and material began flaking and falling away from the bone.

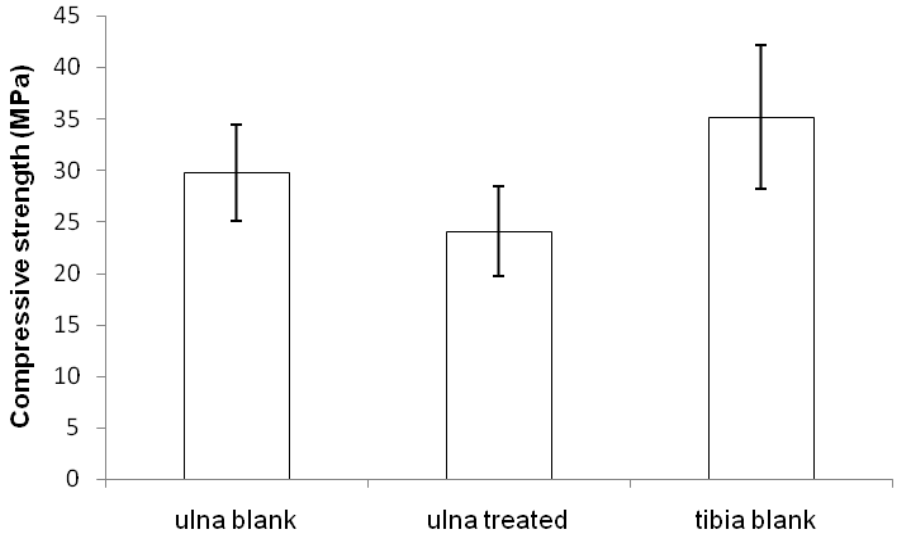

Figure 6-19: Compressive strength of untreated and treated bone parallel to long axis.

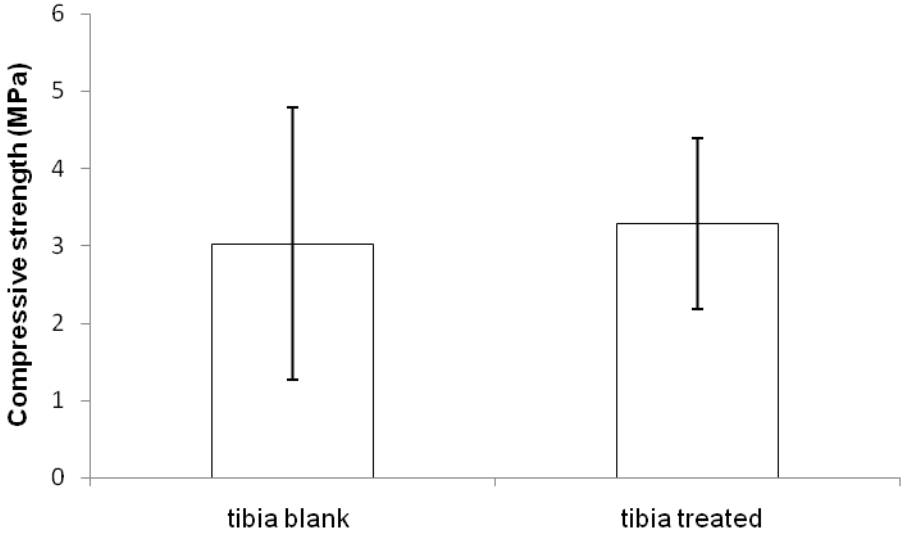

Figure 6-20: Compressive strength of untreated and treated bone perpendicular to long axis.

The strength of the bone according to its bulk density (Table 6-4) was found to be in rough agreement with data reported by Turner-Walker et al. (1995) for poorly preserved archaeological bone tested perpendicular to the long axis.

Bone	Treatment	Load Direction	Strength MPa	Strength s.d.	Bone Density g cm^{-3}	Porosity %
Ulna	u	parallel	29.8	4.7	1.1	48.5
Ulna	t	parallel	24.1	4.4	1.1	48.5
Tibia	u	parallel	35.1	7.0	1.4	54.7
Tibia	u	perpendicular	3.0	1.8	1.4	54.7
Tibia	t	perpendicular	3.3	1.1	1.4	54.7

Table 6-4: Bone compressive strength data. u is untreated and t is treated. All values are averaged.

As all differences between untreated and treated samples are within error values it is not possible to definitively state that the treatment was or was not beneficial. It can be said that these results tentatively give an indication that there may be a positive effect on strength perpendicular to the long axis as can be seen in Figure 6-18. There is also the suggestion that on average the strength parallel to the long axis is slightly decreased but this could be due to natural variation.

6.2.6 Discussion

Bone is a partially wetting substance wherein ethanol exhibits greater sorptivity than water due to a moderate calculated water contact angle of between 82.57^{o} and 85.95^{o} with HAP treatment. This is supported by the calculated R which is between 2.72 and 3.67. This indicates that the material exhibits some water repellency as an R of 1 represents a material that is completely wetting whilst an R of greater than 1.95 is strongly indicative of a material with some level of hydrophobicity (Hallett 2001; Hallett 2004). As intermediately wet substances are of a mixed nature where both hydrophobicity and hydrophilicity occur with neither being overly dominant this indication of bone being an intermediately hydrophobic material fits with the contact angle and sorptivity data.

Whilst it is unusual to encounter solid material which exhibits a level of hydrophobicity resulting in a higher ethanol sorptivity than that for water this behavior is known in some limestones and is a common phenomenon in soils (Taylor et al. 2000; Ioannou et al. 2004; Fuentes et al. 2010; Hall & Hoff 2012). The soils studied by Fuentes et al. (2010) are a good example of a comparison between soil and bone as it can be seen that bone is very similar over the Sw, Se, R and θ_w properties. Using the sorptivity values reported Fuentes et al. (2010) for soil aggregates of cryptocarya alba at a depth of < 10 cm it has been calculated here that the soil has a theoretical θ_w of 85.25^{o}. This is very similar to the θ_w range of bone stated above and signifies the soil is an intermediate wet material as is bone. The water and ethanol sorptivity values of the soil are themselves very similar to those of bone as is the porosity. Soil commonly contains biological and organic material which can be responsible for its degree of hydrophobicity. As bone also contains organic and biological material it is reasonable to postulate the existence of such material either within the structure or on the surface bears some responsibility for the intermediate wetting nature of bone. This is supported by the findings of Taylor et al. (2000) and Ioannou et al. (2004) on some limestones.

HAP particles that are of the size range to penetrate the pore structure of the bone travel up to 6 mm into the bone. This penetration depth is reached due to the high sorptivity of ethanol in which the particles are dispersed. Despite the presence of the particles decreasing the ethanol sorptivity by approximately 83 % the solution

still travels a good height up the bone over the treatment time with the particles reaching just over 18 mm. The internal depth of treatment is confirmed by modelling.

Whilst the bone internal particle location can be seen and so the low concentration in the region can be noted, there is in contrast a high concentration of particles on the bone surface. This is due to treatment surface build up in part due to the comparatively slow treatment uptake compared with pure ethanol. This effect could be minimised by the use of a HAP suspension where all the particles were consistently below 1 μm.

The presence of a low concentration of HAP particles 6 mm within the bone pore structure does not have a definitive effect on bone compressive strength. All strength values are within the s.d. margins for the tests, however the trend over the samples tentatively suggests that the treatment *may* lead to a marginal increase in compressive strength perpendicular to the long axis of the bone. Ideally a further study on a very large scale (hundreds of samples) where only particles up to 600 nm were in the treatment suspension should be able to give a definitive comment on this. For such a test all samples should be as near identical as possible in terms of volume, crushing area, thickness and bulk density to minimize effects of natural variation. Also testing samples treated in different ways, with different treatment concentrations and number of treatments could also have a greater effect on the bone strength.

6.3 Conclusions

HAP particles were synthesised with a size range excluding large agglomerates of 0.02 – 0.6 μm (20 – 600 nm) and including large agglomerates of 0.02 – 15 μm (20 – 15000 nm). The particles have an amorphous morphology and exist in a web-like network structure which forms agglomerates. These HAP particles were suspended in ethanol at a concentration of 25 g per liter and were applied by way of uptake (imbibition experiments) and dropping (strength experiments) to archaeological bone.

The cortical and cancellous bone was found to be similar in structure with the lamellae running along the long axis of the bone. Archaeological bone was found to be an intermediately wet material with a theoretical θ_w of 82.6°, average bulk density 1280 ± 195 kg m^{-3}, 52 ± 4 % average porosity and 1 % air trapping under vacuum.

Capillary uptake of HAP ethanol suspension was found to result in a particle penetration depth of 6 mm. The particles were found to form a permeable layer reducing the permeability by an estimated 1 % with a reduction in porosity from 52% to 51%. Ethanol sorptivity of the bone was found to be greater than the water sorptivity due to the intermediate wetting nature of the bone as a consequence of the θ_w which is likely influenced by biological and organic residues on or within the bone.

There are no existing studies investigating water versus ethanol sorptivity in published literature, nor is there mention of water contact angle for bone capillary rise. From modelling it can be seen that the introduction of HAP particles causes the material to become more wetting in comparison with the partially wetting pure bone. Due to this the studies in this chapter are novel and provide valuable information particularly to those in the conservation community who deal with archaeological bone of any kind as these findings can be applied equally to bone artefacts and to burial remains.

Compressive strength tests comparing untreated and treated bone tentatively suggest the possibility of a beneficial effect on bone strength perpendicular to the long axis but are inconclusive due to variability of the bone causing all changes in strength to be within standard deviation. Because of this, at this point a HAP

suspension cannot be recommended as a new conservation treatment. As mentioned previously there are indications that such a treatment may have a consolidating effect on bone strength but a long study on hundreds of samples would be required to be definitive.

Chapter 7:
Conclusions and Opportunities for Future Work

The general aim of this work was to use nano and fine particle suspension consolidants to investigate treatment location and effects on water transport within limestone, AAC and archaeological bone.

The building materials selected for this study were two different types of limestone, Portland and Lincoln, and a synthetic concrete material, AAC. Quarried stones of both limestone types were used to compare particle location and treatment effects between the limestone types and modalities. Weathered and unweathered medieval Lincoln stones were studied to determine differences in particle location and treatment effects between such types of stone. It was possible to compare the data for quarried and medieval Lincoln stones to determine differences caused by stone weathering. The investigation of particle location and effects on AAC in comparison with the limestone data was able to determine whether pore size range or the nature of the material structure was the determining factor for particle penetration depth. A commercial nanolime suspension was used in these investigations as this is what conservators use in the field. Wet synthesis of nano and fine, stable particles was challenging but it was also possible to tailor particle size and stability by altering parent reagent composition.

As a nanolime treatment is chemically compatible with limestone the viability of a similar like for like chemically compatible treatment for archaeological bone was considered for the first time. Since archaeological bone is composed of hydroxyapatite a treatment suspension of hydroxyapatite particles was investigated. This was a completely novel line of investigation.

Overall this work is of interest to the wider community as it has focused on introducing nanoparticles to chemically different environments. Nanolimes have been absorbed into limestone where the particles and the material are chemically alike. The same is true for the application of HAP to bone. AAC (tobermorite) is a chemically different environment to the introduced nanolime.

It should be recognised that this was a fundamental study and whilst the findings of the work on limestone would be useful knowledge for stone conservators this was not a field conservation study. Also, whilst the work completed herein on a HAP consolidant for archaeological bone is original, it is a starting point and much

more research will be needed before the suitability of a HAP consolidant is definitively determined. If a HAP consolidant could be proven to be effective then further development would be required before any such treatment could be used in the field.

7.1 $Ca(OH)_2$ Particle Synthesis and Sizing Conclusions

It was found that non-classical effects occur in the calcium hydroxide system synthesised in this study. Altering reaction conditions can have a significant effect on the resulting particle size and distribution obtained via the wet synthesis method. Reagent concentration resulting in an alteration in pH within the reaction vessel was found to be the most significant factor in the resulting particle size distribution. Due to particle aggregation it is difficult to obtain stable nano and fine particles. Obtaining true nanoparticles alone appears improbable as even the commercial product consists of a majority (approximately 70 %) of particles that should truly be defined as fine particles according to Potocnik (2011) as the diameter is usually greater than 100 nm.

The Mastersizer instrument has been used in conjunction with the nanoparticle tracking analysis technique to characterize the complete particle size distribution of this particle system for the first time. The nanoparticle tracking analysis and laser diffraction techniques are comparable in the region below 1 μm. Nanoparticle tracking analysis is far more accurate and sensitive than laser diffraction and can also measure particles to smaller sizes so it should be expected that nanoparticle tracking analysis can realize the particle size distribution with greater definition. Due to this a clear understanding of the entire particle size distribution can be obtained by using both techniques.

Both the wet synthesised $Ca(OH)_2$ and commercial CaLoSiL have hexagonal morphology and are present in both nano and fine particles. Some of the particles are aggregates not single particles. Natural carbonation in air of synthesised $Ca(OH)_2$ particles resulted in a dagger morphology whilst fast carbonation of CaLoSiL with DiLoCarb resulted in an anhedral structure. Treatment of a material with nanolime followed by rapid carbonation could allow greater surface contact between particles, and between the particles and the pore structure of the material. This could encourage the particles to remain in the consolidated region.

A study of carbonation of CaLoSiL in real time through particle size analysis was attempted but was inconclusive because the DiLoCarb/water mixture also contained particles which could not be distinguished from the $Ca(OH)_2$ particles.

7.2 Material, Treatment and Particle Transport Conclusions

This study, for the first time, has determined that Lincoln stone has bulk density values of 2283 kg/m^3 and 2151 kg/m^3 and a porosity percentage of 14% and 16% for quarried and medieval stone respectively.

Bone was found, for the first time, to be broadly bimodal with no macroporosity and possess a higher degree of fine microporosity than even AAC (see Figure 2-2). In this study archaeological bone, for the first time, was found to have an average bulk density of 1279 ± 195 kg m^{-3}, 51 ± 4 % average porosity and 1 % air trapping under vacuum.

By determining the above properties of these materials, this study adds to the knowledge of these materials and the understanding of their behavior.

This is the first time a modified sharp front model has been applied to understand water transport through a composite material. Here, also for the first time, we look at composites where particles have been added into a region of a material to give a composite which is comprised of material A (particles plus material B) and material B. Such composite materials can be termed [particle-material]-material composites.

For Lincoln stone it has been found, for the first time, by way of imbibition investigations that the stone exhibits decreasing wettability with weathering. It is possible that organic and biological residues build up on the stone with weathering and this causes the decrease in wettability. This is important for the conservation of Lincoln Cathedral as it suggests that areas of replaced stonework will absorb more rain water than areas of original stonework and that the water will travel further within the new stone. However, over time the wettability of the new stone will decrease. These findings would also suggest that the wettability of all limestones exposed to the environment will decrease over time. This is relevant for all limestone buildings, structures and artefacts where weathering occurs, particularly if some of the original stone has or will be replaced by fresh quarried stone.

Capillary uptake of a commercial nanolime treatment (CaLoSiL) on all limestone samples showed that thin penetration was achieved with small decreases in

estimated material permeability and porosity. It was also seen that the layer remained permeable and that the particles do not appear to block the stone pores. As seen from Lincoln stone of all types it was found that the weathered medieval stone absorbed over 95% of the expected mass of particles absorbed whilst the unweathered medieval and fresh quarried stones were able to absorb only 51% and 47% respectively. This confirms that the more damaged the stone the greater the mass percent of particles absorbed compared with the expected mass of particles absorbed.

Capillary uptake of CaLoSiL in AAC showed that deep penetration of the treatment was possible. AAC, as previously stated, has very small pores, smaller than the limestones', which are connected to large aeration pores. Despite AAC having greater microporosity than both limestones, resulting in less of the structure being accessible to the nanolime particles, it still absorbs by far the greatest concentration of particles which travel to much greater lengths within the material. Therefore it can be stated that the difference in penetration depth between limestone and AAC is due to the nature and not the modality, pore size range of the materials or quantity of microporosity.

Due to these results it is reasonable to suggest that a porous material, regardless of its pore size distribution, will absorb a higher quantity of particles to a greater depth if it has a well defined open pore network structure comparable to AAC. If however the materials structure is more comparable to that of the limestones then a low level of penetration and particle absorption should be expected when treating with nanolime suspension via capillary suction.

Whilst pore blocking and obstruction by the nanolime treatment is not an issue in either limestones it is a significant factor in AAC. This is due to the much greater penetration depth and mass of particles being absorbed by AAC in comparison with all limestone types investigated here. In AAC, pores too small to accept nanolime particles may be blocked, whilst particle build-up in matrix areas accessible to the particles causes the ink bottle effect. It was found that pore blocking is the most dominantly apparent of the two effects.

Strength testing of Portland limestone by a drilling resistance measurement system and scratch tester did not show any difference between the treated and

untreated Portland samples due to the very small penetration depth of less than 0.4 mm. Strength testing by an Instron has shown that a nanolime based Repair Mortar can be used as an adhesive only for very small areas due to the initially weak bond. This also means that if this Repair Mortar was used on an object and an error in placement was made, the bond could easily be broken allowing the mistake to be corrected.

Archaeological bone has, for the first time, also been shown to be somewhat hydrophobic by imbibition experiments. Again this is is likely influenced by biological and organic residues on or within the bone. This could potentially be helpful knowledge for a wide range of fields working with bone.

Capillary uptake of HAP ethanol suspension by archaeological bone was found to result in a particle penetration depth of approximately 6 mm. The layer was permeable and resulted in a minor porosity and permeability reduction. It was found that the HAP treatment resulted in a small increase in bone wettability, possibly suggesting that increased HAP surface area permits more wetting.

Instron compressive strength tests comparing untreated and treated bone tentatively suggest the possibility of a beneficial effect on bone strength perpendicular to the long axis but are inconclusive due to variability of the bone causing all changes in strength to be within standard deviation. This was a novel study and it must be stressed that this could provide a starting point for further investigations.

This study indicates that it would perhaps be beneficial to do further work on HAP alcohol suspensions as treatments for archaeological bone. Whilst in this study it was not possible to produce a stable suspension of nano or very fine particles, if a stable suspension were able to be obtained its use could be thoroughly investigated on archaeological bone. If real benefits of the treatment and its compatibility with scientific tests could conclusively be proven and the irreversibility could, in certain circumstances, be accepted then it is possible that this could form a new compatible conservation treatment. However, at this point in time a HAP suspension cannot be recommended as a new conservation treatment as the results of this initial study are

inconclusive and a long study on hundreds of samples would be required to be definitive.

7.3 Relevance to Conservators

It has been found that the structure of a material is a more determining factor for treatment penetration than the pore size range or modality of the material, providing the pore size range and treatment particle size are compatible.

Lincoln stone is a unimodal coarse bioclastic oolitic grainstone and has a pore size range of 0.01 – 10 μm. There is a significant difference in the water transport properties of medieval weathered and medieval unweathered Lincoln stone, where weathered stone possesses a clear degree of hydrophobicity. It is possible that as limestone ages and weathers it becomes less wetting, possibly due to organic residue on the surface.

The application of a nanolime treatment to both Portland and Lincoln limestones by way of capillary uptake results in only a very small penetration depth (approximately 0.4 mm) of treatment being achieved. Treatment build-up on the surface of a material occurs more rapidly with higher concentration treatments (e.g. surface build-up occurs after 1 treatment with E50 compared to after 5 treatments with E5). The height of the treatment build-up on the surface of the stone suggests that the treatment can travel further along the outside surface of the stone than the inside of the stone. This suggests that it is possible that the internal structure of the stone inhibits particle transport of the treatment.

The concentration of the penetrated treatment gradually decreases as treatment depth increases. This suggests that the change in properties from the treated layer to the untreated material will be more gradual in cases of deep penetration compared to very small penetration depths.

It was found that the archaeological bone used in this study was bimodal with two pore size ranges of 0.004 – 0.15 μm and 0.15 – 5 μm. Archaeological bone has a degree of hydrophobicity as the sorptivity of water is less than that of ethanol. Due to this archaeological bone is an intermediate wetting material. This means that ethanol will penetrate more quickly into the bone than water.

A HAP treatment can penetrate to a depth of 6 mm, under the conditions and uptake time limit of this study, by capillary uptake on archaeological bone. Treatment build up on the bone surface can be seen.

7.4 Opportunities for Future Work

Possible opportunities for future work based on what has been learned from this study are mentioned herein.

7.4.1 Particle Synthesis and Sizing

Future research could be carried out on $Ca(OH)_2$ and HAP particle synthesis and stability. An attempt to filter out the larger agglomerated particles with a molecular sieve (could prove challenging for $Ca(OH)_2$ due to the difficulty in obtaining good long term stability of the particles in suspension) and to try to obtain pure product with the aid of ion exchange resin would be clear next steps. Other synthesis methods could also be investigated along similar lines as in this study. Understanding and predicting colloid stability in concentrated electrolyte solutions is a broad and important topic but still poorly understood. Stability theory is now developing that can predict the behaviour of these systems (Parsons et al. 2011) which in conjunction with good experimental data, could lead to smaller particles, able to move further through a porous network. Studying the carbonation of $Ca(OH)_2$ in real time by nanoparticle tracking analysis might be possible if fluorescent doping was used to tag the carbonising agent.

7.4.2 Application to Limestone

Whilst nanolime (CaLoSiL) absorption by Portland and Lincoln limestones via capillary uptake only resulted in a very thin layer of particles entering the stones other treatment methods could be investigated to determine if it is possible to obtain greater penetration depth in these stones by a different means of treatment (e.g. injection, drip feed etc.). If greater penetration depths in these stones are possible testing of material strength could then be undertaken, possibly by way of a drilling resistance measurement system, to determine if the treatment had an effect on the surface strength of the stone. Testing CaLoSiL suspended in other alcohols, such as isopropanol, could possibly result in greater particle penetration depths as is suggested by IBZ-Salzchemie Gmbh & Co.KG (2013).

7.4.3 Application to Archaeological Bone

Compressive strength tests on HAP treated archaeological bone were inconclusive in terms of whether or not the treatment affected the material strength due to all results being within standard deviation for the samples. Testing a far higher number of samples (hundreds) and ensuring that all samples are as near identical as possible in terms of volume, crushing area, thickness and bulk density could give a clearer overall result. Testing samples treated in different ways, with different treatment concentrations and number of treatments could also have a greater effect on the bone strength. Also using a HAP treatment where all the particles are stable and below 1 μm could be investigated.

If the above is achieved and strength effects were definitively identified then the effects of the treatment on scientific tests that archaeological remains and bone artefacts may be subjected to (such as stable isotope analysis, DNA testing, etc.) must be investigated. If all the above can be achieved and true benefits of treatment conclusively proven then this could form a new completely compatible conservation treatment after significant development before standard use in the field.

There is also room for the development of another method of testing surface friability that can complement the tape test.

References

Abdullah, S.; Wendy-Yeo, W.Y.; Hosseinkhani, H.; Hosseinkhani, M.; Masrawa, E.; Ramasamy, R.; Rosli, R.; Rahman, S.A.; Domb, A.J.; "Gene Transfer into the Lung by Nanoparticle Dextran-Spermine/Plasmid DNA Complexes." *Journal of Biomedicine and Biotechnology*. (2010) doi:10.1155/2010/284840.

Adams, A.E.; Mackenzie, W.S.; Guilford, C.; *Atlas of Sedimentary Rocks Under the Microscope*, Prentice Hall, 1st edition, 1984.

Adan, O.; Brocken, H.; Carmeliet, J.; Hens, H.; Roels, S.; Hagentoft, C.-E.; "Determination of Liquid Water Transfer Properties of Porous Building Materials and Development of Numerical Assessment Methods: Introduction to the EC HAMSTAD project." *Journal of Thermal Envelope and Building Science*. 27 (2004) 253 – 260.

Al-Garni, M.T.; Al-Anazi, B.D.; "Investigation of Wettability Effects on Capillary Pressure, and Irreducible Saturation for Saudi Crude Oil, Using Rock Centrifuge." *Oil and Gas Business*. (2008) 1 – 17.

Ambrosi, M.; Dei, L.; Giorgi, R.; Neto, C.; Baglioni, P.; "Colloidal Particles of $Ca(OH)_2$: Properties and Applications to Restoration of Frescoes." *Langmuir*. 17 (2001) 4251 – 4255.

Anderson,W.G., "Wettability Literature Survey – Part 2: Wettability Measurement." *Journal of Petroleum Technology*. 38 (1986) 1246 – 1262.

Appelbaum, B. "Criteria for Treatment: Reversibility." *Journal of the American Institute for Conservation*. 26 (1987) 65 – 73.

Askew, P. "Fungal and Algal Growth on Stone and its Remediation." A presentation in *Stonecore: Nano Materials for Stone and Mortar Strengthening Conference,* Peterborough, United Kingdom, 7-8 June 2011.

Atkin, P. Team Leader of Masonry and Conservation, Works Department, Lincoln Cathedral. *Personal Communication*, 29/2/12.

Atkins, P.; *The Elements of Physical Chemistry*, 3rd edition, Oxford University Press, 2001.

Atkins, P.; de Paula, J.; *Physical Chemistry*, 7th edition, Oxford University Press, 2002.

Baek, I.; Pitt Jr, W.W.; "Colloid-Facilitated Radionuclide Transport in Fractured Porous Rock." *Waste Management*. 16 (1996) 313 – 325.

Baglioni, P.; Dei, L.; Pique, F.; Sarti, G.; Ferroni, E.; "New Autogenous Lime-Based Grouts Used in the Conservation of Lime-Based Wall Paintings." *Studies in Conservation*. 42 (1997) 43 – 54.

Baglioni, P.; Giorgi, R.; "Soft and Hard Nanomaterials for Restoration and Conservation of Cultural Heritage." *Soft Matter*. 2 (2006) 293 – 303.

Baglioni, P.; Giorgi, R.; Chelazzi, D.; "Conservation of Acid Waterlogged Shipwrecks: Nanotechnologies for de-acidification." *Journal of Applied Physics A*. 83 (2006) 567 – 571.

Baglioni, P.; Giorgi, R.; Dei, L.; "Soft Condensed Matter for the Conservation of Cultural Heritage." *Comptes Rendus Chimie*. 12 (2009) 61 – 69.

Baker, B.J.; Dupras, T.L.; Tocheri, M.W.; Wheeler, S.; *The Osteology of Infants and Children*. 1st edition. Texas A&M University Press, Number Twelve: Texas A&M University Anthropology Series, 2005.

Bard, K. *An Introduction to the Archaeology of Ancient Egypt*. Wiley-Blackwell, 2007.

Beck-Coon, R.J.; Newton, C.W.; Kafrawy, A.H.; "An In Vivo Study of the Use of a Nonresorbable Ceramic Hydroxyapatite as an Alloplastic Graft Material in Periapical Surgery." *Oral Surgery Oral Medicine Oral Pathology*. 71, (1991) 483 – 488.

Bisby, L.A.; Take, W.A.; "Strain Localizations in FRP Confined Concrete: New Insights." *Proceedings of the Institute of Civil Engineers – Structures and Buildings*. 162 (2009) 301 – 309.

Bradley, S. "Preventive Conservation Research and Practice at the British Museum." *Journal of the American Institute for Conservation*. 44, (2005) 159 – 173.

British Museum [Online] Available from: http://www.britishmuseum.org/. [Accessed: 29/3/12].

British Museum, *Fragment of the beard of the Great Sphinx*, [Online] Available from: http://www.britishmuseum.org/explore/highlights/highlight_objects/aes/f/fragment_of_the_beard_of_the_g.aspx. [Accessed: 6/8/11].

BSI, British Standards Institution. PAS 71:2011.

Caiger-Smith. A. *Lustre Pottery: Technique, Tradition and Innovation in Islam and the Western World*. 1st edition. Faber and Faber 1985.

Calvaro, C.; Gopal, R.; "The Crystal Structure of Whitlockite from the Palermo Quarry." *American Mineralogist*. 60 (1975) 120 – 133.

Campbell, A.; Hamilton, A.; Stratford, T.; Modestou, S.; Ioannou, I.; "Calcium hydroxide nanoparticles for limestone conservation: imbibitions and adhesion." In Proceedings of Symposium 2011 Adhesives and Consolidants for Conservation: Research and Applications, Canadian Conservation Institute, Ottawa, Canada, 2011.

Carr, B.; Malloy, A.; "Nanoparticle Tracking Analysis – The Halo™ System." *Particle and Particle Systems Characterization*. 23 (2006) 197 – 204.

Carr, B. “Nanoparticle Tracking Analysis: Complementing DLS for more Complex Dispersions.” *NanoSight Webinar*, 2010.

CCI. *Preserving Aboriginal Heritage: Technical and Traditional Approaches*. Proceedings of Symposium 2007. Canadian Conservation Institute Press, 2008.

Child, A.M. “Microbial Taphonomy of Archaeological Bone.” *Studies in Conservation*. 40 (1995) 19 – 30.

Cooper, J.J.; Hunt, J.A.; “The Significance of Zeta Potential in Osteogenesis.” *Fortoss*, Biocomposites Ltd. 2005

Correia, R.N.; Magalhaes, M.C.F.; Marques, P.A.A.P.; Senos, A.M.R.; “Wet Synthesis and Characterization of Modified Hydroxyapatite Powders.” *Journal of Materials Science: Materials in Medicine*. 7 (1996) 501 – 505.

Cumbie, D.H.; McKay, L.D; “Influence of Diameter on Particle Transport in a Fractured Shale Saprolite.” *Journal of Contaminant Hydrology*. 37 (1999) 1390 – 157.

Czachor, H.; Flis-Bujak, M.; Kafarski, M.; Krol, A.; “Wetting Angle and Water Sorptivity in Mineral Soils.” *Soil and Water Research*. 3 (2008) Special Issue 1, S52 – S57.

Daday, K.A.; Janecek, T.; Klaus, A.; “Dry-Bulk Density: Its Use and Determination.” In Proceedings of the *Ocean Drilling Program, Scientific Results*, Volume 126, by Taylor, B., Fujioka, K., et.al. (1992) 551 – 554.

Daniele, V.; Taglieri, G.; “Nanolime suspensions applied on natural lithotypes: The influence of concentration and residual water content on carbonatation process and on treatment effectiveness.” *Journal of Cultural Heritage*. 11 (2010) 102 – 106.

D'Armada, P.; Hirst, E.; “Nano-lime for the consolidation of plaster and stone.” *Journal of Architectural Conservation*. 18 (2012) 63 – 79.

DCMS. *Guidance for the Care of Human Remains in Museums*. Department for Culture, Media and Sport, 2005.

Dei, L.; Salvadori, B.; “Synthesis of $Ca(OH)_2$ Nanoparticles from Diols.” *Langmuir*. 17 (2001) 2371 – 2374.

Dei, L.; Nanni, A.; “$Ca(OH)_2$ Nanoparticles from W/O Microemulsions.” *Langmuir*. 19 (2003) 933 – 938.

Dei, L.; Salvadori, B.; Capitani, G-C.; Mellini, M.; “A Novel Method to Prepare Inorganic Water-Soluble Nanocrystals.” *Journal of Colloid and Interface Science*. 298 (2006) 487 – 490.

Dei, L.; Salvadori, B.; "Nanotechnology in Cultural Heritage Conservation: Nanometric Slaked Lime Saves Architectonic and Artistic Surfaces from Decay." *Journal of Cultural Heritage*. 7 (2006) 110 – 115.

Dimitrijević, D. "Nanotechnology: the Need for the Implementation of the Precautionary Approach Beyond the EU." In *Understanding and Managing Threats to the Environment in South* 205 *Eastern Europe*, NATO Science for Peace and Security Series C: Environmental Security, G. Meško et al. (eds.), Springer Science + Business Media B.V. (2011) 205 – 224.

Dobrzyńska-Musiela, M. "New Opportunities for Conservation of Mortars, Plasters and Decorative Wall Painting with the Use of Colloidal Solutions of Nano-Paricles of Calcium Hydroxide. A Case Study." A presentation in *Stonecore: Nano Materials for Stone and Mortar Strengthening Conference,* Peterborough, United Kingdom, 7-8 June 2011.

Doehne, E.; Price, C.A.; *Stone Conservation An Overview of Current Research*, 2nd edition. The Getty Conservation Institute, 2010.

Donaldson, K.; Stone, V.; Tran, C.L.; Kreyling, W.; Borm, P.J.A.; "Nanotoxicology." *Occupational and Environmental Medicine*. 61 (2004) 727 – 728.

Drdácký, M.; Slížková, Z.; Ziegenbalg, G.; "A Nano Approach to Consolidation of Degraded Historic Lime Mortars." *Journal of Nano Research*. 8 (2009) 13 – 22.

Dubelaar, C.W.; Engering, S.; van Hees, R.P.J.; Koch, R.; Lorenz, H.-G.; "Lithofacies and Petrophysical Properties of Portland Base Bed and Portland Whit Bed Limestone as Related to Durability." *HERON*. 48 (2003) 221 – 229.

Dunham, D. "Building an Egyptian Pyramid." *Archaeology*. 9 (1956) 159 – 165.

Edwards, H.G.M.; Chalmers, J.M.; *Raman Spectroscopy in Archaeology and Art History*, 1st edition, Cambridge, RSC Analytical Spectroscopy Monographs, Royal Society of Chemistry, 2005.

El Briak-Benabdeslam, H.; Ginebra, M.P.; Vert, M.; Boudeville, P.; "Wet or Dry Mechanochemical Synthesis of Calcium Phosphates? Influence of the Water Content on DCPD-CaO Reaction Kinetics." *Acta Biomaterialia*. 4 (2008) 378 – 386.

El Shafei, G.M.S.; "The Polarizing Power of Metal Cations in (Hydr)Oxides." *Journal of Colloid and Interface Science*. 182 (1996) 249 – 253.

Elakneswaran, Y.; Nawa, T.; Kurumisawa K.; "Electrokinetic Potential of Hydrated Cement in Relation to Absorption of Chlorides." *Cement and Concrete Research*. 39 (2009) 340 – 344.

Feynman, R.P. "There's Plenty of Room at the Bottom." *Journal of Microelectromechanical Systems*. 1 (1992) 60 – 66. Originally published in *Miniaturization*. Horace D. Gilbert, Ed. © Van Nostrand Reinhold.

Filipe, V.; Hawe, A.; Jiskoot, W.; "Critical Evaluation of Nanoparticle Tracking Analysis (NTA) by NanoSight for the Measurement of Nanoparticles and Protein Aggregates." *Pharmaceutical Research*. 27 (2010) 796 – 810.

Flugel, E. *Microfacies of Carbonate Rocks. Analysis, Interpretation and Application*, Springer, 1st edition, 2004.

Fuentes, J.P.; Bustamante, V.; Brown, H.; "Comparison of Soil Water Repellency and Sorptivity Between an Acacia Caven (Highly-Perturbed) and Cryptocarya Alba (Slightly-Perturbed) Dominated Ecosystem." In *19th World Congress of Soil Science, Soil Solutions for a Changing World*, Brisbane, Australia, 1 – 6 August 2010, 26 – 29.

Gbureck, U.; Probst, J.; Thull, R.; "Surface Properties of Calcium Phosphate Particles for Self Setting Bone Cements." *Biomolecular Engineering*. 19 (2002) 51 – 55.

Giorgi, R.; Dei, L.; Baglioni, P.; "A New Method for Consolidating Wall Paintings Based on Dispersions of Lime in Alcohol." *Studies in Conservation*. 45 (2000) 154 – 161.

Giorgi, R.; Dei, L.; Ceccato, M.; Schettino, C.; Baglioni, P.; "Nanotechnologies for Conservation of Cultural Heritage: Paper and Canvas Deacidification." *Langmuir*. 18 (2002) 8198 – 8203.

Giorgi, R.; Ambrosi, M.; Toccafondi, N.; Baglioni, P.; "Nanoparticles for Cultural Heritage Conservation: Calcium and Barium Hydroxide Nanoparticles for Wall Painting Conservation." *Chemistry – A European Journal*. 16 (2010) 9374 – 9382.

Gomez-Villalba, L.S.; Lopez-Arce, P.; Alvarez de Buergo, M.; Fort, R.; "Comportamiento Cristalino de Nanopartículas de Portlandita ($Ca(OH)_2$) en Condiciones de Alta Humedad Relativa." *Revista de la Sociedad Española de Mineralogía*. 13 (2010) 103 – 104.

Goodwin, J.W. (ed); *Colloid Dispersions*. The Royal Society of Chemistry, 1981.

Grant, T. "Conservation of Wet Faunal Remains: Bone, Antler and Ivory." *CCI Notes 4/3*. Canadian Conservation Institute, 2007.

Gronow, J.R.; "Mechanisms of Particle Movement in Porous Media." *Clay Minerals*. 21 (1986) 753 – 767.

Gummerson, R.J.; Hall, C.; Hoff, W.D.; "Water movement in porous building materials – II. Hydraulic suction and sorptivity of brick and other masonry materials." *Building and Environment*. 15 (1980) 101 – 108.

Hadingham, E. "Uncovering Secrets of the Sphinx." *Smithsonian Magazine*. February 2010. [Online] Available from: http://www.smithsonianmag.com/history-archaeology/Uncovering-Secrets-of-the-Sphinx.html?c=y&page=2. [Accessed: 6/8/11].

Hall, C.; Hoff, W.D.; *Water Transport in Brick, Stone and Concrete*, 2nd edition. Oxon: Taylor & Francis, 2012.

Hallet, P.D.; Ritz, K.; Wheatley, R.E.; "Microbial Derived Water Repellency in Golf Course Soil." *International Turfgrass Society Research Journal*. 9 (2001) 518 – 524.

Hallet, P.D.; Nunan, N.; Douglas, J.T.; Young, I.M.; "Millimeter-Scale Spatial Variability in Soil Water Sorptivity: Scale, Surface Elevation, and Subcritical Repellency Effects." *Soil Science Society of America Journal*. 68 (2004) 352 – 258.

Hamilton, A.; Koutsos, V.; Hall, C.; "Direct Measurement of Salt-Mineral Repulsion using Atomic Force Microscopy." *Chemical Communications*. 46 (2010) 5235 – 5237.

Harding, I.S.; Rashid, N.; Hing, K.A.; "Surface Charge and the Effect of Excess Calcium Ions on the Hydroxyapatite Surface." *Biomaterials*. 26 (2005) 6818 – 6826.

Hawass, Z. *The Secrets of the Sphinx: Restoration Past and Present*, 3rd edition. The American University in Cairo Press, 2000.

Heilmann, F.; Standard, O.C.; Muller, F.A.; Hoffman, M.; "Development of Graded Hydroxyapatite/CaCO3 Composite Structures for Bone Ingrowth." *Jounal of Material Science: Material Medicine*. 18 (2007) 1817 – 1824.

Henry, A. Senior Architectural Conservator, Building Conservation and Research Team, English Heritage. *Personal Communication*, 29/6/11.

Hirst, E. "Consideration of Nano Lime for Consolidation of Stone and Medieval Wall Paintings, Including Preliminary Testing." A presentation in *Stonecore: Nano Materials for Stone and Mortar Strengthening Conference,* Peterborough, United Kingdom, 7-8 June 2011.

Holdich, R.; *Fluid Flow in Porous Media*, [Online] Available at: http://vimeo.com/10201454 [Accessed: 10/3/13]

Hosokawa, M.; Nogi, K.; Naito, M.; Yokoyama, T.; *Nanoparticle Technology Handbook*, 2nd edition, Elsevier, 2012.

Howe, E. "A Report on the Conservation of the Lichfield Angel." *Report for the Dean and Chapter of Lichfield Cathedral*, Emily Howe 2007.

Hudson, K. *The Fashionable Stone*, 1st edition. Prescot: C. Tinling & Company Limited, 1971.

Hughes, J.J.; Cuthbert, S.J.; "The Petrography and Microstructure of Medieval Lime Mortars from the West of Scotland: Implications for the Formulation of Repair and Replacement Mortars." *Materials and Structures/Materiaux et Constructions*. 33 (2000) 594 – 600.

IBZ-Salzchemie Gmbh & Co.KG, *Product List 15. Feb 2013*. IBZ-Salzchemie Gmbh & Co.KG, Germany, 2013.

Ioannou, I.; Hoff, W.D.; Hall, C.; "On the Role of Organic Adlayers in the Anomalous Water Sorptivity of Lepine Limestone." *Journal of Colloid and Interface Science*. 279 (2004) 228 – 234.

Ioannou, I.; Hamilton, A.; Hall, C.; "Capillary Absorption of Water and n-Decane by Autoclaved Aerated Concrete." *Journal of Cement and Concrete Research*. 38 (2008) 766 – 771.

Isler, M. *Sticks, Stones and Shadows: Building the Egyptian Pyramids*, University of Oklahoma Press, 2001.

Israelachvili, J.; *Intermolecular and Surface Forces*, 2nd edition. Elsevier Academic Press, 2006 (Reprint).

Johnson, J.S. "Consolidation of Archaeological Bone: A Conservation Perspective." *Journal of Field Archaeology*, 21 (1994) 221 – 233.

Karim, K.H.; Ameen, B.M; *Facies Analysis of the Early Cretaceous Arabian Platform*. [Online] Available from: http://kurdistan-geology.com/?p=448 [Accessed: 25/10/12].

Kasioptas, A.; Perdikouri, C.; Putnis, C.V.; Putnis, A.; "Pseudomorphic Replacement of Single Calcium Carbonate Crystals by Polycrystalline Apatite." *Mineralogical Magazine*. 72 (2008) 77 – 80.

Kirkup, L.; Frenkel, B.; *An Introduction to Uncertainty in Measurement*, Cambridge University Press, 2006.

Kolinkeova B.; Bayer, K.; Macounova, D.; Machacko, L.; "Practical Experience and Results of the Use of Lime Nanosols." A presentation in *Stonecore: Nano Materials for Stone and Mortar Strengthening Conference,* Peterborough, United Kingdom, 7-8 June 2011.

Konigsberger, E. (ed.); Konigsberger, LC. (ed.); *Biomineralization. Medical Aspects of Solubility*. Wiley, 2006.

Koronthalyova, O., "Moisture storage capacity and microstructure of ceramic brick and autoclaved aerated concrete." *Construction and Building Materials*, 25 (2011) 879 – 885.

Lavoie, B.; Mayes, M.A.; McKay, L.D.; "Transport of Explosive Residue Surrogates in Saturated Porous Media." *Water Air and Soil Pollution*. (2011), DOI: 10.1007/s11270-011-0999-y (2011).

Leary, E. *The Building Limestones of the British Isles*, 2nd edition, HMSO Publications, 1989.

Lee, J.; Shin, M.; Ahn, C.-G.; Ah, C.S.; Park, C.W.; Sung, G.Y.; "Effects of pH and Ion Concentration in a Phosphate Buffer Solution on the Sensitivity of Silicon Nanowire BioFETs." *Journal of the Korean Physical Society*. 55 (2009) 1621 – 1625.

Lincoln Cathedral. [Online] Available from: http://lincolncathedral.com/. [Accessed: 28/2/12].

Lopez-Arce, P.; Gomez-Villalba, L.S.; Pinho, L.; Fernandez-Valle, M.E.; Alvarez de Buergo, M.; Fort, R.; "Influence of Porosity and Relative Humidity on Consolidation of Dolostone with Calcium Hydroxide Nanoparticles: Effectiveness Assessment with Non-Destructive Techniques." *Materials Characterisation*, 2009. [Accessed online: 13/1/2010].

Lopez-Polin, L.; Olle, A.; Caceres, I.; Carbonell, E.; de Castro, J.M.B.; "Pleistocene Human Remains and Conservation Treatments: the Case of a Mandible from Atapuerca (Spain)." *Journal of Human Evolution*, 54 (2008) 539 – 545.

Lovell, N.C.; Rossi, D.; de Gruchy, S.; "A Comparative Experiment in the Consolidation of Cremated Bone." *International Journal of Osteoarchaeology*, 14 (2004) 104 – 111.

Maryniak-Piaszczynski, E.; Egloffstein, P.; Ziegenbalg, G.; "The Portal in Tholey – Unconventional Method for the Preservation of Scaling and Shelled Sandstone (Rotliegend-Sandstone)." In *Proceedings of the 11th International Congress on Deterioration and Conservation of Stone, 15–20 September 2008, Torun´, Poland*. (edited by J.W. Lukaszewicz, and P. Niemcewicz). Torun´, Poland: Nicolaus Copernicus University (2008) 1247 – 1256.

Maryniak-Piaszczynski, E.; Ziegenbalg, G.; "Nano-Lime as a Binder for Injection Grouts and Repair Mortars." In *Proceedings of the 2nd Historic Mortars Conference HMC2010 and RILEM TC 203-RHM Final Workshop, Prague, Czech Republic, 22-24 September 2010.* (edited by J. Valek, C. Groot, and J.J. Huges). RILEM Publications S.A.R.I. (2010) 1159-1167.

Maryniak-Piaszczynski, E. "Nano-lime and the Combination of Nano-lime and Silicic Acid Esters as New Possibility for the Structural Consolidation of Scaling and Peeling Surfaces." A presentation in *Stonecore: Nano Materials for Stone and Mortar Strengthening Conference,* Peterborough, United Kingdom, 7-8 June 2011.

Masterton, W.L.; Bolocofsky, D.; Lee, T.P.; "Ionic Radii from Scaled Particle Theory of the Salt Effect." *Journal of Physical Chemistry*. 75 (1971) 2809 – 2815.

Mathew, M.; Takagi, S.; "Structures of Biological Minerals in Dental Research." *Journal of Research of the National Institute of Standards and Technology*, 106 (2001) 1035 – 1044.

Matsumoto, M.; Miyake, T.; Noshi, H.; Kambara, M.; Konishi, K; "Zeta Potential Studies on the Adsorption of Proteins on a Synthetic Hydroxyapatite." *Colloids and Surfaces*. 40 (1989) 77 – 84.

McDowell-Boyer, L.M; Hunt, J.R.; Sitar, N.; "Particle Transport Through Porous Media." *Water Resource Research*, 22 (1986) 1901 – 1921.

McGowan, G.S.; LaRoche, C.T.; "The Ethical Dilemma Facing Conservation: Care and Treatment of Human Skeletal Remains and Mortuary Objects." *Journal of the American Institute for Conservation*. 35 (1996) 109 – 121.

Mehra, A.; Sugih, A.K.; Shukla, D.; Heeres, H.J.; "CaCO3 Nanoparticle Synthesis by Carbonation of Lime Solution in Microemulsion Systems." *Nanotechnology*. 18 (2007), DOI:10.1088/0957-4484/18/3/035607.

Merkus, H.G., *Particle Size Measurements*. Springer, 2009.

Mochales, C.; El Briak-Benabdeslam, H.; Ginebra, M.P.; Terol, A.; Planell, J.A.; Boudeville, P.; "Dry Mechanochemical Synthesis of Hydroxyapatites from DCPD and CaO: Influence of Instrumental Parameters on the Reaction Kinetics." *Biomaterials*. 25 (2004) 1151 – 1158.

NanoSight. *Application Note*. NanoSight Ltd, 2010.

Narayanan, N.; Ramamurthy, K.; "Structure and Properties of Aerated Concrete: a Review." *Cement and Concrete Composites*. 22 (2000) 321 – 329.

Nazzal, F.F.; Wiesner, M.R.; "pH and Ionic Strength Effects on the Performance of Ceramic Membranes in Water Filtration." *Journal of Membrane Science*. 93 (1994) 91 – 103.

Ortner, D.J.; Putschar, W.G.J.; *Identification of Patholodical Conditions in Human Skeletal Remains*. Smithsonian Institution Press, City of Washington, Smithsonian Contributions to Anthropology, 28, (1981).

Parsegian, V.A.; *Van der Waals Forces. A Handbook for Biologists, Chemists, Engineers and Physicists*. Cambridge University Press, 2006

Parsons, D.F.; Bostrom, M.; Lo Nostro, P.; Ninham, B.W.; "Hofmeister Effects: Interplay of Hydration, Nonelectrostatic Potentials, and Ion Size." *Physical Chemistry Chemical Physics*. 13 (2011) 12352 – 12367.

Pettijohn, F.J.; Potter, P.E.; Siever, R.; *Sand and Sandstone,* 2nd edition, Springer-Verlag, 1987.

Plassard, C.; Lesniewska, E.; Pochard, I.; Nonat, A.; "Nanoscale Experimental Investigation of Particle Interactions at the Origin of the Cohesion of Cement." *Langmuir*. 21 (2005) 7263 – 7270.

Potocnik, J., *Commission Recommendation of 18 October 2011 on the Definition of Nanomaterial*, The European Commission, Official Journal of the European Union, (2011) 38 – 40.

Price, T.D.; Manzanilla, L.; Middleton, W.D.; "Immigration and the Ancient City of Teotihuacan in Mexico: a Study Using Strontium Isotope Ratios in Human Bone and Teeth." *Journal of Archaeological Science*, 27 (2000) 903 – 913.

Rao, R.R.; Roopa, H.N.; Kannan, T.S.; "Solid State Synthesis and Thermal Stability of HAP and HAP – β-TCP Composite Ceramic Powders."*Journal of Materials Science: Materials in Medicine*. 8 (1997) 511 – 518.

Roels, S. *Modelling Unsaturated Moisture Transport in Heterogeneous Limestone*. Ph.D. Dissertation. Leuven, Belgium: Katholiek Universiteit Leuven, 2000. Published by Katholiek Universiteit Leuven. [Online] Available from: http://www.carmeliet.arch.ethz.ch/Publications/Publications?action=download&upname=T-Roels.pdf [Accessed: 1/2/11]

Roels, S.; Sermijn, J.; Carmeliet, J.; "Modelling Unsaturated Moisture Transport in Autoclaved Aerated Concrete: a Microstructural Approach." in *Proceedings of the 6th Symposium on Building Physics in the Nordic Countries*, Norwegian Building Research Institute and Norwegian University of Science and Technology, Trondheim, Norway, 2002.

Roels, S.; Carmeliet, J.; Hens, H.; "Hamstad WP1: Final Report, Moisture Transfer Properties and Materials Characterisation." *HAMSTAD project*, KU Leuven, Laboratory of Building Physics, K U Leuven, 2003.

Roels, S.; Carmeliet, J.; Hens, H.; Adan, O.; Brocken, H.; Cerny, R.; Pavlik, Z.; Hall, C.; Kumaran, K.; Pel, L.; Plagge, R.; "Interlaboratory comparison of the hygric properties of building materials." *Journal of Thermal Envelope and Building Science*. 27 (2004) 307 – 325.

Samek, O.; Beddows, D.C.S.; Telle, H.H.; Kaiser, J.; Liska, M.; Caceres, J.O.; Urena, A.G.; "Quantitative Laser-Induced Breakdown Spectroscopy Analysis of Calcified Tissue Samples." *Spectrochimica Acta Part B*, 56 (2001) 865 – 875.

Santos, A.; Bedrikovetsky, P.; "Size Exclusion During Particle Suspension Transport in Porous Media: Stochastic and Averaged Equations." *Computational Applied Mathematics*. 24 (2004) 259 – 284.

Schwartz, J.; Norris, G.; Larson, T.; Sheppard, L.; Claiborne, C.; Koenig, J. "Episodes of High Coarse Particle Concentrations are not Associated with Increased Mortality." *Environmental Health Perspectives*. 107 (1999) 339 – 342.

Shannon, R.D.; "Revised Effective Ionic Radii and Systematic Studies of Interatomic Distances in Halides and Chalcogenides." *Acta Crystallographica*. A32 (1976) 751 – 767.

Simeonova, P.P.; Opopol, N.; Luster, M.I.; *Proceedings of the NATO Advanced Research Workshop on Nanotechnology*. Varna, Bulgaria. Series C: Environmental Security, Springer (2007).

Slížková, Z. "Effects of CaLoSiL Impregnation on Consolidation of Selected Porous Building Materials." A presentation in *Stonecore: Nano Materials for Stone and Mortar Strengthening Conference,* Peterborough, United Kingdom, 7-8 June 2011.

Smithsonian Institution Collections [Online] Available from: http://collections.si.edu/. [Accessed: 29/3/12].

Somasundaran, P.; Agar, G.E.; "The Zero Point of Charge of Calcite." *Journal of Colloid and Interface Science*. 24 (1967) 433 – 440.

Somasundaran, P.; "Zeta Potential of Apatite in Aqueous Solutions and its Change During Equilibration." *Journal of Colloid and Interface Science*. 27 (1968) 659 – 666.

Stone, T. "Care of Ivory, Bone, Horn and Antler." *CCI Notes 6/1*. Canadian Conservation Institute, 2010.

Stonecore [Online] Available from: http://www.stonecore-europe.eu/index.php. [Accessed: 28/1/2012].

Sullivan. C.H.; Krueger, H.W.; "Carbon Isotope Analysis of Separate Chemical Phases in Modern and Fossil Bone." *Nature*. 292 (1981).

Taglieri, G.; Daniele, V.; Quaresima, R.; "The Nanolimes in Cultural Heritage Conservation: Characterisation and Analysis of the Carbonation Process." *Journal of Cultural Heritage*. 9 (2008) 294 – 301.

Taylor, S.C.; Hall, C.; Hoff, W.D.; Wilson, M.A.; "Partial Wetting in Capillary Liquid Absorption by Limestones." *Journal of Colloid and Interface Science*. 224 (2000) 351 – 357.

Taylor, P.D.; Wilson, M.A.;"Palaeoecology and Evolution of Marine Hard Substrate Communities." *Earth-Science Reviews*. 62 (2003) 1 – 103.

Tseng, Y.H.; Kuo, C.S.; Li, Y.Y.; Huang, C.P.; "Polymer-Assisted Synthesis of Hydroxyapatite Nanoparticle." *Materials Science and Engineering C*. 29 (2009) 819 – 822.

Turner-Walker, G.; Parry, T.V.; "The Tensile Strength of Archaeological Bone." *Journal of Archaeological Science*. 22 (1995) 185 – 191.

Tykot, R.H.; van der Merwe, N.J.; Hammond, N.; "Stable Isotope Analysis of Bone Collagen, Bone Apatite, and Tooth Enamel in the Reconstruction of Human Diet. A Case Study from Cuello, Belize." in *Archaeological Chemistry*, American Chemical Society (1996) 355-365.

United States National Nanotechnology Initiative [Online] Available from: http://www.nano.gov/. [Accessed: 29/3/12].

University of Exeter [Online] Available from: http://emps.exeter.ac.uk/csm/facilities/geochem-mineralogy/x-ray-diffraction/. [Accessed: 10/6/13].

Waite, T.D.; Schäfer, A. I.; Fane, A. G.; Heuer, A.; "Colloidal fouling of ultrafiltration membranes: impact of aggregate structure and size." *Journal of Colloid and Interface Science*. 212 (1998) 264 – 274.

Wang, F.; Li, M.S.; Lu, Y.P.; Qi, Y.X.; "A Simple Sol-Gel Technique for Preparing Hydroxyapatite Powders." *Materials Letters*. 59, (2005) 916–919.

Wang, X.Y.; Zou, Y.; Huang, D.; Hou, X.D.; Li, Y.B.; "Comparative Study on Inorganic Composition and Crystallographic Properties of Cortical and Cancellous Bone." *Biomedical and Environmental Sciences*, 23 (2010) 473 – 480.

Webster, T.J.; Gorth, D.J.; Rand, D.M.; "Silver Nanoparticle Toxicity in Drosophila: Size Does Matter." *International Journal of Nanomedicine*. 6 (2011) 343 – 350.

Wilson, M.; Hoff, W.D.; Hall, C.; "Water Movement in Porous Building Materials – XIII. Absorption into a Two-Layer Composite." *Building and Environment*. 30 (1995) 209 – 219.

Wilson, M.; Hoff, W.D.; Hall, C.; "Water Movement in Porous Building Materials – XIV. Absorption into a Two-Layer Composite (SA < SB)." *Building and Environment*. 30 (1995) 221 – 227.

Yousuf, M.; Mollah, A.; Vempati, R.K.; Lin, T.-C.; Cocke, D.L.; "The Interfacial Chemistry of Solidification/Stabilization of Metals in Cement and Pozzolanic Material Systems." *Waste Management*. 15 (1995) 137 – 148.

Zahn, M. "Magnetic Fluid and Nanoparticle Applications to Nanothechnology." *Journal of Nanoparticle Research*. 3 (2001) 73 – 78.

Ziegenbalg, G. "Colloidal calcium hydroxide: A New Material for Consolidation and Conservation of Carbonatic Stones." In *Proceedings of the 11th International Congress on Deterioration and Conservation of Stone, 15–20 September 2008, Torun´, Poland*. (edited by J.W. Lukaszewicz, and P. Niemcewicz). Torun´, Poland: Nicolaus Copernicus University, (2008) 1109 – 1115.

Ziegenbalg, G.; Brümmer, K.; Pianski, J.; "Nano-Lime - a New Material for the Consolidation and Conservation of Historic Mortars." In *Proceedings of the 2nd Historic Mortars Conference HMC2010 and RILEM TC 203-RHM Final Workshop, Prague, Czech Republic, 22-24 September 2010.* (edited by J. Valek, C. Groot, and J.J. Huges). RILEM Publications S.A.R.I. (2010) 1301 – 1309.

Ziegenbalg, G. “Nano-Particles for the Conservation of Stone, Mortar and Plaster State of the Art, Characteristics and Recent Developments.” A presentation in *Stonecore: Nano Materials for Stone and Mortar Strengthening Conference,* Peterborough, United Kingdom, 7-8 June 2011.

Appendix A: Abbreviations, Symbols and Chemical Formulae

Abbreviations

3D	3 dimensional
AAC	Autoclaved aerated concrete
cc	Cubic centimetre
CCD	Charge coupled device
CRG	Capillary rise with gravity
DIC	Digital image correlation
DLS	Dynamic light scattering
DRMS	Drilling resistance measurement system
EDX	Energy-dispersive X-ray spectroscopy
FT-Raman	Fourier-transform Raman spectroscopy
HAMSTAD	Heat, Air and Moisture Standards Development project
HAP	Hydroxyapatite
HOR	Height of rise
HP	High pressure
iRI	Imaginary refractive index
IS	Ionic strength
LD	Laser diffraction
LP	Low pressure
min	minute
MIP	Mercury intrusion porosimetry
NTA	Nanoparticle tracking analysis
PDD	Photo-diode detectors
PEG	Polyethylene glycol
pH	Measure of the activity of the hydrogen ion

PL	Polarised light
PSD	Particle size distribution
PZC	Point of zero charge
R	Repellency index
RI	Refractive index
rpm	Revolutions per minute
RT	Room temperature
s.d.	Standard deviation
SEM	Scanning electron microscopy
SF	Sharp front model
SI	Saturation index
Stonecore	Conservation for the Refurbishment of Buildings project
TEM	Transmission electron microscopy
XPL	Cross polarised light
XRD	X-Ray diffraction

Symbols

Å	Angstrom
cm	Centimetre
cm^3	Cubic centimetre
^oC	Degrees Celcius
d	Diameter
F	Force
F^c_n	Normal force
F^c_s	Tangential force
Fpa	Parallel force
Fpe	Perpendicular force
g	Gram
i	Cumulative absorbed volume
kg	Kilogram
mL	Millilitre
mm	Millimetre
m^3	Cubic metre
N	Newton
nm	Nanometre
S	Sorptivity
T	Temperature
$t^{1/2}$	Root time
θ_w	Contact angle of water
μ	Mean
μm	Micrometer (micron)

ρ_b	Bulk density
σ	Standard deviation

Chemical Formulae

$AgNO_3$	Silver nitrate
Au-Pd	Gold-palladium
Au-Ta	Gold-tantalum
$CaCl_2$	Calcium chloride
$CaCO_3$	Calcium carbonate (calcite)
$Ca(OH)_2$	Calcium hydroxide
Cl	Chlorine
CO_2	Carbon dioxide
EtOH	Ethanol
H_2O	Water
Na	Sodium
NaCl	Sodium chloride
NaOH	Sodium hydroxide

Appendix B: Calcium Hydroxide Particle Size Distribution Fits

This appendix shows the mean graphical component fits for PSDs obtained by LD of Ca(OH)$_2$ formed from all four sets of experiments discussed in Chapter 3. All graphs show the mean experimental data displayed on a $\log_{10}$ scale against the arbitrary intensity.

Sets 1, 2 & 3: Experiment 1

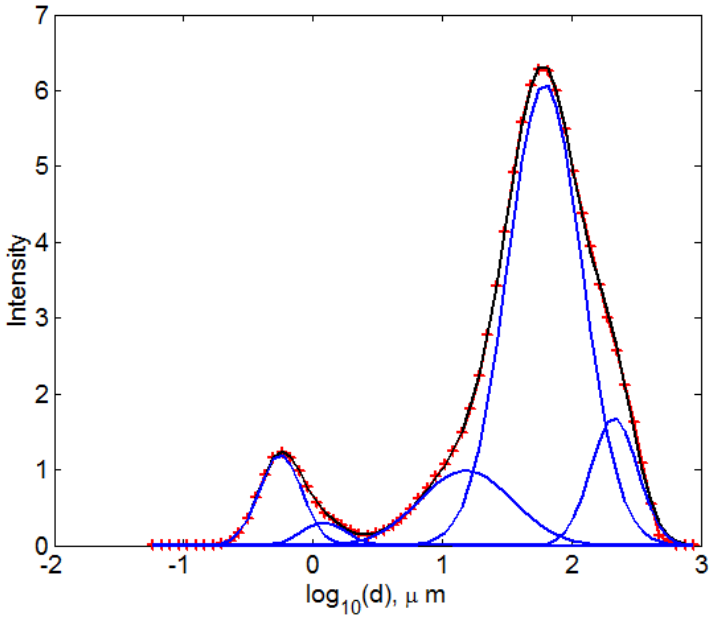

Figure B-1: Peak fitting of mean Set 1 Experiment 1 experimental data (red stars) with five-component fit. The figure shows how five peaks (blue lines) combine to produce the overall PSD, the fit line of which is shown in black.

Set 1: Experiments 2 – 4

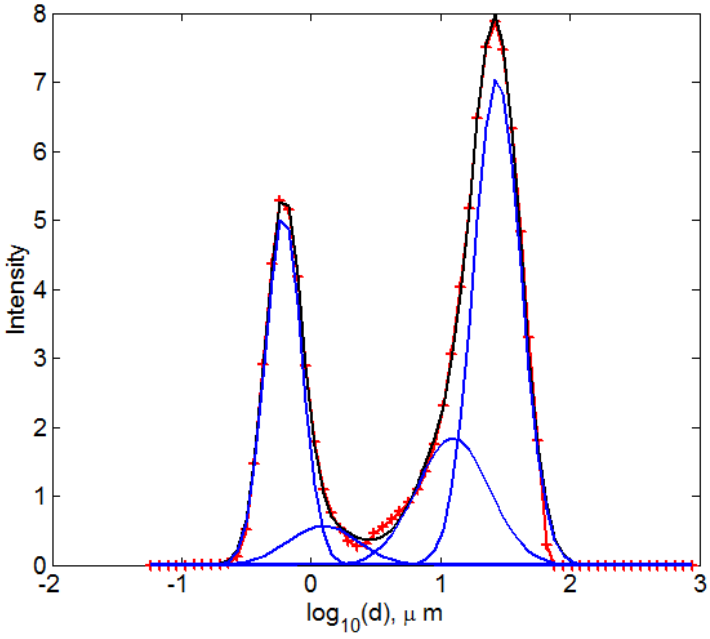

Figure B-2: Peak fitting of mean Set 1 Experiment 2 experimental data (red stars) with five-component fit. The figure shows how five peaks (blue lines) combine to produce the overall PSD, the fit line of which is shown in black.

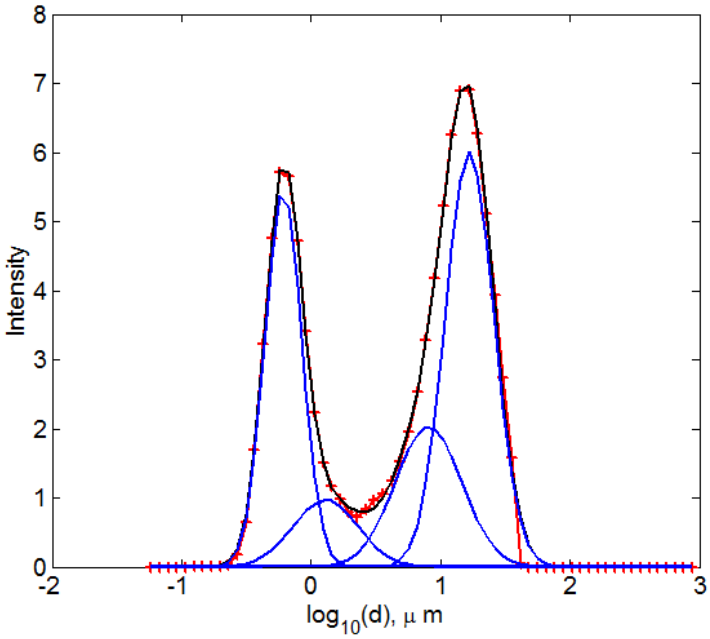

Figure B-3: Peak fitting of mean Set 1 Experiment 3 experimental data (red stars) with four-component fit. The figure shows how four peaks (blue lines) combine to produce the overall PSD, the fit line of which is shown in black.

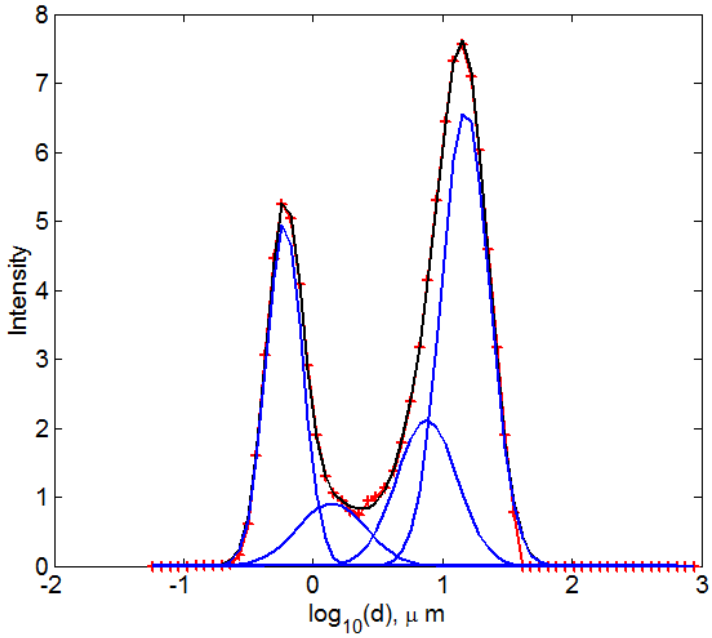

Figure B-4: Peak fitting of mean Set 1 Experiment 4 experimental data (red stars) with four-component fit. The figure shows how four peaks (blue lines) combine to produce the overall PSD, the fit line of which is shown in black.

Set 2: Experiments 2 – 4

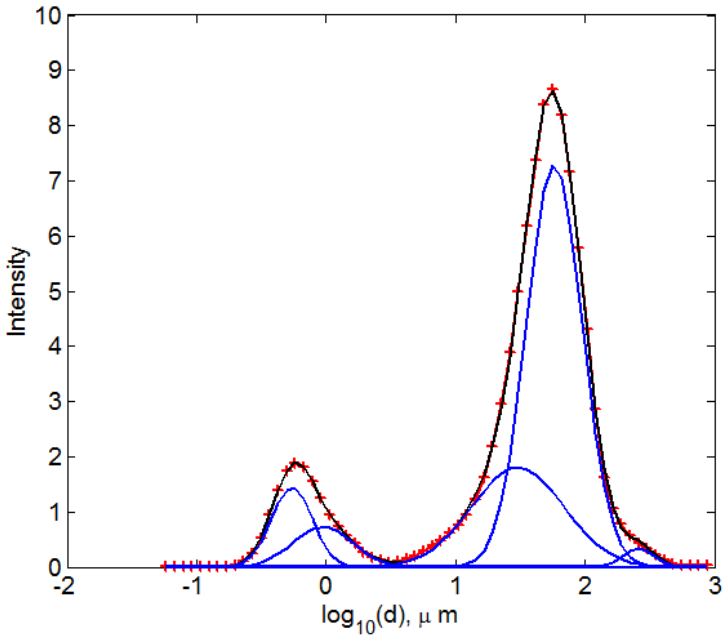

Figure B-5: Peak fitting of mean Set 2 Experiment 2 experimental data (red stars) with five-component fit. The figure shows how five peaks (blue lines) combine to produce the overall PSD, the fit line of which is shown in black.

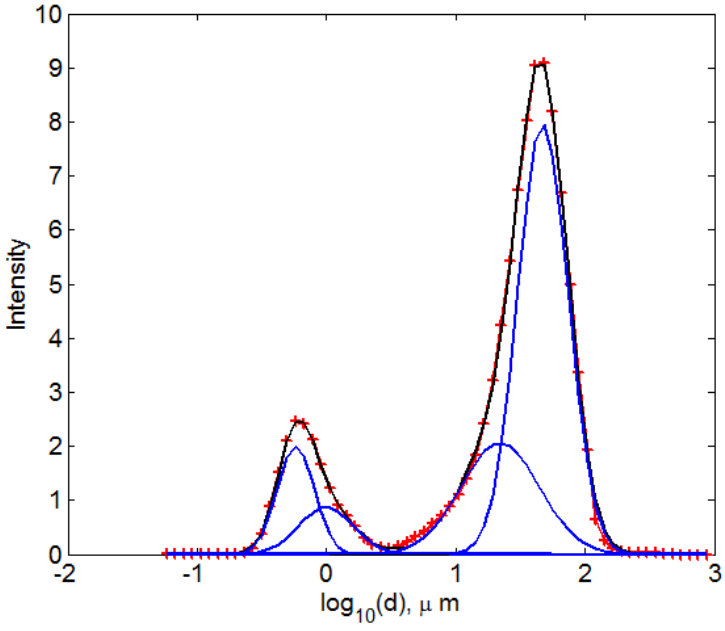

Figure B-6: Peak fitting of mean Set 2 Experiment 3 experimental data (red stars) with four-component fit. The figure shows how four peaks (blue lines) combine to produce the overall PSD, the fit line of which is shown in black.

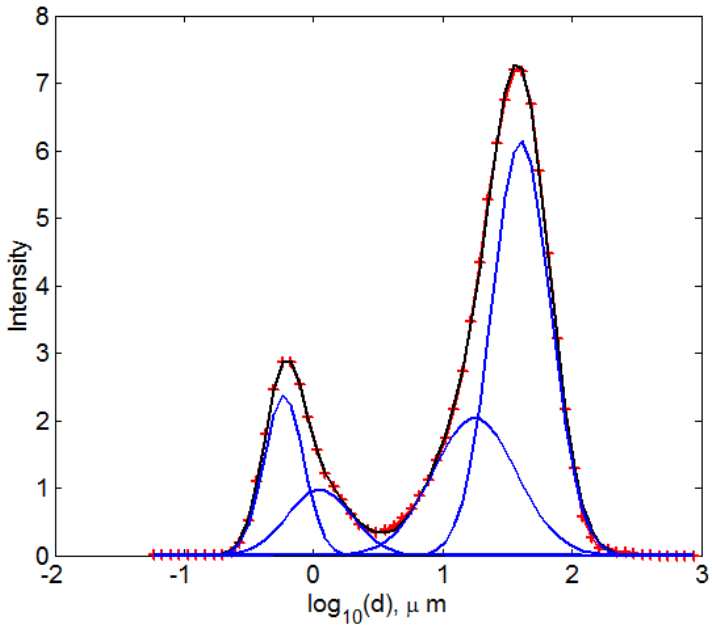

Figure B-7: Peak fitting of mean Set 2 Experiment 4 experimental data (red stars) with four-component fit. The figure shows how four peaks (blue lines) combine to produce the overall PSD, the fit line of which is shown in black.

Set 3: Experiments 2 – 6

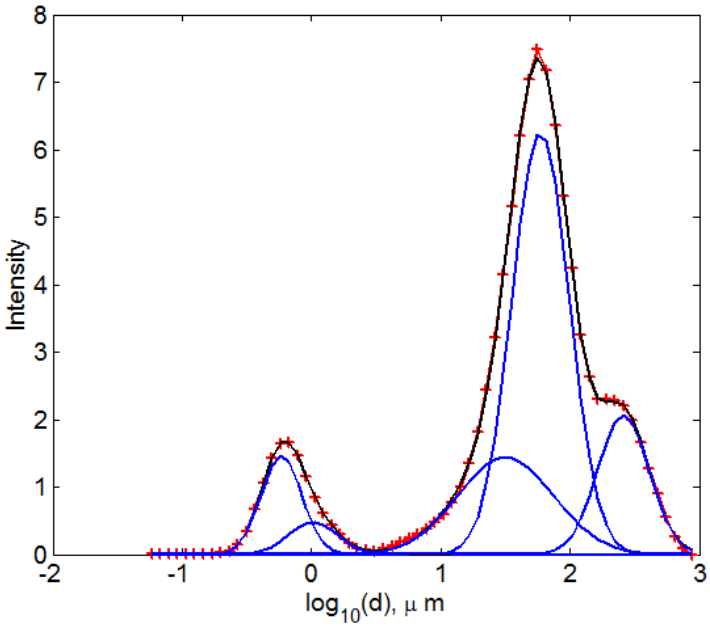

Figure B-8: Peak fitting of mean Set 3 Experiment 2 experimental data (red stars) with five-component fit. The figure shows how five peaks (blue lines) combine to produce the overall PSD, the fit line of which is shown in black.

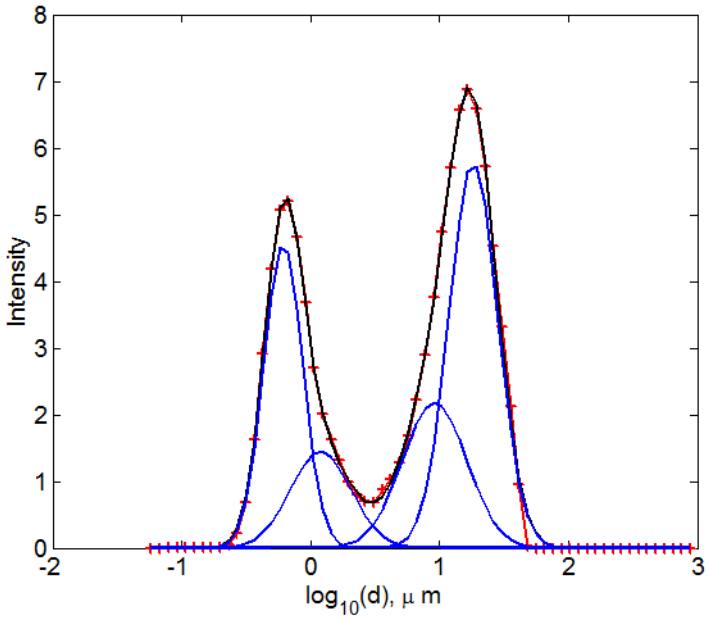

Figure B-9: Peak fitting of mean Set 3 Experiment 3 experimental data (red stars) with four-component fit. The figure shows how four peaks (blue lines) combine to produce the overall PSD, the fit line of which is shown in black.

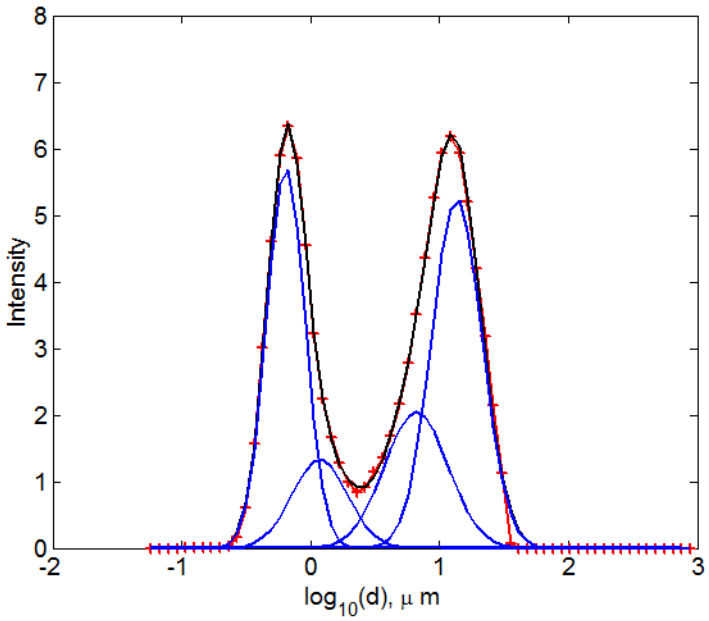

Figure B-10: Peak fitting of mean Set 3 Experiment 4 experimental data (red stars) with four-component fit. The figure shows how four peaks (blue lines) combine to produce the overall PSD, the fit line of which is shown in black.

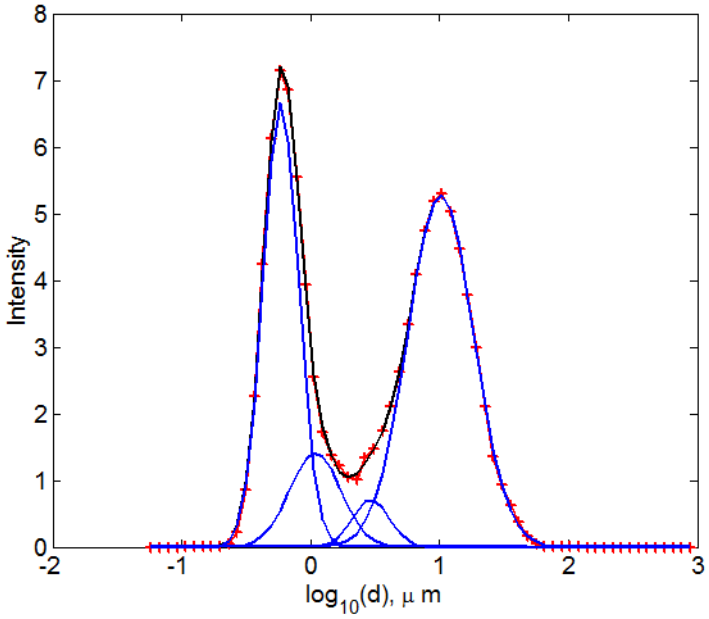

Figure B-11: Peak fitting of mean Set 3 Experiment 5 experimental data (red stars) with four-component fit. The figure shows how four peaks (blue lines) combine to produce the overall PSD, the fit line of which is shown in black.

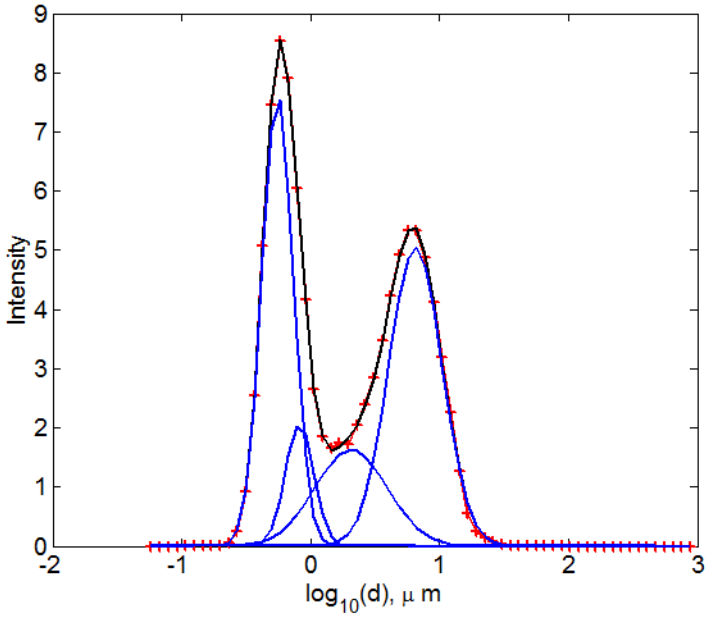

Figure B-12: Peak fitting of mean Set 3 Experiment 6 experimental data (red stars) with four-component fit. The figure shows how four peaks (blue lines) combine to produce the overall PSD, the fit line of which is shown in black.

Set 4: Experiments 1 – 4

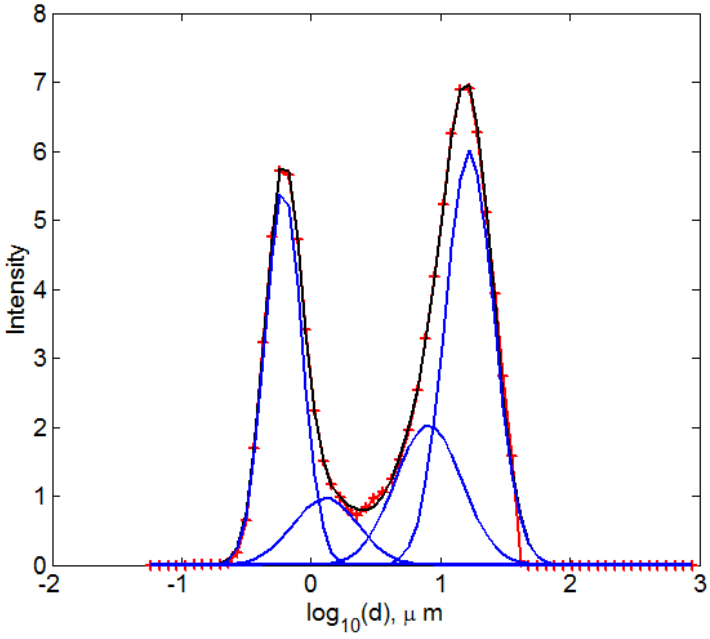

Figure B-13: Peak fitting of mean Set 4 Experiment 1 experimental data (red stars) with four-component fit. The figure shows how four peaks (blue lines) combine to produce the overall PSD, the fit line of which is shown in black.

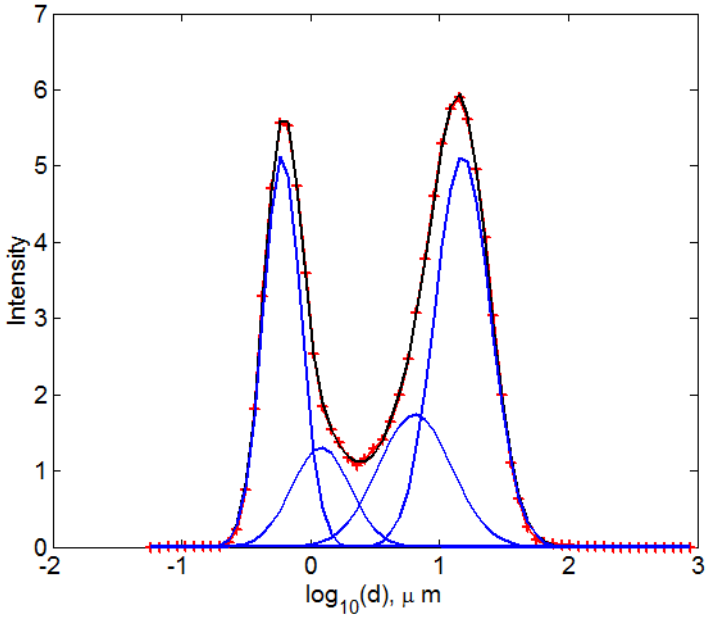

Figure B-14: Peak fitting of mean Set 4 Experiment 2 experimental data (red stars) with four-component fit. The figure shows how four peaks (blue lines) combine to produce the overall PSD, the fit line of which is shown in black.

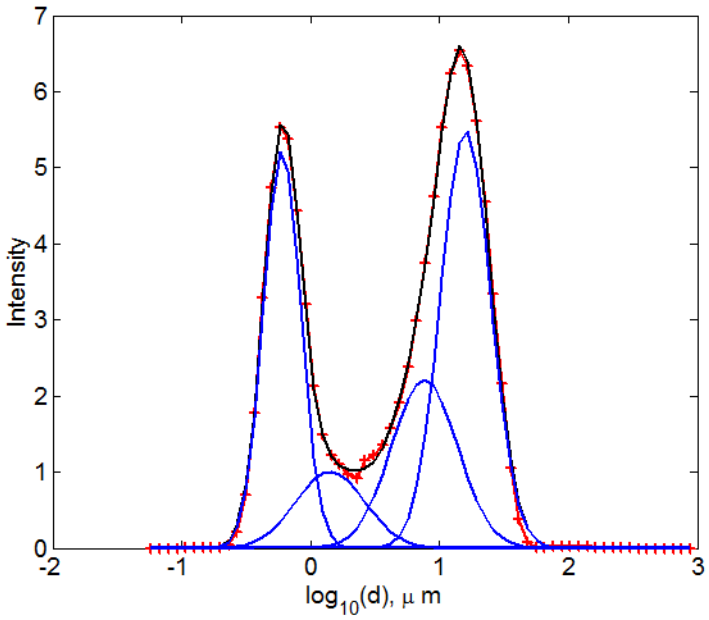

Figure B-15: Peak fitting of mean Set 4 Experiment 3 experimental data (red stars) with four-component fit. The figure shows how four peaks (blue lines) combine to produce the overall PSD, the fit line of which is shown in black.

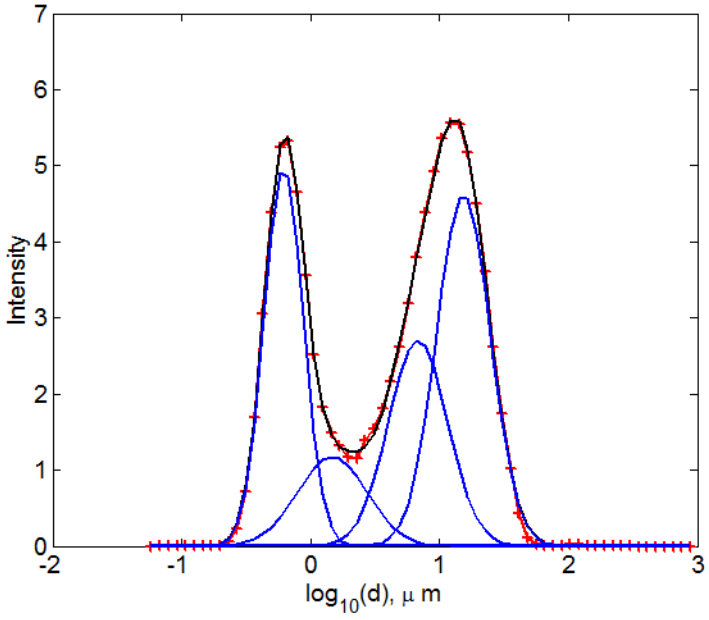

Figure B-16: Peak fitting of mean Set 4 Experiment 4 experimental data (red stars) with four-component fit. The figure shows how four peaks (blue lines) combine to produce the overall PSD, the fit line of which is shown in black.

Appendix C: Calculations for Obtaining Additional Material Properties

This appendix describes calculations undertaken in this study and covers: air trapping, height of rise, cumulative absorption, water repellency index and contact angle of water.

Air Trapping

The quantity of trapped air in a material can be known by the difference between the water saturated material weight obtained by vacuum saturation and the weight after imbibition of water by capillary uptake to the top of the material. The percentage of air trapping can be given by Equation C-1.

C-1) $$A = 100 - \left[\left(\frac{M_i}{M_v}\right) \times 100\right]$$

where M_i is the wet mass after imbibition and M_v is the wet mass after vacuum saturation.

Height of Rise

The height of rise (HOR) of a liquid is the length the wet front travels within the material and can be expressed by Equation C-2. HOR is commonly quoted in units of millimetres. The main issue when calculating HOR is the porosity value used. Because air trapping nearly always occurs, the effective porosity will usually be less than the total porosity by approximately 10 – 15 %.

C-2) $$HOR = M_g/(fa\rho) \times 10$$

where M_g = mass gain, ρ = density of the liquid, a = wicking area and f = material porosity.

The wicking area is the surface area exposed to the liquid. Both the wicking area and the liquid density are in units of cm^2 and g/cm^3 respectively, hence the conversion factor of 10 in the equation.

Cumulative Absorption

The cumulative absorption (i) of a material can be obtained from the volume of liquid absorbed by the material per area of the wicking surface as given by Equation C-3. The units of i are usually reported in millimetres.

C-3) $$i = \left(\frac{V}{a}\right) \times 10$$

where a is the area of the wicking surface in cm^2 and V is volume of liquid absorbed in cm^3 which can be obtained by Equation C-4.

C-4) $$V = \frac{M_g}{\rho}$$

where M_g is the mass gain of the material and ρ is the density of the liquid in g/cm^3.

Water Repellency Index

The water repellency index (R), given by equation C-5, is proportional to the reduction in water sorptivity caused by the material repelling the water. It is most commonly used in soil science to determine a factor by which the actual water sorptivity is reduced from what would reasonably be expected. For no water repellency R = 1 and as the water repellency increases the WRI increases rapidly going to infinity as the water sorptivity goes to zero. An R value of greater than 1.95 will exhibit hydrophobicity (repel water) (Hallet 2004).

C-5) $$R = 1.95\left(\frac{S_e}{S_w}\right)$$

where S_e and S_w are the ethanol and water sorptivities respectively.

The water repellency index is similar to the wetting index used by Hall & Hoff (2012).

Contact Angle of Water

The contact angle of water with a solid material has an effect on the capillary uptake of the liquid and can be calculated by equation C-6. As discussed by Anderson (1986) the wettability can be determined by the water contact angle with three possible states; water wet (hydrophilic), oil wet (hydrophobic) and intermediate wet (mixed wettability). The angle ranges for these states are between 0^o and 60^0-75^o, 60^0-75^o and 105^o-120^o and 105^o-120^o and 180^o for hydrophilic, intermediate and hydrophobic respectively (Anderson 1986, Al-Garni 2008).

C-6) $$cos\,\theta_w = \left(\frac{S_w}{S_e}\right)^2 \times \left(\frac{\eta_w}{\eta_e}\right) \times \left(\frac{\sigma_e}{\sigma_w}\right)$$

where θ_w is the water contact angle, *Sw* and *Se* are the water and ethanol sorptivities respectively, η_w and η_e are the water and ethanol viscosities respectively and σ_w and σ_e are the water and ethanol surface tensions respectively (Czachor 2008).

Appendix D:
Conference Proceedings

Conference Publication

Campbell, A.; Hamilton, A.; Stratford, T.; Modestou, S.; Ioannou, I.

"Calcium hydroxide nanoparticles for limestone conservation: imbibitions and adhesion."

In Proceedings of Symposium 2011 Adhesives and Consolidants for Conservation: Research and Applications, Canadian Conservation Institute, Ottawa, Canada, 2011.

Conference Presentation

Campbell, A.

"Calcium hydroxide nanoparticles for limestone conservation: imbibitions and adhesion."

Presented at Symposium 2011 Adhesives and Consolidants for Conservation: Research and Applications, Canadian Conservation Institute, Ottawa, Canada, 2011.

Conference Demonstration

Campbell, A.

"Effects of calcium hydroxide nanoparticle consolidants on limestone."

Demonstrated at Symposium 2011 Adhesives and Consolidants for Conservation: Research and Applications, Canadian Conservation Institute, Ottawa, Canada, 2011.